

Quantum properties of atomic-sized conductors

Nicolás Agraït

*Laboratorio de Bajas Temperaturas, Departamento de Física de la Materia Condensada C-III,
and Instituto Universitario de Ciencia de Materiales “Nicolás Cabrera”,
Universidad Autónoma de Madrid, E-28049 Madrid, Spain*

Alfredo Levy Yeyati

*Departamento de Física Teórica de la Materia Condensada C-V,
and Instituto Universitario de Ciencia de Materiales “Nicolás Cabrera”,
Universidad Autónoma de Madrid, E-28049 Madrid, Spain*

Jan M. van Ruitenbeek

*Kamerlingh Onnes Laboratorium, Universiteit Leiden,
Postbus 9504, 2300 RA Leiden, The Netherlands
(Dated: February 7, 2020)*

Using remarkably simple experimental techniques it is possible to gently break a metallic contact and thus form conducting nanowires. During the last stages of the pulling a neck-shaped wire connects the two electrodes, the diameter of which is reduced to single atom upon further stretching. For some metals it is even possible to form a chain of individual atoms in this fashion. Although the atomic structure of contacts can be quite complicated, as soon as the weakest point is reduced to just a single atom the complexity is removed. The properties of the contact are then dominantly determined by the nature of this atom. This has allowed for quantitative comparison of theory and experiment for many properties, and atomic contacts have proven to form a rich test-bed for concepts from mesoscopic physics. Properties investigated include multiple Andreev reflection, shot noise, conductance quantization, conductance fluctuations, and dynamical Coulomb blockade. In addition, pronounced quantum effects show up in the mechanical properties of the contacts, as seen in the force and cohesion energy of the nanowires. We review this research, which has been performed mainly during the past decade, and we discuss the results in the context of related developments.

Contents

I. Introduction	3	2. The concept of eigenchannels	18
A. The scope of this review	4	3. Shot Noise	19
1. A brief history of the field	4	4. Thermal transport	20
B. Outline of this review	6	5. Limitations of the scattering approach	21
II. Fabrication of metallic point contacts	6	E. Relation to other formulations: Kubo formula and Green function techniques	22
A. Early developments: spear-anvil and related techniques	7	1. The conductance in terms of Green functions	23
B. The use of scanning tunneling microscopes	7	IV. Theory for current transport in superconducting point contacts	24
C. The mechanically controllable break junction technique	9	A. The Bogoliubov de Gennes equation and the concept of Andreev reflection	24
1. Description of the MCBJ technique	9	B. SNS contacts at zero bias	26
2. Microfabrication of MCBJ devices	10	C. SNS contacts at finite bias voltage	26
3. Calibration of the displacement ratio	11	D. Current biased contacts	28
4. Special sample preparations	12	V. The conductance of atomic-sized metallic contacts: experiment	29
D. Force measurements	12	A. Contact making and breaking	29
E. Nanofabricated contacts	14	B. Jump to contact	31
F. Relays	14	C. Single-atom contacts	33
III. Theory for the transport properties of normal metal point contacts	15	D. Conductance histograms	34
A. Introduction	15	1. The archetypal metal: gold	35
B. Classical Limit (Maxwell)	15	2. Free electron metals: Li, Na and K	36
C. Semiclassical approximation for ballistic contacts (Sharvin)	16	3. The noble metals	37
D. The scattering approach	17	4. Transition metals	38
1. The Landauer formula	18	5. Ferromagnetic metals	38
		6. Aluminum and other <i>sp</i> -metals	40

7. Semimetals and semiconductors	40	IX. Corrections to the bare contact conductance	72
8. Metallic alloys and compounds	41	A. Conductance fluctuations	73
E. Non-linear conductance	42	1. Theory for defect scattering near a point contact	73
VI. Mechanical properties of atomic-sized point contacts	42	2. Experimental results	75
A. Mechanical properties of metals	43	3. Thermopower fluctuations	76
1. Elastic deformations	43	B. The series resistance of a quantum point contact	77
2. Plastic deformations	43	C. Inelastic scattering	78
3. Fracture	45	1. Electron-phonon scattering	78
4. Contact mechanics	46	2. Heating in atomic-sized contacts	79
B. Simultaneous measurement of conductance and force	47	D. Kondo scattering on magnetic impurities	81
C. The shape of mechanically drawn metallic contacts	48	E. Non-magnetic Kondo scattering: the 2-channel Kondo problem	83
VII. Model calculations for atomic-sized contacts	50	F. Environmental Coulomb blockade	83
A. Molecular dynamics simulations of contact evolution	50	X. Superconducting quantum point contacts	84
1. Principles of MD simulations	51	A. Supercurrent quantization	85
2. Implementation of MD simulations	52	B. Current-phase relation	85
3. Calculation of conductance in atomistic MD models	52	C. Shot noise in the subgap regime	87
4. Results for simple metals	53	XI. Formation of a conducting wire of single atoms	88
B. Free-electron gas conductance and force models	55	A. Atomic chains in Transmission Electron Microscopy	89
1. Conductance calculations: conditions for the quantization of the conductance	56	B. Atomic chains in low-temperature experiments	90
2. The relation between cross section and conductance: Corrections to Sharvin's formula	58	1. Return distance	90
3. Effect of magnetic fields	58	2. Length histograms	91
4. Nonlinear effects in the conductance	58	3. Evolution of the force in atomic chains	92
5. Simulation of conductance histograms	59	4. Phonon modes in atomic chains	92
6. Quantum effects in the thermodynamic potential	59	C. Other properties of atomic chains at low temperatures	93
7. Quantum effects in the force	61	D. Numerical calculations of the stability and conductance of Au chains	93
C. Tight-binding models for the conductance	61	E. The mechanism behind atomic chain formation: Ir, Pt and Au	95
1. Results for simple model geometries	62	1. Odd-even behavior in the conductance of atomic chains	96
2. Electron-electron interactions and the charge neutrality condition	62	XII. Shell-filling effects in metallic nanowires	97
3. Eigenchannels analysis	63	A. Introduction: shell effects in metallic clusters	97
D. Ab-initio calculations	64	B. Theory for electronic shell effects in nanowires	99
VIII. The character of the conductance modes in a single atom	65	C. Observation of electronic shell effects in nanowires	100
A. Experiments on the superconducting subgap structure	65	1. Supershell effects	102
1. First experiments: the tunneling regime	66	D. Geometric shell effects	102
2. <i>sp</i> -metals: Al and Pb	66	XIII. Conclusion and Outlook	104
3. Transition metals: Nb	68	References	106
4. <i>s</i> -metals: Au	68		
5. Summary of results and discussion	68		
B. Shot noise: saturation of channel transmission	69		
C. Strain dependence of the conductance	70		

I. INTRODUCTION

The electrical and mechanical properties of a piece of any metal are not different, whether its size is millimeters or kilometers. However, as soon as its size approaches the atomic scale all common knowledge about material properties becomes invalid. The familiar Ohm's Law, from which we learn that the resistance of a conductor scales proportional to its length, breaks down. The reason is that the distance an electron travels between two scattering events is typically much larger than the atomic size. The electrons traverse an atomic-sized conductor ballistically, and the resistance becomes independent of its length. In fact, the character of the resistance changes conceptually and it will be necessary to invoke the wave nature of the electrons in the conductor for a proper description. The energy scales involved are so large that quantum effects are visible at room temperature. The chemical nature of the metallic element starts to play an essential role. As a consequence, while in the macroscopic world gold is a better conductor than lead by an order of magnitude, for conduction through a single atom, lead beats gold by a factor of three. The mechanical properties are quite unusual: plastic deformation in a macroscopic metal occurs via dislocation motion. On the other hand, atomic-sized metal wires flow in response to applied stresses via structural rearrangements and their yield strength is one or two orders of magnitude larger than for bulk materials. Not just the electronic properties are to be described in terms of electron waves, but also understanding metallic cohesion of nanometer-size wires requires taking electron waves into account that extend over the entire conductor.

The experimental investigation of these phenomena requires tools for manipulation and characterization of structures at the atomic and molecular scale. In laboratories worldwide there is rapid progress in this area. The field is known as nanophysics, or nanoscience, where the prefix 'nano' refers to the size scale of nanometers. By its very nature, the boundaries of the field of physics of very small objects with the field of chemistry are fading. Indeed, in parallel, chemists are striving to make ever-larger molecules and metal cluster compounds that start to have bulk material properties. From a third direction, biology has developed to the point where we are able to scrutinize the function and properties of the individual molecular building blocks of living organisms.

An important tool that has stimulated these developments is the Scanning Tunneling Microscope (STM), developed by Gerd Binnig and Heinrich Rohrer, for which they were awarded the Nobel prize in 1986. Over the past two decades the STM has inspired many related scanning probe microscopy tools, which measure a great variety of properties with atomic resolution [1]. By far the most important probe is the Atomic Force Microscope (AFM), which allows the study of poorly conducting surfaces and has been used for the study of such problems as the forces required for unfolding an individual protein molecule [2].

The latter example also illustrates an important aspect of these tools: apart from imaging atoms at the surface of a solid, it is possible to manipulate individual atoms and molecules. Very appealing examples of the possibility to position atoms at pre-designed positions on a surface have been given by Don Eigler and his coworkers [3].

A second ingredient, which has greatly contributed to the rapid developments in nanophysics, is the wide body of knowledge obtained in the field of mesoscopic physics [4]. Mesoscopic physics studies effects of quantum coherence in the properties of conductors that are large on the scale of atoms but small compared to everyday (macroscopic) dimensions. One of the concepts developed in mesoscopic physics which is directly applicable at the atomic scale is the notion that electrical conductance is equivalent to the transmission probability for incoming waves. This idea, which goes back to Rolf Landauer [5], forms one of the central themes of this review, where we discuss conductance in the quantum regime. This applies to atomic-sized metallic contacts and wires, as well as to molecules. A much studied example of the latter is conductance through carbon nanotubes [6], long cylindrical molecules of exclusively carbon atoms with a diameter of order of 1 nm. Even applications to biological problems have appeared, where the techniques of mesoscopic physics and nanophysics have been exploited to study the conductance of individual DNA molecules [7, 8, 9]. There is, however, a characteristic distinction between mesoscopic physics and nanophysics. While the former field concentrates on 'universal' features relating to the wave character of the electrons, to the quantization of charge in units of the electron charge, and the like, at the nanometer scale the composition and properties of the materials play an important role. In nanophysics the phenomena observed are often non-generic and the rich variety of chemistry enters.

The attention to mesoscopic physics, and more recently to nanophysics, is strongly encouraged by the ongoing miniaturization in the microelectronics industry. At the time of this writing the smallest size of components on a mass-fabricated integrated circuit amounts to only 110 nm. It is expected that this trend towards further miniaturization continues for at least another decade and will then reach the level of 30 nm, which corresponds to only ~ 100 atoms in a row. Nanophysics takes these developments to the ultimate size limit: the size of atoms and molecules. One should not be over-optimistic about the chances of this research leading to large-scale fabrication in the foreseeable future of atomically engineered circuits replacing present day silicon technology. Many barriers would have to be taken, including problems of long-term stability at room temperature and the time required for fabrication and design of giga-component circuits. Smaller scale applications may be expected from intrinsically stable structures such as carbon nanotubes. However, the research is most important for understanding what modified properties may be met upon further

size reduction, and searching for new principles to be exploited.

Finally, a third field of research with intimate connections to the work described in this review is related to materials science, where the fundamentals of adhesion, friction and wear are being rebuilt upon the mechanical properties of materials at the atomic scale [10, 11]. This involves, among many other aspects, large-scale computer simulations of atomistic models under applied stress, which allows the macroscopic material properties to be traced to microscopic processes.

A. The scope of this review

Having sketched the outlines of the field of nanophysics, which forms the natural habitat for our work, we will now limit the scope of what will be discussed in this review. We will discuss the electrical and mechanical properties of atomic sized metallic conductors. The central theme is the question as to what determines the electrical conductance of a single atom. The answer involves concepts from mesoscopic physics and chemistry, and suggests a new way of thinking about conductance in general. In metals the Fermi wavelength is comparable to the size of the atom, which immediately implies that a full quantum mechanical description is required. The consequences of this picture for other transport properties will be explored, including those with the leads in the superconducting state, thermal transport, non-linear conductance and noise. It will be shown that the quantum mechanics giving rise to the conductance cannot be separated from the question of the mechanical cohesion of the contact, which naturally leads us to discuss problems of forces and mechanical stability.

Before we present a logical discussion of the concepts and results it is useful to give a brief account of the history of the developments. This is a most delicate task, since we have all been heavily involved in this work, which will make the account unavoidably personally colored. The following may be the least scientific part of this paper, but may be of interest to some as our personal perspective of the events.

1. A brief history of the field

The developments of three fields come together around 1990. To start with, briefly after the invention of the STM in 1986 Gimzewski and Möller [12] were the first to employ an STM to study the conductance in atomic-sized contacts and the forces were measured using an AFM by Dürig *et al.* [13]. They observed a transition between contact and vacuum tunneling at a resistance of about 20 k Ω and the adhesion forces when approaching contact from the tunneling regime. Second, shortly afterwards, in 1988, the quantization of conductance was discovered in two-dimensional electron gas devices [14, 15].

The theory describing this new quantum phenomenon has provided the conceptual framework for discussing transport for contacts that have a width comparable to the Fermi wavelength. Although the connection between these two developments was made in a few theoretical papers [16, 17, 18, 19, 20, 21] it took a few years before new experiments on the conductance of atomic-sized contacts appeared. As a third ingredient, the mechanical properties of atomic-sized metallic contacts were discussed in two seminal papers which appeared in 1990 [22, 23]. Here it was shown, using molecular dynamics computer simulations of the contact between an atomically sharp metallic STM tip and a flat surface, that upon stretching the contact is expected to go through successive stages of elastic deformation and sudden rearrangements of the atomic structure.

These three developments led up to a surge of activity in the beginning of the nineties. In 1992 in Leiden [24] a new technique was introduced by Muller *et al.* dedicated to the study of atomic sized junctions, baptized the Mechanically Controllable Break Junction (MCBJ) technique, based on an earlier design by Moreland and Ekin [25]. First results were shown for Nb and Pt contacts [26], with steps in the conductance and supercurrent. The former have a magnitude of order of the conductance quantum, $G_0 = 2e^2/h$, and the connection with quantization of the conductance was discussed. However, the authors argued that the steps should be explained by the atomic structural rearrangement mechanisms of Landman *et al.* [22] and Sutton and Pethica [23]. This was clearly illustrated in a calculation by Todorov and Sutton [27], which combines molecular dynamics for calculation of the atomic structure and a tight binding calculation of the electronic structure at each step in the evolution of the structure to evaluate the conductance. This subtle interplay between atomic structure and quantization of the conductance would fire a lively debate for a few years to come. This debate started with the appearance, at about the same time, of experimental results for atomic sized contacts obtained using various methods by four different groups [28, 29, 30, 31].

The experiments involve a recording of the conductance of atomic-sized contacts while the contacts are stretched to the point of breaking. The conductance is seen to decrease in a stepwise fashion, with steps of order of the quantum unit of conductance. Each curve has a different appearance due to the many possible atomic configurations that the contact may assume. By far not all plateaus in the conductance curves could be unambiguously identified with an integer multiple of the conductance quantum, nG_0 . In an attempt at an objective analysis of the data, histograms of conductance values were introduced, constructed from a large number of individual conductance curves [32, 33, 34]. These demonstrated, for gold and sodium, that the conductance has a certain preference for multiples of G_0 , after correction for a phenomenological ‘series resistance’. When it was shown that similar results can be obtained under ambi-

ent conditions by simply touching two bulk gold wires [35] many more results were published on a wide variety of metals under various conditions. However, a straightforward interpretation of the conductance behavior in terms of free-electron waves inside smooth contact walls giving rise to quantization of the conductance continued to be challenged. The dynamical behavior of the conductance steps suggested strongly that the allowed diameters of the contact are restricted by atomic size constraints [36]. Also, the free electron model could not account for the differences in results for different materials. Convincing proof for the atomic rearrangements at the conductance steps was finally presented in a paper by Rubio *et al.* in 1996 [37], where they combine conductance and force measurements to show that jumps in the conductance are associated with distinct jumps in the force.

As a parallel development there was an increasing interest in the structure of the current-voltage (I-V) characteristics for quantum point contacts between superconducting leads. I-V curves for contacts between superconductors show rich structure in the region of voltages below $2\Delta/e$, where Δ is the superconducting gap energy. The basis for the interpretation had been given by Klapwijk, Blonder and Tinkham in 1982 [38] in terms of multiple Andreev reflection. However, this description did not take the full phase coherence between the scattering events into account. The first full quantum description of current-voltage curves was given by Arnold [39]. Independently, three groups applied these concepts to contacts with a single conductance channel [40, 41, 42, 43]. A quantitative experimental confirmation of this description was obtained using niobium atomic-sized vacuum tunnel junctions [44].

This led to a breakthrough in the understanding of conductance at the atomic scale. In 1997 Scheer *et al.* [45] published a study of the current-voltage relation in superconducting single-atom contacts. They discovered that the I-V curves did not fit the predicted shape for a single conductance channel [40, 41, 42, 43], although the conductance was close to one conductance unit, G_0 . Instead, a good fit was obtained when allowing for several independent conductance channels, with transmission probabilities $\tau_n < 1$. For a single-atom contact of aluminum three channels turned out to be sufficient to describe the data. The interpretation of the results by Scheer *et al.* was provided by an analysis of a tight binding model of atomic size geometries by Cuevas *et al.* [46]. This picture agrees with earlier first principles calculations [16, 47], where the conductance is discussed in terms of ‘resonances’ in the local density of states. The picture by Cuevas *et al.* has the advantage that it can be understood on the basis of a very simple concept: the number of conductance channels is determined by the number of valence orbitals of the atom. This view was confirmed experimentally by a subsequent systematic study for various superconductors [48].

Within this picture it is still possible to apply free-electron like models of conductance, provided we restrict

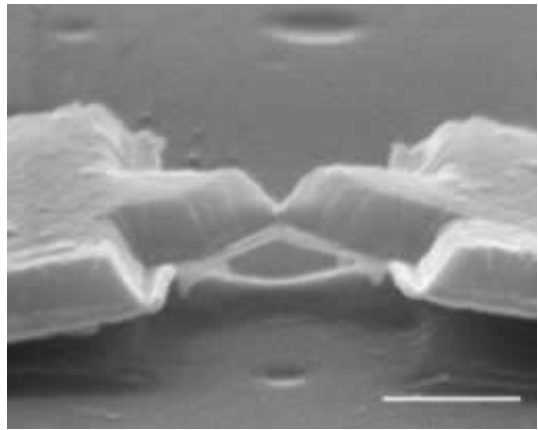


FIG. 1: A lithographically fabricated MCBJ device for gold. The image has been taken with a scanning electron microscope and the colors have been edited to identify the different materials. The contact at the narrowest part is formed in a thin 20 nm gold layer (yellow). The gold layer is in intimate contact with a thick 400 nm aluminum layer (blue). The bridge is freely suspended above the substrate (green), and only anchored to the substrate at the wider regions left and right. When bending the substrate the wire breaks at the narrowest part, and a single gold atom contact can be adjusted by relaxing the bending force. The close proximity of the thick aluminum layer to the contact induces superconducting properties into the atomic sized contact. The horizontal scale bar is $\sim 1 \mu\text{m}$. Courtesy E. Scheer, [48].

ourselves primarily to monovalent metals. When one evaluates the total energy of the occupied states within a constriction¹, using an independent electron model one finds that the energy has distinct minima for certain cross-sections of the constriction [49, 50, 51]. The energy minima are associated with the position of the bottom of the subbands for each of the quantum modes. This suggests that the cohesion force of the constriction is at least partly determined by the delocalized electronic quantum modes. Experimental evidence for this quantum-mode-based picture of the cohesive force was obtained for sodium point contacts, which show enhance mechanical stability at ‘magic radii’ as a result of the quantum mode structure in the density of states [52].

Another discovery of unusual mechanical behavior was found for gold contacts, which were shown to allow stretching into conducting chains of individual atoms. This was inferred from the response of the conductance upon stretching of the contacts [53], and was directly observed in a room temperature experiment of an STM constructed at the focal point of a high-resolution transmis-

¹ The words ‘contact’ and ‘constriction’ are used throughout this paper as equivalent in describing a fine wire-shaped connection between two bulk electrodes, with usually a smooth change in cross-section.

sion electron microscope (HRTEM) [54]. It was suggested that the exceptional stability of these chains may derive from the quantum-mode based mechanism mentioned above [55]. The atomic chains form one-dimensional conductors, with a conductance very close to $1 G_0$. This connects the research to the active research on one-dimensional conductors, with notably the carbon nanotubes as the prime system of interest [6]. A chain of atoms, consisting of two non-metallic Xe atoms, has been constructed by STM manipulation by Yazdani *et al.* [56], and this may point the way to future studies using ultimate atomic-scale control over the construction of the conductors.

B. Outline of this review

Although the field is still rapidly evolving, a number of new discoveries, concepts and insights have been established and deserve to be clearly presented in a comprehensive review. This should provide an introduction of the concepts for those interested in entering the field, and a reference source and guide into the literature for those already active. A few reviews on the subject with a more limited scope have been published recently [57, 58, 59] and one conference proceedings was dedicated to conductance in nanowires [60]. In the following we will attempt to give a systematic presentation of the theoretical concepts and experimental results, and try to be as nearly complete in discussion of the relevant literature on this subject as practically possible.

We start in Sect. II by introducing the experimental techniques for studying atomic-sized metallic conductors. Some examples of results obtained by the techniques will be shown, and these will be used to point out the interesting aspects that require explanation. The theoretical basis for conductance at the atomic scale will be explained in detail in Sect. III. As pointed out above, superconductivity has played an essential role in the discussion on quantum point contacts. Therefore, before we introduce the experimental results, in Sect. IV the various theoretical approaches are reviewed to calculate the current-voltage characteristics for quantum point contacts between superconductors. Then we turn to experiment and begin the discussion with the linear conductance. The behavior of the conductance of the contacts is described as a function of the stretching of the contact. The conductance steps and plateaus, and the conductance histograms are presented. Results for the various experimental techniques, for a range of metallic elements, and the interpretation of the data are critically evaluated. The last conductance plateau before breaking of the contact is usually interpreted as the last-atom contact, and the evidence for this interpretation is presented. Although it will become clear that electrical transport and mechanical properties of the contacts are intimately related, we choose to present the experimental results for the mechanical properties separately in Sect. VI. The

relation between the two aspects is discussed in next section. For the interpretation of the experimental results computer simulations have been indispensable, and this forms the subject of Sect. VII. Molecular dynamics simulations are introduced and the results for the evolution of the structure of atomic-scale contacts are presented. Various approaches to calculate the conductance are discussed, with an emphasis on free-electron gas calculations and the effects of the conductance modes on the cohesive force in these models. The valence-orbitals basis of the conductance modes follows from a discussion of tight-binding models and the results of these are compared to *ab initio*, density functional calculations.

Sect. VIII presents the experimental evidence for the valence-orbitals interpretation of the conductance modes. Analyzing the superconducting subgap structure forms the central technique, but additional evidence is obtained from shot noise experiments, and from de strain dependence of the conductance. The next two sections discuss special electrical properties of metallic quantum point contacts, including conductance fluctuations, inelastic scattering of the conduction electrons, and the Josephson current for contacts between superconducting leads. Sect. XI presents the evidence for the spontaneous formation of chains of single atoms, notably for gold contacts, and the relevant model calculations for this problem. A second unusual mechanical effect is discussed in Sect. XII, which presents the evidence for shell structure in alkali nanowires. We end our review with a few summary remarks and an outlook on further research and unsolved problems.

There are two features that make the subject discussed here particularly attractive. The first is the fact that by reducing the cross section of the conductors to a single atom one eliminates a lot of the complexity of solid state physics, which makes the problem amenable to direct and quantitative comparison with theory. This is a field of solid state physics where theory and experiment meet: all can be very well characterized and theory fits extremely well. A second attractive aspect lies in the fact that many experiments can be performed with simple means. Although many advanced and complex measurements have been performed, some aspects are simple enough that they can be performed in class-room experiments by undergraduate students. A description of a class-room experiment can be found in Ref. [61].

II. FABRICATION OF METALLIC POINT CONTACTS

A wide variety of tools have been employed during the last decade to study the mechanical and transport properties of atomic-sized contacts, and many of these are extremely simple. Before we start a description of the main techniques it is important to stress the great difference between room temperature and helium temperature experiments. At low temperatures atomic-sized contacts

can be held stable for any desired length of time, allowing detailed investigation of the conductance properties. The low-temperature environment at the same time prevents adsorption of contaminating gasses on the metal surface. At room temperature, on the other hand, the thermal diffusion of the atoms prevents long-term stability of a contact of single atom, and ultra-high vacuum (UHV) conditions are required for a clean metal junction. However, using fast scan techniques for the study of the noble metals, in particular gold, a lot of information has been obtained by very simple means.

A. Early developments: spear-anvil and related techniques

Many years before the rise of nanofabrication, ballistic metallic point contacts were widely studied, and many beautiful experiments have been performed [62, 63]. The principle was discovered by Yanson [64] and later developed by his group and by Jansen *et al.* [65]. The technique has been worked out with various refinements for a range of applications, but essentially it consists of bringing a needle of a metal gently into contact with a metal surface. This is known as the spear-anvil technique. Usually, some type of differential-screw mechanism is used to manually adjust the contact. With this technique stable contacts are typically formed having resistances in the range from ~ 0.1 to $\sim 10 \Omega$, which corresponds (see Sect. III C) to contact diameters between $d \simeq 10$ and 100 nm. The elastic and inelastic mean free path of the charge carriers can be much longer than this length d , when working with clean metals at low temperatures, and the ballistic nature of the transport in such contacts has been convincingly demonstrated in many experiments. The main application of the technique has been to study the electron-phonon interaction in metals. Here, one makes use of the fact that the (small but finite) probability for back-scattering through the contact is enhanced as soon as the electrons acquire sufficient energy from the electric potential difference over the contact that they are able to excite the main phonon modes of the material. The differential resistance, dV/dI , of the contact is seen to increase at the characteristic phonon energies of the material. A spectrum of the energy-dependent electron-phonon scattering can be directly obtained by measuring the second derivative of the voltage with current, d^2V/dI^2 , as a function of the applied bias voltage. An example is given in Fig. 2. Peaks in the spectra are typically observed between 10 and 30 mV, and are generally in excellent agreement with spectral information from other experiments, and with calculated spectra. The application of electron-phonon spectroscopy in atomic-sized contacts will be discussed in Sect. IX C 1.

The ballistic character of the transport has been exploited in even more ingenious experiments such as the focusing of the electron trajectories onto a second point contact by the application of a perpendicular magnetic

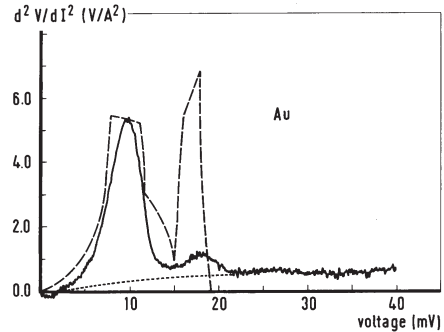


FIG. 2: An example of an electron-phonon spectrum measured for a gold point contact by taking the second derivative of the voltage with respect to the current. The long-dashed curve represents the phonon density of states obtained from inelastic neutron scattering. Courtesy A.G.M. Jansen, [65].

field [66] and the injection of ballistic electrons onto a normal metal-superconductor interface for a direct observation of Andreev reflection [67].

Contacts of the spear-anvil type are not suitable for the study of the quantum regime, which requires contact diameters comparable to the Fermi wavelength, i.e. contacts of the size of atoms. For smaller contacts (higher resistances) the above-described technique is not sufficiently stable for measurement. What is more important, most of the experiments in the quantum regime need some means fine control over the contact size. These requirements can be met using the scanning tunneling microscope (STM) or the mechanically controllable break junction technique (MCBJ).

B. The use of scanning tunneling microscopes

The scanning tunneling microscope (STM)² is a versatile tool that allows studying the topography and electronic properties of a metal or semiconductor surface with atomic resolution, and it is also ideal for studying atomic-sized contacts. In its normal topographic mode a sharp needle (the tip) is scanned over the sample to be studied without making contact. The tip-sample separation is maintained constant by controlling the current that flows between them due to the tunneling effect when applying a constant bias voltage. The control signal gives a topographic image of the sample surface. It is possible to achieve atomic resolution because of the exponential dependence of the tunneling current on the tip-sample separation: only the foremost atom of the tip will see the sample. Typical operating currents are of the order of nanoamperes and the tip-sample separation is just a

² For an overview of STM see e.g. Ref. [1].

few angstroms. Evidently, the sample must be conducting. Essential for the operation of the STM is the control of the relative position of the tip and sample with sub-nanometer accuracy, which is possible using piezoelectric ceramics. Conventionally the lateral scan directions are termed x - and y -directions and the vertical direction is the z -direction.

The distance between tip and sample is so small that accidental contact between them is quite possible in normal STM work, and should usually be avoided. However, it soon became evident that the STM tip could be used to modify the sample on a nanometer scale. The first report of the formation and study of a metallic contact of atomic dimensions with STM is that of Gimzewski and Möller [12]. In contrast to previous works that were more aimed at surface modifications [68, 69], the surface was gently touched and the transition from the tunneling regime to metallic contact was observed as an abrupt jump in the conductance. From the magnitude of the resistance at the jump (~ 10 k Ω) using the semi-classical Sharvin formula (see Sect. III C), the contact diameter was estimated to be 0.15 nm, which suggested that the contact should consist of one or two atoms.

Different groups have performed STM experiments on the conductance of atomic-sized contacts in different experimental conditions: at cryogenic temperatures [28, 70, 71, 72]; at room temperature under ambient conditions [29, 73, 74, 75], and UHV [31, 34, 76].

The presence of adsorbates, contamination, and oxides on the contacting surfaces can prevent the formation of small metallic contacts, and also produce spurious experimental results. This problem can be avoided, in principle, by performing the experiments in UHV with *in situ* cleaning procedures for both tip and sample [12]. However, it is also possible to fabricate clean metallic contacts in non-UHV conditions. After conventional cleaning of tip and sample prior to mounting in the STM, the contacting surfaces of tip and sample are cleaned *in situ* by repeatedly crashing the tip on the spot of the sample where the contact is to be formed (see Fig. 3). This procedure pushes the adsorbates aside making metal-metal contact possible. The tip and sample are bonded (that is, cold welded) and as the tip is retracted and contact is broken fresh surfaces are exposed. Evidence of this welding in clean contacts is the observation of a protrusion at the spot where the contact was formed [12]. This cleaning procedure works particularly well at low temperatures where the surfaces can stay clean for long periods of time since all reactive gasses are frozen. This is adequate if the contact to be studied is homogeneous, since otherwise there will be transfer of material from one electrode to the other. On the other hand, this wetting behavior of the sample metal (e.g. Ni or Au) onto a hard metal (W or PtIr) tip has also been exploited for the study of homogeneous contacts, assuming full coverage of the tip by the sample material [31].

In an STM experiment on metallic contacts, the bias voltage is kept fixed (at a low value, say 10 mV) and the

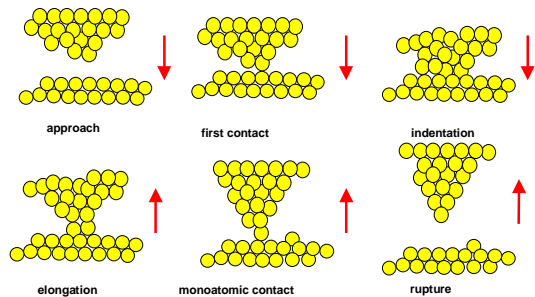


FIG. 3: Cartoon representation of contact fabrication using an STM.

current is recorded as the tip-sample distance is varied by ramping the z -piezovoltage. The results are typically presented as a plot of the conductance (or current) versus z -piezovoltage (or time). Fig. 4 shows a typical STM conductance curve for a clean Au contact at low temperatures. Before contact the current depends exponentially on the distance with an apparent tunneling barrier of the order of the work function of the material. Such a high value of the apparent tunneling barrier is a signature of a clean contact, since adsorbates lower the tunneling barrier dramatically [12] (with the exception of the inert helium gas, see Sect. II C 3 below). Metallic contact takes place as an abrupt jump in the conductance, or the current. After this jump the conductance increases in a stepwise manner as the size of the contact increases. Reversing the motion of the tip shows that these steps are hysteretic. In the case of Au, as we will see, the conductance of the first plateau is quite well defined with a value of approximately $2e^2/h$ and corresponds to a one-atom contact. For other metals the conductance curves will look somewhat different, depending on the electronic structure of the metal. It is important to note that the z -piezovoltage in STM experiments is not directly related to the size of the contact: as the contact is submitted to strain its atomic configuration changes in a stepwise manner, as will be discussed in detail in Sect. V.

For studying nanocontacts a standard STM can be used, but it must be taken into account that currents to be measured are about 2–3 orders of magnitude larger than in usual STM operation. Mechanical stability of the STM setup is an important factor. Careful design makes possible to achieve noise vibration amplitudes of the order of a few picometers at low temperatures.

Direct observation of metallic nanocontacts is possible using high-resolution transmission electron microscopy (HRTEM). Several groups have constructed an STM with the tip apex at the focal point of a HRTEM. Kizuka and co-workers have observed the atomic contact formation processes in gold using a piezo-driven specimen holder [77, 78, 79], Fig. 5, and Takayanagi and co-workers have studied the structure of gold nanowires [80], and atomic wires [54]. The conditions for the experiments are (ultra-)high vacuum and ambient temperature and a time res-

olution of 1/60 s for the video frame images.

C. The mechanically controllable break junction technique

In 1985 Moreland and Ekin [25] introduced “break” junctions for the study of the tunneling characteristics for superconductors. They used a thin wire of the superconductor mounted on top of a glass bending beam. An electromagnetic actuator controlled the force on the bending beam. Several extensions and modifications to this concept have been introduced later, initially by Muller *et al.* [24, 26], who introduced the name Mechanically Controllable Break Junction (MCBJ). The technique has proven to be very fruitful for the study of atomic-sized metallic contacts.

1. Description of the MCBJ technique

The principle of the technique is illustrated in Fig. 6. The figure shows a schematic top and side view of the mounting of a MCBJ, where the metal to be studied has the form of a notched wire, typically 0.1mm in diameter, which is fixed onto an insulated elastic substrate with two drops of epoxy adhesive (Stycast 2850FT and curing agent 24LV) very close to either side of the notch. The notch is manually cut into the center of a piece of wire of the metal to be studied. For most metals, except the hardest, it is possible to roll the wire under the tip of a surgical knife in order to obtain a diameter at the notch of about one third of the original wire diameter. A photograph of a mounted wire is shown in Fig. 7. The distance between the drops of epoxy adhesive can be reduced to only about 0.1mm by having the epoxy cure at ambient conditions for about 3 hours before apply-

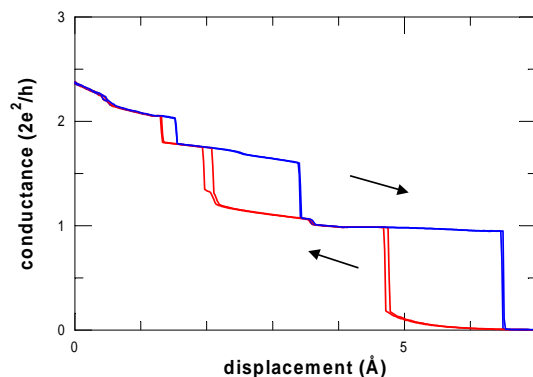


FIG. 4: Conductance curves of a gold nanocontact at low temperature (4.2 K) using a stable STM. Two complete consecutive cycles of approach-retraction are shown. The lower and higher curves correspond to approach and retraction, respectively.

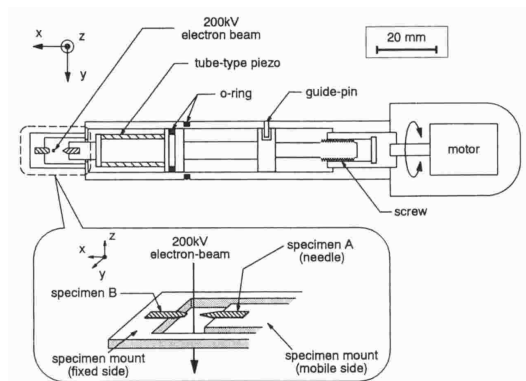


FIG. 5: Schematic representation of the sample holder allowing piezo control of the tip-sample distance in the very limited space available in a HRTEM. Reprinted with permission from [77]. Copyright 1997 American Physical Society.

ing it. This prevents that the small drops deposited at some distance from the notch flow together. The epoxy is still malleable, and under a microscope the drops can be gradually pushed towards the center.

The substrate is mounted in a three-point bending configuration between the top of a stacked piezo-element and two fixed counter supports. This set-up is mounted inside a vacuum can and cooled down to liquid helium temperatures. Then the substrate is bent by moving the piezo-element forward using a mechanical gear arrangement. The bending causes the top surface of the substrate to expand and the wire to break at the notch. By breaking the metal, two clean fracture surfaces are exposed, which remain clean due to the cryo-pumping action of the low-temperature vacuum can. The fracture surfaces can be brought back into contact by relaxing the force on the elastic substrate, where the piezoelectric element is used for fine control. The roughness of the fracture surfaces usually results in a first contact at one point.

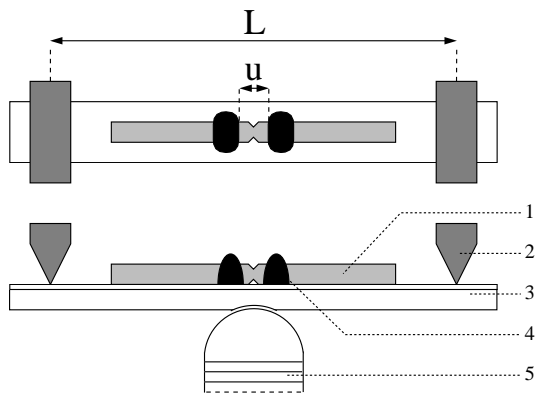


FIG. 6: Schematic top and side view of the mounting of a MCBJ, with the notched wire (1), two fixed counter supports (2), bending beam (3), drops of epoxy adhesive (4) and the stacked piezo element (5).

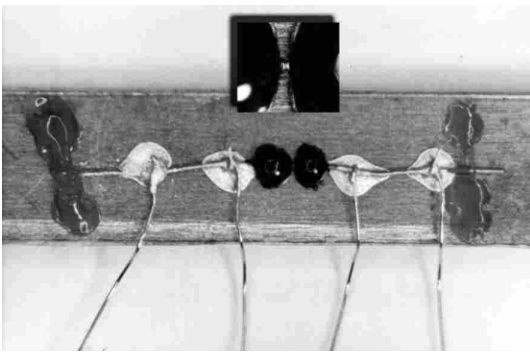


FIG. 7: Top view of a MCBJ seen under an optical microscope. The substrate is 4.5 mm wide and the sample wire is a 0.1 mm diameter gold wire. The inset shows an enlargement of the wire with the notch between the two drops of epoxy. On each side of the notch two wires make contact to the sample wire using silver paint.

In addition to a clean surface, a second advantage of the method is the stability of the two electrodes with respect to each other. From the noise in the current in the tunneling regime one obtains an estimate of the vibration amplitude of the vacuum distance, which is typically less than 10^{-4} nm. The stability results from the reduction of the mechanical loop which connects one contact side to the other, from centimeters, in the case of an STM scanner, to ~ 0.1 mm in the MCBJ.

The most common choice for the bending beam is a plate of phosphorous bronze, about 0.5–1 mm thick, 20 mm long and 3–5 mm wide. The top surface is usually insulated by covering it with a thin polymer foil (Kapton) using regular epoxy. The advantage over brittle materials, such as glass as was used in the experiments by Moreland and Ekin [25], is that one avoids the risk of fracture of the bending beam. For brittle materials the maximum strain before breaking is usually about 1%. The principle of the MCBJ lies in the concentration of the strain in the entire length of the unglued section u (Fig. 6) of the top surface of the bending beam onto the notch of the wire. Since metals tend to deform plastically this strain concentration is often still not sufficient to break the wire, unless the notch is cut very deep. Since the cutting of a deep notch without separating the wire ends is not always very practical, one mostly chooses a metallic bending beam such as phosphor bronze. The rate of success for this arrangement is very good (of order 90%), but one often needs to bend the substrate beyond the elastic limit in order to obtain a break in the wire. This poses no serious problems, except that the displacement ratio r_d , i.e. the ratio between the distance over which the two wire ends are displaced with respect to each other and the extension of the piezo-element, is reduced and not very predictable.

For the ideal case of homogenous strain in the bending

beam the displacement ratio can be expressed as

$$r_d = \frac{3uh}{L^2},$$

where u and L are the unglued section and the distance between the two counter supports, respectively, as indicated in Fig. 6, and h is the thickness of the bending beam. For the dimensions indicated above for a typical MCBJ device we obtain $r_d \simeq 10^{-3}$. In practice, the plastic deformation of the bending beam may result in a reduction of the displacement ratio by about an order of magnitude. For experiments where it is necessary to have a calibrated displacement scale, a calibration is required for each new sample and the procedure is described in Sect. II C 3. For optimal stability of the atomic-sized junctions it is favorable to have a small displacement ratio, since the external vibrations that couple in through the sample mounting mechanism, are also reduced by this ratio.

Although it cannot be excluded that contacts are formed at multiple locations on the fracture surfaces, experiments usually give no evidence of multiple contacts. As will be explained in more detail in Sect. VI, from the mechanical response of the contacts one can deduce that upon stretching the shape of the contact evolves plastically to form a connecting neck between the two wire ends. The neck gradually thins down and usually breaks at the level of a single atom.

In the first experiments using the MCBJ for a study of conductance in atomic-sized metallic contacts [24, 26], distinct steps were observed in the conductance of Pt and Nb contacts. Figure 8 shows two examples of recordings of the conductance as a function of the voltage V_p on the piezo-element, which is a measure of the displacement of the two wire ends with respect to each other. In the experiment, when coming from the tunneling regime, a contact is formed by moving the electrodes together. The contact is then slowly increased while recording the conductance. The scans as given in Fig. 8 are recorded in about 20 minutes each. The conductance is observed to increase in a step-wise fashion, which is different each time a new contact is made. Although the steps are of order of the conductance quantum, the authors caution against a direct interpretation in terms of conductance quantization. This point will be discussed in more detail in Sect. V.

2. Microfabrication of MCBJ devices

The principle of the break junction technique can be refined by employing microfabrication techniques to define the metal bridge. The advantage is a further improved immunity to external vibrations and the possibility to design the electronic and electromagnetic environment of the junction. Fig. 9 shows a lithographically fabricated MCBJ device on a silicon substrate, as developed by Zhou *et al.* [81]. These authors used a $\langle 100 \rangle$ -

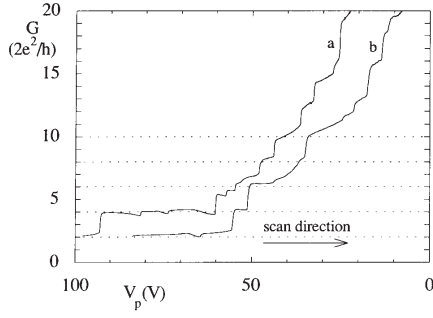


FIG. 8: Two examples of traces of the conductance, G , measured on Pt contacts using the MCBJ technique at a temperature of 1.2 K. The electrodes are pushed together by decreasing V_p . An estimate for the corresponding displacement is $10\text{V} \sim 0.1\text{ nm}$. Reprinted with permission from [26]. Copyright 1992 American Physical Society..

oriented, $250\text{ }\mu\text{m}$ thick silicon substrate, covered by a 400 nm thick SiO_2 insulating oxide layer. On top of this they deposit a 8 nm gold film, which is defined into the shape of a 100 nm wide bridge by standard electron beam lithography. Using the metal film as a mask, they etch a triangular groove into the silicon substrate below the bridge. The bridge can be broken at the narrowest part, as for the regular MCBJ devices, by bending the substrate. The parameters for the bridge need to be chosen such that the metal bridge breaks before breaking the silicon substrate itself.

Alternatively, one can microfabricate the MCBJ device on a phosphorous bronze substrate [82]. After polishing the substrate it is covered with a polyimide layer by spin coating, which serves to smoothen the substrate and insulate the junction electrically. The metal bridge is defined into a metal film deposited onto the polyimide layer by techniques similar to those used by Zhou *et al.*, after which the polyimide layer is carved in an reactive ion etcher, producing a freely suspended bridge over a length of approximately $2\text{ }\mu\text{m}$.

The displacement ratio for the microfabricated MCBJ devices is about two orders of magnitude smaller than that for a regular device, $r_d \sim 10^{-4}$. As a consequence the immunity to vibrations and drift is such that the electrode distance changes by less than 0.2 pm per hour and it is possible to manually adjust the bending to form a single atom contact. On the other hand, a drawback is the fact that the displacement of the electrodes that can be controlled by the piezovoltage is limited to only a few angstroms due to the small displacement ratio and the limited range of expansion of the piezo-element. For larger displacements a mechanical gearbox arrangement in combination with an electromotor can be used, but such systems have a rather large backlash, which hampers a smooth forward and backward sweep over the contact size.

The major advantage of the microfabricated MCBJ de-

vices is the possibility to define the environment of the atomic-sized contact. An example was given in Fig. 1 showing a device that allows to form an atomic-sized contact for gold with superconductivity induced through the close proximity of a thick aluminum film. This experiment will be discussed in Sect. VIII and in Sects. IX F and X B some examples will be given of designing the electromagnetic environment of the junction.

3. Calibration of the displacement ratio

Usually the displacement ratio cannot be determined very accurately from the design of the MCBJ and it is necessary to make a calibration for each new device. The simplest approach is to exploit the exponential dependence of the resistance R with distance δ between the

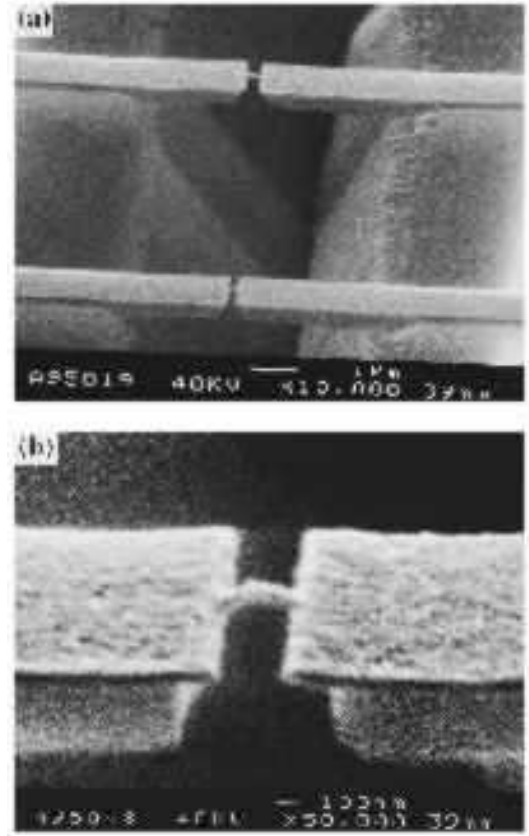


FIG. 9: (a) Electron microscopy image of two microfabricated bridges suspended above a triangular pit in the silicon substrate. The close-up in (b) shows the two SiO_2 cantilevers, which are about 700 nm apart. The cantilevers are covered by a gold layer from which the final conducting bridge of about 100 nm wide is formed, and which is broken by bending of the silicon substrate. Reprinted with permission from [81]. Copyright 1995 American Institute of Physics.

electrodes in the tunneling regime,

$$R \propto \exp\left(\frac{2\sqrt{2m\Phi}}{\hbar}\delta\right). \quad (1)$$

Here, Φ is the workfunction of the metal, and m the electron mass. Kolesnychenko *et al.* introduced a more accurate method, using the Gundlach oscillations in the tunnel current [83]. These oscillations arise from resonances in the tunnel probability under conditions of field emission. For bias voltages larger than the workfunction of the metal the tunnel current increases exponentially, and on top of this rapid increase a modulation can be observed resulting from partial reflection of the electron wave in the vacuum between the two electrodes. Several tens of oscillations can be observed, allowing not only an accurate calibration of the displacement, but also an independent measurement of the workfunction. Surprisingly, from these studies it was found that the workfunction obtained is strongly influence by the presence of helium at the surface of the metal. Full helium coverage was found to *increase* the workfunction by about a factor of two [84]. Since helium is often used as a thermal exchange gas for cooling down to low temperatures, this result explains the rather large variation obtained in previous work for the distance calibration for any single device.

4. Special sample preparations

The principle of the MCBJ technique, consisting of exposing clean fracture surfaces by concentration of stress on a constriction in a sample, can be exploited also for materials that cannot be handled as described above. Delicate single crystals [85, 86] and hard metals can be studied with the single modification of cutting the notch by spark erosion, rather than with a knife.

The alkali metals Li, Na, K, etc., form an important subject for study, since they are nearly-free electron metals and most closely approach the predictions of simple free-electron gas models. The experiments will be discussed in Sects. V and XII. A schematic view of the MCBJ technique for alkali metals is given in Fig. 10 [33, 52]. While immersed in paraffin oil for protection against rapid oxidation, the sample is cut into the shape of a long thin bar and pressed onto four, 1 mm diameter, brass bolts, which are glued onto the isolated substrate, and tightened by corresponding nuts. Current and voltage leads are fixed to each of the bolts. A notch is cut into the sample at the center. This assembly is taken out of the paraffin and quickly mounted inside a vacuum can, which is then immersed in liquid helium. By bending the substrate at 4.2 K in vacuum, the sample is broken at the notch. The oxidation of the surface and the paraffin layer covering it simply break at his temperature and contact can be established between two fresh metal surfaces. This allows the study of clean metal contacts

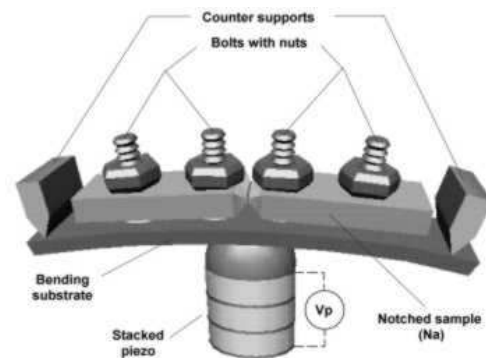


FIG. 10: Principle of the MCBJ technique adapted for the reactive alkali metals.

for the alkali metals for up to three days, before signs of contamination are found.

One of the draw-backs of the MCBJ technique compared to STM-based techniques is that one has no information on the contact geometry. Attempts have been made to resolve this problem by using a hybrid technique consisting of an MCBJ device with additional thin piezo-elements inserted under each of the two wire ends. One of these thin piezo plates is used in regular extension-mode, and for the other a shear-mode piezo is used. This allows scanning the two fracture surfaces with respect to each other, as in the STM [87, 88]. Although some successful experiments have been performed, the fact that there is no well-define tip geometry makes the images difficult to interpret, and atomic-like features are only occasionally visible.

D. Force measurements

The simultaneous measurement of conductance and forces in metallic contacts of atomic size is not an easy task as evidenced by the scarcity of experimental results. Conventional contact-mode atomic force microscopy (AFM) sensors are not adequate for this task because they are too compliant. In order not to perturb the dynamics of the deformation process, the force sensor must be stiffer than the contact itself and yet have sub-nanonewton sensitivity. The forces are of the order of 1 nN, changing over distances of less than 0.1 nm. It is required to have the force constant of the cantilever to be at least an order of magnitude larger than that of the atomic structure, which imposes that it should be at least several tens N/m. An additional complication is that the presence of contamination or adsorbates on the contacting surfaces can cause forces much larger than those due

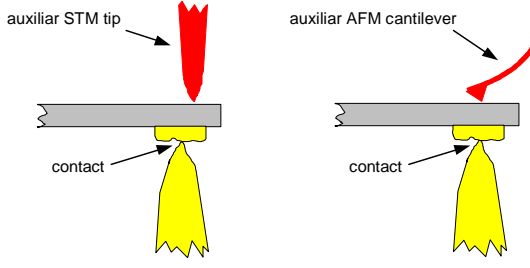


FIG. 11: Measuring the deflection of the cantilever beam on which the sample is mounted using an auxiliar STM tip or AFM cantilever.

to metallic interaction. Capillary forces due to water rule out experiments in ambient conditions.

In all experimental measurements of forces in atomic-sized contacts the force sensor is a cantilever beam onto which either the sample or tip is mounted, but different detection methods are used. Most of the experiments measure either the deflection of the beam or the variation of its resonant frequency. The beam deflection is directly proportional to the force exerted on the contact, while the resonant frequency of the beam is influenced by the gradient of this force. Dürig *et al.* [13] used an Ir foil beam with dimensions $7.5 \times 0.9 \times 0.05 \text{ mm}^3$ and spring constant 36 N/m to measure the interaction forces between tip and sample as a function of tip-sample separation up to the jump-to-contact in UHV. The changes in the oscillation frequency were determined from the tunneling current. Recently, quartz tuning fork sensors have been implemented in MCBJ and STM. One electrode is attached to one of the legs of the tuning fork while the other is fixed. These sensors are very rigid with spring constants larger than several thousands N/m , can be excited mechanically or electrically, and their motion is detected by measuring the piezoelectric current [89].

The deflection of the cantilever can be measured directly using various methods (see Fig. 11). A second STM acting as deflection detector has been used to measure forces in relatively large contacts using a phosphorous bronze cantilever beam of millimeter dimensions at low temperature (spring constant $\sim 700 \text{ N/m}$) [90, 91] and at room temperature (spring constant 380 N/m) [92]. Rubio-Bollinger *et al.* [93] used the sample, a 0.125 mm diameter, 2 mm length, cylindrical gold wire as a cantilever beam. They measured the forces during the formation of an atomic chain at 4.2 K . In all these experiments the auxiliary STM works on the constant current mode, which implies that the tip-cantilever distance and interaction are constant, minimizing the effect on the measurement. A conventional AFM can also be used to measure the deflection of the cantilever beam on which the sample is mounted. Rubio *et al.* [37] measured the picometer deflection of the $5 \text{ mm} \times 2 \text{ mm}$ cantilever beam by maintaining the $100 \mu\text{m}$ conventional AFM cantilever at constant deflection. Metal-coated non-contact mode

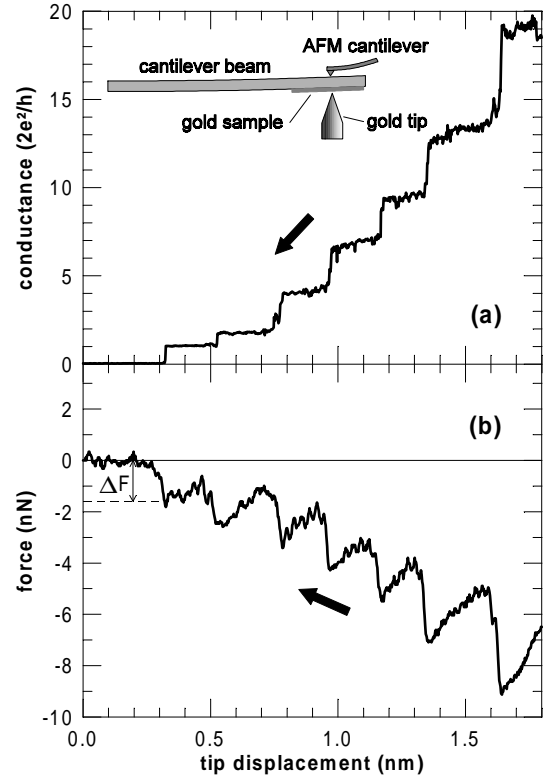


FIG. 12: Simultaneous force and conductance measurement in an atomic-sized contact at 300 K . The inset shows the experimental setup. Reprinted with permission from [37]. Copyright 1996 American Physical Society.

AFM cantilevers with spring constants of $20\text{-}100 \text{ N/m}$ have also been used in experiments at room temperature in air [94] and UHV [95] in conventional AFM setups.

A different approach was followed by Stalder *et al.* [96] who detected the changes of resonant frequency of a tensioned carbon-fiber coupled to the cantilever beam.

In Fig. 12, an example of simultaneous measurement of forces and conductance is shown. The saw-tooth shape of the force curve indicates that a mechanical deformation process takes place in the form of elastic stages (the linear portions of the curve), in which the nanostructure is deformed elastically, followed by sudden relaxations (the vertical portions of the curve) in which the system becomes unstable and its atomic configuration changes. It must be remarked that the slope of the elastic stages measures the *local* effective spring constant of the contact in series with the *macroscopic* effective spring constant of the constriction, which depends on its shape and could be comparable to the that of the contact itself in the case of sharp, long tips, and the spring constant of the force sensor. The system becomes unstable when the local gradient of the force at the contact exceeds the effective spring constant of the combined constriction-sensor system, with its strength given by the maximum force before relaxation. Note that even in the absence of a force sen-

or the dynamical evolution of a long constriction (lower effective elastic constant) will be different to that of a short constriction (higher effective elastic constant). The conductance curve in Fig. 12, shows that during the elastic stages the conductance is almost constant, changing suddenly as the system changes configuration, implying that the sudden jumps in the conductance are due to the changes in geometry.

E. Nanofabricated contacts

Various approaches have been explored to produce fixed contacts by nanofabrication techniques. The first of these approaches was introduced by Ralls and Buhrman [97]. They used electron-beam lithography to fabricate a nanometer size hole in a free standing thin film of Si_3N_4 , and a metal film was evaporated onto both sides of the silicon nitride film, filling up the hole and forming a point contact between the metal films on opposite sides. These structures are very stable, and contacts only several nanometers wide can be produced. The great advantage, here, is that the point contact can be cycled to room temperature and be measured as a function of field or temperature without influence on the contact size.

Such contacts are still fairly large compared to atomic dimensions and in order to reduce the size down to a single atom one has used methods employing feedback during fabrication by monitoring the contact resistance. There exist roughly two approaches: anodic oxidation of a metal film and deposition from an electrolytic solution. The first approach was introduced by Snow *et al.* [98, 99]. A metal film (Al or Ti, ~ 10 nm thick) can be locally oxidized from the surface down to the substrate induced by the current from an AFM tip operating under slightly humid ambient conditions. By scanning the tip current over the surface they produced a constriction in the metal film, which they were able to gradually thin down to a single atom. When the contact resistance comes in the range of kilo-ohms the resistance is seen to change step-wise and the last steps are of order of the conductance quantum, $2e^2/h$, which is an indication that the contact is reduced to atomic size. At room temperature such contacts usually reduce spontaneously into a tunnel junction on a time scale of a few minutes. However, some stabilize at a conductance value close to $2e^2/h$ for periods of a day or more. The controlled thinning of the contact can also be achieved by the current through the contact in the film itself [100].

A second approach consists of controlled deposition or dissolution by feedback of the voltage polarity on the electrodes immersed in the electrolyte. Li and Tao [101, 102] thinned down a copper wire by electrochemical etching in a copper sulphate solution. Atomic-sized contacts are found to be stable for many hours, before the conductance drops to zero. The deposition or dissolution rate can be controlled by the electrochemical potential of the wire and by feedback the contact resistance can be held

at a desired value. A further refinement of the technique starts from a lithographically defined wire, but is otherwise similar in procedure [102], and gold junctions can be fabricated from a potassium cyanaurate solution [103].

A hybrid technique was used by Junno *et al.* [104] who first patterned two gold electrodes onto a SiO_2 layer on top of a silicon wafer, with a gap of only 20 to 50 nm separating the two electrodes. Subsequently a grid pattern of 30–100 nm gold particles was formed on the same substrate in a second e-beam lithography fabrication step. The particles were then imaged by an AFM, and a proper particle was selected and manipulated into the gap between the electrodes by the AFM tip. This process allows *in situ* control over the contacts down to atomic size, and would also be suitable for contacting other types of metal particles or even molecules.

Recently Davidovic and coworkers produced atomic-sized contacts by evaporating gold on a Si_3N_4 substrate that contains a slit of 70 nm, while monitoring the conductance across the slit [105]. As soon as a tunneling current is detected the evaporation is interrupted and a contact is allowed to form by electromigration under the influence of the current through the contact. After annealing at room temperature the samples were cooled to cryogenic temperatures. Contacts with long-term stability were produced, but the technique will be less suitable for metals that are more reactive than gold.

Ohnishi *et al.* exploited the heating by the electron beam in a HRTEM to produce atomic-sized wires while imaging the structures [54, 106]. The method starts from a thin metal film and by focusing the electron beam on two nearby points one is able to melt holes into the film. The thermal mobility of the atoms results in a gradual thinning of the wire that separates the two holes, down to a single atom or chain of atoms. The advantage is that the structure is very stable and the process can be followed with video-frame time resolution. The conductance cannot be measured in this configuration.

F. Relays

Under the name relay we refer to all techniques bringing two macroscopic metallic conductors into contact by some means of mechanical control. In its simplest form it can be achieved by lightly touching two wires which are allowed to vibrate in and out of contact while measuring the conductance with a fast digital recorder [35]. For more reliable operation and in order to obtain sufficient statistics over many contact breaking cycles commercial or home made relays have been used [107, 108, 109], based on electromagnetic or piezo controlled operation. Gregory [110] used the Lorentz force on a wire in a magnetic field to push it into contact with a perpendicularly oriented wire. Although this produces very stable tunnel junctions, atomic sized contacts have not been demonstrated.

The relay techniques are suitable for averaging the con-

ductance properties of atomic-sized contacts over large numbers of breaking cycles at room temperature.

III. THEORY FOR THE TRANSPORT PROPERTIES OF NORMAL METAL POINT CONTACTS

A. Introduction

Macroscopic conductors are characterized by Ohm's law, which establishes that the conductance G of a given sample is directly proportional to its transverse area S and inversely proportional to its length L , i.e.

$$G = \sigma S/L, \quad (2)$$

where σ is the conductivity of the sample.

Although the conductance is also a key quantity for analyzing atomic-sized conductors, simple concepts like Ohm's law are no longer applicable at the atomic scale. Atomic-sized conductors are a limiting case of mesoscopic systems in which quantum coherence plays a central role in the transport properties.

In mesoscopic systems one can identify different transport regimes according to the relative size of various length scales. These scales are, in turn, determined by different scattering mechanisms. A fundamental length scale is the *phase-coherence length*, L_φ which measures the distance over which quantum coherence is preserved. Phase coherence can be destroyed by electron-electron and electron-phonon collisions. Scattering of electrons by magnetic impurities, with internal degrees of freedom, also degrades the phase but elastic scattering by (static) non-magnetic impurities does not affect the coherence length. Deriving the coherence length from microscopic calculations is a very difficult task. One can, however, obtain information on L_φ indirectly from weak localization experiments [111]. A typical value for Au at $T = 1$ K is around $1 \mu\text{m}$ [112]. The mesoscopic regime is determined by the condition $L < L_\varphi$, where L is a typical length scale of our sample.

Another important length scale is the elastic mean free path ℓ , which roughly measures the distance between elastic collisions with static impurities. The regime $\ell \ll L$ is called *diffusive*. In a semi-classical picture the electron motion in this regime can be viewed as a random walk of step size ℓ among the impurities. On the other hand, when $\ell > L$ we reach the *ballistic* regime in which the electron momentum can be assumed to be constant and only limited by scattering with the boundaries of the sample. These two regimes are illustrated in Fig. 13.

In the previous discussion we have implicitly assumed that the typical dimensions of the sample are much larger than the Fermi wavelength λ_F . However, when dealing with atomic-sized contacts the contact width W is of the order of a few nanometers or even less and thus we have $W \sim \lambda_F$. We thus enter into the *full quantum* limit which cannot be described by semi-classical arguments. A main

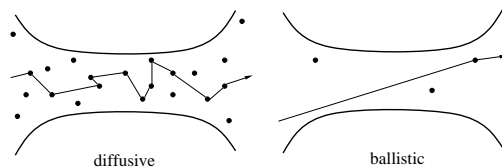


FIG. 13: Schematic illustration of a diffusive (left) and ballistic (right) conductor

challenge for the theory is to derive the conductance of an atomic-sized conductor from microscopic principles.

The objective of this section will be to review the basic theory for transport properties of small conductors. We find it instructive to start first by discussing the classical and semi-classical theories usually employed to analyze point contacts which are large with respect to the atomic scale. We shall then discuss the scattering approach pioneered by Landauer [5] to describe electron transport in quantum coherent structures and show its connection to other formalisms, such as Kubo's linear response theory. The more specific microscopic models for the calculation of conductance in atomic-sized contacts will be presented in Sect. VII.

B. Classical Limit (Maxwell)

Classically the current I passing through a sample that is submitted to a voltage drop V , depends on the conductivity of the material σ and on its geometrical shape. At each point of the material the current density \mathbf{j} is assumed to be proportional to the local electric field \mathbf{E} , that is, $\mathbf{j}(\mathbf{r}) = \sigma \mathbf{E}(\mathbf{r})$, which is the microscopic form of Ohm's law. The electric field satisfies Poisson's equation and the boundary conditions specify that the current density component normal to the surface of the conductor must be zero.

To calculate the conductance of a point-contact, we can model the contact as a constriction in the material. This problem was already studied by Maxwell [113], who considered a constriction of hyperbolic geometry. Then it is possible to obtain an analytic solution using oblate spheroidal coordinates (ξ, η, φ) defined as

$$\begin{aligned} x &= a \cosh \xi \cos \eta \cos \varphi, \\ y &= a \cosh \xi \cos \eta \sin \varphi, \\ z &= a \sinh \xi \sin \eta, \end{aligned}$$

where $2a$ is the distance between the foci, and $(0 \leq \xi < \infty)$, $(-\pi/2 \leq \eta \leq \pi/2)$, $(-\pi < \varphi \leq \pi)$, see Fig. 14. The constriction is then defined by the surface $\eta = \eta_0 = \text{const.}$ and the radius of the narrowest section is given by $r_0 = a \cos \eta_0$. Since a metal can be considered effectively charge neutral, Poisson's equation reduces to Laplace's equation

$$\nabla^2 V(\mathbf{r}) = 0, \quad (3)$$

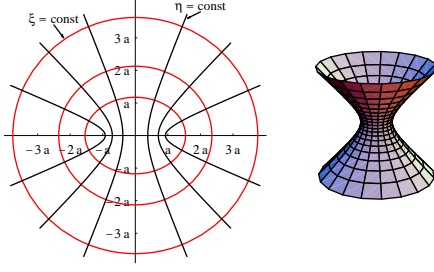


FIG. 14: Oblate spheroidal coordinates, and $\eta = \text{const.}$ surface.

where $V(\mathbf{r})$ is the electrostatic potential. Anticipating a solution that depends only on ξ , the equipotential surfaces are ellipsoids and the boundary conditions are automatically satisfied. The solution is then given by

$$V(\xi) = -\frac{V_0}{2} + \frac{2V_0}{\pi} \arctan(e^\xi), \quad (4)$$

where V_0 is the voltage drop at the constriction.

The total current is then obtained using Ohm's law and integrating over the constriction, and by dividing out the applied potential V_0 we can express the conductance of the constriction as

$$G_M = 2a\sigma (1 - \sin \eta_0) = 2r_0\sigma \frac{1 - \sin \eta_0}{\cos \eta_0}. \quad (5)$$

This gives the so-called Maxwell conductance of the constriction. In the limiting case $\eta_0 = 0$ the contact is simply an orifice of radius a in an otherwise non-conducting plate separating two metallic half-spaces, and its conductance is

$$G_M = 2a\sigma = 2a/\rho, \quad (6)$$

where ρ is the resistivity.

C. Semiclassical approximation for ballistic contacts (Sharvin)

When the dimensions of a contact are much smaller than their mean free path ℓ , the electrons will pass through ballistically. In such contacts there will be a large potential gradient near the contact, causing the electrons to accelerate within a short distance. The conduction through this type of contacts was first considered by Sharvin [114], who pointed out the resemblance to the problem of the flow of a dilute gas through a small hole [115].

Semiclassically the current density is written as

$$\mathbf{j}(\mathbf{r}) = \frac{2e}{L^3} \sum_{\mathbf{k}} \mathbf{v}_{\mathbf{k}} f_{\mathbf{k}}(\mathbf{r}), \quad (7)$$

where $f_{\mathbf{k}}(\mathbf{r})$ is the semiclassical distribution function and gives the occupation of state \mathbf{k} at position \mathbf{r} and $\mathbf{v}_{\mathbf{k}}$ is

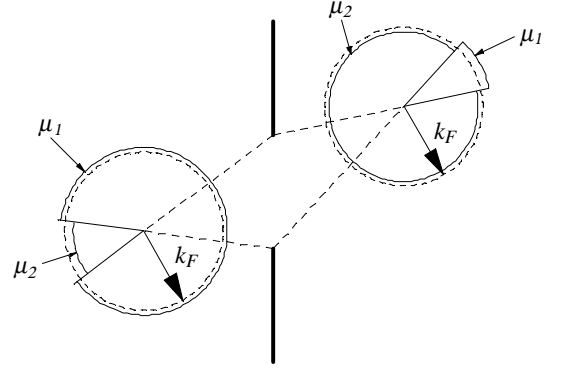


FIG. 15: Electron distribution function in the vicinity of the orifice. k_F is the equilibrium Fermi wavevector; μ_1 and μ_2 are the chemical potentials for each side, which far from the orifice, in the presence of an applied potential V , are equal to $E_F - eV/2$ and $E_F + eV/2$, respectively.

the group velocity of the electrons. In the absence of collisions, the distribution function at the contact is quite simple: for the right-moving states the occupation is fixed by the electrochemical potential within the left-hand-side electrode, and conversely for the left-moving states. Thus for an applied voltage V , the right-moving will be occupied to an energy eV higher than the left-moving states, which results in a net current density, $j = e\langle v_z \rangle \rho(\epsilon_F) eV/2$ where $\rho(\epsilon_F) = mk_F/\pi^2\hbar^2$ is the density of states at the Fermi level, and $\langle v_z \rangle = \hbar k_F/2m$ is the average velocity in the positive z -direction. The total current is obtained by integration over the contact, and hence the conductance (the so-called Sharvin conductance) is given by

$$G_S = \frac{2e^2}{h} \left(\frac{k_F a}{2} \right)^2, \quad (8)$$

where h is Planck's constant, k_F is the Fermi wave vector, and a is the contact radius. Note that the Sharvin conductance depends only on the electron density (through k_F), and is totally independent of the conductivity σ and mean free path ℓ . Quantum mechanics enters only through Fermi statistics.

In a more detailed calculation, the distribution function $f_{\mathbf{k}}(\mathbf{r})$ is obtained from Boltzmann equation in the absence of collisions [65],

$$\mathbf{v}_{\mathbf{k}} \cdot \nabla_{\mathbf{r}} f_{\mathbf{k}}(\mathbf{r}) - (e/\hbar) \mathbf{E} \cdot \nabla_{\mathbf{k}} f_{\mathbf{k}}(\mathbf{r}) = 0. \quad (9)$$

Far from the contact $f_{\mathbf{k}}$ is the Fermi distribution function, $f_0(\epsilon_{\mathbf{k}})$, with the adequate electrochemical potential in each electrode. Fig. 15 shows how the distribution function in the vicinity of the contact is modified with respect to the Fermi sphere. The states at a given point on the left side of the orifice are occupied to $E_F - eV/2$, unless they arrive from the other electrode, which defines a 'wedge-of-cake' in the electron distribution. Now, the electrostatic potential at this point is fixed by the requirement of charge neutrality, $\sum_{\mathbf{k}} [f_{\mathbf{k}}(\mathbf{r}) - f_0(\epsilon_{\mathbf{k}})] = 0$, i.e. the total volume of the two parts must be equal to

the equilibrium charge density. Far away from the orifice the ‘wedge’ vanishes and the Fermi spheres in both electrodes are equal in magnitude, but the bottom of the conduction band differs by eV . At the point in the middle of the orifice the electrons on the left hemisphere arrive from the right, and vice versa, which implies that to first approximation the number of excess electrons exactly balances the number of deficit electrons on the other side, and this defines the point $V = 0$. The voltage away from this point changes proportional to the solid angle of view of the orifice and approaches the limiting values $\pm eV/2$. The important conclusion is that the voltage drop is concentrated on a length scale of order a near the contact.

It is instructive to point out that the power $P = IV$ is entirely converted into kinetic energy of the electrons that are shot ballistically into the other electrode. As for the full-quantum point contacts that will be discussed next, energy relaxation of the electrons is not taken into account. This is a good approximation as long as the mean free path for inelastic scattering is much longer than the dimensions of the contact. Energy dissipation then takes place far away into the banks by scattering with phonons. In reality a small but finite amount of inelastic scattering takes place near the contact, which will be discussed later.

D. The scattering approach

In a typical transport experiment on a mesoscopic device, the sample (which in our case is an atomic-sized constriction) is connected to macroscopic electrodes by a set of *leads* which allow us to inject currents and fix voltages. The electrodes act as ideal electron reservoirs in thermal equilibrium with a well-defined temperature and chemical potential. The basic idea of the scattering approach is to relate the transport properties (conductances) with the transmission and reflection probabilities for carriers incident on the sample. In this one-electron approach phase-coherence is assumed to be preserved on the entire sample and inelastic scattering is restricted to the electron reservoirs only. Instead of dealing with complex processes taking place inside the reservoirs they enter into the description as a set of boundary conditions [116]. In spite of its simplicity, this approach has been very successful in explaining many experiments on mesoscopic devices.

Let us consider a two terminal configuration as depicted in Fig. 16. One can model the conductor as a scattering region connected to the electron reservoirs by perfect leads. On these leads the electrons propagate as plane waves along the longitudinal direction, while its transverse momentum is quantized due to the lateral confinement. As in the usual wave-guide problem, the quantization of transverse momentum defines a set of incoming and outgoing modes on each lead (let us call N_α the number of modes on lead α). Notice that the

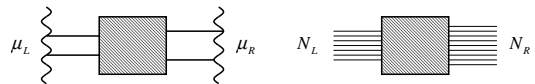


FIG. 16: Schematic representation for a ballistic two-terminal conductance problem. The gray box represents the sample, or the scattering area. The reservoirs (or electrodes) the left and right of the wiggly lines emit electrons onto the sample with an energy distribution corresponding to the electrochemical potentials μ_L and μ_R , respectively. Electrons reflected from the sample are perfectly absorbed by the reservoirs. The straight sections connecting the reservoirs to the sample represent perfect leads, where the number of modes in the left and right lead is N_L and N_R , respectively, and these numbers are not required to be equal.

perfect leads do not really exist in actual systems: they are an auxiliary construction of the scattering approach which greatly simplifies the formalism. The more general case can be analyzed using Green function techniques (see Sect. III E 1). Nevertheless, as we discuss below, the use of perfect leads does not affect the results as long as the number of modes considered is sufficiently large.

Another hypothesis that considerably simplifies the scattering approach is that there is a “perfect” coupling between the leads and the electron reservoirs. This perfect coupling fixes the distribution of the incoming modes, which is determined by the Fermi distribution on the corresponding electrode. On the other hand, the outgoing modes on the leads are transmitted into the electrodes with probability one. The boundary conditions on the incoming and outgoing modes become thus very simple.

Before going further in the discussion of the general formalism, it is instructive to consider the simple case where the sample is just a perfect one-dimensional conductor, having a single mode occupied. Let us assume that there is a voltage difference V applied between the electrodes. A net current will arise from the imbalance between the population of the mode moving from left to right (fixed by the Fermi distribution on the left electrode, f_L) and the population of the mode moving in the opposite sense (fixed by f_R). The current is then simply given by

$$\begin{aligned} I &= \frac{e}{L} \sum_{k\sigma} v_k (f_L(\epsilon_k) - f_R(\epsilon_k)) \\ &= \frac{e}{\pi} \int dk v_k (f_L(\epsilon_k) - f_R(\epsilon_k)), \end{aligned} \quad (10)$$

where L is the length of the conductor and σ is the electron spin. For a long conductor one can replace the sum over allowed k values by an integral over k . As we are dealing with a one system the density of states is $\rho(\epsilon) = 1/v_k \hbar$ and the current can be written as

$$I = \frac{2e}{h} \int d\epsilon (f_L(\epsilon) - f_R(\epsilon)). \quad (11)$$

At zero temperature $f_L(\epsilon)$ and $f_R(\epsilon)$ are step functions, equal to 1 below $\epsilon_F + eV/2$ and $\epsilon_F - eV/2$, respectively, and 0 above this energy. Thus the expression leads to $I = GV$, where the conductance is $G = 2e^2/h$.

This simple calculation demonstrates that a perfect single mode conductor between two electrodes has a finite resistance, given by the universal quantity $h/2e^2 \approx 12.9\text{k}\Omega$. This is an important difference with respect to macroscopic leads, where one expects to have zero resistance for the perfectly conducting case. The proper interpretation of this result was first pointed out by Imry [117], who associated the finite resistance with the resistance arising at the interfaces between the leads and the electrodes.

1. The Landauer formula

Let us now discuss the general scattering formalism for the two-terminal configuration. The amplitudes of incoming and outgoing waves are related by a (energy dependent) scattering matrix

$$\hat{S} = \begin{pmatrix} \hat{s}_{11} & \hat{s}_{12} \\ \hat{s}_{21} & \hat{s}_{22} \end{pmatrix} \equiv \begin{pmatrix} \hat{r} & \hat{t}' \\ \hat{t} & \hat{r}' \end{pmatrix}, \quad (12)$$

where $\hat{s}_{\alpha\beta}$ is a $N_\alpha \times N_\beta$ matrix whose components $(\hat{s}_{\alpha\beta})_{mn}$ are the ratio between the outgoing amplitude on mode n in lead α and the incoming amplitude on mode m in lead β .

Following Ref. [118], it is convenient to introduce creation and annihilation operators $a_{m\alpha}^\dagger(\epsilon)$ and $a_{m\alpha}(\epsilon)$ which create and destroy an incoming electron on mode m in lead α with energy ϵ . Similarly we introduce creation and annihilation operators for the outgoing states $b_{m\alpha}^\dagger(\epsilon)$ and $b_{m\alpha}(\epsilon)$. These are naturally related to the $a_{m\alpha}$ operators by

$$b_{m\alpha} = \sum_{n\beta} (\hat{s}_{\alpha\beta})_{mn} a_{n\beta}. \quad (13)$$

According to the hypothesis of perfect coupling between leads and electrodes, the population of the incoming modes is fixed by $\langle a_{m\alpha}^\dagger(\epsilon) a_{n\beta}(\epsilon) \rangle = \delta_{mn} \delta_{\alpha\beta} f_\alpha(\epsilon)$, where $f_\alpha(\epsilon)$ is the Fermi distribution function on the electron reservoir connected to lead α .

The current on mode m in lead α is due to the imbalance between the population of incoming and outgoing states and is given by

$$I_{m\alpha} = \frac{2e}{h} \int_{-\infty}^{\infty} d\epsilon [\langle a_{m\alpha}^\dagger(\epsilon) a_{m\alpha}(\epsilon) \rangle - \langle b_{m\alpha}^\dagger(\epsilon) b_{m\alpha}(\epsilon) \rangle]. \quad (14)$$

As in the single mode case, this expression arises due to the exact cancellation between the density of states and the group velocity on each mode. The factor 2 is due to spin degeneracy. Using the scattering matrix this

expression can be reduced to

$$I_{m\alpha} = \frac{2e}{h} \int_{-\infty}^{\infty} d\epsilon \left[\left(1 - \sum_n |\hat{r}_{mn}|^2 \right) f_\alpha - \sum_{\beta \neq \alpha} \sum_n |\hat{t}_{mn}|^2 f_\beta \right] \quad (15)$$

Adding the contribution of all modes, the net current on lead 1 will be given by

$$I_1 = \frac{2e}{h} \int_{-\infty}^{\infty} d\epsilon [(N_1 - R_{11})f_1 - T_{12}f_2], \quad (16)$$

where $R_{11} = \text{Tr}(\hat{r}^\dagger \hat{r})$ and $T_{12} = \text{Tr}(\hat{t}^\dagger \hat{t})$. Unitarity of the scattering matrix (which is required by current conservation) ensures that $\hat{r}^\dagger \hat{r} + \hat{t}^\dagger \hat{t} = \hat{I}$ and, therefore, taking the trace over all modes one has $T_{12} + R_{11} = N_1$, and thus

$$I_1 = \frac{2e}{h} \int_{-\infty}^{\infty} d\epsilon T_{12}(f_1 - f_2). \quad (17)$$

The linear response conductance is thus given by

$$G = \frac{2e^2}{h} \int_{-\infty}^{\infty} d\epsilon \left(-\frac{\partial f}{\partial \epsilon} \right) T_{12}, \quad (18)$$

which at zero temperature reduces to the well known Landauer formula $G = (2e^2/h)T_{12}$ [119].

2. The concept of eigenchannels

The Landauer formula teaches us that the linear conductance can be evaluated from the coefficients t_{nm} which give the outgoing amplitude on mode m in lead 2 for unity amplitude of the incoming mode n in lead 1. Notice that although \hat{t} is not in general a square matrix (the number of modes on each lead need not to be the same) the matrix $\hat{t}^\dagger \hat{t}$ is always a $N_1 \times N_1$ square matrix. Current conservation certainly requires that $T_{12} = T_{21} = \text{Tr}((\hat{t}^\dagger \hat{t}))$. This property is a simple consequence of time reversal symmetry of the Schrödinger equation which ensures that $t_{nm} = (t'_{mn})^*$.

Being the trace of an Hermitian matrix, T_{12} has certain invariance properties. For instance, there exists a unitary transformation \hat{U} such that $\hat{U}^{-1} \hat{t}^\dagger \hat{t} \hat{U}$ adopts a diagonal form. Due to hermiticity of $\hat{t}^\dagger \hat{t}$ its eigenvalues $\tau_i, i = 1, \dots, N_1$ should be real. Moreover, due to the unitarity of the scattering matrix one has $\hat{t}^\dagger \hat{t} + \hat{r}^\dagger \hat{r} = \hat{I}$ and then both $\hat{t}^\dagger \hat{t}$ and $\hat{r}^\dagger \hat{r}$ should become diagonal under the same transformation \hat{U} . As also both $\hat{t}^\dagger \hat{t}$ and $\hat{r}^\dagger \hat{r}$ are positive definite it is then easy to show that $0 \leq \tau_i \leq 1$ for all i .

The eigenvectors of $\hat{t}^\dagger \hat{t}$ and $\hat{r}^\dagger \hat{r}$ are called *eigenchannels*. They correspond to a particular linear combination of the incoming modes which remains invariant upon reflection on the sample. In the basis of eigenchannels the

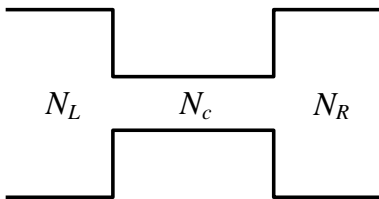


FIG. 17: Two perfect cylindrical leads connecting to a sample in the form of a narrow cylindrical conductor.

transport problem becomes a simple superposition of independent single mode problems without any coupling, and the conductance can be written as

$$G = \frac{2e^2}{h} \sum_i \tau_i. \quad (19)$$

At this point the definition of eigenchannels may seem somewhat arbitrary and dependent on the number of channels of the perfect leads attached to the sample. For instance, the dimension of the transmission matrix $\hat{t}^\dagger \hat{t}$ can be arbitrarily large depending on the number of modes introduced to represent the leads, which suggests that the number of eigenchannels is not a well defined quantity for a given sample.

In order to convince ourselves that this is not the case, let us consider a situation where the sample is a narrow cylindrical constriction between two wide cylindrical leads as shown in Fig. 17. Let us call N_c the number of propagating modes at the Fermi energy on the constriction. Clearly one has $N_c \ll N_1, N_2$. This geometry can be analyzed as two ‘wide-narrow’ interfaces connected in series. In such an interface the number of conduction channels with non-vanishing transmission is controlled by the number of propagating modes in the narrowest cross-section. This property is a simple consequence of current conservation along each conduction channel. Mathematically, one can show that the non-vanishing eigenvalues of $\hat{t}^\dagger \hat{t}$ (a $N_1 \times N_1$ matrix) should be the same as those of $\hat{t} \hat{t}^\dagger$ (a $N_c \times N_c$ matrix). Therefore, there should be $N_1 - N_c$ channels with zero transmission. By applying the same reasoning to the second ‘narrow-wide’ interface we conclude that only a small fraction of the incoming channels could have a non-zero transmission. The number of relevant eigenchannels is thus determined by the narrowest cross-section of the constriction.

For a constriction of only one atom in cross section one can estimate the number of conductance channels as $N_c \simeq (k_F a/2)^2$, which is between 1 and 3 for most metals. We shall see that the actual number of channels is determined by the valence orbital structure of the atoms.

3. Shot Noise

Shot noise is another important quantity for characterizing the transport properties of mesoscopic systems

[120, 121]. It refers to the time-dependent current fluctuations due to the discreteness of the electron charge. In a mesoscopic conductor these fluctuations have a quantum origin, arising from the quantum mechanical probability of electrons being transmitted or reflected through the sample. In contrast to thermal noise, shot noise only appears in the presence of transport, i.e. in a non-equilibrium situation.

Shot noise measurements provide information on temporal correlations between the electrons. In a tunnel junctions, where the electrons are transmitted randomly and correlation effects can be neglected, the transfer of carriers of charge q is described by Poisson statistics and the amplitude of the current fluctuations is $2qI$. In mesoscopic conductors correlations may suppress the shot noise below this value. Even when electron-electron interactions can be neglected the Pauli principle provides a source for electron correlations.

The relation between shot noise and the transmitted charge unit q has allowed the detection of the fractional $q = e/3$ charge carriers in the fractional quantum Hall regime [122, 123]. It has also been proposed that measurements of shot noise in superconducting atomic contacts could give evidence of transmission of multiple ne charges associated with multiple Andreev reflection processes [124, 125]. This issue will be discussed in Sect. X.

Qualitatively, the shot noise in ballistic samples can be understood from the diagram in Fig. 18. For the right moving states, which have been transmitted through the contact with an excess energy between 0 and eV , the average occupation number, \bar{n} , is given by the transmission probability τ_n . For the fluctuations in this number we find

$$\overline{\Delta n^2} = \overline{n^2} - \bar{n}^2 = \tau_n(1 - \tau_n), \quad (20)$$

where in the last step we used the fact that $\overline{n^2} = \bar{n}$, since for fermions n is either zero or one. Hence, the fluctuations in the current are suppressed both for $\tau_n = 1$ and for $\tau_n = 0$. According to Eq. (20) the fluctuations will be maximal when the electrons have a probability of one half to be transmitted. The shot noise is thus a non-linear function of the transmission coefficients, which can provide additional information on the contact properties to that contained in the conductance, as will be discussed in Sect. VIII.

Although there has recently appeared a specialized review on this subject [121] we shall re-derive here the main results concerning shot noise in quantum point-contacts for the sake of completeness.

In noise measurements the quantity one is interested in is the *noise power* spectrum given by the following current-current correlation function

$$S_{\alpha\beta}(\omega) = \frac{1}{2} \int e^{i\omega t} \langle \Delta \hat{I}_\alpha(t) \Delta \hat{I}_\beta(0) + \Delta \hat{I}_\beta(0) \Delta \hat{I}_\alpha(t) \rangle dt, \quad (21)$$

where $\Delta \hat{I}_\alpha = \hat{I}_\alpha - I_\alpha$ is the operator measuring the current fluctuations on lead α . This operator can be written

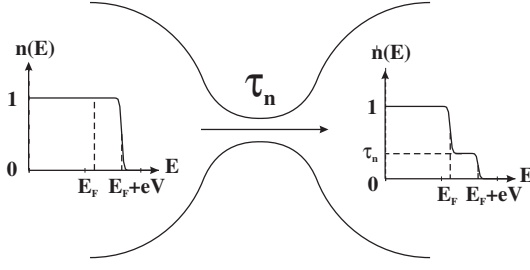


FIG. 18: In a ballistic quantum point contact with bias voltage, V , the transmission probability, τ_n , determines the distribution function, $n(E)$, of a transmitted state as a function of its energy, E . In the right reservoir, states with energy lower than the Fermi energy are all occupied, while right-moving states with higher energy can only be coming from the left reservoir, and therefore their average occupation is equal to the transmission probability, τ_n . This argument applies to every individual eigenchannel

in terms of creation and annihilation operators on each channel as in Sect. III D 1, i.e.

$$\hat{I}_\alpha(t) = \frac{2e}{h} \sum_m \int d\epsilon d\epsilon' e^{i(\epsilon - \epsilon')t/\hbar} \times [a_{m\alpha}^\dagger(\epsilon) a_{m\alpha}(\epsilon') - b_{m\alpha}^\dagger(\epsilon) b_{m\alpha}(\epsilon')]. \quad (22)$$

Thus, to obtain the noise spectrum one has to evaluate the expectation value of products of four operators. These products can be decoupled into all possible contractions of creation and annihilation operators taken by pairs, as dictated by Wick's theorem. This decoupling is valid as far as we are dealing with non-interacting electrons. In this way, a typical expectation value contributing to the power spectrum can be reduced as follows

$$\begin{aligned} & \langle a_{m\alpha}^\dagger(\epsilon_1) a_{n\beta}(\epsilon_2) a_{l\gamma}^\dagger(\epsilon_3) a_{k\delta}(\epsilon_4) \rangle \\ & - \langle a_{m\alpha}^\dagger(\epsilon_1) a_{n\beta}(\epsilon_2) \rangle \langle a_{l\gamma}^\dagger(\epsilon_3) a_{k\delta}(\epsilon_4) \rangle = \\ & \delta_{\alpha\delta} \delta_{\beta\gamma} \delta_{mk} \delta_{nl} \delta(\epsilon_1 - \epsilon_4) \delta(\epsilon_2 - \epsilon_3) f_\alpha(\epsilon_1) [1 - f_\beta(\epsilon_2)]. \end{aligned} \quad (23)$$

After some algebra one obtains the following general expression for the noise spectrum [118]

$$\begin{aligned} S_{\alpha\beta}(\omega) &= \frac{2e^2}{h} \sum_{\gamma\delta} \sum_{mn} \int d\epsilon A_{\gamma\delta}^{mn}(\alpha; \epsilon, \epsilon + \hbar\omega) \\ &\times A_{\delta\gamma}^{mn}(\beta; \epsilon + \hbar\omega, \epsilon) \\ &\times \{f_\gamma(\epsilon) [1 - f_\delta(\epsilon + \hbar\omega)] + f_\delta(\epsilon + \hbar\omega) [1 - f_\gamma(\epsilon)]\}, \end{aligned} \quad (24)$$

where

$$A_{\delta\gamma}^{mn}(\beta; \epsilon, \epsilon') = \delta_{mn} \delta_{\delta\beta} \delta_{\gamma\beta} - \sum_k \left(\hat{s}_{\beta\delta}^\dagger \right)_{mk}(\epsilon) (\hat{s}_{\beta\gamma})_{kn}(\epsilon').$$

This general expression is more than we need to analyze a noise experiment in atomic contacts. On the one

hand, as we are dealing with a two terminal geometry the expression can be considerably simplified. In practice what is measured is the time dependent current on one of the two leads which will be related to S_{11} or S_{22} . On the other hand, typical frequencies in noise experiments are of the order of 20 GHz or even much lower. For these frequencies $\hbar\omega$ is much smaller than the typical energy scale for variation of the transmission coefficients and thus one can safely adopt the zero frequency limit. Under these conditions the quantity that can be related to the experimental results is

$$\begin{aligned} S_{11}(0) &= \frac{2e^2}{h} \int d\epsilon \{ \text{Tr} [\hat{t}^\dagger(\epsilon) \hat{t}(\epsilon) \hat{t}^\dagger(\epsilon) \hat{t}(\epsilon)] \\ &\times [f_1(1 - f_1) + f_2(1 - f_2)] \\ &+ \text{Tr} [\hat{t}^\dagger(\epsilon) \hat{t}(\epsilon) (\hat{I} - \hat{t}^\dagger(\epsilon) \hat{t}(\epsilon))] \\ &\times [f_1(1 - f_2) + f_2(1 - f_1)] \}. \end{aligned} \quad (25)$$

As one can observe, this expression has two parts: the terms in $f_1(1 - f_1)$ and $f_2(1 - f_2)$ vanish at zero temperature and correspond to thermal fluctuations, and the terms in $f_1(1 - f_2)$ and $f_2(1 - f_1)$ which remain finite at zero temperature when there is an applied bias voltage correspond to the shot noise. One can further simplify this expression using the basis of eigenchannels as

$$\begin{aligned} S_{11}(0) &= \frac{2e^2}{h} \sum_n \int d\epsilon \{ \tau_n(\epsilon)^2 [f_1(1 - f_1) + f_2(1 - f_2)] \\ &+ \tau_n(\epsilon) [1 - \tau_n(\epsilon)] [f_1(1 - f_2) + f_2(1 - f_1)] \}. \end{aligned} \quad (26)$$

Moreover, as in general the energy scale for the variation of the transmission coefficients is larger than both temperature and applied voltage we can evaluate these coefficients at the Fermi energy and perform integration over the energy taking into account the Fermi factors, which yields [126]

$$\begin{aligned} S_{11}(0) &= \frac{2e^2}{h} [2k_B T \sum_n \tau_n^2 \\ &+ eV \coth\left(\frac{eV}{2k_B T}\right) \sum_n \tau_n (1 - \tau_n)]. \end{aligned} \quad (27)$$

4. Thermal transport

The scattering approach can be extended to study thermoelectric phenomena in mesoscopic systems [127, 128]. In the previous discussion it was implicitly assumed that the leads are connected to electron reservoirs which have the same temperature. If there is a temperature difference between the electrodes there will be an energy flux in addition to the electric current. Let us consider a two terminal geometry and call T_1 and T_2 the temperature on the left and right electrode respectively. The

total entropy current moving to the right on the left lead will be given by

$$J_{1S}^{\rightarrow} = -\frac{k_B}{h} \int [f_1 \ln f_1 + (1 - f_1) \ln(1 - f_1)] dE, \quad (28)$$

where $f_1 = f(E, \mu_1, T_1)$ denotes the Fermi function on the left electrode. On the other hand the entropy current going to the left on the same lead is given by

$$J_{1S}^{\leftarrow} = -\frac{k_B}{h} \int [(R_{11}f_1 + T_{12}f_2) \ln(R_{11}f_1 + T_{12}f_2) + (1 - R_{11}f_1 - T_{12}f_2) \ln(1 - R_{11}f_1 - T_{12}f_2)] dE. \quad (29)$$

By subtracting (28) and (29) the following expression for the heat current is obtained [127]

$$U_1 = T J_{1S} = \frac{1}{h} \int T_{12}(E)(E - \mu) [f_1 - f_2] dE, \quad (30)$$

where T and μ are the average temperature and chemical potential.

In the linear transport regime it is convenient to cast Eqs. (30) and (17) in matrix form,

$$\begin{pmatrix} I_1 \\ U_1 \end{pmatrix} = \begin{pmatrix} L_0 & \frac{1}{T} L_1 \\ L_1 & \frac{1}{T} L_2 \end{pmatrix} \begin{pmatrix} \mu_1 - \mu_2 \\ T_1 - T_2 \end{pmatrix}, \quad (31)$$

where

$$L_n = \frac{2e}{h} \int T_{12}(E)(E - \mu)^n \left(-\frac{\partial f}{\partial E} \right) dE. \quad (32)$$

An important property which can be determined experimentally is the thermoelectric power or thermopower, defined by

$$S(\mu, T) = \frac{1}{eT} \frac{L_1}{L_0}. \quad (33)$$

Thermoelectrical properties of 2DEG quantum point contacts have been studied experimentally by van Houten *et al.* [129]. The experimental results on the thermopower in atomic contacts will be discussed in Sect. IX A 3.

5. Limitations of the scattering approach

In spite of its great success in describing many properties of mesoscopic systems, the scattering approach is far from being a complete theory of quantum transport. The scattering approach is mainly a phenomenological theory whose inputs are the scattering properties of the sample, contained in the \hat{s} matrix. No hints on how these properties should be obtained from a specific microscopic model

are given within this approach. Moreover, the scattering picture is a one-electron theory which is valid only as long as inelastic scattering processes can be neglected. A strong assumption lies in considering electron propagation through the sample as a fully quantum coherent process. According to normal Fermi-liquid theory, such a description would be strictly valid at zero temperature and only for electrons at the Fermi energy. Under a finite bias voltage and at finite temperatures deviations from this simple description might occur.

Between all possible limitations we shall concentrate below in analyzing the following three: 1) lack of self-consistency in the electrostatic potential, 2) inelastic scattering within the sample, 3) electron correlation effects.

Self-consistency: Although the expression (17) for the current in a two-terminal geometry is in principle valid for an arbitrary applied voltage one should take into account that the transmission coefficients can be both energy and voltage dependent. This dependence is in turn determined by the precise shape of the electrostatic potential profile developing on the sample, which should in principle be calculated self-consistently. There are only few studies of non-linear transport in mesoscopic devices which include a self-consistent determination of the potential profile. Between these studies we mention the one by Pernas *et al.* [130] in which the current through a finite linear chain modeled by a tight-binding Hamiltonian is calculated by means of non-equilibrium Green functions. More recently Todorov [131] calculated by similar methods the non-linear conductivity for disordered wires. Brandbyge *et al.* [132] developed a method based on density functional theory to calculate the high-bias conductance for atomic-sized wires.

Inelastic scattering: At finite bias coherent propagation of electrons through the sample may be limited by inelastic scattering processes due to electron-phonon and electron-electron collisions. Büttiker [133] has proposed a phenomenological description of these processes within the scattering approach. In this description the inelastic scattering events are simulated by the addition of voltage probes distributed over the sample. The chemical potential on these probes is fixed by imposing the condition of no net current flow through them. Thus, although the presence of the probes does not change the total current through the sample they introduce a randomization of the phase which tends to destroy phase coherence. The current in such a structure will contain a coherent component, corresponding to those electrons which go directly from one lead to the other, and an inelastic component, corresponding to those electrons which enter into at least one of the voltage probes in their travel between the leads. A specific realization of this construction using a tight-binding model has been presented by D'Amato and Pastawski [134]. On the other hand, Datta [135] and others [136] have demonstrated the equivalence

between this phenomenological approach and the case where there is an interaction between electrons and localized phonon modes distributed over the sample treated in the self-consistent Born approximation. We should point out that the restricted problem of one electron interacting with phonons in a one-dimensional conductor can be mapped into a multichannel scattering problem [137, 138].

Electron correlation effects: The presence of strong Coulomb interactions may alter completely the description of transport given by the scattering approach. This occurs, for instance, when the sample is a small conducting region weakly coupled to the external leads. In this case electronic transport is dominated by charging effects and could be completely suppressed by the Coulomb blockade effect [139]. Although there have been some proposals to find the equivalent to the Landauer formula for the case of strongly interacting electrons [140] it is in general not possible to account for electron correlation effects within the simple scattering approach presented above. For this case more sophisticated methods based on Green function techniques are needed. The interested reader is referred to chapter 8 in Ref. [111] for an introduction to these techniques.

E. Relation to other formulations: Kubo formula and Green function techniques

The more traditional approach to transport properties of solids is based on linear response theory in which the conductivity tensor is given by the well known Kubo formula [141]. In this section we shall discuss the connection between this approach and the scattering picture of transport presented above. We shall first give a short derivation of the Kubo formula for bulk materials and then analyze the relation between conductance and non-local conductivity for a mesoscopic sample connected to macroscopic leads. This relation permits establishing a link between linear response theory and the scattering approach. We shall finally discuss how to express transport properties in terms of one-electron Green functions.

When a finite electric field \mathbf{E} , oscillating with frequency ω , is applied to the sample, the relation between the current density and the field is given by

$$\mathbf{J}(\mathbf{r}) = \int d^3r' \sigma(\mathbf{r}, \mathbf{r}', \omega) \mathbf{E}(\mathbf{r}'), \quad (34)$$

where $\sigma(\mathbf{r}, \mathbf{r}', \omega)$ is the non-local conductivity tensor (for simplicity we shall ignore the tensorial character of σ and assume an isotropic response of the electron system). We shall be interested in the zero frequency limit. In this limit we may assume that the electric field is uniform on the mesoscopic sample and vanish on the leads. This situation is illustrated in Fig. 19.

Let us first analyze the simpler case of an infinite homogeneous conductor under an applied constant field. In

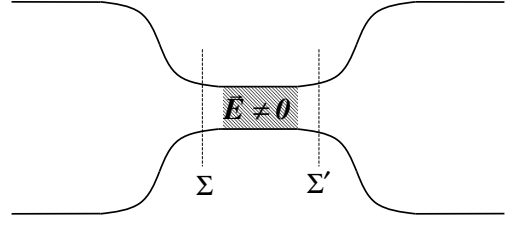


FIG. 19: Schematic representation of a two-terminal conductance system with the positions of the integration planes indicated.

this case the relation between field and current density becomes local, i.e. $\mathbf{J} = \sigma(\omega)\mathbf{E}$. One can obtain $\text{Re}\sigma(\omega)$ by evaluating the energy absorption rate P due to electronic transitions induced by the applied field. Taking the temporal average over one cycle one obtains

$$P = \langle \mathbf{E} \cdot \mathbf{J} \rangle = \text{Re}\sigma(\omega)E^2. \quad (35)$$

Notice that $\text{Re}\sigma(\omega)$ determines the dissipative part of the current and that $\text{Re}\sigma(\omega) \rightarrow \sigma(0)$ for $\omega \rightarrow 0$. Within lowest order perturbation theory, the energy absorption rate is given by

$$P = \sum_{\alpha\beta} W_{\alpha\beta} (f_\alpha - f_\beta) (\epsilon_\alpha - \epsilon_\beta), \quad (36)$$

where

$$W_{\alpha\beta} = \frac{2\pi}{\hbar} |\langle \alpha | \hat{V} | \beta \rangle|^2 \delta(\epsilon_\alpha + \hbar\omega - \epsilon_\beta). \quad (37)$$

In this expression α and β denote different electron eigenstates of the system, f_α and f_β being the corresponding Fermi factors. The perturbation term \hat{V} corresponds to a uniform electric field in the x direction, i.e.

$$\langle \alpha | \hat{V} | \beta \rangle = -eE \langle \alpha | \hat{X} | \beta \rangle. \quad (38)$$

Combining Eqs. (35–38) one obtains for the conductivity

$$\begin{aligned} \text{Re}\sigma(\omega) &= \frac{2\pi e^2}{\hbar} \sum_{\alpha\beta} |\langle \alpha | \hat{X} | \beta \rangle|^2 (\epsilon_\alpha - \epsilon_\beta) \\ &\quad \times (f_\alpha - f_\beta) \delta(\epsilon_\alpha + \hbar\omega - \epsilon_\beta). \end{aligned} \quad (39)$$

This expression can be rewritten in terms of the momentum operator by using the property

$$\langle \alpha | \hat{p}_x | \beta \rangle = \frac{im}{\hbar} \langle \alpha | \hat{X} | \beta \rangle (\epsilon_\alpha - \epsilon_\beta), \quad (40)$$

where m is the electron mass. Thus, in the limit $\omega \rightarrow 0$ the conductivity can be written as

$$\begin{aligned} \sigma(0) &= \frac{2\pi e^2 \hbar}{m^2} \int dE \sum_{\alpha\beta} |\langle \alpha | \hat{p}_x | \beta \rangle|^2 \left(-\frac{\partial f}{\partial E} \right) \\ &\quad \times \delta(E - \epsilon_\alpha) \delta(E - \epsilon_\beta). \end{aligned} \quad (41)$$

Eq. (41) is known as the Kubo formula and relates the conductivity to the equilibrium current fluctuations for a homogeneous conductor. In order to analyze the conductance of a finite sample it is necessary to go back to the non-local conductivity. This quantity is obtained from (41) by replacing $\langle \alpha | \hat{p}_x | \beta \rangle$ by $m \langle \alpha | \hat{j}_x(\mathbf{r}) | \beta \rangle / e$, where $\hat{j}_x(\mathbf{r})$ is the current operator at position \mathbf{r} , yielding

$$\sigma(\mathbf{r}, \mathbf{r}', 0) = 2\pi\hbar \int dE \sum_{\alpha\beta} \langle \alpha | \hat{j}_x(\mathbf{r}) | \beta \rangle \langle \beta | \hat{j}_x(\mathbf{r}') | \alpha \rangle \times \left(-\frac{\partial f}{\partial E} \right) \delta(E - \epsilon_\alpha) \delta(E - \epsilon_\beta). \quad (42)$$

One can obtain the total current through the sample I by integrating the current density on an arbitrary transversal cross-section Σ oriented perpendicularly to the current direction x (see Fig. 19), i.e.

$$I = \int_{\Sigma} ds J_x(\mathbf{r}) = \int_{\Sigma} ds \int_{\Omega} d^3r' \sigma(\mathbf{r}, \mathbf{r}', 0) E_x(\mathbf{r}'), \quad (43)$$

Now, the integration over the volume of the sample Ω in (43) can be divided into integration along the x direction and over a transversal cross-section Σ' . We thus have

$$I = \int_{\Sigma} ds \int_{\Sigma'} dx' \int_{\Sigma'} ds' \sigma(\mathbf{r}, \mathbf{r}', 0) E_x(\mathbf{r}'), \quad (44)$$

This expression can be simplified further by noticing that the integration over the transversal cross-section Σ' does not depend on its position on the x axis. This property arises from current conservation which implies

$$\int_{\Sigma} ds \langle \alpha | \hat{j}_x(\mathbf{r}) | \beta \rangle = \int_{\Sigma'} ds' \langle \alpha | \hat{j}_x(\mathbf{r}') | \beta \rangle. \quad (45)$$

One can thus interchange the integration over x' and integration over the transversal cross-section Σ' , to obtain

$$I = \int_{\Sigma} ds \int_{\Sigma'} ds' \sigma(\mathbf{r}, \mathbf{r}', 0) \int dx' E_x(\mathbf{r}'). \quad (46)$$

As the integration of the electric field along the x axis gives the voltage drop along the sample V , this expression has the form $I = GV$, where the conductance G is given by

$$G = \int_{\Sigma} ds \int_{\Sigma'} ds' \sigma(\mathbf{r}, \mathbf{r}', 0). \quad (47)$$

Notice that, due to current conservation, this expression does not depend on the position of the transversal cross-sections Σ and Σ' along the x axis. For convenience these surfaces can be taken well inside the leads, i.e. far away from the region where the voltage drop is located. In this asymptotic region the electron states become plane waves along the x direction.

1. The conductance in terms of Green functions

The Kubo formula for the conductivity is usually expressed in terms of Green functions [141, 142]. It is then possible to find an expression for the conductance in terms of Green functions through (47) and establish a connection between the scattering picture of transport and linear response theory [143, 144].

Let us first introduce the retarded and advanced Green functions $G^{r,a}(\mathbf{r}, \mathbf{r}', E)$ using an eigenstates representation

$$G^{r,a}(\mathbf{r}, \mathbf{r}', E) = \lim_{\eta \rightarrow 0} \sum_{\alpha} \frac{\psi_{\alpha}^*(\mathbf{r}) \psi_{\alpha}(\mathbf{r}')}{E - \epsilon_{\alpha} \pm i\eta}, \quad (48)$$

which have the property

$$G^a(\mathbf{r}, \mathbf{r}', E) - G^r(\mathbf{r}, \mathbf{r}', E) = 2\pi i \sum_{\alpha} \psi_{\alpha}^*(\mathbf{r}) \psi_{\alpha}(\mathbf{r}') \delta(E - \epsilon_{\alpha}). \quad (49)$$

Then, Eqs. (42) and (47) allow us to write the conductance G in the form

$$G = \frac{e^2 \hbar^3}{8\pi m^2} \int dE \left(-\frac{\partial f}{\partial E} \right) \int_{\Sigma} ds \int_{\Sigma'} ds' \left[\frac{\partial}{\partial x} \frac{\partial}{\partial x'} (G^a - G^r) (\tilde{G}^a - \tilde{G}^r) + (G^a - G^r) \frac{\partial}{\partial x} \frac{\partial}{\partial x'} (\tilde{G}^a - \tilde{G}^r) - \frac{\partial}{\partial x} (G^a - G^r) \frac{\partial}{\partial x'} (\tilde{G}^a - \tilde{G}^r) - \frac{\partial}{\partial x'} (G^a - G^r) \frac{\partial}{\partial x} (\tilde{G}^a - \tilde{G}^r) \right], \quad (50)$$

where $G^a - G^r = G^a(\mathbf{r}, \mathbf{r}', E) - G^r(\mathbf{r}, \mathbf{r}', E)$ and $\tilde{G}^a - \tilde{G}^r = G^a(\mathbf{r}', \mathbf{r}, E) - G^r(\mathbf{r}', \mathbf{r}, E)$.

We can simplify this expression considerably by taking the surfaces Σ and Σ' well inside the left and the right lead respectively. When \mathbf{r} and \mathbf{r}' correspond to points well inside the left and right leads the eigenstates are simple combinations of plane waves. Each plane wave corresponds to a lead mode n with wave number k_n in the x direction. In terms of the modes wavefunctions, χ_n , the Green functions can be expanded as

$$G^{r,a}(\mathbf{r}, \mathbf{r}', E) = \sum_{nm} \chi_m(\vec{\rho}) \chi_n^*(\vec{\rho}') G_{nm}^{r,a}(x, x'), \quad (51)$$

where the indexes n and m refer to the modes on the left and right leads respectively, and $\vec{\rho}$ and $\vec{\rho}'$ indicate the position on the transversal surfaces. For $x \rightarrow -\infty$ and $x' \rightarrow +\infty$ the Green functions components $G_{nm}^{a,r}(x, x')$ behave as

$$G_{nm}^{a,r}(x, x') \sim e^{\mp i k_n x} e^{\pm i k_m x'}, \quad (52)$$

and in this way the derivatives in (50) can be easily computed. As a final result one obtains

$$G = \frac{e^2 \hbar^3}{\pi m^2} \int dE \left(-\frac{\partial f}{\partial E} \right) \sum_{nm} k_n k_m |G_{nm}^a(x, x', E)|^2. \quad (53)$$

By comparing with the Landauer formula (18) the transmission coefficient in terms of Green functions is the just given by [143]

$$T_{12}(E) = \hbar^2 \sum_{nm} v_n v_m |G_{nm}^a(x, x', E)|^2, \quad (54)$$

where $v_n = \hbar k_n / m$ is the velocity on channel n . We should point out that the above expression is useful to obtain the transmission for realistic microscopic models. We shall come back to this point in Sect. VII.

IV. THEORY FOR CURRENT TRANSPORT IN SUPERCONDUCTING POINT CONTACTS

When one or both electrodes in a point contact are superconducting, transport properties may be dramatically affected. For instance, the conductance in normal-metal–superconductor (N-S) or superconductor–superconductor (S-S) contacts exhibits very peculiar non-linear behavior which is associated with the presence of an energy gap in the excitation spectrum of the superconductor. In addition, in S-S point contacts one can observe manifestations of the ground state phase-coherence like the Josephson effect.

In this section we shall review the basic theoretical developments which allow to understand the transport properties of superconducting point contacts. It will provide one of the most powerful approaches for experimentally determining the number of conductance channels in atomic-sized contacts.

A. The Bogoliubov de Gennes equation and the concept of Andreev reflection

In a tunnel junction, where the coupling between the electrodes is exponentially small, one can calculate the current-voltage characteristic starting from the electron states of the isolated electrodes and then using first order perturbation theory in the coupling [145]. Such calculations predict that the current should vanish at zero temperature in a N-S junction when the bias voltage eV is smaller than the superconducting energy gap Δ . In the same way, they would predict that the current vanishes for $eV < 2\Delta$ in a symmetric S-S junction at zero temperature (see for instance [146]).

These type of calculations are, however, not suitable for point contacts with finite normal conductance. In this case it is in general necessary to adopt a non-perturbative

approach. The Bogoliubov-de Gennes (BdeG) equations [147], describing the quasi-particle excitations in non-uniform superconductors, provide a useful starting point for this case.

In a superconductor the quasi-particle excitations consist of a mixture of electron-like and hole-like states. The BdeG equations are two coupled linear differential equations from which the amplitudes $u(r, E)$ and $v(r, E)$ of an excitation of energy E on the electron and hole states can be obtained. These equations can be written as [147]

$$\begin{aligned} Eu(r, E) &= \left[-\frac{\hbar^2 \nabla^2}{2m} + U(r) - E_F \right] u(r, E) \\ &\quad + \Delta(r) v(r, E) \\ Ev(r, E) &= - \left[-\frac{\hbar^2 \nabla^2}{2m} + U(r) - E_F \right] v(r, E) \\ &\quad + \Delta^*(r) u(r, E), \end{aligned} \quad (55)$$

where $U(r)$ and $\Delta(r)$ are effective potentials to be determined self-consistently [147]. In the case of a uniform superconductor the BdeG equations can be solved trivially in terms of plane waves to obtain the well known dispersion law for quasi-particles in the superconductor

$$E_k = \sqrt{(\epsilon_k - E_F)^2 + \Delta^2}, \quad (56)$$

where $\epsilon_k = (\hbar k)^2 / 2m$, and the coefficients

$$u_k^2 = \frac{1}{2} \left(1 + \frac{\epsilon_k - E_F}{E_k} \right) \quad v_k^2 = \frac{1}{2} \left(1 - \frac{\epsilon_k - E_F}{E_k} \right). \quad (57)$$

The dispersion relation can be inverted to obtain the wavevector modulus in terms of the energy of the excitation

$$\hbar k^\pm = \sqrt{2m \left[E_F \pm \sqrt{E^2 - \Delta^2} \right]}. \quad (58)$$

The excitations with k^+ arise from states above the Fermi surface in the normal case and are called ‘quasi-electrons’ and the ones with k^- arise from states below the Fermi surface and are called ‘quasi-holes’.

Let us now consider the case of a point-contact between a normal metal and a superconductor. For simplicity we shall assume that there is a single channel connecting both electrodes and call x a coordinate along the point contact. We shall also assume that the pairing potential $\Delta(x)$ exhibits a step-like behavior from zero to a constant value Δ at the N-S interface.

Let us consider an incident electron with energy E . The wave functions at each side of the interface can be written as

$$\begin{aligned} \Psi(x, E) &= \begin{pmatrix} 1 \\ 0 \end{pmatrix} e^{iq^+ x} + r_{eh} \begin{pmatrix} 0 \\ 1 \end{pmatrix} e^{iq^- x} \\ &\quad + r_{ee} \begin{pmatrix} 1 \\ 0 \end{pmatrix} e^{-iq^+ x} \quad \text{for } x < 0 \end{aligned}$$

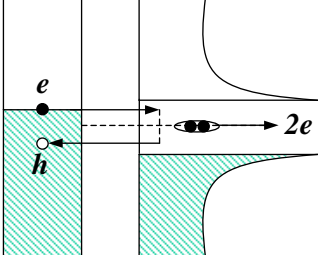


FIG. 20: Schematic representation of an Andreev reflection process.

$$\Psi(x, E) = t_{ee} \begin{pmatrix} u(E) \\ v(E) \end{pmatrix} e^{ik^+ x} + t_{eh} \begin{pmatrix} v(E) \\ u(E) \end{pmatrix} e^{-ik^- x} \text{ for } x > 0, \quad (59)$$

where $\hbar q^\pm = \sqrt{2m(E_F \pm E)}$ and the two elements in each column vector represent the electron and hole components of the excitation. The four coefficients r_{ee} , t_{ee} , r_{eh} and t_{eh} can be determined by imposing the conditions of continuity of the wave function and its derivative at the interface. They describe the four possible processes that can take place for an incident electron on the N-S interface, i.e. reflection as an electron, transmission as a quasi-electron, reflection as a hole and transmission as a quasi-hole. An additional approximation is to assume that for $E \sim \Delta$ one has $q^+ \simeq q^- \simeq k^+ \simeq k^-$, which is valid as long as $\Delta/E_F \ll 1$. This assumption is usually called the Andreev approximation.

In the simplest case of a perfect N-S interface with no mismatch in the electrostatic potential one obtains $r_{ee} = t_{eh} = 0$ and

$$r_{eh}(E) = v(E)/u(E), \quad (60)$$

which gives the probability amplitude for reflection as a hole or *Andreev reflection*. Taking into account the expressions for the coefficients given by (57) it is easy to show that for $E < \Delta$, r_{eh} is just a phase factor given by

$$r_{eh}(E) = \exp[-i \arccos(E/\Delta)], \quad (61)$$

while for $E > \Delta$, r_{eh} decays exponentially. The probability of Andreev reflection is then equal to 1 for incident electrons with energy inside the superconducting gap. It should be noticed that in the whole process two electrons are injected from the normal electrode, which finally gives rise to a new Cooper pair in the superconductor as illustrated in Fig. 20. This is the basic mechanism for converting a normal current into a supercurrent at a N-S interface, first discussed by Andreev in 1964 [148].

In order to analyze the case of an imperfect interface with arbitrary normal transmission one can use the model introduced by Blonder, Tinkham and Klapwijk [149]. Within this model the electron potential at the interface is represented by a delta function, i.e $U(x) = H\delta(x)$. The

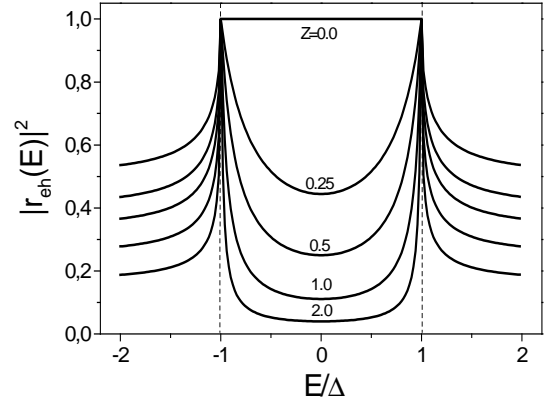


FIG. 21: Andreev reflection probability in the model by Blonder, Tinkham and Klapwijk [149].

boundary conditions on the wavefunctions should now take into account the presence of this delta-like potential. A straightforward calculation then yields for $E < \Delta$ [149]

$$|r_{eh}(E)|^2 = \frac{\Delta^2}{E^2 + (\Delta^2 - E^2)(1 + 2Z)^2}, \quad (62)$$

where $Z = k_F H / 2 E_F$ is a dimensionless parameter controlling the strength of the delta-like potential. The energy dependence of the Andreev reflection amplitude for increasing values of Z is represented in Fig. 21. As can be observed, for $Z = 0$ one recovers the case of a perfect interface with $|r_{eh}(E)|^2 = 1$ inside the gap, while for $Z \rightarrow \infty$, $r_{eh}(E) \rightarrow 0$ inside the gap, as expected for a tunnel junction.

These results can be used to obtain the linear conductance of a N-S quantum point. For this purpose, the scattering approach described in Sect. III has to be extended in order to incorporate Andreev reflection processes (see for instance [150]). At zero temperature and for a single conduction channel one obtains

$$G_{NS} = \frac{4e^2}{h} |r_{eh}(0)|^2, \quad (63)$$

where the factor 4 instead of the usual 2 in the Landauer formula reflects the fact that two electrons are transmitted in an Andreev reflection process. This expression has been generalized to the multi-channel case by Beenakker [150] who obtained

$$G_{NS} = \frac{4e^2}{h} \sum_n \frac{\tau_n^2}{(2 - \tau_n)^2}, \quad (64)$$

where τ_n denotes the transmission probability on the n -th conduction channel. Eq. (64) shows that the normal conduction channels are not mixed by Andreev reflection processes, i.e. an electron incident on a given conduction channel is reflected as a hole on the *same* channel. This is reasonable since the energy scale for superconducting

correlations is much smaller than the energy between the bottoms of the conductance channels. We shall come back to this property when analyzing the case of biased SNS contacts (Sect. IV C).

B. SNS contacts at zero bias

In a similar way as in the previous subsection one can use the BdeG equations to analyze the excitation spectrum in a SNS structure. Let us consider the case of two superconducting electrodes connected by a single normal channel of length L . For simplicity let us first consider the case of perfect matching at both interfaces. An electron in the normal region with energy $E < \Delta$ will be Andreev reflected into a hole when reaching one of the interfaces and, conversely, this hole will be converted into an electron with the same energy at the other interface. The combination of these processes gives rise to an infinite series of Andreev reflections. The resonance condition can be easily established by taking into account the amplitude for an individual Andreev reflection given by Eq. (61) and the phase accumulated by electrons and holes when propagating through the normal region, which yields

$$E = \Delta \cos \left\{ \frac{\varphi}{2} - \frac{k_F L}{2} (E/E_F) - n\pi \right\}, \quad (65)$$

where φ is the phase difference between the superconducting electrodes (notice that the superconducting phase enters into the Andreev reflection amplitude (61) simply as an additional phase factor). This equation admits multiple solutions which correspond to bound states inside the superconducting gap, usually called Andreev states or Andreev-Kulik states [151]. In the limit $L \ll \xi_0$, $\xi_0 = \pi v_F / \Delta$ being the superconducting coherence length, only two bound states are found at energies [152]

$$E = \pm \Delta \cos \left\{ \frac{\varphi}{2} \right\}. \quad (66)$$

For finite phase difference these states carry a Josephson current with opposite directions that can be computed using the thermodynamic relation $I \sim dF/d\varphi$, where F is the free energy of the system. This relation yields $I \sim \sin \varphi / 2$ for perfect interfaces, a result which was first derived by Kulik and Omelyanchuk [153] in 1978. For a quantum point contact with an smooth (or adiabatic) geometry accommodating N conduction channels the current-phase relation is given by [154]

$$I(\varphi) = \frac{Ne\Delta}{\hbar} \sin \left(\frac{\varphi}{2} \right) \tanh \left(\frac{E}{2k_B T} \right). \quad (67)$$

The case of a SNS structure with arbitrary normal transmission can also be analyzed using the BdeG equations. For a single conduction channel in the limit $L \ll \xi_0$ one obtains two bound states at energies [154]

$$E = \pm \Delta \sqrt{1 - \tau \sin^2 \left(\frac{\varphi}{2} \right)}, \quad (68)$$

where τ is the normal transmission. From this expression the current-phase relation turns out to be

$$I(\varphi) = \frac{e\tau\Delta}{2\hbar} \frac{\sin(\varphi)}{\sqrt{1 - \tau \sin^2 \left(\frac{\varphi}{2} \right)}} \tanh \left(\frac{E}{2k_B T} \right). \quad (69)$$

This result has been obtained by several authors using different techniques [150, 155, 156, 157]. It interpolates between the tunnel limit where the behavior $I \sim \sin(\varphi)$ first predicted by Josephson [158] is recovered, to the perfect transmission limit where the $\sin(\varphi/2)$ behavior of Kulik-Omelyanchuk is recovered. The maximum supercurrent at zero temperature as a function of the contact transmission is given by [159]

$$I_{max} = \frac{e\Delta}{\hbar} [1 - \sqrt{1 - \tau}]. \quad (70)$$

In superconducting quantum point-contacts the effect of thermal fluctuations on the supercurrent can be rather large. Thermal noise in a phase polarized contact has been calculated Averin and Imam [160] for the case of perfect transmission and by Martín-Rodero *et al.* [161] for the case of arbitrary transmission.

C. SNS contacts at finite bias voltage

When applying a finite voltage the phase difference in a SNS contact increases linearly with time according to the Josephson relation, i.e. $\varphi = \omega_0 t$, where $\omega_0 = 2eV/\hbar$ is the Josephson frequency. The response of the system cannot in general be described by Eq. (69) in an adiabatic approximation due to the fact that excitations of quasiparticles come into play and can give the main contribution. The total current through the contact contains all the harmonics of the Josephson frequency and can be written as [40, 41]

$$I(V, t) = \sum_n I_n(V) e^{in\omega_0 t}. \quad (71)$$

In this decomposition one can identify a dissipative part, which is an odd function of V , and a non-dissipative part, which is an even function of V . These two parts are given by [41]

$$I_D = I_0 + 2 \sum_{m>0} \text{Re}(I_m) \cos(m\omega_0 t), \quad (72)$$

and

$$I_S = -2 \sum_{m>0} \text{Im}(I_m) \sin(m\omega_0 t). \quad (73)$$

The quantity which is more directly accessible by experiments is the dc component I_0 , which we will discuss in more detail below.

As an example, the measured current voltage characteristic of an Al atomic contact at 17 mK is shown in Fig. 22, and the experiment will be discussed more extensively in Sect. X. In this curve one can clearly distinguish the supercurrent branch at zero voltage. On the other hand, the dissipative branch exhibits a very peculiar structure for bias voltages smaller than $2\Delta/e$, which is called the *subgap structure* (SGS). The SGS consists of a series of more or less pronounced current jumps located at $eV = 2\Delta/n$. This structure cannot be understood in terms of single quasi-particle processes.

The first observations of the SGS were made in tunnel junctions by Taylor and Burstein [163] and Adkins [164] in 1963. Since then, there have been several attempts to explain this behavior theoretically. In the early 60's Schrieffer and Wilkins [165] proposed a perturbative approach which is known as multi-particle tunneling theory. In this approach the current is calculated up to second order perturbation theory in the tunneling Hamiltonian. Although it explains the appearance of a current step at $eV = \Delta$ the theory is pathological as the current becomes divergent at $eV = 2\Delta$. Another theory, proposed by Werthamer in 1966, suggested that the SGS is due to the coupling of the tunneling electrons with the Josephson radiation [166]. This theory predicted a different behavior for even and odd n , which is not observed experimentally.

There is nowadays clear evidence that the SGS can be understood in terms of multiple Andreev reflections (MAR), as first proposed by Klapwijk, Blonder and Tinkham [38]. A qualitative explanation of the SGS in superconducting contacts in terms of MAR is illustrated in Fig. 23. Single quasi-particle processes as those illustrated in Fig. 23(a) are only possible when $eV > 2\Delta$ in

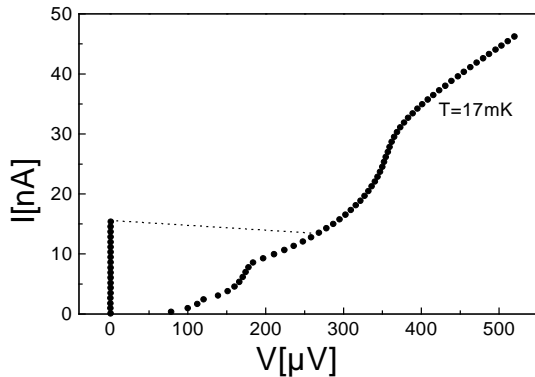


FIG. 22: Current-voltage characteristic for an Al atomic contact at 17 mK. As the current is ramped up the contact is seen to switch from the supercurrent branch near zero voltage to the finite-voltage dissipative branch, which is highly non-linear. Reprinted with permission from [162]. Copyright 2000 American Physical Society.

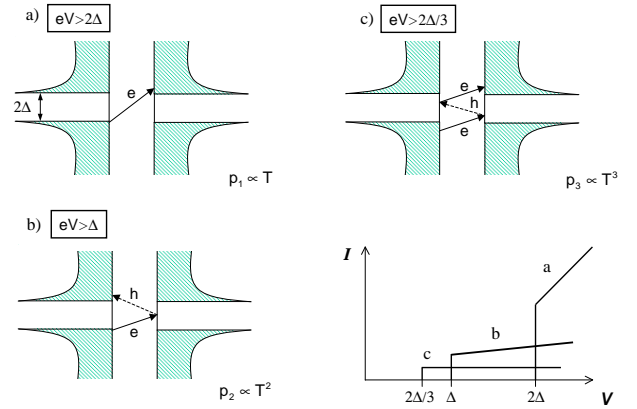


FIG. 23: Schematic explanation of the subgap structure in superconducting contacts.

order for the transferred quasi-particle to reach the available states on the right superconductor. The probability of these type of processes is proportional to the contact transmission and they give a contribution to the current-voltage relation as indicated schematically in the lower right panel in Fig. 23. At lower bias voltages current is possible due to Andreev processes. The simplest Andreev process is depicted in Fig. 23(b), where two quasi-particles are transmitted with a probability proportional to the square of the normal transmission, creating a Cooper pair on the right side. These processes give a contribution to the IV with a threshold at $eV = \Delta$. At even lower biases higher order Andreev processes can give a contribution. In general, a n -th order process in which n quasiparticles are transmitted gives a contribution proportional to the n -th power of the transmission and with a threshold at $eV = 2\Delta/n$.

The first semi-quantitative determination of the SGS in terms of MAR was presented by Klapwijk, Blonder and Tinkham [38] for the case of a one-dimensional SNS structure with perfect interfaces and generalized by Octavio *et al.* [167] for the case of arbitrary transparency. These last calculations were based on a Boltzmann kinetic equation corresponding to a semi-classical description of transport. Fully microscopic calculations using Green function techniques were first presented by Arnold in 1987 [39].

A deeper and more quantitative insight into the SGS has been obtained in the last decade by analyzing the case of single-mode contacts [40, 41, 42]. In 1995 Bratus *et al.* [42] and Averin and Bardas [40] calculated the current in a voltage biased superconducting contact by matching solutions of the time-dependent BdeG equations with adequate boundary conditions (scattering approach). While Bratus *et al.* analyzed the low transmission regime, Averin and Bardas calculated the IV curves for arbitrary transmission. On the other hand, Cuevas *et al.* [41] used a Hamiltonian approach together with non-equilibrium Green function techniques to obtain the current in a one channel contact with arbitrary trans-

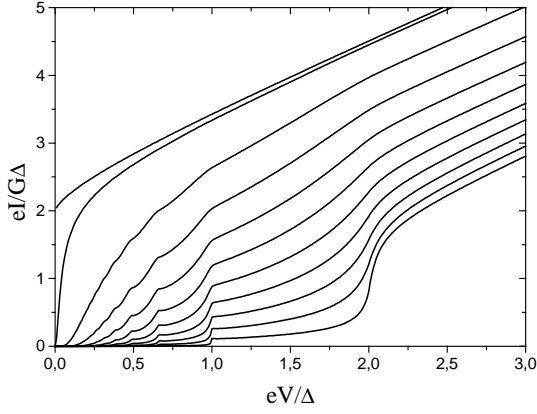


FIG. 24: The zero-temperature dc component of the current in a single mode superconducting contact, where the values of the normal transmission increase from $\tau = 0.1$ in the lower curve by increments of 0.1. The upper two curves correspond to $\tau = 0.99$ and $\tau = 1$. Reprinted with permission from [41]. Copyright 1996 American Physical Society.

parency. The results of the scattering and the Hamiltonian approaches have been shown to be equivalent [41]. Moreover, the approach presented in [41] demonstrates that the pathologies of the multi-particle tunneling theory of Schrieffer and Wilkins disappear when calculations are performed up to infinite order in the tunneling Hamiltonian.

The theoretical results for the dc component of the current in a single-mode contact for a number of transmission values are presented in Fig. 24. The two relevant features of these curves are the SGS for $eV < 2\Delta$ and the excess current with respect to the normal case which is found for $eV \gg \Delta$. As can be observed, the SGS is very pronounced at low transmission and becomes smoother when the transmission is close to 1. At perfect transmission the structure in the IV curve completely disappears and the excess current reaches the value $e\Delta/\hbar$.

In the limit of small bias voltages the transport properties of the contact can be understood in terms of the non-equilibrium population of the Andreev states given by (68) [40, 41]. The theory predicts a crossover from supercurrent to dissipative current which takes place for $eV \sim \Delta\sqrt{1-\tau}$. At larger biases the two Andreev states can be connected by Landau-Zener transitions [40].

More recently shot noise in a single channel superconducting contact has been studied [124, 125]. It has been demonstrated that the effective charge, defined as the ratio between noise and current, i.e. $q^* = S/2I$, is quantized in the limit of low transmission and increases as $1 + \text{Int}(2\Delta/V)$ for decreasing bias voltage. This prediction is consistent with the fact that the current is due to transfer of multiple quasi-particles mediated by Andreev processes as schematically depicted in Fig. 23.

For the purpose of this review the most important result is the fact that the theory produces current-voltage curves that have a very characteristic shape, which exclu-

sively depends on the transmission probability τ . The results obtained above can be easily generalized to the multichannel case. As in the N-S case, one may assume that the conduction channels are the same as in the normal state, i.e. that Andreev reflection processes do not mix the normal channels. This is true as far as one can neglect the energy dependence of the normal scattering matrix within the superconducting gap region. The validity of this approximation will be discussed in Sect. VIII. Further, the theory is exact and can therefore be exploited to extract the transmission probabilities and the number of relevant conduction channels from the experiment. The analysis of experimental IV -curves for superconducting atomic-sized contacts will be presented in Sect. VIII.

D. Current biased contacts

In practice it is not possible to impose a constant voltage at very low bias ($eV \ll \Delta$). In this limit the effective impedance of the contact tends to zero due to the presence of the supercurrent branch and the impedance of the circuit in which the contact is embedded starts to play an important role. A way to study this limit in detail is to impose a dc current bias through the contact shunted with an external resistance R . This is the equivalent to the ‘Resistively Shunted Junction’ (RSJ) model well studied in connection with superconducting tunnel junctions. As in that case, provided that the contact capacitance is large enough, the dynamics of the phase in this configuration is analogous to the motion of a massless particle in a tilted ‘wash-board’ potential, governed by a Langevin equation. However, in the case of an atomic contact the potential is not the usual sinusoid but has a more general form, which depends on the occupation of the Andreev states, given by [160]

$$U_p = -I_b \varphi + \sum_{i=1}^N (n_{i+} - n_{i-}) E(\varphi, \tau_i) \quad (74)$$

where I_b is the imposed current bias, $E(\varphi, \tau) = -\Delta\sqrt{1-\tau\sin^2(\varphi)}$ gives the lower Andreev level energy in a quantum channel of transmission τ and $n_{i\pm}$ denote the occupation of the upper and lower Andreev states in the i -th quantum channel. The Langevin equation which determines the phase evolution is given by

$$\frac{d\varphi}{dt} = -\frac{\partial U_p}{\partial \varphi} + \frac{2eR}{\hbar} i_n(t) \quad (75)$$

where $i_n(t)$ is a fluctuating current arising from thermal noise in the shunting resistor. The noise intensity should satisfy the fluctuation-dissipation theorem.

As a final ingredient one has to impose thermal equilibrium population of the Andreev states at $\varphi = 2n\pi$ as boundary conditions. The corresponding Langevin equations can be solved either by direct numerical simulation

or by mapping the problem onto a Fokker-Planck equation, following a procedure introduced by Ambegaokar and Halperin [168] for the traditional RSJ model. The results of this model and the comparison with experimental measurements have been presented by Goffman *et al.* [162] and will be discussed in Sect. X.

V. THE CONDUCTANCE OF ATOMIC-SIZED METALLIC CONTACTS: EXPERIMENT

As we have seen above, in a conductor for which the dimensions are much smaller than the phase coherence length the linear conductance, G , is given in terms of the Landauer expression

$$G = \frac{2e^2}{h} \sum_n \tau_n, \quad (76)$$

where the τ_n describe the transmission probabilities for each of the eigenmodes of the conductor and the sum runs over all occupied modes. If we can contrive our experiment in such a way that the τ_n are equal to 1, up to a mode number N , and equal to zero for all other modes, then the conductance assumes values which are an integer times the quantum unit of conductance, $G_0 = 2e^2/h$. It turns out to be possible to fabricate conductors which have precisely this property, using a two-dimensional electron gas (2DEG) semiconductor device, as was beautifully demonstrated in the seminal experiments by van Wees *et al.* [14] and Wharam *et al.* [15].

For atomic-sized metallic contacts the Landauer expression is also applicable and the number of channels involved is expected to be small. This can be judged from the fact that the Fermi wavelength in metals is of the order of the atomic diameter, $\lambda_F \simeq 5 \text{ \AA}$. This implies that, while the 2DEG experiments require cooling to helium temperatures in order to be able to resolve the splitting of $\sim 1 \text{ meV}$ between the quantum modes, in metals the mode splitting is $\pi^2 \hbar^2 / 2m\lambda_F^2 \sim 1 \text{ eV}$, which is sufficiently high to allow the observation of quantum effects at room temperature. The number of relevant conductance channels in a single-atom contact can be estimated as $N = (k_F a/2)^2$. For copper we have $(k_F a/2)^2 = 0.83$, which is close to 1, suggesting that a single atom corresponds to a single conductance channel. This implies that the atomic granularity will limit our ability to smoothly reduce the contact size, in order to directly observe quantum effects in the conductance. Moreover, a priori we cannot expect the conductance for metallic atomic-sized contacts to be given by simple multiples of the conductance quantum. The wave function of the electrons inside the contact will resemble the atomic wave functions, and the matching of these to the wave functions in the leads will critically influence the transmission probabilities for the quantum modes. The atomic structure of the contact and the composition of the electronic quantum modes will be interwoven, and we will

now discuss the experimental observations and what we can conclude from them.

A. Contact making and breaking

The experimental techniques most frequently employed in the study of conductance of atomic-sized contacts involve mechanically driven breaking and making cycles of a contact between two metal electrodes. Examples of conductance curves for gold at low temperatures were already shown in Sect. II, Fig. 4, when we discussed the various experimental techniques. A further example of a conductance curve measured on a gold sample at room temperature is shown in Fig. 25. The curves are recorded while breaking the contact and, although the conditions for the two experiments are widely different, the main features in the curves are similar. We recognize a series of plateaus in the conductance, which are nearly horizontal for the lowest conductance values, but have a negative slope for larger contact size. At the end of a plateau a sharp jump is observed, at which the conductance usually decreases by an amount of order of the quantum unit, G_0 . Although one is inclined to see a coincidence of the plateaus with multiples of G_0 this coincidence is far from perfect, and in many cases clearly absent. A marked exception to this rule is the position of the last conductance plateau before contact is lost. For gold this plateau is reproducibly found very near $1 G_0$. The latter property is generally observed for monovalent metals (Cu, Ag and Au, and the alkali metals Li, Na and K). For *sp* and *sd*-metals the plateaus are generally less regularly spaced, and the last plateau before tunneling can be a factor of two or more away from $1 G_0$. An example for the *sp*-metal aluminum is shown in Fig. 26 and for the *sd*-metal platinum in Fig. 8. The behavior is much less regular than for gold and in many regions the conductance is even seen to rise while pulling the contact. Similar anomalous slopes are also seen for other metals, an explanation for which will be presented in Sect. VIII C.

Let us now discuss the problem of the interpretation of the sharp steps that are observed in the conductance (Figs. 4, 8, 25, 26). As was pointed out in some of the early papers [26, 27], the dynamics of the contact conductance around the steps strongly favors an interpretation in terms of atomic rearrangements, which result in a stepwise variation of the contact diameter. This interpretation has been corroborated by a number of recent experiments and by molecular dynamics simulations. The molecular dynamics calculations of mechanics, force and conductance will be discussed in Sect. VII. The most direct experimental evidence comes from simultaneous measurements of the conductance and the force in the contact, which is to be discussed in Sect. VI. However, already from the dynamic behavior of the conductance around the steps we can obtain very strong evidence for this interpretation, and we will first review this experimental evidence.

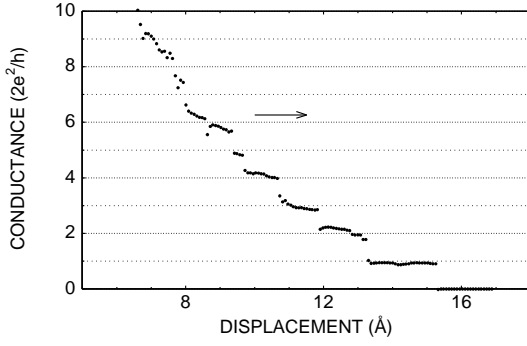


FIG. 25: Conductance curve for a gold contact measured at room temperature in UHV by pressing and STM tip into a clean gold surface and recording the conductance while retracting the tip. The time for recording the curve was approximately 20 ms. Both the current and voltage were measured since both varied during the experiment, but the voltage was smaller than 3 mV until entering the tunneling regime. Reprinted with permission from [76]. Copyright 1995 American Physical Society.

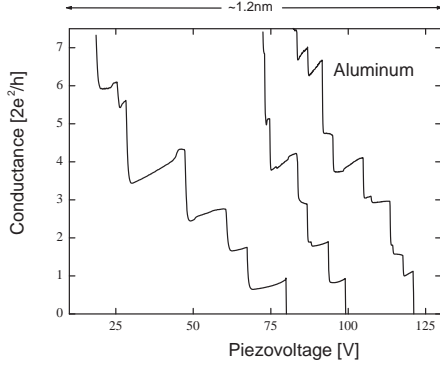


FIG. 26: Three examples of conductance curves for aluminum contacts measured at 4.2 K as a function of the piezovoltage. In most cases the last “plateau” before contact is lost has an anomalous positive slope. An approximate scale for the range of the displacement is indicated at the top of the graph. Reprinted with permission from [30]. Copyright 1993 American Physical Society.

The first observation is that the steps are so steep that the slopes cannot be resolved in the experiment on a time scale of the order of 1 ms, suggesting that they correspond to very fast jumps in the conductance. Further, the conductance traces are different in each measurement. This is to be expected, since we do not control the structural arrangement of the atoms in the contact, and each time the contact is pressed together and slowly separated again, the shape of the contact evolves through a different sequence of structures. However, in the low temperature experiments reproducible cycles can be obtained after ‘training’ the contact by repeatedly sweeping the piezovoltage, V_p , over a limited range [90, 169]. In

such cycles, the steps often show hysteresis in the position at which they occur for the forward and backward sweeps. The hysteresis is sensitive to the bath temperature of the experiment, and could in some cases be removed by raising the temperature by only a few Kelvins [169, 170] (see Fig. 27). For other steps, such hysteresis was not observed, but instead the conductance showed spontaneous fluctuations of a two-level type, between the values before and after the step. This phenomenon is observed only in a very narrow range of V_p around the steps; at the plateaus the conductance assumes stable values. These two-level fluctuations (TLF) are discussed in more detail in Sect. IX C 2, where it is shown that the properties of the system are consistent with two configurations of the contact being nearly equal in energy, and the energy barrier separating the two states can be overcome by thermal activation. When the barrier is too high for thermal activation to be observable, we observe hysteresis of the conductance steps, which can be viewed as being the result of tilting of the potential of the two-level system by the strain applied to the contact. For gold van den Brom *et al.* [169] investigated about one hundred individual steps, all of which showed either hysteresis or TLF, and the steps were always steep, with the slope limited by the experimental resolution.

All these observations are clearly not consistent with a smoothly varying contact radius and steps resulting directly from the quantization of the conductance. A natural interpretation, rather, is formed by a model that

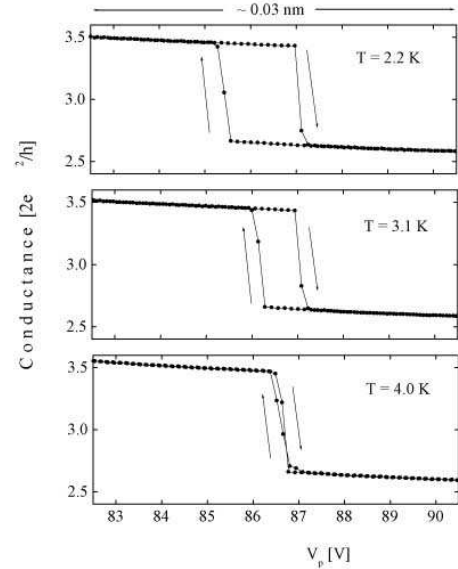


FIG. 27: Measurement of the conductance for an atomic-sized Au contact while sweeping the piezo voltage forward and backward around a single step. Clear hysteresis of the order of 0.1 Å is observed at 2.2 K. At 3.1 K the width of the hysteresis is reduced, and at 4.0 K it is entirely suppressed. From [170].

describes the contact as having a stable atomic geometry over the length of a plateau in the conductance, where the total energy finds itself in a local minimum. At the jumps in the conductance, the local energy minimum for a new geometry drops below that of the present state as a result of the stress applied to the contact. When the energy barrier between the old and the new minimum is large compared to the thermal energy, we will observe hysteresis, and when it is small enough thermally activated fluctuations between the two states will be observed.

The lengths of the plateaus are quite irregular in the low-temperature experiments. For Au at room temperature the elongation of the contact appears to be often more regular and Marszalek *et al.* [94] have shown that the lengths of the plateaus can be classified into three groups of about 0.175, 0.335 and 0.535 nm. They propose that this result can be interpreted in terms of an elongation process of a series of slip events along $\{111\}$ planes. The mechanical deformation properties of atomic contacts will be further discussed in Sect. VI.

The height of the steps is of the order of the conductance quantum, but no systematic correlation between the position of the plateaus and quantized values can be discerned, except for the last two or three conductance plateaus before the jump to the tunneling regime, and only for simple metals. Again, this is consistent with the picture of atomic rearrangements, where the contact changes size by approximately the area of one atom, and as we have seen, one atom contributes $\sim 1 G_0$ to the conductance, even in the semiclassical approximation.

This should be different for semimetals, such as antimony and bismuth, where the density of electrons is more than three orders of magnitude smaller than in ordinary metals. From the electron density in Sb one estimates a Fermi wavelength of 55 Å, which is much larger than the atomic diameter. Experiments on point contacts for this semimetal [86] show indeed that the jump from vacuum tunneling to contact is found at $\sim 1 M\Omega$, or $\sim 0.01 G_0$. Continuing to increase the contact, steps in the conductance were again observed, with a step height that is also of order $0.01 G_0$. This is consistent with the notion of steps resulting from atomic rearrangements and with a semi-classical estimate for the conduction of one atom of Sb. An interpretation of the steps in terms of conductance quantization is definitely ruled out.

We would like to stress again that there is an important difference in experiments performed at room temperature compared to those performed at low temperatures. The detailed study of hysteresis and TLF behavior for individual steps is only possible at low temperatures, where the drift of the contact is sufficiently low. Further, it is important to guarantee a clean metallic contact. At low temperatures this is a simple procedure. Either by employing the MCBJ technique or by repeated indentation of an STM tip into the sample [92] clean contact surfaces can be exposed, which remain clean for very long times due to the cryogenic vacuum conditions. Clean contacts

are seen to form a neck during stretching of the contact. In contrast, when a surface is contaminated and the tip is pushed into it, the surface is indented and contact is only formed upon deep indentation. Even under UHV conditions the latter is frequently observed, as was already noted by Gimzewski *et al.* [12]. A conductance well below $1 G_0$ often observed for atomic-sized metallic contacts in air should in our view be attributed to contamination. Even Au is very reactive for low coordination numbers of the atoms, and the claim of the observation of localization in Au nanowires [73] should be judged in this context.

Many authors have attempted to argue that the conductance values at the plateaus should be strictly quantized. Deviations from perfect quantization are then primarily attributed to back scattering on defects near the contact. An ingenious argument was presented by de Heer *et al.* [171] attempting to show that the conductance for gold contacts can be described as effectively being due to two quantized conductors in series. However, in our view the interpretation hinges on the assumption that the numbers of channels into which an electron scatters are well-defined integer numbers, which is not expected. An analysis of defect scattering near the contact is presented in Sect. IX.

Kassubek *et al.* [172] even consider the possibility that the dynamic behavior of the contact around the steps can be explained by considering the sensitivity to shape distortions of the total energy for a free-electron system confined to a cylindrical wire. The model will be discussed further in Sect. VII B. Although it is very interesting to investigate how far one may go with this ‘minimal model’, it seems more natural to take the constraints to the contact size imposed by the atomic granularity as the fundamental cause for the jumps in the conductance. The fact that the dynamical behavior of the steps, showing hysteresis and TLF, is very similar for monovalent metals, which may be favorable for observing quantum induced force jumps, as well as for *p*- and *d*-metals (where this is excluded as we will see) argues strongly in favor of this point of view.

It is instructive to single out a specific jump in the conductance, namely the one between contact and tunneling. This will help to illustrate the points discussed above, and we will show how we can distinguish the contact regime from the tunneling regime of a junction in the experiments.

B. Jump to contact

At sufficiently large distances between two metal surfaces one observes a tunnel current that decreases exponentially with the distance and that depends on the work-function of the metal according to Eq. (1). As the two metal surfaces are brought closer together at some point a jump to contact occurs, as first observed by Gimzewski and Möller [12]. Once in contact this is followed by a

staircase-like conductance curve due to the atomic structure, as described above. Thus, we will take this characteristic distinction of smooth exponential distance dependence versus staircase-like structure as the signatures for tunneling and contact regimes, respectively. In some cases we will see that the distinction is not as clear-cut. For clean metals the first contact is always of the order of 10 k Ω . Only clean contacts form this adhesive jump after which a connective neck is pulled when separating the electrodes. After only 6 hours in UHV the tip was seen to be sufficiently contaminated that indenting it in a silver surface caused a dip in the surface rather than pulling a neck, due to a repulsive interaction caused by adsorbates [12].

There are several mechanisms that may lead to deviations from strict exponential tunneling. We do not want to digress too far into the field of vacuum tunneling, and limit the discussion to the two main influences. The first is the image potential that a tunneling electron experiences from the two metallic surfaces, which modifies the barrier. However, the apparent barrier, given by the slope in a logarithmic plot of tunnel resistance versus distance, is only affected at very small distances [173, 174, 175]. Second, since tunneling of electrons is a result of a weak overlap of the electronic wave function of the two metals in the vacuum space between them, the overlap also results in a bonding force. For metals the attractive interaction pulls the surface atoms closer to the other electrode, effectively reducing the tunneling distance. This attractive force in the tunneling regime was directly measured by Dürig *et al.* [13] using a combination of an STM and a sample mounted on a cantilever beam, Fig. 28. The shift in the resonance frequency of the cantilever beam served as a measure for the force gradient. A semilogarithmic plot of the tunnel resistance as a function of the distance was found to be linear over the entire range of about 4 decades in resistance. This was confirmed by Olesen *et al.* [176], who argue that the effect of the attractive force is almost exactly canceled by the decrease of the tunnel barrier due to image potential corrections. Deviations from exponential tunneling at close distance to contact observed in low temperature MCBJ experiments [30, 177] were attributed to the attractive force and the observation of this effect is probably allowed by the higher stability of the instrument. Understanding this force is important for quantitative analysis of the surface corrugation measured in STM [18, 178, 179, 180, 181].

From continuum models and atomistic simulations Pethica and Sutton [182] predicted that the attractive force between two clean metal surfaces should lead to an intrinsic instability at a distance of 1–3 Å. This ‘avalanche in adhesion’ [183] is expected to cause the surfaces to snap together on a time scale of the order of the time it takes a sound wave to travel an inter-planar spacing (~ 100 fs, see Sect. VII A 4). Originally it was believed that one should be able to bring surfaces together in a continuous fashion because atoms are more

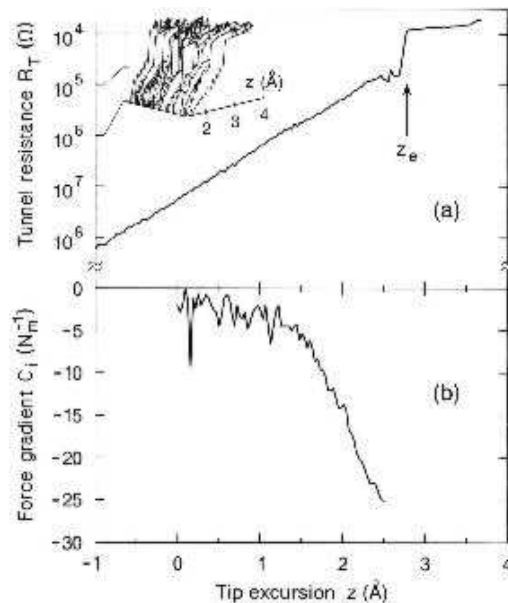


FIG. 28: (a) Tunnel resistance vs. tip excursion z measured on an Ir surface using an Ir tip at room temperature in UHV, averaged over 64 cycles. Positive z corresponds to decreasing the tunneling-gap width. The transition to contact is indicated by the arrow at z_e . Inset: Degree of reproducibility at the transition. (b) Interaction force gradient vs. tip excursion measured simultaneously with the tunnel resistance. Reprinted with permission from [13]. Copyright 1990 American Physical Society.

strongly bound to their neighboring atoms than to the opposite layer. However, the elastic response of many atomic layers produces an effective spring constant by which the surface atoms are held. When the gradient of the force pulling the surface atoms across the vacuum gap is greater than this spring constant the surfaces snap together. When this elastic medium is absent, as for a single atom held between two rigid surfaces, a perfectly smooth transition takes place, as can be shown by simple model calculations [184].

It is this jump-to-contact that was observed in STM and MCBJ experiments [12, 28, 30] (Figs. 28, 29). The jump is associated with hysteresis, as expected, where the forward and reverse jumps are separated by distances of the order of 1 Å, but can be as small as 0.2 Å. The tunneling-resistance from which the jump-to-contact occurs is typically between 30 and 150 k Ω . The well-defined switching of the resistance between values differing by an order of magnitude has been proposed for applications as a quantum-switch device [185]. For some systems the jump-to-contact was found to be absent [186, 187], although these appear to be exceptions to the general rule. A possible explanation may be that in these cases the force gradient never exceeds the effective spring constant of the elasticity of the metal, but more work is needed to investigate this.

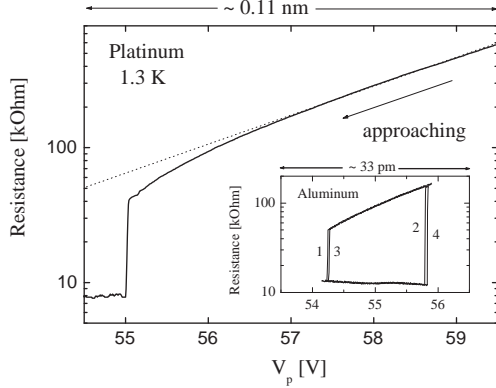


FIG. 29: Semi-logarithmic plot of an ac-resistance measurement of a Pt MCBJ sample at 1.3 K as a function of piezovoltage, V_p . The curve is recorded starting at the high-resistance tunneling side (right). The dotted line is an extrapolation from larger V_p . Between ~ 500 k Ω and ~ 40 k Ω a downward deviation from exponential behavior is observed, followed by a jump to a stable value. The inset shows two successive cycles of an Al break junction at 4.2 K, illustrating the hysteresis of the jumps. The numbers indicate the sequential order of the jumps, first up (1), then down (2) and up and down again (3 and 4). Reprinted with permission from [30]. Copyright 1993 American Physical Society.

At higher temperatures a jump-to-contact of quite different nature has been observed by Kuipers and Frenken [188]. When studying lead surfaces between room temperature and the surface melting temperature it was found that the tip jumps into contact with the surface already from a distance of at least 10 Å. In order to break this contact it was necessary to rapidly retract the tip. From the relation between retraction speed and the distance at which the contacts were broken the authors were able to demonstrate that a neck spontaneously grows by surface diffusion of Pb atoms. This is the result of the tendency of surface atoms to diffuse towards points of highest concave curvature. Later, Gai *et al.* [189] showed that there is a competition between the concave curvature *along* the neck and the convex curvature around it. This leads to a spontaneous growth of the cross section for short necks, but long thin necks tend to diffuse out of contact. This forms a likely explanation for the observation of spontaneous contact breaking for clean gold contacts at room temperature [190]. This also implies that the protrusion that is left behind on the surface after breaking of the neck diffuses away at room temperature, which significantly increases the hysteresis cycle for returning to contact. In a molecular dynamics simulation for contact formation at room temperature Sørensen *et al.* [191] show that a sequence of atom hops is involved in the contacting process, which they refer to as ‘diffusion-to-contact’. The same mechanism has been invoked to

describe the formation of a neck of silicon atoms between a tip and a clean Si(111) surface [192].

C. Single-atom contacts

After indenting the STM tip into the sample surface, or pressing the electrodes together in an MCBJ experiment, and subsequently pulling the contact apart again, the above described staircase structure in the conductance is observed. The conductance at the last plateau prior to the jump back into the tunneling regime is usually fairly reproducible and is believed to be associated with a contact of a single atom. In Sects. VI, VII, and VIII we will encounter many arguments that support this interpretation, based on measurements of the force, on model calculations, and on the experimentally determined number of conductance channels, respectively. However, already at this point we can see that this is a reasonable point of view. In particular for gold, Fig. 28, the last contact conductance is very reproducible, and close to $1 G_0$, suggesting a single atom contact provides a single conductance channel. If a single atom were not enough to open a conductance channel we would expect to find many contacts with smaller last conductance values. Moreover, the hysteresis between contact and tunneling for many metals is of the order of one tenth of the size of an atom. If several atoms were involved in the contact configuration one would expect to see much larger hysteresis since there is more room for reconfiguration.

There have been very few direct experimental tests of single-atom contacts. A very controlled experiment has been performed by Yazdani *et al.* [56] using a stable low temperature STM. A clean nickel surface was prepared in UHV and a low concentration of xenon adatoms was deposited on the surface. Making contact to a Xe atom with a bare W tip and with a Xe-atom terminated tip allowed measuring the resistance of a Xe atom contact and a two-Xe-atom chain. The results were compared to model calculations for this system and the agreement was very satisfactory. Unfortunately, Xe is not a metal, which is reflected in the high resistance for the ‘contact’ of about 80 k Ω and 10 M Ω for the single and two-atom chain, respectively. Also, no jump-to-contact is observed, consistent with the weak adsorption potential for Xe.

Rather direct evidence comes from the observation of the atomic structure of a gold contact in a room temperature UHV high-resolution transmission electron microscope [54]. For contacts that have a single atom in cross section the conductance is found to be close to 12.9 k Ω , or half this value. Ohnishi *et al.* argue from the intensity profile that the higher conductance in the later case is associated with a double row of atoms along the line of view. For the lower-intensity profiles the conductance agrees with a value of $1 G_0$.

Single-atom contacts can be held stable for very long times at low temperatures. At room temperature, on the other hand, clean gold contacts drift away from their

starting value on a time scale of milliseconds due to drift and thermal diffusion of the atoms making up the contact, as discussed above. Although several authors report a “surprising stability” over time scales of order of an hour of atomic-sized gold contacts [73, 74, 193, 194, 195], Hansen *et al.* [196] have demonstrated that this enhanced stability is very likely associated with adsorbates or other contaminants. Since the presence of contaminants is seen to be associated with non-linear IV characteristics we will return to this point in Sect. V E. An influence of adsorbates as capillary forces mainly by moisture stabilizing the contacts was also suggested by Abellán *et al.* [194].

Although the various results are not very explicit or sometimes contradicting, it appears that any conductance value can be held stable for gold contacts in air, not just those with a conductance near a multiple of G_0 [194]. However, the experiments in high vacuum at room temperature seem to suggest that multiples of G_0 are preferentially formed when the contact is allowed to choose its own size by diffusion of atoms [190]. At low temperatures diffusion is too slow, and in air adsorbates inhibit the surface diffusion of atoms. Additional evidence is given by Li *et al.* [102] who use an electrochemical fabrication technique with feed-back (see Sect. II E) to stabilize the conductance. They find that non-integer multiples of G_0 cannot be held stable for very long times in contrast to integer multiples. Similar observations were made by Junno *et al.* using AFM manipulation of nanoparticles [104]. These observation may be related to a stabilization of the contact by the filling of the quantum modes, as will be discussed in Sect. VII B. It may also be related to the observation by Ohnishi *et al.* [54] of the formation of multiple parallel strands of single-atom gold wires in their HRTEM images. This aspect certainly deserves further study.

D. Conductance histograms

From the discussion in the previous paragraphs it is clear that contacts fabricated by these methods show a wide variety of behavior, where the atomic structure of the contact plays a very important role. The methods used, with the exception of very few experiments [54, 56], do not permit detailed knowledge over the atomic-scale built-up of the contact. Nevertheless, one would like to investigate possible quantization effects in the conductance and some experiments that we have discussed seem to suggest that these exist. However, it is very difficult to objectively separate the stepwise conductance behavior as a function of contact size resulting from the atomic structure and the stepwise pattern due to quantization of the conductance.

In order to perform an objective analysis of the data it has become customary to construct conductance histograms from large sets of individual conductance versus displacement curves. The method exploits the large variability in the data resulting from the many possi-

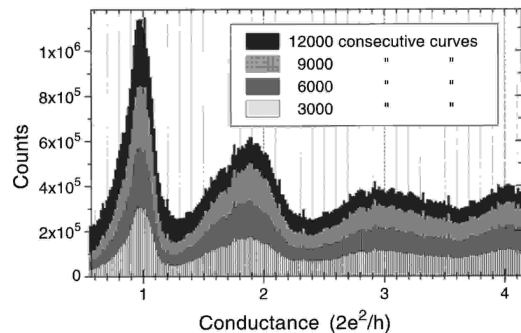


FIG. 30: Conductance histogram for gold contacts recorded in air at room temperature, using a dc voltage bias of 90.4 mV. The numbers of curves used for the construction of the histogram is given in the inset, showing the gradual evolution of the peaks in the histogram. The data have been corrected for an effective series resistance of 490 Ω . Reprinted with permission from [197]. Copyright 1997 American Physical Society.

ble atomic-scale contact configurations, and assumes that all possible configurations, or effective contact sizes, are equally likely to be formed. Under this assumption, one expects to find peaks in the histogram corresponding to conductance values that are preferred by the *electronic* system. A smooth, adiabatic shape of the contact for a free-electron gas would then lead to peaks at integer multiples of the quantum unit G_0 . We shall see that the assumption underlying this method is generally not fulfilled, but with some caution one may still extract evidence for quantization effects in the conductance from the data.

An example of a conductance histogram for gold recorded at room temperature in air is given in Fig. 30. The conductance axis is usually divided into a number of bins, and the conductance values falling within the range of each bin are collected from a large number of individual scans of contact breaking. The resolution is obviously limited by the width of the bins but also by the digital resolution of the analog-to-digital converter (ADC), and the mismatch of these two may produce artificial periodic structures or ‘noise’ in the histograms. Modern 16-bit ADC’s have ample resolution by which such artifacts can be avoided. Alternatively, one may employ the method of constructing a distribution curve introduced by Brandbyge *et al.* [76]. Here, all the conductance values are collected in a single file and sorted in increasing order of the conductance. The height of the distribution H at a conductance measurement point G_i is then calculated as $H(G_i) = (2w/N)/(G_{i+w} - G_{i-w})$, where w is a conveniently chosen interval, determining the width of the smearing of the distribution. The factor $1/N$ normalizes the area under the distribution to 1.

In order to improve statistics one would like to average over as many curves as required to resolve the smaller peaks. Since it turns out that several thousands of curves are usually needed, the contact breaking is done in a short

time, of order of a second or shorter. Also, when studying the breaking of macroscopic contacts, as in relays, the final breaking process of the last few atoms takes place on a time scale of the order of $10\ \mu\text{s}$. For the recording of these fast processes one employs fast digital oscilloscopes equipped with flash-ADC's. The latter have usually a limited resolution (8 or 10 bits) and a significant differential non-linearity, as was pointed out by Hansen *et al.* [107], meaning that the effective width of the digitization intervals has a large spread. This results in artificial 'noise' in the histograms, which can be avoided [107] by dividing the measured data by a normalizing data set recorded for a linear ramp using the same digital recorder settings.

Below, we will present an overview of histograms recorded for various metals. Before we start we would like to point out that the results have been obtained under widely different circumstances, some of which are known to influence the results, and some influences have not yet been systematically investigated. Clearly the environment should be considered, whether working in air or in UHV. The purity of the sample material should be specified, but when working in UHV the surface preparation technique is even more important. In STM techniques one often employs a tip of a hard metal, such as tungsten or platinum/iridium, and indents this tip into a soft metal surface such as gold. There is good evidence that the soft metal wets the tip surface, so that after a few indentations, one has a homogeneous contact of the sample metal only. However, this depends on the wetting properties of the combination of the tip and surface material, and one should be aware of possible contaminations of the contacts by the tip material. Further, the temperature has an effect on the results, but also the measurement current, which may locally heat the contact, or modify the electronic structure due to the finite electric field present in the contact. The shape of the connective neck that is formed during elongation of the contact may be influenced by these factors, but also by the depth of indentation of the two electrodes and the speed of retraction. The sample material may be in the form of a polycrystalline wire, a single crystal or a thin film deposited on a substrate and this has an effect on the mechanical response of the metal but also on the electron mean free path. Even with all these factors taken into account, and for one and the same sample, some details of the histograms do not always reproduce. We speculate that the local crystalline orientation of the electrodes forming the contact may play a role, which has not yet been thoroughly investigated. Nevertheless, it turns out that there are many features that are very robust, and reproduce under most circumstances, as we will see below.

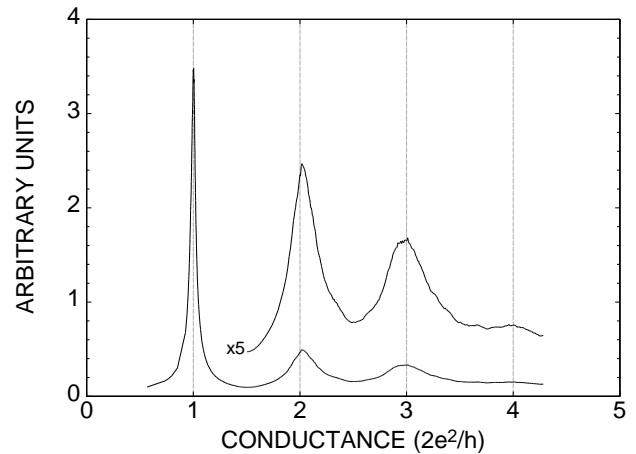


FIG. 31: Histogram for gold contacts measured at room temperature in UHV by pressing an STM tip into a clean gold surface and recording the conductance while retracting the tip. The data have been corrected for an effective series resistance of $150\ \Omega$. Reprinted with permission from [76]. Copyright 1995 American Physical Society.

1. The archetypal metal: gold

Gold contacts are the most widely investigated by the histogram method [34, 71, 95, 107, 108, 109, 170, 171, 197, 198, 199, 200, 201, 202, 203, 204]. The first results were presented by Brandbyge *et al.* [76], Fig. 31, using a room-temperature STM under UHV. Many features of the histograms recorded under widely different circumstances seem to reproduce (cf. Fig. 30). This is presumably due to the low reactivity of the gold surface and the fact that it is easily cleaned. One generally observes peaks near 1 , 2 and $3\ G_0$, which are shifted to somewhat lower values compared to exact multiples of G_0 . This shift has been attributed to backscattering of the electrons on defects near the contact, as will be discussed in Sect. IX. Sometimes a broad feature at 4 – $5\ G_0$ can be resolved, and there is one report of individual peaks near 4 and $5\ G_0$ [199]. The shape of the peaks and their relative amplitudes are not reproducible in detail, but the first peak is always very pronounced, and much higher than the others. The other peaks tend to decrease in height with increasing conductance. The first peak is very robust against the applied bias voltage [109, 205] and survives up to about $2\ \text{V}$, corresponding to formidable current densities of the order of $2 \cdot 10^{15}\ \text{A/m}^2$. Even the other structure in the histogram is unchanged up to $500\ \text{mV}$. Also the atmosphere does not have a dramatic influence, and only by intentionally increasing the concentration of reactive molecules in the atmosphere some changes are observed. Li *et al.* [101] report that the peaks at higher conductance values are gradually suppressed in going from air to vapors of ethanol, pyridine and 4-hydroxyl thiophenol, in increasing order of adsorption strength. However, the peak near $1\ G_0$ survives under all circumstances.

Between helium- and room-temperatures no qualitative changes in the histograms are observed [71], but the relative height of the first peak grows toward lower temperatures. Although no influence of the retraction speed was observed in the range from 30 to 4000 nm/s [197], the experiment by Muller *et al.* [190] seems to suggest that in the extremely slow limit, where surface diffusion of gold atoms at room temperature is expected, the shape of the histogram changes considerably. In the latter experiment the peaks at higher conductance are more pronounced.

Two reports give evidence for peaks near half-integer multiples of G_0 , notably near 0.5 and 1.5 G_0 . Both use a thermally evaporated gold film on a mica substrate. One was measured with an STM at room temperature under UHV [95]. The other [204] is special, in that the histogram was recorded with an STM tip immersed in an electrochemical cell, containing a 0.1 M NaClO₄ or HClO₄. In this case the histogram had the regular appearance, but below a threshold voltage in the electrochemical potential in the cell the half-integer peaks appeared. The authors discuss various possible explanations, but discard all except the one proposed by de Heer *et al.* [171]. However, as argued above, we believe also this explanation is not viable, and the problem remains to be solved.

When we assume that the contact breaking process produces any effective contact diameter with equal probability, then the histograms represent a derivative of the conductance with respect to the effective diameter of the contact. It is instructive to calculate the integral of the histogram, as was first done by Gai *et al.* [34]. Fig. 32 shows such a curve, obtained from a gold histogram similar to the one shown in Fig. 31. This curve is to be compared to conductance traces obtained for 2DEG semiconductor devices [14, 15], for which the width of the contact can directly and continuously be adjusted by the gate electrostatic potential. Compared to the latter, the conductance steps in Fig. 32 are poorly defined, with the exception of the first conductance quantum. Moreover, the first quantum feature results from the fact that our assumption mentioned above is not valid. The effective diameters produced during contact breaking are strongly influenced by the possible atomic configurations. As we will argue Sect. XI, the step at 1 G_0 , corresponding to the strong peak in the histogram for gold, results from the formation of a chain of gold atoms during the last stages of contact breaking. Disregarding the first level in Fig. 32, we find that the conductance is not strictly quantized, as the probability of finding a contact with a conductance of, e.g., 2 G_0 is only twice that of finding 1.5 G_0 . However, the conductance is still determined by the quantum states, as described in Sect. III and is carried by a limited number of modes. We will show in Sects. VIII and IX how the quantum nature for monovalent metals is revealed by a tendency for the modes to open one-by-one as the contact becomes larger.

The well-defined and robust features in the histograms for gold are rather unique, and for other materials it is

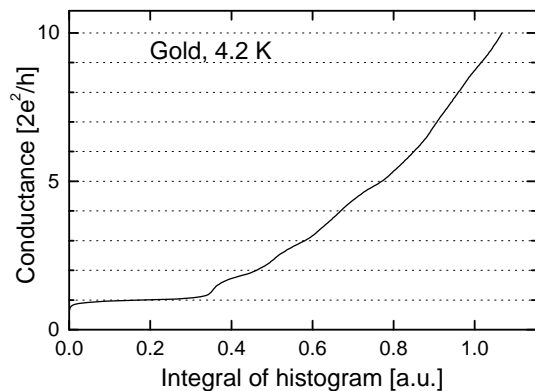


FIG. 32: Curve obtained by integrating a gold histogram similar to Fig. 31. From [206].

usually necessary to work under clean UHV or cryogenic conditions to obtain reproducible results.

2. Free electron metals: Li, Na and K

For sodium in a low temperature experiment using the MCBJ technique, a histogram with peaks near 1, 3, 5 and 6 G_0 was observed [33]. Similar results have been obtained for potassium (Fig. 33), lithium [52, 206, 207], and cesium [208]. Notice the sharpness of peaks, the absence of peaks at 2 and 4 G_0 (disregarding the little shoulder below 3 G_0) and the low count in between the peaks. For lithium, the histogram looks qualitatively similar, but the first two peaks are much smaller and the shift below integer multiples of G_0 , attributed to an effective series resistance due to scattering on defects (Sect. IX), is bigger [206].

The characteristic series 1-3-5-6, and the fact that peaks near 2 and 4 G_0 are nearly absent points at an interpretation in terms of a smooth, near-perfect cylindrical symmetry of the sodium contacts. Sodium indeed forms a very good approximation to a free electron system, and the weakly bound *s*-electrons strongly reduce surface corrugation. As will be discussed in Sect. VII B 1, for a model smooth, cylindrically symmetric contact with continuously adjustable contact diameter [209, 210], the conductance increases from zero to 1 G_0 as soon as the diameter is large enough so that the first conductance mode becomes occupied. When increasing the diameter further, the conductance increases by two units because the second and third modes are degenerate. The modes are described by Bessel functions (assuming a hard wall boundary potential) and the first mode is given by the $m = 0$ Bessel function, which is not degenerate. The second and third modes are the degenerate $m = \pm 1$ modes, followed by $m = \pm 2$ for further increasing contact diameter. The next mode that will be occupied corresponds to the second zero of the $m = 0$ Bessel function, and is again *not* degenerate. Thus the conductance for such a contact should increase by 1, 2, 2 and 1 units, produc-

ing just the series of conductance values observed in the sodium experiment.

Note that the conductance steps observed in the individual conductance traces are still due to atomic reconstructions. Indeed, the sharpness of the steps is limited by the experimental resolution, and they are associated with hysteresis and two-level fluctuations as for any other metal. This picture can be reconciled with the notion of conductance quantization in a free-electron gas by considering the model calculation by Nakamura *et al.* [211], Fig. 34. Without going into the details of the calculations, which will be addressed in Sect. VII, we find from the model that a single-atom contact corresponds to a single mode, which is nearly perfectly transmitted. At a unit-cell length of 22 Å three modes are transmitted adding-up to a total conductance close to $3G_0$, and the narrowest cross section is made up of three atoms. The potential that the electrons experience in this contact is nearly cylindrical due to the fact that the electrons in Na are so weakly bound. The calculation does not reproduce the abrupt transition from 3 to $1G_0$, probably due to the limited size of the model system. The small shoulder at the lower end of the peak at $3G_0$ in Fig. 33 could then be due to the occasional formation of a contact with two atoms in cross section, which is too small for the three channels to be fully transmitted.

This picture of a strict separation of the effect of the atomic structure in determining the geometry and the conduction modes setting the conductance as dictated by this geometry, may need to be refined by taking into account that the occupation of the quantum modes may energetically favor specific atomic configurations, as will be discussed in Sects. VII B and XII.

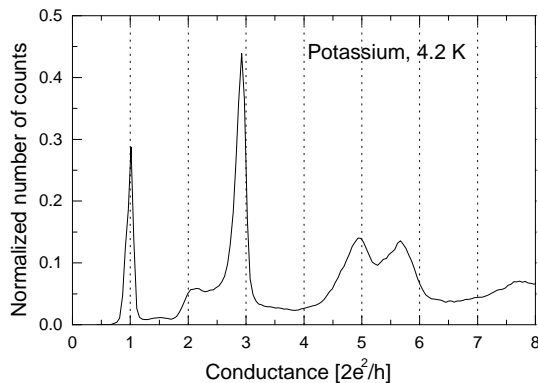


FIG. 33: Histogram of conductance values, constructed from $G(V_p)$ -curves measured for potassium at 4.2 K with an MCBJ device, involving several thousand individual measurements. The measurements were done with a constant bias voltage of 10 mV. The characteristic sequence of peaks ($G = 1, 3, 5, 6$) is regarded as a signature for conductance quantization. From [206].

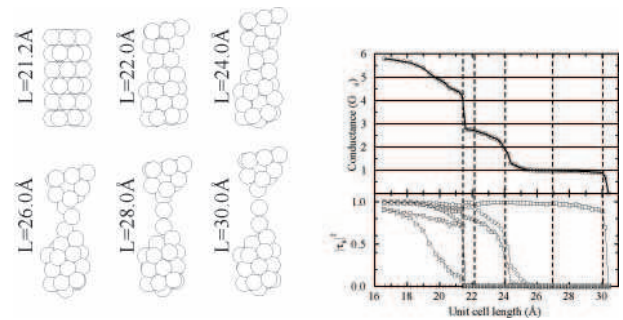


FIG. 34: Conductance for the configurations of sodium atoms illustrated at the left for several elongation stages of the unit cell. The authors used a self-consistent local-density approximation potential. The lower panel on the right shows the evolution of the individual transmission probabilities for each conductance channel in the system. Reprinted with permission from [211]. Copyright 1999 American Physical Society.

3. The noble metals

Similar as for gold, conductance histograms for copper and silver have a dominant peak at or just below $1G_0$ [30, 33, 101, 107, 190, 204, 207, 212, 213]. Above this peak one generally finds two additional peaks. At room temperature in air these peaks are broad and form more or less a single broad peak having two maxima [107, 212]. Attempts to interpret these observations in terms of conductance quantization peaks shifted by a series resistance are not quite satisfactory since the series resistance required is rather large, of the order of 500Ω , and the correction does not shift all peaks simultaneously to the desired positions. At low temperatures the second and third peaks are more clearly separated [33, 207]. In contrast to gold where the height of the peaks decreases systematically for increasing conductance, for copper the third peak is often much more pronounced than the second one. For silver the difference is less extreme, but a reverse peak intensity has also been observed. Furthermore, the third peak is much closer to $3G_0$ compared to the distance of the second peak below $2G_0$. This suggests that Cu has an appearance intermediate between that found for Au and for Na and K. The second peak would then be mainly due to the atomic structure of a two-atom contact, while the third peak represents all configurations that admit three near-fully transmitted modes. Some indirect evidence for this interpretation was given in [202, 207]. As was observed for gold, using slow scans at room temperature more peaks can be seen and the peaks tend to be closer to integer multiples of G_0 [101, 190, 204], which we propose to attribute to the effect of surface diffusion of atoms.

Three studies fall outside this picture. Rodrigues *et al.* [214] have used a MCBJ under UHV at room temperature and found a conductance histogram for Ag that, apart from the peak just below $1G_0$, has a rather strong peak at $2.4G_0$ and a broader feature just above $4G_0$.

They attribute the peak at $2.4 G_0$ to a stable nanowire geometry along the $[110]$ crystallographic direction, which they have identified in HR-TEM images. Although this is plausible, the difference with the commonly observed histograms remains to be explained. Ono *et al.* [213] use a home-built relay-type set up which switches the contact formed between the apex of a thin Cu wire and a thin Cu film evaporated onto a glass substrate, under ambient conditions. The histogram shows only two peaks, but sharp and centered at 1 and $2 G_0$. It is not clear what distinguishes the technique used here from the other studies, but it should be noted that the histograms are built from a very limited number of curves (~ 20) and that the curves were selected to “have at least one plateau”. It is also remarkable, as we shall discuss below, that they find several sharp peaks for Ni. It is likely that these peaks are the result of stable contact cycles, which result after training of the contact as discussed in Sect. V A, and therefore reflect recurring contact configurations. Finally, Li *et al.* [215] use an STM to study the influence of adsorbate molecules on Cu atomic-sized contacts and find that after the addition of an organic molecule, 2,2'-bipyridine, the conductance histogram shows additional peaks near the half-integers 0.5 and $1.5 G_0$. These results resemble those for Au obtained by the same group [204], suggesting that also the latter may be attributed to the effect of adsorbates. A full explanation for the effect is still lacking, but Li *et al.* have proposed to exploit this sensitivity of the atomic conductance to the presence of certain molecules as a chemical sensor.

4. Transition metals

For the non-magnetic transition metals (we will discuss the ferromagnetic ones below) the histograms show generally very few features. In MCBJ experiments at low temperatures the transition metals with partially filled d -shells, as far as they have been studied, show a single broad peak centered well above $1 G_0$. This peak can generally not be identified with an integer value of the conductance; for example niobium shows a wide peak centered near 2.3 – $2.5 G_0$ (Fig. 35). The peak at zero conductance arises from the fact that there was no low-conductance cut-off applied in the data and the conductance measured in the tunneling regime causes an accumulation of points at low conductance. The jump between contact and tunneling is relatively small for Nb, and the tunnel current can rise even somewhat above $1 G_0$ just before the jump to contact, leading to a nearly continuous cross-over from the data points obtained in tunneling and those obtained in contact. Results for vanadium are comparable to those for Nb [206].

Similarly, for Rh, Pd, Ir and Pt at low temperatures histograms with a single peak, centered in the range from 1.5 to $2.5 G_0$ have been obtained [30, 72, 206, 216], with some weaker features at higher conductances. At room temperature, both in UHV [32] and in air [197] the first

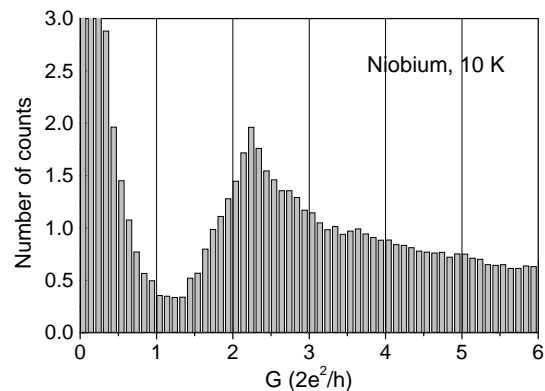


FIG. 35: Histogram constructed from 2400 individual conductance curves for a niobium sample. Each curve was recorded while stretching the contact to break, using the MCBJ technique at a temperature of 10 K, which is just above the superconducting transition temperature. The conductance was measured using a DC voltage bias of 20 mV. Reprinted with permission from [220]. Copyright 2000 American Physical Society.

peak for Pt is surprisingly found near $1 G_0$. Recent work suggests that this peak near $1 G_0$ may arise from contamination of the metal surface with hydrogen [217]. On the other hand, histograms for Ru, Rh, and Pt obtained by a very fast relay technique under ambient conditions but at high voltage-bias show features that are somewhat similar to the low-temperature data [218, 219].

Contamination of the contacts is most likely responsible for the fact that most experiments on transition metals at room temperature do not show any reproducible structure. When concentrating therefore on the data obtained under cryogenic vacuum, these seem to point at a general interpretation of the first peak in terms of the characteristic conductance of a single-atom contact. This is in excellent agreement with the expected conductance, see Sects. VII C and VIII, where it is argued that a single-atom contact for a transition metal with a partially filled d -band has five conductance channels available, which are only partially open.

For Zn, having a completed d -band, there is a first dominant peak well below 1, at about $0.7 G_0$, which resembles the results for aluminum, and a second smaller peak near $2 G_0$ [206, 221].

5. Ferromagnetic metals

The ferromagnetic metals have attracted special interest as a result of speculations that the strong exchange splitting of the electron bands may lift the spin-degeneracy of the conductance modes, which would give rise to half-integer (e^2/h instead of $2e^2/h$) conductance steps as obtained for simple free-electron models. However, as mentioned above, the number of channels for a single atom is expected to be five, and all modes are only partially open so that the total conductance is in

the range of $1.5\text{--}3G_0$. This is consistent with what is observed at low temperatures in MCBJ experiments on Fe [207], where the conductance histogram shows a single peak at $2.2G_0$ very similar to that observed for Nb in Fig. 35. Low-temperature STM experiments similarly show that the last contact value for Ni is typically $1.6G_0$ [72]. At room temperature in air the histograms for Fe, Co and Ni are entirely featureless [107, 197], at least in some of the early experiments. This is attributed to a contamination of the contacts by adsorbates from the atmosphere, which washes out all regular metallic conductance features.

More recently there have been a few reports of sharp features for the ferromagnets [213, 222, 223, 224]. Ott *et al.* [222] obtain three sharp peaks near 1, 2 and $3G_0$ for Fe, using a relay-type technique under ambient conditions, while for Ni they find the more familiar featureless histogram. The authors suggest that the state of magnetization may be of importance, since they report having saturated the magnetization state of their wires. Note that the histogram was constructed from a rather limited set of 80 conductance traces. The data have some resemblance with those of Ref. [224] recorded at 4.2 K. In this work the number of accumulated scans is also limited, but in addition the contact was first ‘trained’ and only very shallow indentation cycles to a depth of about $4G_0$ were used. This implies that the histogram is not obtained by averaging over many contact configurations, but rather represents a reproducible contact-configuration cycle. The histogram can then not be interpreted in terms of intrinsic conductance properties.

Ono *et al.* [213] showed data for Ni comparable to those for Fe by Ott *et al.* The technique is not very different from the method by Ott *et al.*, except that they contact the Ni wire to a thin Ni film evaporated onto a glass substrate, as also used for Cu, see above. However, in addition they report that the ‘integer’ peaks near 1 and $2G_0$ that are observed without magnetic field are joined by additional peaks near 0.5 and $1.5G_0$ for fields above 5 mT. The number of curves in each histogram is only 20, and the curves have been selected to have at least one plateau. The latter suggests that many individual curves are featureless.

Oshima and Miyano [223] constructed a relay between a Ni wire and a Ni coil that could be heated by a current well above room temperature. The set-up was placed in a vacuum chamber with a pressure in the range $0.5\text{--}1 \cdot 10^{-4}$ Pa and a magnetic field up to 0.12 T. At room temperature a peak at $1G_0$ is observed, which survives up to 610 K (Fig. 36). However, above the Curie temperature for Ni ($T_C = 631$ K) the histogram changes into a broad peak centered around $2.7G_0$. Also the application of a magnetic field removes the sharp feature at $1G_0$. The results are remarkable, but the explanation offered is qualitative and not entirely convincing. Note the similarity of the high-T and high-field data to the low-temperature results for the *d*-metals. The authors mention that the application of the magnetic field changes

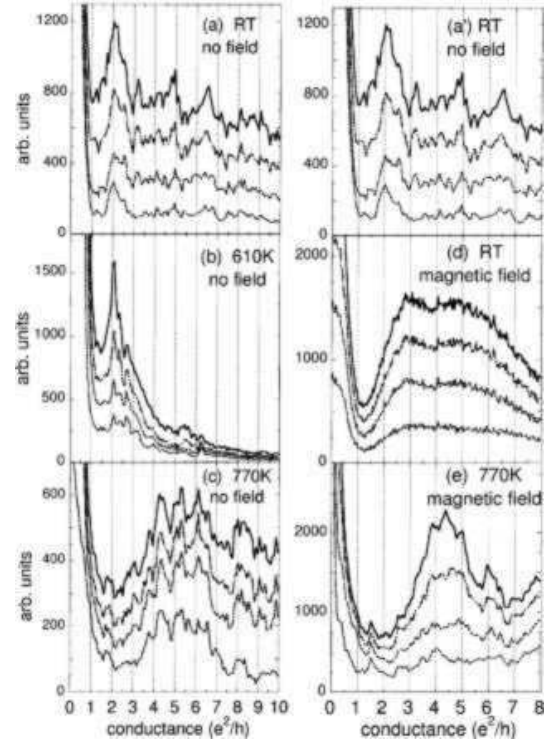


FIG. 36: Conductance histogram constructed from conductance curves for Ni. The left column of panels shows the evolution of the histograms with temperature: (a) room temperature, (b) 610 K, (c) 770 K. The right column shows the effect of applied magnetic field: (a') same as (a), (d) in a field of 0.12 T at room temperature and (e) the same field at 770 K. The histograms are presented in a cumulative fashion for 40, 140, 240 and 340 traces in (a),(a') and for 100, 200, 300 and 400 traces in (b)–(e). Reprinted with permission from [223]. Copyright 1998 American Institute of Physics.

the mechanics of the contact breaking, because the repulsive magnetic force between the like-oriented electrodes results in a contact breaking on microsecond time scales.

Finally, García *et al.* [225] have produced stable atomic-sized Ni contacts at room temperature by embedding the contact between two Ni wires in a resin. The magnetization state of the two wires was switched by field coils wound around the wires. The contact resistance was seen to switch between ~ 3 and ~ 10 k Ω upon reversing the applied field of 2 mT. Reference experiments on Cu-Cu and Cu-Ni contacts of similar conductance did not show any significant response to the magnetic field. An explanation of these results has been proposed in terms of scattering on the domain wall trapped inside the constriction [226].

Clearly, the results on the ferromagnets are not all consistent, but some evidence exists that the magnetization state modifies the conductance and the histogram. However, it is not yet clear what are the conditions to go from featureless histograms to histograms showing peaks near integer and even half-integer values of G_0 . More work is

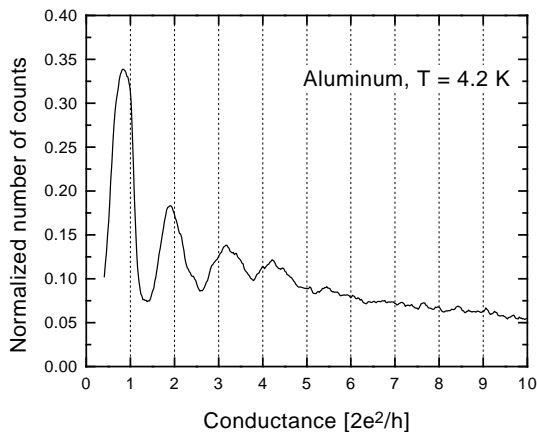


FIG. 37: Histogram constructed from 30 000 individual conductance curves for two different samples of aluminum, using the MCBJ technique at 4.2 K at a sample bias voltage of 10 mV. Reprinted with permission from [227]. Copyright 1997 American Physical Society.

needed to clarify the experimental situation.

6. Aluminum and other *sp*-metals

Figure 37 shows a histogram for aluminum obtained at 4.2 K [207, 227]. In [227] these data were taken as evidence that structure in the histogram cannot exclusively be interpreted as arising from quantum structure in the conductance modes. Indeed, the strong first peak lies even somewhat below 1, at about $0.8 G_0$, while a single-atom contact for the *sp*-metals is believed to be associated with three partially transmitting conductance channels (see Sect. VIII). Also, a series resistance interpretation of the shift of the peaks is inconsistent with the fact that the first two peaks lie somewhat below integer values, while the next two weaker features lie above 3 and $4 G_0$, respectively. As will be discussed below, the total conductance for the three channels in a one-atom contact are expected to add up to about $1 G_0$, which suggests that the peak is due to an *atomic configuration* of a single atom in the contact. It further suggests that also the higher conductance peaks are due to preferred atomic configurations.

This interpretation is strongly supported by calculations by Hasmy *et al.* [228]. They obtained a histogram of the effective contact cross sections deduced from a large series of molecular dynamics simulations for the stretching of Al nanowires. At low temperatures (4 K) clear peaks are found at the positions corresponding to 1, 2, 3 and 4 atoms in cross section. Although the conductance could not be obtained from the same calculation, it demonstrates that these specific contact areas contribute with more than average weight in the histograms. Taking a typical conductance of $0.92 G_0$ per atom one obtains

a fair agreement with the experimental conductance histogram, without taking any quantum effects of the electron gas into account. Further, the authors observe that the peaks in the cross section histogram are not equally well pronounced for different crystalline orientations of the wire, which may explain the small variations in appearance of the conductance histograms.

Histograms for Pb and Sn measured at low temperatures have a single dominant peak at about $1.7 G_0$ that is more than $1.5 G_0$ wide, with some weaker features at higher conductances [206]. The width of the peak is consistent with the gradual variation of the conductance over the last plateau, stretching often from $\sim 3 G_0$ to $1 G_0$ (see Refs. [90, 229] and Sect. VIII C). The interpretation fits with the conductance expected for a single-atom contact geometry.

Lewis *et al.* [230] reported conductance histograms measured on 5N-purity Ga samples, using a variable-temperature STM. The histograms, constructed from 500–1000 curves, while featureless at room temperature, gradually develop a peak at (or slightly above) $1 G_0$ plus a wider feature near $2 G_0$.

7. Semimetals and semiconductors

As mentioned above, for antimony the jump-to-contact was observed at about $1 M\Omega$ [86], a value much higher than for the regular metals. This is consistent with the fact that electron density for Sb is three orders of magnitude lower than for common metals, giving a corresponding Fermi wavelength of about 55 \AA . Although the bulk bandstructure for such materials may not be applicable at the atomic scale, one can still infer that a one-atom contact will not be sufficiently large to transmit a full channel. The conductance is then reduced by orders of magnitude compared to the conductance quantum, since only tunneling contributes to the current transport. At still larger contact diameters, no evidence was found for quantization around the unit values of conductance [86]. The conductance is observed to increase in a stepwise fashion, similar to metallic contacts, but the step heights are much smaller than a quantum unit. This behavior is naturally attributed to the atom-by-atom decrease of the contact size with elongation. Similar steps at high-resistance contacts have been observed for the semiconductor Si [231]. The Si contacts are found to show Schottky-like rectification characteristics that is influenced by the type of doping of the Si material.

Costa-Krämer *et al.* [232] measured a conductance histogram for Bi using an STM at helium temperatures. The histogram collected from 3000 curves shows a broad peak with a maximum at $\sim 2 G_0$, and a shoulder near $1 G_0$. Although the authors make the connection with quantized conductance, the data are insufficient to support such conclusion. One of the further complications is the fact that the data are recorded for a voltage bias of 90 mV, whereas the Fermi energy, E_F , for Bi is only

25 meV. At $eV \gg E_F$ the simple models that produce quantized conductance cross over to a regime where half-integer conductance values dominate [233, 234, 235].

More recently, Rodrigo *et al.* [236] recorded histograms for Bi at 4 K and 77 K, using a voltage bias of 10–20 mV. They observed a strikingly different behavior for the two temperatures. At 4 K they observed sub-quantum conductance steps similar to Sb. The curves between the conductance jumps are typically short, of order 0.1 to 0.2 nm, and often curve strongly upward upon stretching. At 77 K on the other hand the plateaus are much more regular and flat, and stretch over several nanometers. Most significant is the observation that nearly all curves have a well-defined plateau near $1 G_0$, which results in a pronounced peak in the conductance histogram. A smaller peak near $2 G_0$ can also be seen. Rodrigo *et al.* propose an interesting explanation for these observations based on the bandstructure for Bi. Besides the band with a light effective electron mass, that is responsible for the usual Fermi surface properties of Bi, they identified a low-lying heavy-electron band. Under conditions of lateral quantum confinement the quantum level in the light band, which has a strong dispersion, is pushed above the lowest level in the heavy-electron band. At low temperatures the heavy electron band determines the conductance in the atomic contacts. However, at 77 K the light electrons can be observed to determine the conductance for larger-size contacts, when the confinement is less severe. The authors present a simplified model for the evolution of the contact size that appears to explain the data. Despite the complications of the bandstructure for Bi and the anomalous temperature dependence this appears to be the most clear-cut evidence for conductance quantization, that does not suffer from the discreteness of the atomic structure.

8. Metallic alloys and compounds

The number of experiments on compounds and alloys is very limited. The additional complication here is that the interpretation of the data requires knowledge of the atomic structure formed at the contact. The composition of the material at the atomic scale may be very different from the bulk composition due to surface segregation and the mechanical work done on the contact.

Many alloys may have properties similar to those for elemental metals, as indicated by experiments on Au with approximately 5% Co [107]. The first experiment shows that the addition of a few percent Co does not significantly modify the histogram compared to pure Au. For Au and Ag one can form random alloys in the entire concentration range and one finds a gradual cross-over from the Au to the Ag histograms [237]. In studies for alloys of Cu, Ag and Au with transition metals it is found that the peak at $1 G_0$, that is characteristic for the noble metals, survives for transition metal concentrations well over 50% [237, 238, 239]. The interpretation for this

observation requires further study. There is evidence for segregation of the noble metals away from the contact under the application of a high bias current [239].

Volkov *et al.* [240] used a low-temperature STM to study the contact between a Pt tip and the narrow-gap semiconductor $\text{Pb}_{1-x}\text{Sn}_x\text{Se}$. They find a jump-to-contact sometimes to a conductance near $1 G_0$, and sometimes to plateaus with a much smaller conductance. The latter can be explained by the semiconducting nature of the sample. The histogram they present shows three rather broad peaks, near 1, 2 and $4 G_0$ for which the authors do not attempt to offer an explanation. Ott *et al.* [222] apply the same technique as for Fe described above to the ferromagnetic perovskite $\text{La}_{0.75}\text{Sr}_{0.25}\text{MnO}_3$ and show a histogram with seven rather sharp peaks. However, the number of scans used is limited to 60 and they mention that “...it is possible that some of the features could shade off if much larger data sets were considered. Unfortunately these ceramic crystals are unsuitable for high rate measurements because of the difficulty of establishing reliable contacts...”. The latter agrees with experience from MCBJ experiments on heavy fermion metals, high-temperature superconductors and organic conductors at low temperatures [241], where it was seen that it is usually impossible to identify a clear jump-to-contact, and the mechanical properties of atomic-sized contacts for these unconventional materials differ fundamentally from the plastic behavior observed for the elemental metals.

A rather exceptional material studied using conductance histograms is that composed of multiwalled nanotubes [242]. It is beyond the scope of this review to discuss the rapid developments in the study of these interesting materials for which one may consult a recent review [6] and references therein. Single-walled carbon nanotubes come in various modes of chirality, most of which are semiconductors while some are metallic. The metallic nanotubes are predicted to have two conductance channels. Direct measurements of this number of channels has been difficult, since the conductance is severely modified by the contact barriers to the leads and by defects along the nanowires, but recent work agrees with two conductance channels per nanowire [243]. For multiwalled nanotubes no general predictions can be made. In experiments on a multiwalled carbon nanotube attached to the gold tip of an STM and measured at room temperature by immersing it into liquid metals Frank *et al.* [242] found a conductance histogram with two very sharp peaks. The best results were obtained using liquid Hg and the peaks were found very close to 1 and $2 G_0$. Part of the explanation may be that only a single carbon wall, possibly the outer one, contributes to the conductance, but that still leaves a factor of 2 to be explained.

E. Non-linear conductance

The discussions above have mostly been limited to the linear conductance for small bias. We defer discussion of non-linear contributions to the conductance at low temperatures due to superconductivity and due to scattering on defects to Sects. VIII and IX, respectively. However, even at room temperature many authors have reported non-linear contributions to the conductance for fairly large bias voltages, in the range from 0.1 to 1 V [73, 74, 108, 193, 244]. Most of these experiments were performed for gold under ambient conditions and the current-voltage (IV) relation generally has a significant cubic term, $I = g_0 V + g_3 V^3$, with $g_3 > 0$ so that the current at high bias lies above the extrapolation from the zero-bias conductance. As was pointed out by Hansen *et al.* [196] this contradicts the observations of Sakai and coworkers [109, 203] that the peaks in the conductance histogram for gold remain at their initial positions up to bias voltages larger than 0.5 V, as discussed in Sect. VD 1 above.

Hansen *et al.* made a careful study of this problem and developed a technique that allows them to record accurate IV -curves within about $10 \mu\text{s}$ [196, 245]. They show convincingly that under clean UHV conditions the IV -curves for gold at room temperature are nearly linear up to at least 0.5 V. Only when the surface is intentionally contaminated do they observe non-linearities of the magnitude reported before. In addition, they observe that the clean contacts tend to break spontaneously on a time scale of milliseconds, while the contaminated contacts can be held stable at a conductance near the quantum unit for hours. They accompany their observations with a calculation based on a tight binding model for the atomic-sized contact under the application of a finite bias voltage (see also [246]). The calculations reproduce the experimentally observed nearly linear IV -characteristics, and only above about 1 V a slight curvature was obtained with a sign opposite to that observed in the room temperature experiments. The authors propose that contaminated contacts contain a tunnel barrier composed of adsorbates, which naturally explains the observed curvature in the IV -curves. At the same time, the mechanical contact area would be much larger than that for a metallic contact with the same conductance, explaining the enhanced stability. The proposed effect of impurities has been confirmed by *ab initio* calculations that self-consistently include the applied bias voltage [247]. The linear IV dependence for clean Au is modified to have a pronounced g_3 -term when a sulfur impurity is inserted in a gold atomic contact.

For metals other than gold there are not many results on the IV -characteristics available yet. However, from the work on gold we learn that great care is needed to ensure clean contacts, since most other metals will be more sensitive to adsorbates than gold. Recent work by Nielsen *et al.* shows that clean Pt contacts have a much stronger non-linear voltage dependence, which was shown

to agree with first-principles calculations [248].

VI. MECHANICAL PROPERTIES OF ATOMIC-SIZED POINT CONTACTS

How do the mechanical properties of matter change as size is reduced down to the atomic scale? This question is of fundamental interest, not only theoretically but also from an applied point of view since contact in macroscopic bodies typically occurs at numerous asperities of small size, whose mechanical properties determine those of the contact. This explains the interest of investigating small size contacts for many technologically important problems like adhesion, friction, wear, lubrication, fracture and machining [22, 23, 249, 250]. The appearance of proximal probes like the STM and related techniques, together with computational techniques for simulating tip-surface interactions with atomic detail have contributed to the growth of the new field of nanotribology.

In metallic contacts mechanical and electrical properties are intimately related. Experiments in which mechanical and electrical measurements are combined are essential for understanding the physics of these systems. Not many of this kind of experiments have been done due to the technical difficulties involved. Note that in most of the experiments reviewed in the foregoing sections

the geometry of the contact and its evolution during an experiment are result of the stresses acting on them. Hence the evolution of the conductance in these experiments reflects not only the changes in size of the constriction but also the mechanical processes taking place at the constriction itself.

In this section, we first review some of the basic concepts of the mechanical properties of metals, specifically elastic and plastic deformation, fracture, and contact mechanics. The elastic properties of a metal are not expected to change much as size is decreased to nanometer dimensions, since they reflect the resistance of atomic bonds to stretching. However for one-atom contacts or atomic chains things could be otherwise. Nanometer-size specimens are also stronger since the strength (i.e., the resistance to plastic deformation) depends on the presence of dislocations which could be absent in small specimens. We will discuss some simple models of metallic constrictions based on contact mechanics. These are based on macroscopic continuum theory, which is applicable, in principle, for distances large compared with the distances between the atoms. Hence such models cannot be expected to describe atomic-sized systems accurately, but they can serve as a starting point for interpreting the experimental results. We will see in Sect. VII that many of the phenomena displayed by these continuum models can be recognized in the microscopic, atomistic models. In Sect. VIC, we use these models combined with the experimental results to deduce, approximately, the shape of mechanically drawn contacts. The experiments in which the conductance and forces of contacts down

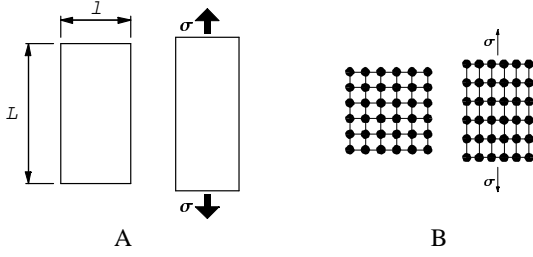


FIG. 38: (A) Elastic deformation of a rod under uniaxial stress. (B) Atomistic view of elastic uniaxial deformation.

to one atom are simultaneously measured are discussed in Sect. VI B. Experiments on the mechanical properties of atomic chains will be described in Sect. XI. Theoretical work on the mechanical and electrical properties of atomic contacts using molecular dynamics simulations will be reviewed in Sect. VII A.

A. Mechanical properties of metals

1. Elastic deformations

When a solid is subjected to a load it undergoes a change in shape. For small loads this deformation is elastic and the specimen recovers its original dimensions as the load is removed. For isotropic materials, the stress tensor σ and the strain tensor ϵ are linearly related [251, 252]

$$\sigma_{ik} = \frac{E}{1 + \nu} \left[\epsilon_{ik} + \frac{\nu}{1 - 2\nu} \left(\sum_l \epsilon_{ll} \right) \delta_{ik} \right], \quad (77)$$

where E is the modulus of elasticity or Young's modulus, and ν is Poisson's ratio. This law, valid for small deformations, is called Hooke's law.

For homogeneous deformations, in which case the strain and stress are constant in all the solid, the relation between strain and stress is particularly simple. For example (see Fig. 38(A)), the uniaxial extension or compression of a rod of length L and lateral dimension l , whose axis is in the z -direction, due to a force F , is given by

$$\epsilon_{zz} = \frac{\sigma}{E} \quad \text{or} \quad \frac{\delta L}{L} = \frac{1}{E} \frac{F}{l^2}, \quad (78)$$

and the lateral deformation by

$$\epsilon_{xx} = \epsilon_{yy} = -\nu \epsilon_{zz}. \quad (79)$$

For metals, values of Poisson's ratio range between 0.25 and 0.4, which implies that the volume is not conserved during elastic deformation. We may write the response of the bar as an effective spring constant $k_{\text{eff}} = El^2/L$.

Single crystals are not isotropic and in order to specify the elastic properties several elastic constants are needed,

their number depending on the symmetry of the crystal. The least number of non-zero constants is three, for cubic symmetry. In this case, the Young's modulus depends on the direction of the applied stress relative to the crystal axes [251, 252]. For instance, in the case of Au, the maximum value of the Young's modulus is $E_{\langle 111 \rangle} = 117$ GPa, and the minimum is $E_{\langle 100 \rangle} = 43$ GPa. Macroscopic polycrystalline samples are in practice isotropic, since they are composed of crystallites with random orientations. The Young's modulus for polycrystalline gold is taken to be 80 GPa.

On an atomic scale, elastic strain consists in small changes in the inter-atomic spacing, that is, in the stretching of inter-atomic bonds, as illustrated in Fig. 38(B). Consequently the modulus of elasticity E is a measure of the resistance of the inter-atomic bonds to deformation.

2. Plastic deformations

For most metallic materials elastic deformation is possible only for strains smaller than about 0.005 (or 0.5%). As the material is deformed beyond this point, permanent, nonrecoverable, or *plastic deformation* occurs. In macroscopic metal specimens this transition from elastic to plastic behavior, or yielding, occurs gradually, and it is difficult to assess accurately the lower limiting stress below which no plastic deformation is found. Conventionally the *yield strength* σ_y is defined as the stress necessary to produce a plastic strain of 0.002 under uniaxial stress. The yield strength of a metal is very sensitive to any prior deformation, to the presence of impurities and to heat treatment, in contrast to the modulus of elasticity which is insensitive to these factors.

When the material is in a complex state of stress, as in the case of a point-contact, the load at which plastic yield begins is related to the yield strength σ_y through an appropriate yield criterion, which is written in terms of the principal stresses or eigenvalues of the stress tensor, σ_1 , σ_2 , and σ_3 ³. The simplest criterion is due to Tresca

$$\max\{|\sigma_1 - \sigma_2|, |\sigma_2 - \sigma_3|, |\sigma_3 - \sigma_1|\} = \sigma_y, \quad (80)$$

and a somewhat more accurate criterion is von Mises' criterion

$$\frac{1}{\sqrt{2}} [(\sigma_1 - \sigma_2)^2 + (\sigma_2 - \sigma_3)^2 + (\sigma_3 - \sigma_1)^2]^{1/2} = \sigma_y. \quad (81)$$

These criteria [253], which in practice are equivalent, are in fact based on the idea that plastic flow is caused by shear stresses. It can be shown that the greatest shear stress, that is, the maximum value of the

³ The stress tensor is symmetric and consequently can be diagonalized at any point.

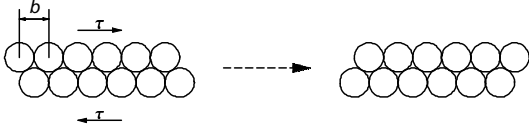


FIG. 39: Slip in a perfect crystal under shear stress.

off-diagonal elements of the stress tensor, is given by $\tau_{\max} = (\sigma_{\max} - \sigma_{\min})/2$, where σ_{\max} , and σ_{\min} are the largest and smallest eigenvalue, respectively.

On an atomic scale, plastic deformation corresponds to the breaking of bonds between neighboring atoms and the reforming of bonds with the new neighbors. The atoms change positions, that is, they change their configuration. Upon removal of the stress they do not return to their original positions and there is a permanent change in the shape of the body. The simplest model of plastic deformation of a ‘perfect’ crystal, that is, one with no defects, considers the sliding of two compact planes with respect to each other. Frenkel [254] calculated the maximum shear stress required for this process to occur. He considered two neighboring planes in a crystal with a repeat distance b in the direction of shear and spacing h . These planes are assumed to be undistorted as a shear stress τ is applied, as illustrated in Fig. 39. It is then assumed that τ varies with shear displacement x as

$$\tau = \frac{Gb}{2\pi h} \sin \frac{2\pi x}{b}, \quad (82)$$

where G is the shear modulus⁴. The maximum value of τ is then

$$\tau_{\max} = \frac{Gb}{2\pi h}. \quad (83)$$

For the $\{111\}$ planes of a face-centered cubic metal we take $b = a/\sqrt{6}$, and $h = a/\sqrt{3}$, where a is the lattice parameter, thus $\tau_{\max} \approx G/9$. A more extensive discussion [255] gives $\tau_{\max} \approx G/30$.

These values of the shear stress are much larger than those observed in macroscopic metal specimens. This discrepancy is explained by the presence of dislocations, which can glide at low stress values [252, 255]. The atomic distortions accompanying the motion of dislocations, which are linear defects, are considerably less than those happening during “perfect slip”, which requires glide of atomic planes in a correlated manner. High values of the shear stress, close to the theoretical prediction, are observed in experiments with dislocation-free specimens like whiskers in bending or uniaxial tension [255], and are also to be expected for nanometer volumes of metals, since dislocations are unstable and are quickly expelled from small-volume samples.

In macroscopic specimens plastic flow involves the motion of large numbers of dislocations in response to stress. Dislocation motion occurs through a process termed *slip*, which occurs in a preferred crystallographic plane (slip plane) and along a specific direction (slip direction). The combination of the slip plane and slip direction (called the slip system) is such that the atomic distortion that accompanies the motion of a dislocation is minimal. The slip plane is the plane of the most dense atomic packing and the slip direction corresponds to the direction, in this plane, having the highest linear density. For the fcc structure the slip planes are the $\{111\}$ planes and the slip directions are of the $\langle 110 \rangle$ -type, and there are 12 slip systems. The sliding of atomic planes in a perfect crystal will also occur in the slip plane and along the slip direction, because this is the least energetic process. In some crystal structures, the unit dislocation dissociates into partial dislocations, the so-called *Shockley partials*. For example, in fcc crystals atomic glide on a $\{111\}$ plane is somewhat easier if the motion is divided in two partial slip steps. Such a partial slip leads to a disruption of the characteristic ABC stacking of the fcc structure, producing a stacking fault.

In a single crystal, the various slip systems are oriented differently, and plastic flow will initiate in the slip system which has the greatest resolved shear stress, i.e. the greatest stress acting on the slip plane and in the slip direction. The critical value of the resolved shear stress τ_{CRSS} , for which plastic flow is initiated when the single crystal is subjected to a tensile (or compressive) stress, depends on the orientation of the crystal with respect to the tensile axis and is characteristic of the material and smaller than the yield strength σ_y . The value of τ_{CRSS} depends on temperature and strain rate. For high temperatures ($T \geq 0.7T_m$, with T_m being the material’s melting temperature in Kelvin), τ_{CRSS} decreases rapidly with increasing temperature and decreasing strain rate as a result of the important role played by diffusive processes. At these temperatures plastic deformation can be effected over a period of time at a stress level well below the materials yield strength. This time-dependent deformation is called *creep*. At intermediate temperatures ($0.25T_m \leq T \leq 0.7T_m$, τ_{CRSS} is essentially constant. For $T \leq 0.25T_m$, τ_{CRSS} is again a function of temperature and strain rate, increasing with decreasing temperature and increasing strain rate. This is a result of the resistance to dislocation motion presented by short-range barriers [252].

Although dislocation glide is the dominant mechanism in plastic deformation in macroscopic crystals, permanent shape changes can be effected by the mechanism of *twinning* [252]. Twinning is more likely to be observed in bcc materials than in fcc metals.

A peculiarity of nanometer-scale specimens is that they have a high surface-to-volume ratio, and as a consequence surface energy effects may be of importance in plastic deformation. Let us consider a cylindrical specimen of radius a , which for simplicity will be assumed perfectly

⁴ $G = E/2(1 + \nu)$ in polycrystalline materials.

plastic with yield strength σ_y , and which is elongated a small distance Δl . The work E_v required to deform its volume may be written as

$$E_v = \pi a^2 \sigma_y \Delta l, \quad (84)$$

and the work E_s required to extend its surface, while conserving volume, in the form

$$E_s = \gamma \pi a \Delta l, \quad (85)$$

where γ is the surface energy. Using the values of γ and σ_y for typical metals, we find that E_s becomes larger than E_v for $a \sim 1\text{--}10$ nm. Hence, surface energy effects which are negligible for larger specimens are important in atomic-sized contacts. One may expect a liquid-like behavior in the final stages of rupture where the contact necks down to atomic dimensions.

3. Fracture

Fracture is the separation of a body in two pieces in response to an imposed stress at temperatures below the melting temperature of the material. A given material may fracture in a variety of ways, depending on temperature, stress state and its time variation, and environmental conditions [252]. Tensile fracture occurs by the stress-assisted separation of atomic bonds across the plane of fracture. As with plastic deformation, at relatively high temperatures, it is aided by diffusion. Fatigue fracture is associated with cyclically applied strains or stresses. Static fatigue and embrittlement are associated with hostile or corrosive environments.

Let us consider the ideal theoretical strength of a solid in the same spirit as for plastic deformation. For a perfect crystal, fracture would take place by the simultaneous rupture of all atomic bonds across the fracture plane as depicted in Fig. 40. A simple estimate of the expected tensile stress or cleavage stress [252, 255] is obtained by considering that the variation of the force to pull apart two adjacent atomic planes, separated by a distance a_0 , is of the form

$$\sigma = \frac{E}{\pi} \left(\frac{a}{a_0} \right) \sin \frac{\pi}{a} (x - a_0), \quad (86)$$

where a is a measure of the range of the inter-atomic forces. The work done to separate the two atomic planes should be related to the surface energy γ for the two newly exposed surfaces,

$$\int_{a_0}^{a_0+a} \sigma \, dx = 2\gamma, \quad (87)$$

whence $a^2 = \pi^2 \gamma a_0 / E$. The theoretical cleavage stress σ_{th} is given by the maximum value of σ in Eq. (86),

$$\sigma_{th} = \sqrt{\frac{E\gamma}{a_0}}. \quad (88)$$

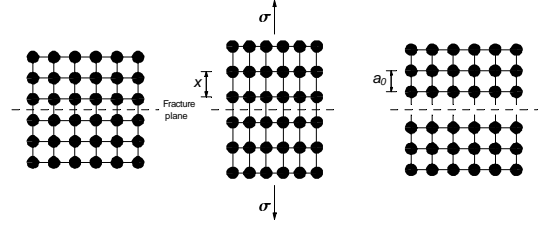


FIG. 40: Atomistic model of theoretical tensile fracture. The equilibrium structure (A) is altered due to the application of stress σ (B). After fracture (C), two new surfaces form and the atoms return to their equilibrium positions. After [252].

The values obtained from this estimate are much larger than those found experimentally. This is due to the existence of interior or surface cracks that catalyze fracture. Cracks may also be introduced in the material by plastic deformation. For a completely brittle solid the theoretical strength will be attained at the tip of the crack.

When the sample does not contain preexisting cracks tensile fracture may be preceded by varying degrees of plastic deformation. When fracture takes place prior to any plastic deformation it is termed *brittle* (Fig. 41a). The fracture mechanism is called *cleavage* if fracture occurs within grains (or in a single crystal) or *brittle intergranular fracture* if it progresses along grain boundaries in a polycrystal. *Ductile fracture* is preceded by varying degrees of plastic deformation. In a single crystal fracture may occur by gliding on a slip plane, in which case the fracture will be atomically flat (Fig. 41b). *Rupture fracture* corresponds to a 100 % reduction of the minimal cross section of the specimen by plastic deformation. In single crystals this is effected by multiple slips (Fig. 41c), whereas in a polycrystal is associated with necking (Fig. 41d). Rupture fracture is the extreme case of ductile fracture. In some materials there is a gradual transition from brittle to ductile as temperature is increased. In ductile metals plastic yield is related to shear stresses because the maximum shear stress is smaller than the theoretical cleavage stress, and consequently plastic deformation takes place by shearing not by cleaving. Even, if we consider perfect metal crystals the ideal maximum shear stress τ_{max} will be reached much before σ_{th} , indicating that the metal will prefer to flow by shear rather than to cleave. For instance, for gold in the $\langle 111 \rangle$ direction σ_{th} is 27 GPa, while τ_{max} is 0.74 GPa.

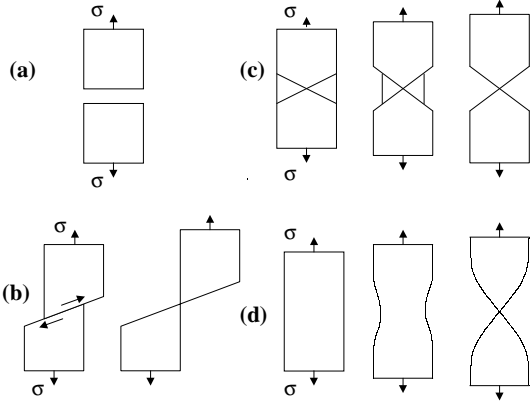


FIG. 41: Schematic illustration of the various modes of fracture. (a) Brittle fracture. (b) Fracture occurring by glide on a single slip plane. (c) Rupture fracture in a single crystal. (d) Rupture fracture in a polycrystal. After [252].

4. Contact mechanics

Bodies whose surfaces are non-conforming⁵ when brought into contact, touch first at a point or along a line and, even under load, the dimensions of the contact area are generally small compared to the dimensions of the bodies themselves. In these circumstances the contact stresses are highly concentrated and decrease rapidly away from the point of contact. The shape of the bodies is not important and the stresses can be calculated assuming that each body is an elastic half-space [251, 253]. For high loads, when the elastic limit is exceeded, only the region of the contact will deform plastically.

The response of the elastic half space to a concentrated load can be calculated in terms of the pressure distribution. For a load acting on a circular region of radius a , solutions can be found in closed form for pressures of the form $p = p_0(1 - r^2/a^2)^n$ [253]. Defining an effective elastic constant k_{eff} as the ratio of the load

$$F = 2\pi \int_0^a p(r)rdr \quad (89)$$

to the average displacement of the surface

$$\langle u_z \rangle = 2\pi \int_0^a u_z r dr, \quad (90)$$

we obtain

$$k_{\text{eff}} = \frac{CEa}{(1 - \nu^2)}. \quad (91)$$

The constant C equals $3\pi^2/16$, for $n = 0$, the uniform pressure distribution. For $n = 1/2$, the so-called Hertzian pressure, which is the pressure distribution resulting from the contact of two spheres, or Hertzian contact, we have $C = 16/9$. For $n = -1/2$, we have $C = 2$ and the pressure distribution corresponds to a uniform displacement of the contact area, as in the case of an ideally rigid punch indenting a softer surface. Note that the effective elastic constant k_{eff} is not very sensitive to the detailed pressure distribution.

Plastic deformation of the elastic half space will start when the yield condition is satisfied, that is, when the maximum shear stress τ_{max} reaches the value $\sigma_y/2$ anywhere in the solid. For the Hertzian pressure distribution, we have $\tau_{\text{max}} = 0.44F/\pi a^2$ and for the uniform pressure distribution $\tau_{\text{max}} = 0.31F/\pi a^2$. Both values above are computed for $\nu = 0.4$ which applies for gold. These maximal values are reached within the solid directly below the center of the contact, at a depth of $z = 0.51a$ and $z = 0.67a$ for the Hertzian and uniform pressures, respectively.

The standard model contact considered in textbooks [251, 253] is the so-called Hertzian contact, first considered by H. Hertz ([256], p. 409). In a Hertzian contact the contacting bodies are assumed to have spherical surfaces at the point of contact. In this case, the contact radius varies with load as the surfaces deform elastically. This model has been used to interpret the results of nanoindentation experiments [257], and also of friction experiments using AFM [258, 259] but it is not adequate for metallic contacts since the effective radius of curvature is too small and plastic deformation takes place before the area could vary due to elastic deformation.

As the simplest model for metallic nanocontacts, we can consider a short cylinder of radius a and length L between two semi-infinite half planes (the electrodes) as depicted in Fig. 42(a). This is similar to the model we have used for the transport properties. The response of this system to the applied strain is linear, in contrast to the response of Hertzian contacts. The elastic constant of this constriction is given by $k = (1/k_{\text{cyl}} + 2/k_{\text{ele}})^{-1}$, where k_{cyl} and k_{ele} are the elastic constants of the cylinder and electrodes, respectively. As seen above, for the cylinder we have $k_{\text{cyl}} = E\pi a^2/L$, and for the electrodes (the half spaces), $k_{\text{ele}} = BEa/(1 - \nu^2)$, with $B \approx 2$. Note that the elasticity of the electrodes can be more important than that of the constriction itself if this is short, namely $L < \pi a$. In this model the contact radius is almost constant, only decreasing (increasing) slightly during elongation (contraction) due to Poisson's ratio.

A somewhat more elaborate model of the constriction consists of slabs varying cross-section [260, 261] (see Fig. 42(b)). In this case, the elasticity is given by all the slabs acting like a series of spring $1/k = \sum_i 1/k_i$. This model is valid only if the diameters of two adjacent slabs are not too different, that is, if the changes in cross section of the constriction are not very abrupt.

⁵ Two surfaces are said to be conforming if they fit together without deformation.

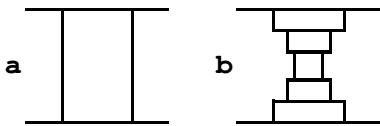


FIG. 42: Model geometry for metallic nanocontacts. (a) Simple cylindrical shape model for a constriction. (b) Slab model.

Note that for a contact composed of slabs the stress is concentrated in the narrowest cross-section which, consequently, will govern the yield condition. The maximum load F_{\max} that a contact can sustain before plastic deformation either for long or short constrictions, is given by $F_{\max} = \pi a^2 \sigma_Y$.

This completes our brief summary of the relevant concepts in continuum mechanics. We shall see that many of these familiar properties of solids can be observed with slight modifications down to the atomic scale, but quantum effects may lead to dramatic modifications, as we will see most clearly in Sects. XI and XII.

B. Simultaneous measurement of conductance and force

In experiments measuring the conductance and force simultaneously in atomic-sized contacts pressures consistent with the ideal strength of the metals were found, much larger than those for macroscopic contacts. In experiments for Pb [90] at 4.2 K, using an STM supplemented by a force sensor, it was found that for contact radii between 3 nm and 13 nm the pressure in the contact during plastic deformation was approximately 1 GPa. Improved resolution in subsequent experiments, on Au contacts between 2 and 6 nm in diameter, at 4.2 K [91] and at room temperature [92], and for contacts down to a single atom at room temperature [37], show that the deformation process, either for contraction or elongation, proceeds in alternating elastic and yielding stages (see Fig. 43). These elastic stages are linear and the elastic constant obtained from the slope is consistent with the model of a short constriction, using the bulk Young's modulus. Yield takes place for pressures of 2–4 GPa, consistent with the ideal strength, increasing up to about 13 GPa before rupture. In these experiments the mechanical relaxations are perfectly correlated to the jumps in the conductance, showing beyond doubt that they have a mechanical origin. Somewhat larger values for the pressure have been reported for experiments on Au at room temperature [262]. However, in this latter experiment the resolution was not enough to resolve the conductance plateaus or the elastic stages in the force.

High strengths have also been observed in microindentation experiments, where contacts were much larger. These experiments were pioneered by Gane and Bowden [263] who, using a 600 nm diameter flat punch on a spec-

imen of annealed gold, measured a yield stress of 1 GPa. This is close to the shear strength $\tau_Y = 0.74$ GPa calculated for the slip of an ideal Au lattice on {111} planes [255], and much higher than the typical value of 0.2 GPa for bulk polycrystalline gold. The experiment was performed inside of a scanning electron microscope which permitted to perform microindentation tests on regions of the specimen free from dislocations. More recently, similar results were obtained in nano-scale contacts by Michalske and his collaborators using a variant of AFM (the so-called interfacial force microscope). These experiments were performed on gold thin films of 200 nm thickness [257, 264], and the curvature of the W tip was ~ 400 nm. The surface of gold was passivated by a self-assembling monolayer film to avoid the adhesive interaction between probe and substrate, and the results could be described by the Hertzian contact theory. They found that for small contacts (radii of the order of 30 nm) the yield stress was $\sigma_Y \sim 1$ GPa.

Catastrophic fracture-like yielding in Au nanocontacts (of diameter larger than 5 nm) has been reported in experiments performed at room temperature [262]. In these catastrophic events the neck cross-section changes by one order of magnitude. This observation contrasts with the abovementioned experiments [91, 92] in contacts of similar sizes, at low and room temperatures, and can be traced to the different elastic constants of the sensor used (160 N/m in [262] vs 705 and 380 N/m in [91] and [92], respectively). A relatively soft sensor causes elastic energy accumulation that is suddenly released in a catastrophic avalanche.

Gold nanocontacts typically deform plastically down to the last atom contact before fracture takes place, as demonstrated by the numerous experiments in Au contacts showing a well-defined value of the conductance of $1 G_0$. This is the extreme mode of ductile fracture (rupture). The force necessary to break this one-atom contact is found to be also quite well defined with a value of 1.5 ± 0.1 nN [37], as shown in Fig. 12. Similar results have been found for the mechanical forces during the elongation and rupture of an atomic chain of gold atoms [93] which will be reviewed in the Sect. XI.

The stiffness (or the effective spring constant) of the contact has been measured directly using an ac method in UHV [95]. In this experiment an Pt-coated tip was used to form contacts on a gold sample, and the first conductance step was observed at approximately half integer values of the quantum of conductance.

The variations of length of the plateaus for gold contacts at room temperature [94], which was found to be quantized, has been related to the underlying processes during plastic deformation.

The effect of temperature on the mechanical properties of metallic atomic contacts has not been studied systematically. For Au contacts no significant difference is observed between the mechanical properties at room temperature and those at 4.2 K [37, 92, 93], except for the much larger stability of the contacts at low temperatures,

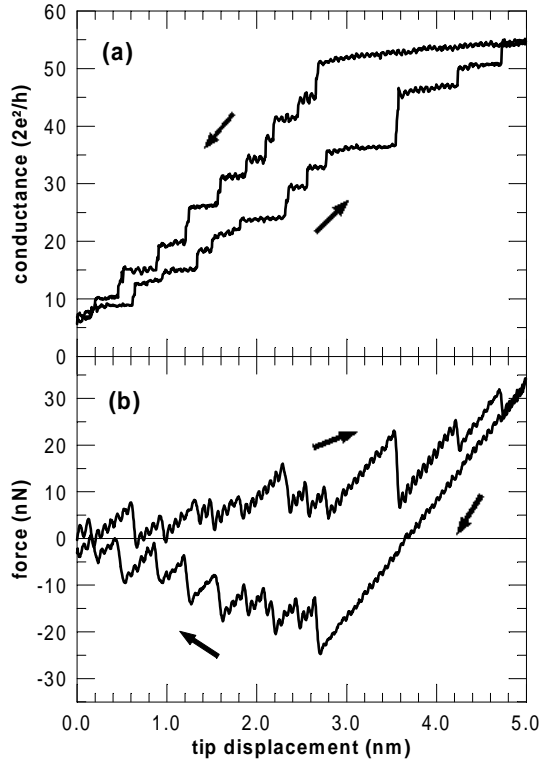


FIG. 43: Simultaneous recording of conductance (a) and force (b) during a cycle of contraction and elongation of a constriction without breaking the contact. Reprinted with permission from [37]. Copyright 1996 American Physical Society.

which is in part due to the slowing down of diffusion processes and in part due to the higher stability of the experimental setup.

In a contact, since stresses are concentrated in the minimal cross section, it is natural to assume that plastic deformation will involve mostly the narrowest part of the constriction, which also controls the conductance. Using this assumption in conjunction with volume conservation it is possible to estimate the length involved in plastic deformation from the curves of conductance vs elongation [261, 262] (see the next section). For the smallest contacts it is found to be independent of contact diameter and involves 5 to 6 atomic layers [262], while for larger contacts it varies.

From the experimental results for nanometer-scale contacts of Au we can conclude that atomic constrictions go through a sequence of discrete atomic configurations. Each of these configurations deforms elastically (and reversibly) until it yields, changing to a new configuration in order to relax the stress. This new configuration is of the order of one atomic spacing shorter (for contraction) or longer (for elongation) than the previous one. For each configuration the conductance is approximately constant, with a variation that can be accounted for by the elastic changes in the constriction due to Poisson's

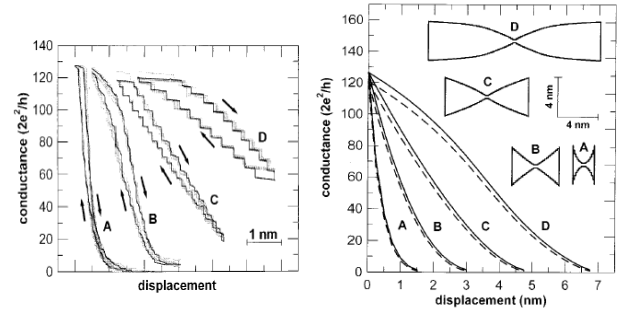


FIG. 44: Experimental conductance curves for four different Au contacts at low temperature (left panel). Fitting of the experimental curves gives the estimated shapes just before breaking depicted in the right panel. All the necks have the same initial cross section. Reprinted with permission from [261]. Copyright 1997 American Physical Society.

coefficient. The measured slope during the elastic stages is proportional to $k_c + k_s$ where k_s is the finite stiffness of the force sensor, and k_c is the effective spring constant of the contact, including the electrodes. The measured effective spring constants are consistent with the macroscopic Young's modulus for Au, taking into consideration the uncertainty in the exact geometry of the constriction [37, 91]. The yield point for each atomic configuration presents very large values consistent with the ideal strength in the absence of dislocations. The yield point for each atomic configuration is independent of the sensor stiffness but if the sensor is too soft an avalanche will occur during elongation and some of the configurations will not be accessible. Ideally the force sensor should have zero compliance, in order not to affect the dynamics of the measurement.

C. The shape of mechanically drawn metallic contacts

The scanning capabilities of STM have been used to obtain an estimate of the contact geometry. In the first work on metallic contacts, Gimzewski *et al.* [12], studied the local modifications induced by point contacts of a Pt-Ir tip and an Ag substrate in UHV, by imaging the area where the tip has touched the sample surface. They found that for clean metal-metal contacts, after gentle indentation of the substrate, the topography shows a pronounced protrusion of nanometer dimensions, consistent with formation, stretching and breaking of necks of atomic dimensions. The same approach has been used for contacts of different sizes [29, 91, 92, 265] and serves at best to give an estimate of the maximum dimensions attained by the contact during the indentation by measuring the extent of the plastically distorted area in the substrate but gives no information of the relation between shape and electrical or mechanical properties.

The shape of the constriction produced by plastic de-

formation can be estimated from the conductance vs displacement curves (I - z curves) [261], using the fact that the conductance of a ballistic constriction is to a good approximation proportional to the contact area, Eq. 8 with a small perimeter correction which depends on the shape (Sect. VII B 2). In a constriction submitted to a tensile force, stresses are largest in the narrowest part and, consequently, we may safely assume that plastic deformation occurs mostly in this area, in a zone of extent λ , leaving the rest of the neck unmodified. Assume that the contact at any point of its evolution can be represented by the slab model of the previous section, which can be considered symmetrical with respect to the center of the contact for simplicity. Under tensile force the whole constriction will deform elastically until the yield stress is reached in the narrowest slab whose cross sectional area is A_i . We assume that only a central portion of this slab of length λ_i deforms plastically generating a longer and narrower slab in order to relax stress. The cross sectional area of the new slab A_{i+1} is given by volume conservation

$$A_{i+1} = \frac{A_i \lambda_i}{(\lambda_i + \Delta l)}, \quad (92)$$

where $\lambda_i + \Delta l$ is the length of the new slab. Since only the central portion of the narrowest slab is modified, the shape of the constriction after a number of this plastic deformation stages can be deduced from the sequence of values of A_i and λ_i .

The plastic deformation length, λ , defined above, is related to the portion of the constriction that participates in the plastic deformation process, and in general it will depend on the cross-section, length, and history of the constriction. It can be calculated from the experimental $I(z)$ curve by noting that in the limit $\Delta l \rightarrow 0$, $\lambda = -(d \ln A / dl)^{-1}$, where A is the cross-section of the narrowest portion of the contact [261]. For small contacts λ is typically constant ranging from 0.2 to 1 nm and corresponding to an exponential behavior of $A(z)$. These results imply that for small contacts only a few atomic layers participate in the plastic deformation process [262]. In contrast experiments on larger contacts show that λ depends on the cross section A and also on the deformation history of the contact. As shown in Fig. 44 contacts of similar cross sections can have very different shapes. Typically, constrictions that have been submitted to *training* by repeatedly compressing and elongating before breaking are longer and have $\lambda \propto A^{1/2}$. Thus, in this case the plastic deformation length is proportional to the radius of the contact. Au necks formed at low temperature are not very different from those at room temperature. For the latter long necks are somewhat easier to form and they are typically about 30% longer. This small difference is expected, since room temperature is still much lower than the melting temperature for gold.

The effects of surface tension and surface diffusion have been included in a continuum model calculation for the shape evolution of a constriction in order to explain the

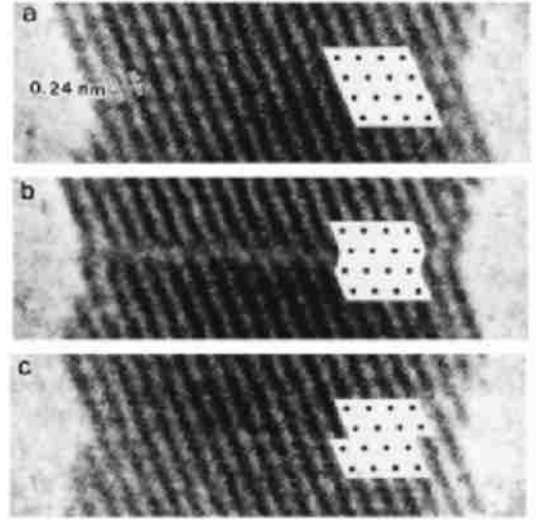


FIG. 45: Time-sequence series of high-resolution images of elemental processes of slip during shear deformation of a Au contact. Reprinted with permission from [79]. Copyright 1998 American Physical Society.

experimental results in Pb contacts at room temperature [189]. These results show that surface diffusion can either lead to the growth of the neck or to its thinning and breaking depending on its curvature. Note that at room temperature, surface diffusion effects are expected to be more important in Pb than in Au due to the much lower melting temperature of Pb.

The shape and even direct atomistic visualization of the process of mechanical deformation in gold contacts has been possible using high resolution transmission electron microscopy (HRTEM). A simplified STM-like setup (piezo-driven specimen holder without tunneling current feedback control) was mounted inside a 200 keV HRTEM, and a time resolution of 1/60 s and space resolution of 0.2 nm were achieved [77]. Compression, tensile and shear deformation experiments were performed in nanometer-sized gold contacts [78, 79], showing that deformation proceeds by slip and twinning in dislocation-free contacts of about 4 nm width (see Fig. 45). Pillar-like structures were observed during retraction in 2 nm wide contacts [78]. For these smaller contacts, it was not clear whether lattice slips proceed by a dislocation mechanism (*i.e.*, by introduction of a dislocation or dislocation-like localized strain) or by simultaneous displacement of lattice planes, whereas in the 4nm wide necks the introduction of rapidly disappearing partial dislocations was observed during the deformation [79]. At room temperature surface diffusion contributes to neck growth in addition to compressive deformation for the smaller contacts [78].

Another possibility for the observation of the structure of nanowires using HRTEM is to generate the nanowires *in situ* by focusing the electron beam with a large current density on different sites of a self-supported metal thin

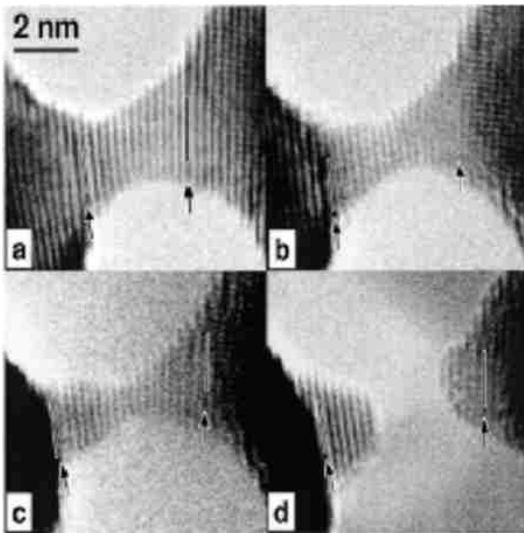


FIG. 46: Nanowire evolution when stretched along the $[111]$ direction for gold. After the rupture the two apices reorganize and retract. Reprinted with permission from [266]. Copyright 2000 American Physical Society.

film, which produces holes that are allowed to grow until a nanometric neck is formed [54, 80, 106, 266]. The beam intensity is then reduced to perform image acquisition. Kondo *et al.* [80] studied the structure of stable nanowires ranging from 0.8 to 2 nm in thickness, and from 5 to 10 nm in length, formed in a 3 nm thick Au(001) film. These nanowires, which are remarkably straight and of uniform thickness along their axes, are probably stabilized by their hexagonal surface reconstructions. Rodrigues [266] formed nanowires in a polycrystalline film of 5 nm thickness. The apexes forming the contact appeared to move spontaneously with respect to each other, probably due to thermal expansion of the whole film, leading to a slow elongation of the nanowires. They observed that just before rupture the gold nanowires are crystalline and display only three atomic configurations where either $[100]$, $[110]$ or $[111]$ directions lie approximately parallel to the elongation direction. Mechanical behavior was brittle or ductile depending on orientation. Single atom wires have also been resolved [80, 106, 267, 268] but discussion of this aspect will be deferred to Sect. XI.

VII. MODEL CALCULATIONS FOR ATOMIC-SIZED CONTACTS

A full description of the transport and mechanical properties of atomic-sized contacts requires a quantum-mechanical treatment of both their nuclear and electronic degrees of freedom. This is the idea behind *ab-initio* molecular dynamics simulations. The problem is that the computational requirements are so high that systems that can be studied this way are limited to a small num-

ber of atoms (see Sect. VII D). Different approaches can be followed to simplify this problem, dealing with different aspects separately. In classical molecular dynamics (MD) simulations (see Sect. VII A), the dynamics and energetics of the system are calculated assuming that the atoms respond to adequately parameterized forces. The electrons, which in fact give rise to these interatomic forces, are not taken into account explicitly. The conductance can be obtained from the calculated structure using different models but neglecting its effect on the dynamics and energetics. On the other hand, it is possible to concentrate on the electronic effects. The atomic structure can be assumed fixed like in tight-binding (TB) (see Sect. VII C) and *ab initio* models or completely ignored like in free electron (FE) (see Sect. VII B) models. These partial approaches have been very illuminating, clarifying important aspects of the problem.

A. Molecular dynamics simulations of contact evolution

The first molecular dynamics (MD) simulations of the formation and fracture of metallic nanocontacts were carried out by Landman *et al.* [22] and by Sutton and Pethica [23]. These simulations modeled the interaction between a tip and a substrate showing that contact formation is associated with an atomic-scale instability which leads to the jump-to-contact phenomenon and involves the inelastic motion of atoms in the vicinity of the interfacial region. The process of elongation of the atomically thin neck formed during pull-off proceeds via structural atomic rearrangements, which occur when the constriction becomes mechanically unstable. In between this structural transformations the constriction deforms elastically.

The conductance of a metallic contact during the process of contact formation and fracture using MD was first calculated by Todorov and Sutton [269] using a tight-binding (TB) scheme. They found that the abrupt variations of the conductance observed experimentally [26] are related to the sudden structural atomic rearrangements of the atoms in the contact. The possible relation of the conductance steps with conductance quantization in metallic contacts and the contradictory experimental evidence [26, 28, 29, 31, 76], led to more MD simulations using either TB [270] or free-electron (FE) [31, 76, 270] schemes for the calculation of the conductance. In particular, the question was whether the steps were due to abrupt decreases in the contact cross section or whether they were due to the abrupt pinching off of conductance channels during a smooth decrease in the cross section. The correlation of the changes in conductance with the changes in cross sectional area and the effect on the conductance of scattering from the surface rugosity of the constriction [76, 270] and internal defects [270] was also investigated. In these early simulations not much attention was paid to the total force on the contact, since the

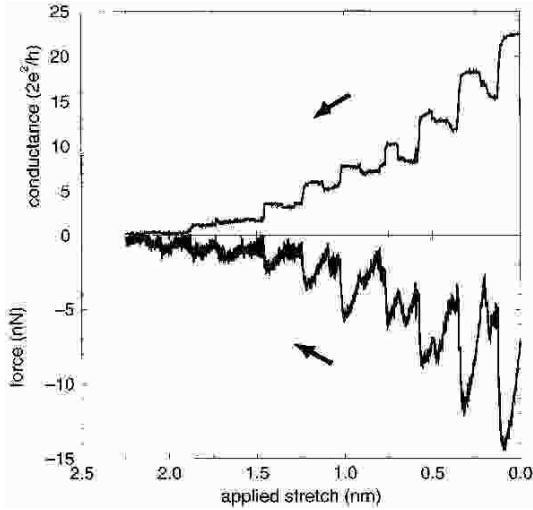


FIG. 47: The force and conductance throughout a dynamic simulation of the pull off of a Au contact at 1 K, with a pull-off rate of 4.08 m/s. Reprinted with permission from [271]. Copyright 1996 American Physical Society.

experimental results were not widely available.

Later, Todorov and Sutton [271] found a correlation between the force applied to the contact and the conductance jumps, as shown in Fig. 47, in good agreement with the experimental observations [37, 91]. Brandbyge *et al.* [198] analyzed the conductance of realistic contacts in terms of transmission eigenchannels. They found that, except for the smallest contacts ($1-3 G_0$), there are several partially open channels due to scattering in the constriction. That is, conductance quantization is lost above about $3 G_0$. The effect of crystalline orientation, and temperature was considered by Mehrez *et al.* [272, 273].

Landman *et al.* [75, 250] studied the atomistic mechanisms of deformation in relatively large constrictions, their results explain the ‘reversibility’ of plastic deformation observed experimentally [28, 261]. Sørensen *et al.* [274] also studied larger contacts and considering the effect of crystalline orientation on the deformation and fracture processes.

Barnett and Landman [275] and Nakamura *et al.* [211] used *ab initio* MD to simulate the breaking of a sodium wire. For Al atomic contacts the jump-to-contact has been simulated by [276]. The mechanisms of formation, evolution and breaking of atomically thin gold nanowires have been recently investigated using classical MD simulations by Rubio-Bollinger *et al.* [93] and tight-binding MD simulations by da Silva *et al.* [277].

1. Principles of MD simulations

Molecular dynamics (MD) simulations consist of the modeling of the motion of the individual atoms or molecules within a system of interacting species. The en-

ergetics and dynamics of the atoms are obtained from interaction potentials from which the Newtonian forces experienced by these atoms are derived. In *ab initio* or first principles methods the evaluation of the potential energy is obtained from a quantum-mechanical description of the system, and is limited, at present, to systems with a small number of atoms and relatively short simulation times due to computational demands. In contrast, the empirical and semi-empirical potentials used in conventional MD simulations make it possible to simulate much larger systems for much longer times. In between first principles and empirical methods is the tight-binding molecular dynamics (TBMD) method [278], which is more accurate than empirical potential methods because it explicitly includes the electronic structure and much faster than first principles methods.

Conventional MD simulations use phenomenological inter-atomic potentials to model the energetics and dynamics of the system. Although simple pair potentials of the Lennard-Jones type have been used [23], an accurate description of metallic systems requires more complex potentials that include many-body interactions. These potentials contain the physics of the model systems and their functional form is selected on the basis of theoretical considerations and are typically fitted to a number of experimental or theoretically calculated data.

The embedded atom method (EAM) [279] and effective medium theory (EMT) [280] potentials derived from density functional theory (DFT) in its quasi-atom [281] or effective medium [282] versions are often used to model metallic systems. In these models the potential energy of the system is written as a sum of a short-range pair-interaction repulsion, and an embedding energy for placing an atom in the electron density of all the other atoms:

$$E_{\text{pot}} = \sum_i F_i[\rho_{h,i}] + \frac{1}{2} \sum_i \sum_{j \neq i} V_{ij}(r_{ij}), \quad (93)$$

where $V_{ij}(r_{ij})$ is a two-body potential which depends on the distance r_{ij} between atoms i and j , and $F_i[\rho_{h,i}]$ is the *embedding energy* for placing an atom at position i , where the host electron density due to the rest of the atoms in the system is $\rho_{h,i}$. The latter is given by

$$\rho_{h,i} = \sum_{j \neq i} \rho(r_{ij}), \quad (94)$$

$\rho(r_{ij})$ being the ‘atomic density’ function. The first term in Eq. (93) represents, in an approximate manner, the many-body interactions in the system. These potentials provide a computationally efficient approximate description of bonding in metallic systems, and have been used with significant success in different studies [283].

Closely related are the Finnis-Sinclair (FS) potentials, which have a particularly simple form

$$E_{\text{pot}}^{\text{FS}} = \epsilon \left[\frac{1}{2} \sum_i \sum_{j \neq i} V(r_{ij}) - c \sum_i \sqrt{\rho_i} \right], \quad (95)$$

with $V(r_{ij}) = (a/r_{ij})^n$, and $\rho_i = \sum_{j \neq i} (a/r_{ij}^m)$, where a is normally taken to be the equilibrium lattice constant, m and n are positive integers with $n > m$, and ϵ is a parameter with the dimensions of energy. For a particular metal the potential is completely specified by the values of m and n , since the equilibrium lattice condition fixes the value of c . The square root form of the second term, which represents the cohesive many-body contribution to the energy, was motivated by an analogy with the second moment approximation to the tight binding model [283].

It must be emphasized that the applicability and predictive power of MD simulations using empirical potentials is limited in circumstances where the system evolves into regions of configuration space not covered by the fitted data. That is, potentials fitted to bulk properties may not be adequate to describe low-coordinated systems such as surfaces or clusters or, in particular, atomic-sized contacts. An improvement to this situation consists in expanding the database used for the fitting to include a set of atomic configurations calculated by *ab initio* methods. This set may include not only three-dimensional crystals with different lattice parameters but also slabs, layers and atomic chains [284].

2. Implementation of MD simulations

An MD simulation proceeds by constructing a finite portion of an infinite model system with any desired configuration in a primary computational cell. The cell is replicated generating periodic images of the system. This periodic boundary condition is introduced to remove the undesirable effects of the artificial surfaces associated with the finite size of the simulated system. In MD simulations of atomic-sized contacts the periodic boundary conditions have been applied either along all three sides of the computational cell [23], or only parallel to the contact, keeping static several atomic layers on the top and bottom of the computational cell and using them as grips [22]. In the first case, all atoms are treated dynamically, but cells above and below the contact are in mechanical contact. In the second case, only a two-dimensionally periodic array of contacts is modeled, but two artificial interfaces in each cell between dynamic and static atoms are introduced.

The equations of motion are integrated via the velocity Verlet algorithm or predictor-corrector algorithms, with time steps varying from 1 fs [277] to 100 fs [272]. Constant temperature is imposed by controlling the average temperature by means of an adequate thermostat, which can be applied to all the atoms in the cell or, in the case where there are static layers, just to the deepest dynamic layer.

Three different geometries have been used in MD simulations of nanocontacts. A tip that is lowered into contact with a slab and then is pulled off [22, 23, 73, 76, 269, 271, 285, 286, 287, 288], a neck that is either pulled off [76, 270, 274], or elongated and compressed [250], and a

nanowire that is pulled off [31, 228, 277].

The displacement of the tip with respect to the substrate, or elongation and contraction of the constriction, is simulated by either varying uniformly the height of the periodic cell or rigidly displacing the grip layers. The speed of increment or decrement of the height of the computational cell ranged from 0.004 m/s [272, 273] to 60 m/s [269]. These speeds, although well below the speed of sound in the material (of the order of 10^3 m/s), are several orders of magnitude higher than the speeds attained in STM and MCBJ experiments of contact formation and fracture which are in the range of 10^{-10} and 10^{-7} m/s, and may be too fast to take into account diffusive, thermally activated motion (see below).

The validity of the MD simulations for the interpretation of real life experiments must be carefully evaluated due to the enormous difference in time scales [271, 289]. In an experiment there can be different relaxation mechanisms, spanning a wide range of time scales. As the strain rate is decreased, or the temperature raised, slower relaxation processes, like collective relaxation processes, come into play resulting in differences in the mechanical evolution of the contact as put in evidence by performing the same simulation at different rates [271, 272]. This could be particularly important in the evolution of the shape of the neck in the final stages of the pull off.

3. Calculation of conductance in atomistic MD models

The calculation of the conductance in a MD simulation of atomic contacts is essential for comparison with the experimental results, since in most of the experiments only the conductance is measured. One possibility is to use a tight-binding (TB) model (see Sect. VII C) to calculate the conductance of a given atomic configuration using the atomic coordinates generated by the classical MD simulations. This method has been used to study the formation and fracture of Ir [269] and Au [271] contacts, and of the elongation and fracture of a Ni constriction [270]. These calculations only utilize one atomic orbital (1s) and consequently do not represent the electronic structure of the metals accurately, however, the method enables a sufficiently rapid calculation of the conductance to be made, in which the positions of all the atoms within the contact are taken into account explicitly.

Another possibility to calculate the conductance in an MD simulation is to use a free electron (FE) model (Sects. VII B 1). In the FE methods the internal structure of the constriction is replaced by a free electron jellium in a hard-wall potential defined by the positions of the atoms obtained from classical MD. This leaves out the effects of the ionic disorder which may be present in real contacts. The constriction potential profile is constructed by putting solid spheres with the Wigner-Seitz radius at the atomic positions obtained from the MD simulations [270] or by overlapping the free atom electron densities and calculating the effective one-electron

potential in the local density approximation (LDA) [76]. Once the hard-wall boundary is defined the free-electron cross section along the constriction is determined, and a smoother axisymmetric [270] or rectangular [76] equivalent profile is defined. The Schrödinger equation in this profile is solved exactly including interchannel scattering [270] or approximately neglecting interchannel scattering [76] to obtain the transmission probabilities of the different modes. The boundary roughness can be treated perturbatively [270]. An earlier, rather too simplified approach was adopted by Olesen *et al.* [31] who assumed that the constriction was adiabatic and, consequently, transmission channels would be either totally open or closed.

Comparison between TB and FE results [270], show that the conductance is roughly the same in both cases but the detailed structure is rather different. An important difference between TB and FE calculations is that in the FE model the conductance is determined solely by the profile of the contact, while in the TB model the conductance depends on the precise atomic structure of the contact. This difference becomes particularly important in situations where the contact develops structural defects [270].

Scattering due to internal disorder can be also taken into account in FE models. Brandbyge *et al.* [290] and Sørensen *et al.* [274] rather than using a hard-wall potential for the constriction, considered a one-electron potential generated from the atomic coordinates by constructing the electronic density as a sum of free-atom electron densities. The potential is then generated from the density using the local density approximation (LDA). The macroscopic electrodes are described by a free-electron model and join the contact in a smooth manner. This potential is not self-consistent but gives a good description of the corrugation near the boundary. The quantum transmission of electrons through the three-dimensional potential is calculated using a numerical exact, recursive multichannel method [198]. A similar approach is followed by Mehrez *et al.* [272, 273]. However, these authors axisymmetrize the potential and use the transfer matrix method to calculate the conductance.

In the case of larger contacts an estimate of the conductance of a contact can be obtained from the contact radius using a semiclassical modification of Sharvin's expression [210] (see Sect. VII B 2).

4. Results for simple metals

Several questions have been elucidated by the classical MD simulations of atomic scale contacts, namely, the mechanisms of contact formation and fracture for homogeneous and heterogeneous contacts; the mechanism of plastic deformation for small and relatively large contacts; and the conductance of realistic atomic contacts and its relation with the plastic deformation processes. We will discuss neither one-atom contacts nor atomic

chains since classical MD simulations are not reliable in situations where metallic atoms have low coordination.

Contact formation between the approaching surfaces of tip and sample is associated with an atomic-scale instability which causes the atoms of the interfacial region to irreversibly jump to contact at a distance of a few angstroms, in a short time span of ~ 1 ps (compare to the experimental results in Sect. V B). Further advance of the tip results in the onset of plastic deformation. Separating the tip and sample leads to ductile deformation of the contact, producing an atomic-sized constriction or neck, which eventually fractures. The mechanism of elongation of this constriction consists of a sequence of brief atomic structural rearrangements during which the constriction disorders and re-orders with the introduction of a new atomic layer. In between these rearrangements, which occur when the contact becomes mechanically unstable due to stress accumulation, the contact deforms elastically. This mechanism of plastic deformation seems to be a feature of atomic-sized metallic contacts. This was shown in the MD simulations of the Au/Ni system by Landman *et al.* [22, 285] using EAM potentials. Qualitatively similar results were obtained by Sutton and Pethica [23] using a Lennard-Jones pair potential.

In the case of contacts between different metals most of the plastic deformation takes place in the softest metal [22, 283, 285]. In the process of contact formation, most of the jump-to-contact is due to the atoms of the softer metal, irrespective of their being part of the tip or substrate. As the tip continues advancing beyond this point, a hard tip will indent a soft substrate, whereas a soft tip will flatten against a hard substrate. If the softest metal wets the hardest metal, the atomic sized constriction that forms upon retraction consists solely of the softest metal atoms. After fracture a patch of the softest metal atoms remains on the hardest metal surface.

Atomic scale contacts show very high yield strengths. For Au contacts, Landman and collaborators [22, 285] obtained maximum pressures of the order of 10 GPa both under tensile and compressive stress, which implies shear strengths even larger than the theoretical value for bulk Au in the absence of dislocations [255].

New mechanisms of deformation are revealed in simulations with larger constrictions. In these simulations, the initial state of the simulation is a constriction cut from a perfect crystal in a given orientation. Initially, the atomic positions are fully relaxed for a certain interval of time. As the contact is stretched, the constriction deforms via a succession of alternating stress accumulation and relief stages, during which it undergoes inelastic structural transformations. In the case of fcc metals, like Au, and Ni, these transformations consist preferentially of slip in one or several closed-packed $\{111\}$ planes [250, 270, 274]. When slip occurs in several nonparallel planes, defects and some local disorder can be introduced. When disordered regions are present, the subsequent deformation mechanisms tend to involve the atoms in these regions, thereby changing the atomic structure and, in

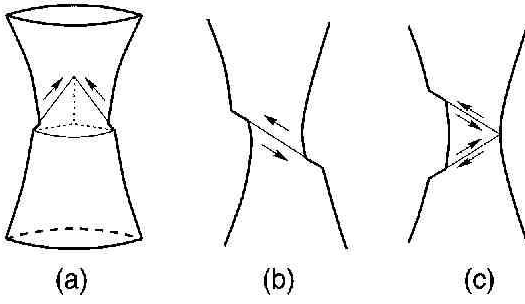


FIG. 48: Schematic illustration of selected slip processes. (a) A three plane slip. (b) A simple single-plane slip. (c) A slip in two nonparallel slip planes. Reprinted with permission from [274]. Copyright 1998 American Physical Society.

general, reducing the amount of disorder. In this way disorder often anneals out during the elongation process. The zone involved in the structural transformations, i.e. the *active zone*, extends over many atomic layers in the contact, and is not limited to the narrowest cross section [274]. Two distinct mechanisms for slip have been identified. For relatively large constrictions, slip occurs via glide of a dislocation nucleated at the surface of the contact [250, 270, 271, 274]. Typically, the dislocation is dissociated into Shockley partials, which glide completely across the constriction in a structural rearrangement, producing a stacking fault. The second partial could glide through the same path in a subsequent rearrangement and remove the stacking fault. For thinner constrictions slip is a homogeneous shear of one plane of atoms over another plane of atoms [274]. In this case the slip is also dissociated into partials. Sørensen *et al.* find that in their simulations the crossover between these two mechanisms takes place at contact diameters around 15 Å [274]. However, dislocation glide has also been described by Bratkovsky *et al.* [270] in smaller diameters. Probably not only the diameter but also the aspect ratio of the constriction and the type of metal play a role.

Deformation of constrictions with different crystalline orientations differ substantially due to the different orientation of the slip planes [272, 274]. In the fcc structure, there are four sets of $\{111\}$ planes, which lie parallel to the sides of a regular tetrahedron. For a constriction oriented in the $[111]$ direction, one set of these planes is perpendicular to the constriction axis. The other three are inclined with respect to this axis, and they are the active planes in which slip can occur to relieve stress. These three active slip planes are equivalent and a three-plane slip is possible (see Fig. 48). For a constriction oriented in the $[110]$ direction, two sets of close-packed $\{111\}$ planes lie parallel to the axis and are, consequently, inactive. In contrast, for a constriction oriented in the $[100]$ direction all four sets of slip planes are active. Formation of an atomic chain before rupture also seems to depend on the crystalline orientation, being more likely, in the case of Au, in contacts oriented in the $[100]$ direction [274].

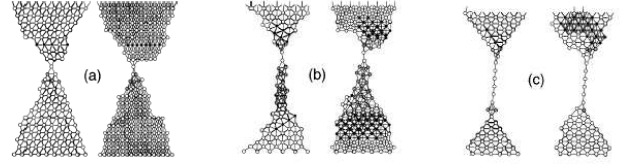


FIG. 49: Snapshots of atomic configurations from MD simulations of Au contacts. The pictures show, from two different viewpoints, the final configuration just before rupture of three different contacts; (a) Au[111], (b) Au[110], and (c) Au[100]. Reprinted with permission from [274]. Copyright 1998 American Physical Society.

Due to the possibility of having a large number of active glide planes in various regions, the separation between force relaxations may be quite irregular [250, 274]. In contrast, as the wire thins down stresses concentrate on the narrowest region and the number of active glide planes decreases, resulting in a more regular pattern [272].

This slip mechanism explains the reversibility of plastic deformation [250], observed experimentally for elongation-contraction cycles in relatively large contacts. In the experiments the contact could go over and over again through the same sequence of conductance steps, the traces of the successive cycles superposing almost exactly [28, 261]. In the simulation by Landman *et al.* [250], similar stress accumulation and relief mechanisms, and atomic structural rearrangement processes, including glide, occur during both extension and compression of the contact. Overall mechanical and structural reversibility is observed, but equivalent configurations may differ in the position of some atoms.

In the last stages of elongation of a large constriction, as it becomes relatively thin, the nature of the deformation changes. The process in this regime involves localized atomic rearrangements similar to those described for small constrictions [250, 270, 272, 274]. Depending on their crystalline orientation, contacts may become permanently disordered in the narrowest region for the last part of the elongation until rupture of the contact (see Fig. 49).

As in the case of small constrictions the maximum axial stress before yield (the yield strength) is very high. It depends on the precise atomic configuration, and for Au it is in the range 3–6 GPa [75, 274]. This value, as mentioned above, is of the order of magnitude expected for bulk Au in the absence of dislocations. The mechanical ideal nature of the nanowires can be related to their characteristic small dimensions and the inability to support dislocation sources.

MD simulations show qualitative differences in the fracture behavior for different materials [274]. Contacts of Au tend to be longer and smoother in the central region than Ni contacts. Ni contacts often break at a cross section of two atoms or more which is seldom observed in Au contacts. Quantitatively, differences are those to be

expected from the difference in macroscopic properties. The yield strength for Ni is found to be 10–20 GPa, while for Au it is 4–6 GPa.

Higher temperatures [270, 272, 274] and lower deformation rates [271, 272] favor a higher degree of crystallinity during the process of elongation. Disordered contacts are found to be not only weaker than well-ordered contacts of similar thickness but can also be pulled longer and thinner than ordered contacts in the last part of the elongation. As a consequence, lower temperature and higher pulling rate favors longer contacts.

Note that these pulling rates are still at least 5 and 3 orders of magnitude faster than the experiments. This indicates that the real structure could be more ordered than those observed in the simulations. As remarked above, the observed phenomena in the MD simulations must be interpreted with some caution, since phenomena on a longer time scale, inaccessible to the simulation, could play a role in the deformation of atomic contacts. For example, the contact could disorder in an atomic rearrangement, and have insufficient time to reorder before the next rearrangement. For a given volume of disordered material the time taken to reorder will decrease with increasing temperature up to the melting point. However, simulations performed at different temperatures offer, at best, only a qualitative idea of the effect of temperature. A process that occurs in an experiment at a given temperature might not take place in a MD simulation at the same temperature as, for instance, diffusion processes may be inaccessible.

The effect of the compliance of the setup has been considered by Brandbyge *et al.* [290] and Sørensen *et al.* [274]. A high compliance can arise from a soft cantilever or the compliance of the macroscopic wires (say, a sharpened tip). As a result new mechanical instabilities appear, which prevent some atomic configurations to be probed during the experiment. Conductance plateaus become flatter and the jumps in the conductance or force are more pronounced. Well-ordered contact structures, which are relatively strong, will tend to be probed rather than weaker disordered configurations.

As we will see below in Sect. VII B 1, transport through an adiabatic constriction (one that varies sufficiently smoothly) is quantized, in the sense that transmission eigenchannels are either open or closed. The results of the MD simulations show that mechanically drawn metallic constrictions are, in general, non-adiabatic and, although quite crystalline, can have a number of defects, like surface rugosity, stacking faults, vacancies, and local disorder. These defects cause backscattering that can easily perturb the conductance quantization [76, 270, 290]. Brandbyge *et al.* [290] analyzed the conductance of Au contacts resulting from MD simulations in terms of transmission eigenchannels, and found that, except for the smallest contacts (one or two atoms), several eigenchannels were partially open, and the conductance had steps at non-integer values of $2e^2/h$. Due to the irregularities in the contact the conductance is not always controlled

by the narrowest cross section, as would be the case for smooth contacts. Bratkovsky *et al.* [270] found that higher temperatures favored more regular constrictions and, consequently, the observation of a quantized conductance. The effect of the temperature on conductance histograms was considered by Hasmy *et al.* [228] by simulating cross-section histograms at 4, 300 and 450 K.

It is now well-established from the results of numerous MD simulations with realistic parameters that the abrupt jumps in the conductance are the result of sudden structural atomic rearrangements leading to stress relaxation [76, 269, 270, 271, 272, 274, 290]. As a consequence, jumps in the force and conductance generally coincide with each other [271, 274, 290]. The variations of the narrowest cross section do not always coincide with the conductance jumps [270], but this is not surprising since the conductance does not depend exclusively on the narrowest cross section of the contact. Occasionally atomic rearrangements occur far from the narrowest part, specially when the constriction is long, which cause a mechanical relaxation and only a small change in the conductance.

B. Free-electron gas conductance and force models

In this section we will consider the free-electron (FE) models of atomic contacts. The free electron approximation has proven its value for the calculation of various properties of metals. It works best for simple, monovalent metals, in particular the alkali metals, for which the Fermi surface is nearly spherical. In FE models of atomic contacts electrons move freely in a confining potential, which consists of wide (bulk) regions separated by a more or less abrupt constriction whose dimension is of the order of the wavelength of the electrons. In most cases the electrons are considered independent, that is, the electron-electron interaction is neglected. The only effect of the positive ions is to create a uniform positive charge background that confines the electrons. One is interested in the electronic properties of this system as the shape of the constriction is varied smoothly in an arbitrary but prescribed way. The lateral electronic confinement leads to the quantization of the electronic spectrum with the formation of subbands, and under certain circumstances to the quantization of the conductance. Electronic cohesion, thermoelectric effects, noise properties and magnetic effects have also been studied in the FE approximation. These FE models are useful and instructive as they permit the study of electronic effects without unnecessary complications. Nevertheless, they have a fundamental deficiency: the atomic nature of metals is completely ignored in the FE models. This is particularly relevant when the mechanical properties of the material are considered. Indeed, the mechanical response of materials involves structural changes through displacement and discrete rearrangement of the atoms, as we have seen in the previous section. As a consequence, interpretation

of experimental results exclusively in terms of FE models can lead to serious errors. Note that, in the experiments, the variation in the shape of a metallic contact is, in fact, a mechanical process, and since the atomic dimensions in metals are of the order of the Fermi wavelength, variations in the shape of the constriction cannot be smooth. These more realistic effects can be taken into account by obtaining the shape of the confining potential from an MD calculation as was discussed above.

1. Conductance calculations: conditions for the quantization of the conductance

As a first simplified model of a contact or constriction we may consider a uniform cylindrical wire of radius R and length L , with free and independent electrons connected to two bulk reservoirs [209]. We have to solve Schrödinger's equation,

$$-\frac{\hbar^2}{2m^*}\nabla^2\psi(\mathbf{r}) = E\psi(\mathbf{r}), \quad (96)$$

with the boundary condition $\psi[r = R] = 0$. In this coordinate system and for these boundary conditions the Schrödinger equation is separable, and the eigenstates are given by

$$\psi_{mn}(r, \phi, z) = J_m(\gamma_{mn}r/R)e^{im\phi}e^{ikz}, \quad (97)$$

where the z coordinate is taken along the cylinder axis; $m = 0, \pm 1, \pm 2, \pm 3, \dots$, $n = 1, 2, 3, \dots$, are the quantum numbers; and γ_{mn} is the n -th zero of the Bessel function of order m , J_m . The energies of the eigenstates are

$$E_{mn}(k) = \frac{\hbar^2 k^2}{2m^*} + E_{mn}^c, \quad (98)$$

where

$$E_{mn}^c = \frac{\hbar^2}{2m^*} \frac{\gamma_{mn}^2}{R^2}. \quad (99)$$

Since $J_{-m}(r) = (-1)^m J_m(r)$, the states m and $-m$ are degenerate. The electron states are divided into a set of parabolic one-dimensional subbands. The bottom of each subband is located at an energy E_{mn}^c . The separation of these subbands increases as the radius of the cylinder decreases. Neglecting scattering from the connections to the reservoirs, the conductance of the wire is simply given by the number of subbands that cross the Fermi level, E_F , with each subband contributing $2e^2/h$ to the conductance (see Sect. III D). The conductance as a function of the diameter of the contact will show perfectly sharp steps, increasing by one unit at each zero of J_0 and by two units at each zero of any of the other Bessel functions [209]. In the limit of low voltage and low temperature, that is, $k_B T$ and eV much smaller than the subband splitting, the conductance will be *quantized* showing steps at $G_0, 3G_0, 5G_0, 6G_0, \dots$

A more realistic model for an atomic contact should take into consideration explicitly the connections with the electrodes. Consider a narrow axisymmetric constriction in a much larger wire whose axis is in the z -direction. The profile of the constriction is given by $R(z)$. Now we have to solve Schrödinger equation with the boundary condition $\psi[r = R(z)] = 0$. We find the solution by separating the lateral and the longitudinal motion of the electron [76, 291],

$$\psi(r, \phi, z) = \sum_{mn} \chi_{mn}(z) u_{mn}^z(r, \phi), \quad (100)$$

where $u_{mn}^z(r, \phi)$ is a solution of radial motion,

$$-\frac{\hbar^2}{2m^*} \left(\frac{\partial^2}{\partial r^2} + \frac{1}{r} \frac{\partial}{\partial r} + \frac{1}{r^2} \frac{\partial^2}{\partial \phi^2} \right) u_{mn}^z(r, \phi) = E_{mn}^c(z) u_{mn}^z(r, \phi), \quad (101)$$

with the boundary condition $u_{mn}^z[r = R(z)] = 0$, and has the following form:

$$u_{mn}^z(r, \phi) = \frac{1}{\sqrt{\pi} R(z) J_{m+1}(\gamma_{mn})} J_m(\gamma_{mn} r / R(z)) e^{im\phi}, \quad m = 0, \pm 1, \dots \quad (102)$$

Substituting this solution in Schrödinger equation, multiplying it by $u_{pq}^*(z)$, and integrating over r and ϕ at a given z , we obtain the following system of equations:

$$\left(-\frac{\hbar^2}{2m^*} \frac{d^2}{dz^2} + E_{mn}^c(z) \right) \chi_{mn}(z) + \sum_{pq} F_{mnpq} \chi_{pq}(z) = E \chi_{mn}(z), \quad (103)$$

where

$$E_{mn}^c(z) = \frac{\hbar^2}{2m^*} \left(\frac{\gamma_{mn}}{R(z)} \right)^2. \quad (104)$$

The operators F_{mnpq} which depend on dR/dz and d^2R/dz^2 couple the different solutions $\chi_{mn}(z)$. The system of differential equations in Eq. (103) can be solved exactly [291]. However, if the variation of R with z is sufficiently slow, the coupling between the different modes (*mode mixing*) can be neglected, and we are left with a one-dimensional Schrödinger equation for each pair of quantum numbers (m, n) with an effective potential barrier $E_{mn}^c(z)$ as depicted in Fig. 50. This is called the *adiabatic* approximation. The pair of quantum numbers (m, n) , describe the transverse motion, and define the individual *conductance channels*, which in this approximation are also eigenmodes of the wire without the constriction. In contrast, for contacts of arbitrary shape, the eigenchannels are given by linear combinations of the eigenmodes of the system without the constriction. The constriction *mixes* the different modes (mode mixing) as described in Sect. III D 2.

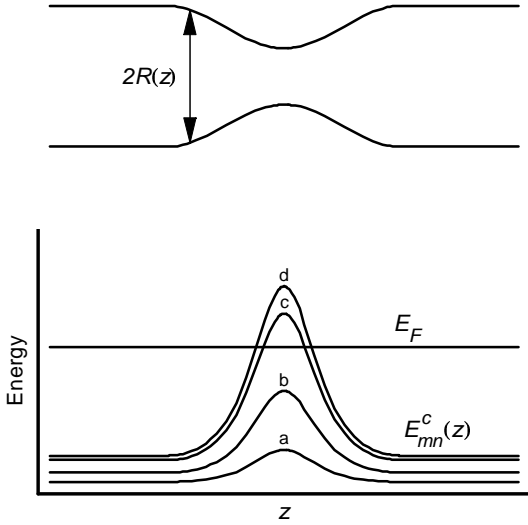


FIG. 50: Quantization in an adiabatic constriction. In a constriction with a slowly varying profile the electrons moving in the z direction see an effective potential energy $E_{mn}^c(z)$. The curves labeled a, b, c, and d correspond to the profiles of $E_{mn}^c(z)$ for (m, n) equal $(0, 2)$, $(2, 1)$, $(1, 1)$, and $(0, 1)$, respectively. Only modes with a barrier less than E_F contribute to the conductance.

In the adiabatic approximation, modes for which the maximum of the potential barrier $E_{mn}^c(z_0)$ falls below the Fermi energy E_F , will be perfectly transmitted and those for which it is above will be reflected. However, when E_F falls just below the maximum of the barrier part of the mode will be transmitted by tunneling through the barrier. When E_F falls just above the maximum of the barrier, part of the mode will be reflected due to the variation of the potential height (over-the-barrier scattering). Thus, the conductance, which is controlled by the minimal radius of the contact a_0 , will show steps, as in the case of the cylindrical constriction, but the steps will be somewhat smeared due to tunneling and over-the-barrier scattering. Only in the case of very long and slowly varying constrictions is this effect negligible.

The transition from adiabatic to non-adiabatic contact is elegantly illustrated in the calculation by Torres *et al.* [210]. These authors modeled the constriction as a hyperbola of revolution and calculated the conductance exactly using spheroidal oblate coordinates, taking advantage of the fact that in these coordinates Schrödinger's equation is separable. For small opening angles of the hyperbola, θ_0 , the constriction has an elongated shape that tends to a cylinder, whereas for $\theta_0 = \pi/2$, the model represents an infinitely thin barrier separating the two electrodes, pierced by a circular hole. Their results are shown in Fig. 51. The sharp steps obtained for a long cylindrical wire ($\theta_0 = 0$) gradually smear as θ_0 approaches $\pi/2$ as a consequence of tunneling and over-the-barrier scattering which become important as adiabaticity is lost. This shows that only in the case of adiabatic constrictions the

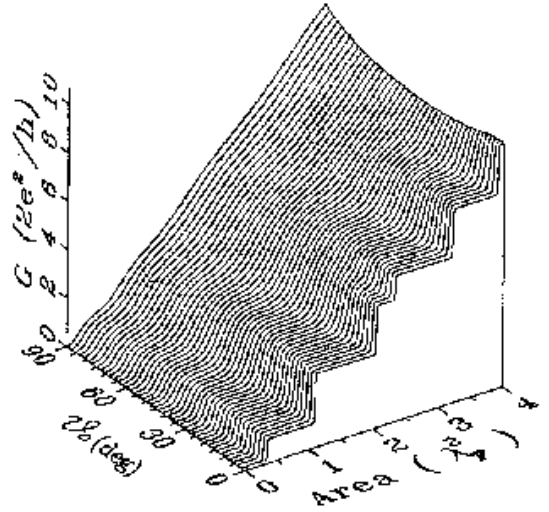


FIG. 51: Conductance of a quantum constriction modeled as a hyperbola of revolution, as a function of the area of the narrowest section and as a function of the opening angle θ_0 of the constriction. Reprinted with permission from [210]. Copyright 1994 American Physical Society.

conductance is strictly quantized, that is, transmission channels are either open or closed. For general geometries, several evanescent channels with transmissions less than one contribute to the conductance [292].

Contacts with cylindrical symmetry always have an orbital degeneracy of the wave functions, which results in steps of height $2G_0$ when a degenerate channel opens. This degeneracy is lifted when the constriction is not exactly symmetrical, and only conductance steps of height G_0 will be observable [291]. Modeling a constriction using a saddle point potential may result in steps with higher degeneracies which are also partially broken for non axisymmetric contacts [293].

Boundary roughness tends to suppress conductance quantization. This question has been addressed by Bratkovsky and Rashkeev [291] for axisymmetric contacts using a perturbative approach, and by Brandbyge *et al.* [198] for contacts with arbitrary shape using the recursion transfer-matrix method [294]. They found that the conductance steps shift downward, and for strong corrugations, resonances start to build up. In contrast, the effect of a localized scatterer within the constriction is to smear or close single steps selectively [198]. The reason is that the modes that have a node at the position of the scatterer will suffer less scattering. These factors suppress conductance quantization since there will be partially open modes. Nevertheless the stepped structure might still be observable though not at integer values of the conductance.

As we mentioned in Sect. VII A 3 the shape of the contacts obtained from MD simulations can be used to define a FE constriction and their evolution with plastic deformation [76, 270]. These calculations show plateaus in

the conductance but not always at integer values of the conductance. The correlation observed in the MD simulations [76, 270] between the changes in conductance and the atomic rearrangements in the contact show that the conductance plateaus are related to mechanically stable atomic configurations.

Now, we can summarize the circumstances under which conductance quantization can be observed within a FE model. Perfect quantization in a contact is only obtained when the contact, in addition to being ballistic, i.e. the length and diameter of the contact being shorter than the electron mean free path, is adiabatic, i.e. its cross section is a smooth function of the longitudinal coordinate. Surface roughness and internal defects cause backscattering that destroy conductance quantization. Additionally, all energies eV and $k_B T$ must be smaller than the subband splitting.

2. The relation between cross section and conductance: Corrections to Sharvin's formula

According to the semi-classical formula of Sharvin the conductance of a small contact is proportional to the area of the contact. This result is based on the proportionality of the number of modes, with energies smaller than a given value in a 2-dimensional system, to the area. However, in a finite system it is necessary to add corrections. Consider a 2-dimensional rectangular box, whose sides are a and b , and assume that the modes have zero amplitude at the boundary. The number of modes N with energies smaller than $E_F = \hbar^2 k_F^2 / 2m^*$ is given by the so-called Weyl expansion [295, 296, 297, 298]

$$N = \frac{k_F^2}{4\pi} ab - \frac{k_F}{2\pi} (a + b) + \frac{1}{4}, \quad (105)$$

where the second term arises because the modes with k_x or k_y equal to zero are not to be included. The third term appears because the mode $k_x = 0$ and $k_y = 0$ appears twice in the second term. For a general connected boundary without sharp corners having an area A and a perimeter P , the number of modes is given by [295]

$$N = \frac{k_F^2}{4\pi} A - \frac{k_F}{4\pi} P + \frac{1}{6}, \quad (106)$$

Note that the third term changes from $1/4$ to $1/6$. The semi-classical conductance, in the case of a uniform constriction with cross section A and perimeter P will be simply given by

$$G = \frac{2e^2}{h} N. \quad (107)$$

For an adiabatic constriction A and P correspond to the narrowest cross section. The quantum oscillations are superimposed to this smooth Sharvin conductance.

In the context of quantum point contacts this result was first noted by Sáenz and coworkers who found from

their exact quantum computation mentioned above [210], that the conductance of a circular point contact deviates from Sharvin's result. They observed that the perimeter correction (the second term in Eq. (106)) depends on the opening angle since for large opening angle the constriction is no longer adiabatic. Thus we may write

$$G \approx \frac{k_F^2}{4\pi} A - \alpha \frac{k_F}{2\pi} P. \quad (108)$$

In the limit of a circular hole (opening angle $\theta_0 = \pi/2$), $\alpha = 1/4$, while for an adiabatic constriction (opening angle $\theta_0 = 0$) $\alpha = 1/2$.

Another correction to the Sharvin conductance comes from the fact that, in a real metal, electrons are not so strongly confined [299, 300]. There will be a certain spill out of the wave functions that depends on the work function of the metal. The main influence of the 'soft wall' boundary condition is to increase the effective radius of the constriction relative to the 'hard wall' case. This spill out can be taken into account by using an effective radius $a_0 + \delta a_0$ for the constriction. For metals $k_F \delta a_0 = 0.72$ – 1.04 and $\alpha = 0.13$ – 0.025 [299].

3. Effect of magnetic fields

Scherbakov *et al.* [293] used a saddle-point potential to study the effect of a longitudinal magnetic field on the conductance. They found that for relatively weak magnetic fields (diameter of the constriction much smaller than the cyclotron radius), the conductance exhibits Aharonov-Bohm-type oscillations. This behavior transforms, in the strong field limit, into Shubnikov-de Haas oscillations with an Aharonov-Bohm fine structure. The magnetic fields necessary to observe these effects in small constrictions are quite high since they depend on the magnetic flux embraced by the contact. To observe the Aharonov-Bohm oscillations or the splitting of the thermopower peaks the magnetic flux through the contact area should be of the order of the flux quantum (hc/e), and much higher for the Shubnikov-de Haas oscillations. A reasonably high magnetic field is of the order of 10 T. This means that the area of the contact should be at least 100 nm^2 , which for a metal gives a conductance of the order of $1000 G_0$. In the case of a semimetal the situation is much better since the Fermi wavelength is much larger. For example, in bismuth such a large contact would have of the order of 2 channels.

Field effects have also been calculated for the thermoelectric properties [301] and for shot noise [291, 302], in the framework of FE models.

4. Nonlinear effects in the conductance

Although the validity of the scattering approach is limited to the linear regime due to the lack of self-consistency (see Sect. III D 5), one can still get a qualitative idea of

the effect of a finite voltage using the Landauer approach. Under finite voltage V electrons within an energy range eV around the Fermi level E_F contribute to the current. The current is then given by

$$I = \frac{2e}{h} \int_{E_F - eV/2}^{E_F + eV/2} \sum_n \tau_n(\epsilon, V) d\epsilon, \quad (109)$$

where $\tau_n(\epsilon, V)$ is the transmission probability of an electron with energy ϵ . Thus, the opening of new transmission channels will be gradual, i.e. a new channel will be opening while the bottom of the band traverses an interval eV around the Fermi energy, and the sharp steps in $G = I/V$ will be smeared [303].

For a symmetric contact, the differential conductance $g = dI/dV$ may be approximated by [234, 300, 303]

$$g(V) \approx \frac{2e^2}{h} \left(\frac{1}{2} \sum_n \tau_n \left(E_F + \frac{eV}{2}, 0 \right) + \frac{1}{2} \sum_n \tau_n \left(E_F - \frac{eV}{2}, 0 \right) \right). \quad (110)$$

Thus, g can be regarded as the average of two zero voltage conductances at different effective Fermi energies. As a consequence the plateaus at integer values of $2e^2/h$ evolve into half-integer values [234, 300, 303]. The sequence of values for these plateaus depends on the geometry of the contact. For a non-axisymmetric contact at voltages of the order of $0.2E_F/e$, there will be plateaus at half-integer and integer values of G_0 , while for contacts with cylindrical geometry the sequence is $0.5G_0, 1G_0, 2G_0, 3G_0, 4G_0, 4.5G_0, 5.5G_0, 6G_0, \dots$. For abrupt constrictions, nonadiabatic effects manifest themselves as an overall decrease of the conductance towards saturation at very high voltages [234].

The combined effect of a magnetic field and high bias voltage has been discussed by Bogachek *et al.* [300].

5. Simulation of conductance histograms

Conductance histograms are useful for presenting the experimental results on the evolution of the conductance of metallic contacts with size, due to the variability of the particular features in each experimental curve (see Sect. VD). In order to approach the experimental situation Sáenz and coworkers [292, 303] have introduced the use of histograms in model calculations. They assume a certain evolution of the contact area A and opening angle θ as a function of elongation d . The dependence of A on d is taken to be almost exponential, as observed for the last part of the elongation in the experiments [261, 262]. The qualitative results will not depend on the exact dependence, however. The actual evolution will result in a discrete set of points on a conductance curve $G(A(d), \theta(d))$. Assuming that the contact can take any cross section along this curve, a conductance

histogram is obtained. The histogram shows peaks at $1G_0, 2G_0, 3G_0, 4G_0, 5G_0, \dots$ for non-axisymmetric contacts and $1G_0, 3G_0, 5G_0, 6G_0, \dots$ for axisymmetric contacts. The peaks in the histogram become more smeared as the conductance increases, reflecting the fact the conductance does not show sharp steps for larger values of the opening angle. Thus, the quantum nature of transport manifests itself in the peaks of the histogram, but the conductance is not quantized as any value is possible.

In an earlier work [260] the evolution of the conductance was obtained from a mechanical slab model similar to that described in Sect. VIC. Histograms have been also used [303] to compare the nonlinear effects due to a large bias voltage with experimental results [109, 203].

6. Quantum effects in the thermodynamic potential

The free electron model assumes that the chemical potential is fixed by the electrodes and is constant as the wires change configuration. Calculations under these assumptions lead to a strong variation in the electron density within the wire as a result of ignoring the effect of electron screening. Following the discussion in [50], we consider a wire of constant cross section A and length L sufficiently long to neglect tunneling effects. We are also neglecting the effect of the non-adiabatic geometry. Electrons are assumed free and independent. Due to the quantization of the transverse degrees of freedom the electron states are divided in parabolic one-dimensional subbands. The density of states (DOS) $\eta(E)$ per unit volume in the wire is given by

$$\eta(E) = \frac{1}{A} \sum_{mn}^+ \sqrt{\frac{2m}{\hbar^2 \pi^2}} \frac{1}{\sqrt{E - E_{mn}^c}}. \quad (111)$$

For a cylindrical wire, E_{mn}^c was defined in Eq.(99); and for a wire of square cross section $W \times W$, $E_{mn}^c = (\hbar^2 \pi^2 / 2mW^2)(m^2 + n^2)$, where m and n are positive integers. The $+$ on the summation indicates that m and n run to the maximum value for which the argument of the square root is positive. The density of electrons in the wire is obtained by integration,

$$\eta(E) = \frac{2}{A} \sum_{mn}^+ \sqrt{\frac{2m}{\hbar^2 \pi^2}} \sqrt{E - E_{mn}^c}, \quad (112)$$

and density of the total (kinetic) energy E_{tot} can be found by integrating over the product of the DOS and the energy,

$$E_{\text{tot}} = \sum_{mn}^+ \frac{2L}{3} \sqrt{\frac{2m}{\hbar^2 \pi^2}} \sqrt{E - E_{mn}^c} (E_F + 2E_{mn}^c). \quad (113)$$

The DOS, total energy density, and density of electrons are plotted in Fig.52(a-c) for a wire of square cross section. As clearly shown in the figure, the total energy density and the electron density are much lower

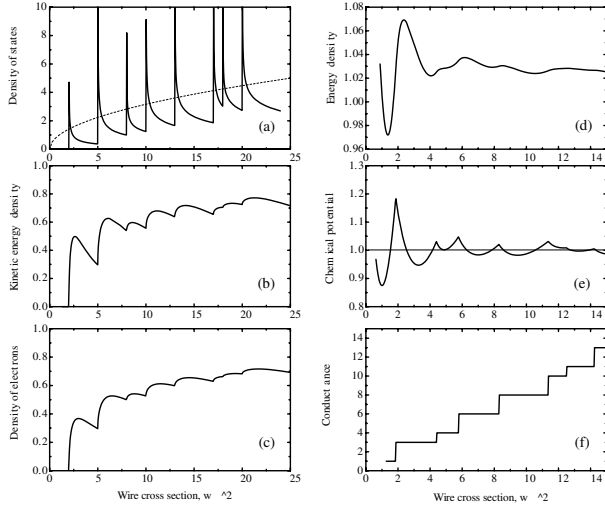


FIG. 52: Free electron calculations for a wire of square cross section $W \times W$. (a) DOS compared to the bulk (dashed curve) as a function of $w^2 = (2W/\lambda_F)^2$. (b) Total kinetic energy density. (c) Density of electrons, both normalized to the bulk value $\eta_0 = (k_F^3/3\pi^2)$. (d) Normalized total kinetic energy of the wire calculated while keeping the density of electrons constant by adjusting the chemical potential, shown in (e) in units of E_F . The cusps in the chemical potential are found at the steps in the conductance (f). Reprinted with permission from [50]. Copyright 1997 American Physical Society.

than the bulk values, with strong fluctuations as a function of the width. These low values result from the strong confinement imposed by the hard-wall potential and from the non-uniform distribution of states in momentum space, since states with $k_x = 0$ or $k_y = 0$ are excluded (Sect. VII B 2). The electron density must be normalized to $\eta'_0 = (k_F^3/3\pi^2)(1 - 3\lambda_F/4W' + 3\lambda_F^2/8\pi W'^2)$, where the second and third term are surface corrections, and the spill out of the wave function beyond the geometrical boundary is taken into account by taking a larger width $W' = W + \delta W$ [299]. This normalization causes the total energy density and electron density to fluctuate around the proper bulk limit.

These fluctuations from the bulk density are largest for small values of the width, the most dramatic consequence is that the electron density drops to zero when the last channel is closed, whereas in practice every atom will continue to be surrounded, on the average by one electron (assuming a monovalent metal). The screening in metals is very effective down to the scale $\sim 1\text{\AA}$, and the positive background charge density will tend to be almost exactly compensated. This screening effect can be taken into account by fixing the electron density, and allowing the chemical potential to vary. As a consequence, the width at which a new channel opens is considerably smaller than in the case when the chemical potential is maintained fixed. In fact, within the approximations of this model, the first channel opens for a width $w = 0$. This is unrealistic since the chemical potential cannot

be raised indefinitely. The difference between the bulk Fermi energy and the chemical potential in the wire is maintained by adjusting the electric potential of the wire with respect to the bulk by an amount $V = (\mu - \epsilon_F)/e$. These oscillations in the chemical potential would be reflected in the work function [50, 304]. Setting up this electrical potential difference between the wire and the bulk electrodes requires the formation of a charged dipole layer at the interfaces, in addition to the accumulation of some charge at the surface of the wire and the electrodes. The electrostatic energy involved needs to be taken into account in the evaluation of the total energy of the wire configuration, and it should be small compared to the total kinetic energy, otherwise we must accept that the electron density deviates from the bulk value. This electrostatic energy can be estimated as that of the capacitance of an isolated wire of length L , $C \approx 2\pi\epsilon_0 L$, and charged to a potential $V = (\mu - \epsilon_F)/e$. For the larger wire diameters this is a minor correction, but for the smaller diameters the charging energy cannot be ignored. At small diameters neither a constant electron density, nor a constant chemical potential is a good approximation, with the balance determined by the charging energy.

There are a number of other corrections to the energy, such as an increased spill out of the wave function for a higher chemical potential and a tendency for the charge to accumulate at the surface due to electron-electron repulsion, resulting in a nonhomogeneous density profile. Estimating such corrections goes beyond the validity of the model.

The conclusions from this simple model are in good agreement with more elaborate calculations that go beyond the free electron approximation. Yannouleas *et al.* [51, 305] solved the electronic structure of jellium wires using the so-called shell-correction method, which uses non-selfconsistent electronic structures from an extended Thomas-Fermi theory, but takes shell structure into account as a correction. This method is not selfconsistent but has been shown, in clusters, to yield results in excellent agreement with experiments and selfconsistent calculations. Zabala *et al.* [306] use the stabilized jellium model within spin-dependent density-functional theory in order to obtain a more realistic description which takes into account not only screening but also electron-electron interactions.

The presence of distinct local minima in the total energy (see Fig. 52) suggests that the formation of quantum modes in the contact has a significant influence in the stability of specific wire diameters. In contrast to calculations that ignore screening effects [49, 307], the minima of the energy do not coincide with the steps in the conductance, but are found on the plateaus. This suggests that the minima in the total energy may play a role in explaining the fact that quantized values of the conductance are more frequently observed in experiment, compared to non-quantized values [50]. Up to fairly large diameters this principle leads to the appearance of ‘magic’ wire configurations of enhanced stability, as will be discussed

more thoroughly in Sect. XII.

Another effect that is to be expected is a Jahn-Teller type of distortion that would lift the degeneracy of the modes and remove the double quantum steps [50]. No clear experimental evidence for this distortion has yet been reported.

7. Quantum effects in the force

The variations in the total energy as a function of wire diameter can be translated into a force acting in the longitudinal direction. If the chemical potential is assumed to be fixed at the Fermi energy for all wires configurations, the force can be obtained from the derivative of the thermodynamic potential $\Omega = E_{\text{tot}} - E_F N$ [49, 307, 308, 309, 310],

$$F = -\frac{d\Omega}{dL}. \quad (114)$$

However, as discussed in the previous section, this approach neglects the strong screening effect in metals. Assuming that the number of electrons is kept fixed by varying the electrochemical potential, the force will be given by [50]

$$F = -\frac{dE_{\text{tot}}}{dL}. \quad (115)$$

Again for the smallest contacts the truth will be somewhere in between, since screening will not be fully effective for short contacts and for contacts with a small number of channels [50, 310].

The total force during the elongation of a metallic nanocontact can be divided into a smooth component, due to the increase of surface area, and an oscillating component, which is of the order of E_F/λ_F (*universal force fluctuations*) [49, 311]. The oscillating component is correlated with the conductance, presenting sharp local minima (taking elongational forces as negative) at the locations of the step-rises in the conductance [49, 307]. Qualitatively, each quantized mode contributing $2e^2/h$ to the conductance of the nanowire also contributes an amount of order E_F/λ_F to the cohesive force. Similar results are obtained using the shell-correction method [51, 305] and the self-consistent stabilized jellium model [306].

The magnitude of the force oscillations is similar to the magnitude of the forces observed experimentally [37], and it has been suggested [49] that the abrupt atomic rearrangements observed during deformation of metallic contacts may be caused by the breaking of extended metallic bonds formed by each conductance channel. In spite of the fact that the discreteness of the ionic background is neglected, these free electron models clearly show the role played by conduction electrons in the mechanical properties of mesoscopic systems. This approach is complementary to molecular dynamics simulations, where the

atomic arrangements are followed in detail, while the effects of conduction electrons is taken into account only in an averaged way [49, 309]. The effect of disorder [308, 309] and charge fluctuations [310] have also been studied using the scattering matrix approach introduced by Stafford and coworkers [308].

C. Tight-binding models for the conductance

Tight-binding models provide a simple description of electron states in solids that can be considered as complementary to the FE models. Instead of using plane waves as a starting point, TB models are based on localized orbitals. TB models were originally developed to describe the bands arising from tightly bound *d* or *f* valence orbitals in transition metals. There exist, however, several parameterization schemes which allow describing the bands in *sp*-like metals rather accurately using these type of models. TB models can also be regarded as a discretization of the Schrödinger equation which allows studying the electron states in non-homogeneous systems of arbitrary geometry.

In its simplest version, the TB model uses an orthogonal basis $\{|i\rangle\}$ corresponding to a spherically symmetric local orbital at each atomic site in the system. Within this basis, the model Hamiltonian adopts the form

$$\hat{H} = \sum_i \epsilon_i |i\rangle\langle i| + \sum_{i \neq j} t_{ij} |i\rangle\langle j|, \quad (116)$$

where the ϵ_i correspond to the site energies and t_{ij} denote the hopping elements between sites *i* and *j*, which are usually assumed to be non-zero only between nearest neighbors.

Within these models, electronic and transport properties are conveniently analyzed in terms of Green function techniques. The retarded and advanced Green operators are formally defined as

$$\hat{G}^{r,a}(\omega) = \lim_{\eta \rightarrow 0} [\omega \pm i\eta - \hat{H}]^{-1}. \quad (117)$$

The matrix elements of $\hat{G}^{r,a}(\omega)$ are directly related to the local densities of states (LDOS) by

$$\rho_i(\omega) = \mp \frac{1}{\pi} \text{Im} \langle i | \hat{G}^{r,a}(\omega) | j \rangle. \quad (118)$$

In order to study the conductance of a finite system described by a tight-binding Hamiltonian one may consider the geometry depicted in Fig. 53 in which a central region of atomic dimensions is connected to two semi-infinite systems playing the role of current leads. The total Hamiltonian for this system can be decomposed as $\hat{H} = \hat{H}_L + \hat{H}_R + \hat{H}_C + (\hat{V}_{L,C} + \hat{V}_{C,R} + h.c.)$, where $\hat{H}_{L,R}$ describe the electronic states in the uncoupled left and right leads, \hat{H}_C corresponds to the central region and the

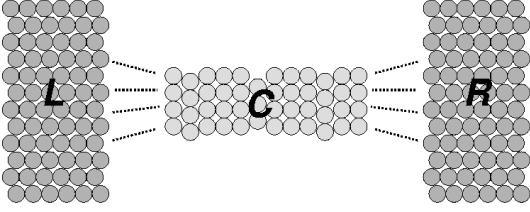


FIG. 53: Typical geometry for conductance calculations of atomic-sized conductors using TB models

$\hat{V}_{\alpha,\beta}$ terms describe the coupling between the central region and the left and right leads. The zero-temperature linear conductance is given in terms of Greens functions by the following expression

$$G = \frac{8e^2}{h} \text{Tr} \left[\text{Im} \hat{\Sigma}_L^a(E_F) \hat{G}_C^a(E_F) \text{Im} \hat{\Sigma}_R^a(E_F) \hat{G}_C^r(E_F) \right], \quad (119)$$

where $\hat{\Sigma}_{\alpha}^{r,a} = \lim_{\eta \rightarrow 0} \hat{V}_{\alpha,C} \left[\omega \pm i\eta - \hat{H}_{\alpha} \right]^{-1} \hat{V}_{C,\alpha}$ (with $\alpha = L, R$) are self-energy operators introducing the effects on the dynamics of the electrons in the central region due to the coupling with the leads, and $\hat{G}_C^{r,a}$ are the Green operators projected on the central region.

Different versions of Eq. (119) have been derived by many different authors using different approaches [269, 312, 313]. This expression is in fact similar to the one derived using linear response theory in Sect. III E 1. However, it does not rely on the assumption of ideal leads used in that case. For more technical details the reader may consult Ref. [111]. By using the cyclic property of the trace, the expression (119) can be written in the usual form $G = (2e^2/h) \text{Tr}[\hat{t}(E_F) \hat{t}^\dagger(E_F)]$, where [46]

$$\hat{t}(E) = 2 \left[\text{Im} \hat{\Sigma}_L^a(E_F) \right]^{1/2} \hat{G}_C^r(E) \left[\text{Im} \hat{\Sigma}_R^a(E_F) \right]^{1/2}.$$

The existence of $\left[\text{Im} \hat{\Sigma}_{L,R}^a(E_F) \right]^{1/2}$ is warranted by $\text{Im} \hat{\Sigma}_{L,R}^a(E_F)$ being positive definite matrices. The knowledge of the $\hat{t}\hat{t}^\dagger$ matrix in terms of Green functions allows determining the conduction channels for a given contact geometry, as will be discussed below.

1. Results for simple model geometries

TB models allow obtaining some analytical results for the conductance in certain limiting cases. Martín-Rodero *et al.* [17, 314] developed a model for the transition from tunneling to contact between a STM tip and metallic sample for which the conductance is given by

$$G = \frac{8e^2}{h} \frac{\pi^2 T^2 \rho_1^0 \rho_2^0}{|1 + \pi^2 T^2 \rho_1^0 \rho_2^0|^2}, \quad (120)$$

where T is the hopping element between the tip apex atom and the nearest atom on the sample surface, and

$\rho_{1,2}^0$ is the unperturbed local densities of states on these two sites. This expression predicts that the conductance quantum is reached when $\pi^2 T^2 \rho_1^0 \rho_2^0 \simeq 1$, a condition that is approximately fulfilled when using parameters appropriate for simple metals.

Todorov *et al.* [269] analyzed the conductance for a single atom between two semi-infinite fcc crystals cut along their (111) planes using a tight-binding model with one $1s$ orbital per site. They found that the conductance reaches the maximum value $2e^2/h$ for half-filled band when the atom is connected to the three first neighbors on each surface with the same hopping element as in the bulk crystal.

The conductance for model geometries of single-atom contacts have also been analyzed using more realistic TB models including several orbitals per atom in order to account for s , p and d bands in simple and transition metals. Sirvent *et al.* [71] studied in this way the influence of d orbitals in the conductance of Au, Ni and Pt. They used two types of model geometries: one in which a single atom is at the center of a small cluster having a threefold or a fourfold symmetry; and one in which they replaced the central atom by two atoms along the symmetry axis of the cluster. In both cases the semi-infinite leads were simulated by Bethe lattices attached to the outermost sites of the cluster. They showed that Ni and Pt clusters exhibit a larger conductance than the corresponding Au clusters for all the geometries considered. While in the case of Ni and Pt the obtained conductance values ranged from G_0 to $3G_0$, in the case of Au these values were in general smaller than G_0 . These differences have been attributed to the contribution of d orbitals in transition metals which provide additional channels for conduction [71].

2. Electron-electron interactions and the charge neutrality condition

One question which was still open at that time was the strong tendency to quantized values in first steps of the experimental conductance traces for monovalent metals like Au, Ag or Cu. In FE models, one can adjust the contact cross section and the electron density according to the type of atom in order to get nearly perfect quantization for simple metals [76, 260]. However, these results depend critically on the ratio between the Fermi wavelength and the contact diameter. In the case of TB models, conductance quantization is harder to obtain using realistic models for the contact atomic structure [270]. The issue of the apparent robustness of conductance quantization in experiments on atomic contacts of monovalent metals was addressed in [315] using TB models in combination with model geometries for the atomic structure. A fundamental difference with previous TB or FE calculations was the inclusion of the charge neutrality condition which provides a simple way to account for electron-electron interactions in the neck region.

The assumption of local charge neutrality is reasonable for metallic systems with a screening length comparable to interatomic distances [130], as was also pointed out in the context of FE models in VII B 6. Within a TB model this is achieved by a self-consistent variation the diagonal elements of the Hamiltonian at each site in the contact region [315]. The charge neutrality condition provides thus a certain consistency between the Hamiltonian parameters and the contact geometry.

In the first part of [315] it was shown that sharp tips modeled by pyramids grown along different crystallographic axis on a fcc lattice exhibit narrow resonances in their LDOS. They showed that these resonances become very sharp for tips grown along the (111) axis while broader resonances are obtained for the (100) direction. When forming a contact by connecting two of these pyramids by a central common atom the resonances still survive and tend to be pinned at the Fermi level due to the charge neutrality condition. The conductance for such a situation can be approximated by the expression $G \simeq \frac{8e^2}{h} \frac{x}{(1+x)^2}$, where $x = \text{Im}[\Sigma_R(E_F)]/\text{Im}[\Sigma_L(E_F)]$ measures the asymmetry between the left and right sides of the contact. The conductance quantization due to this resonance mechanism is thus very robust to fluctuations in the atomic positions: even with $x \sim 2$ one still obtains $G \simeq 1.8e^2/h$, i.e. 90% of the quantum unit.

Recently, Kirchner *et al.* [316] have proposed a sum rule that would allow to include electron-electron interactions in a parameterized Hamiltonian for an atomic contact beyond the charge neutrality condition.

3. Eigenchannels analysis

In [46], Cuevas *et al.* analyzed the conductance channels in atomic contacts of *sp* metals, like Al and Pb, using a TB model. This work was motivated by the experimental results of Scheer *et al.* [45], discussed in Sect. VIII A, indicating that three channels contribute to the conductance of Al one-atom contacts. This result was rather surprising in view of the fact that the conductance on the first plateau of Al is usually smaller than $1G_0$.

For describing the *sp* bands in Al Cuevas *et al.* [46] used a TB model with parameters obtained from fits to ab-initio calculations for bulk metals [317]. For self-consistency between the atomic geometry and the electronic structure they imposed the charge neutrality condition as in [315]. They showed that for the case of Al one-atom contacts with an ideal geometry the conductance arises from the contribution of three channels: a well transmitted channel having sp_z character (here z indicates the axis along the contact) and two degenerate poorly transmitted channels having $p_x p_y$ character. These results were shown to be robust with respect to disorder in the leads surrounding the central atom. It should be pointed out that, within these type of models, the maximum number of channels for one atom is fixed by the number of valence orbitals having a significant con-

tribution to the bands at the Fermi energy, which would yield 4 in the case of *sp* metals. However, as these authors pointed out, the anti-symmetric combination of s and p_z orbitals do not contribute to the conductance due to a destructive interference effect which holds even for large deviations from the ideal geometry [46], so that one-atom contacts for *sp* metals are expected to have three conductance channels.

Ref. [48] discusses the results of a combined theoretical and experimental effort designed to test the predictions of TB models for the conduction channels of one-atom contacts for a large variety of materials ranging from *sp* metals, like Al and Pb; transition metals, like Nb; and simple metals like Au. The theoretical calculations predicted 3 channels for *sp* metals, 5 for transition metals and only one for monovalent metals. The experimental evidence supporting these predictions will be discussed in Sect. VIII A.

TB models provide a direct microscopic insight on the conduction channels of atomic-sized contacts. This is illustrated in Fig. 54 where both the LDOS at the central atom and the transmissions as a function of energy for each individual channel are shown for Au, Al and Pb one-atom contacts. In the case of Au the calculation predicts the presence of a single relevant channel at the Fermi energy. This channel arises mainly from the contribution of the 6s orbitals. As can be observed in the top panel of Fig. 54, the LDOS exhibits a resonance around the Fermi energy. The charge neutrality condition pins the corresponding transmission resonance to the Fermi energy and provides, as discussed in [315], a strong mechanism for the almost perfect conductance quantization for Au at the first plateau. For the case of Al (middle panel in Fig. 54) both 3s and 3p orbitals have an important weight at the Fermi energy. Although the relative position and shape of the s and p bands is similar to the case of Au, the Fermi level lies closer to the p bands. One thus finds three channels with non-negligible transmission: the sp_z channel with transmission ~ 0.6 , and the $p_{x,y}$ channels with transmission of the order of 0.1. Finally, in the case of Pb, with an extra valence electron as compared to Al, the Fermi level moves to a region where both sp_z and $p_{x,y}$ are widely open. the calculated conductance for the ideal geometry is $\sim 2.8G_0$.

More recently, Brandbyge *et al.* [246] have used a non-orthogonal TB model to study the conduction channels of Au one-atom contacts at finite bias voltage. The parameters for a non-orthogonal basis (consisting of s , p and d orbitals) are obtained from fits to ab-initio band calculations [317]. These fits are in general more accurate than the ones obtained using an orthogonal basis. On the other hand, Brandbyge *et al.* imposed the charge neutrality condition in order to obtain self-consistently the voltage drop along the contact in a voltage bias situation. They considered chains of 3 or 6 gold atoms attached to layers of 4 and 9 atoms in both ends, which again are connected to the (100) faces of perfect semi-infinite electrodes. They found that the current is due

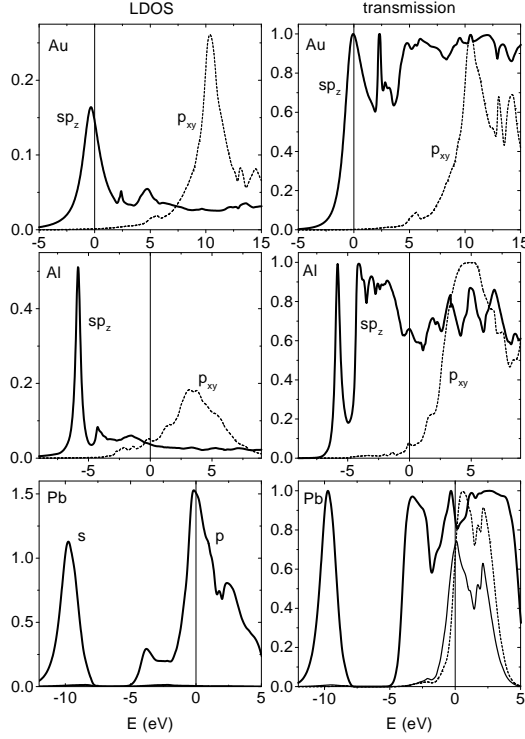


FIG. 54: LDOS at the central atom and transmissions vs energy for ideal geometries representing Au, Al and Pb one-atom contacts. The vertical line indicates the position of the Fermi level. Reprinted with permission from [229]. Copyright 1998 American Physical Society.

to the contribution of a single channel with nearly perfect transmission up to bias voltages of the order of 1 V. They also analyzed model geometries with (111) oriented electrodes, for which they found a rather narrow resonance with perfect transmission around the Fermi energy in agreement with [315] and [46]. The voltage drop along the contact was found to have no symmetry despite the left-right symmetry of the model geometry. This was attributed to the absence of electron-hole symmetry in the LDOS.

D. Ab-initio calculations

In classical MD simulations and TB models of metallic point-contacts of the previous sections the interaction potentials and hopping parameters are given as parameterized functional forms. However, a full description of the energetics and dynamics of a material requires a quantum-mechanical treatment of all its constituents (electronic and nuclear). The total energy of a system of ions and valence electrons can be written as [318]

$$E_{\text{total}}(\{\mathbf{r}_I\}, \{\dot{\mathbf{r}}_I\}) = \sum_I \frac{1}{2} m_I |\dot{\mathbf{r}}_I|^2 +$$

$$\sum_{I>J} \frac{Z_I Z_J}{|\mathbf{r}_I - \mathbf{r}_J|} + E_{\text{elect}}(\{\mathbf{r}_I\}), \quad (121)$$

where \mathbf{r}_I , m_I , and Z_I are the position, mass, and charge of the I -th ion, and $E_{\text{elect}}(\{\mathbf{r}_I\})$ is the ground-state energy of the valence electrons evaluated for the ionic configuration $\{\mathbf{r}_I\}$. The first two terms in this equation correspond to the ionic kinetic and interionic interaction energies, respectively. In this equation we have considered that the electrons follow the instantaneous configuration of the ions (Born-Oppenheimer approximation).

The major task in first principles or *ab initio* methods is to calculate the ground-state electronic energy which is typically done via the Kohn-Sham (KS) formulation [319] of the density functional theory (DFT) of many-electron systems within the local density (LDA) or local-spin-density (LSD) approximation. The ground-state energy of the valence electrons, which according to the Hohenberg-Kohn theorem [320] depends only on the electronic density, is given by

$$E_{\text{elect}} = T_e + E_{eI} + E_{ee}, \quad (122)$$

where T_e is the kinetic energy; E_{eI} is the electron-ion interaction energy, with the interaction between ions and valence electrons typically described by pseudopotentials; and E_{ee} is the electron-electron interaction energy, which consists of Hartree and exchange-correlation parts.

In the Kohn-Sham (KS) method the many-body problem for the ground-state electronic density $n(\mathbf{r})$ of an inhomogeneous system of N electrons in a static external potential (due to the positive ions) is reduced to solving self-consistently the independent-particle Schrödinger equation

$$[-\nabla^2 + v_{\text{eff}}(n)]\psi_j = \epsilon_j \psi_j, \quad (123)$$

with the electronic density given by

$$n = \sum_j f_j |\psi_j|^2, \quad (124)$$

where f_j are the occupation of the j th (orthonormal) orbital. The KS effective potential v_{eff} is given by the functional derivative of E_{elec}

$$v_{\text{eff}} = \frac{\delta E_{\text{elec}}}{\delta n}, \quad (125)$$

and since it depends on the electronic density it must be obtained self-consistently.

Ab initio calculations of the structure and properties of metallic point-contacts have been performed using different degrees of approximation. Self-consistent electronic structure, field and current calculation have been performed by Lang and collaborators [16, 47, 321, 322, 323, 324] and Kobayashi and collaborators [325, 326, 327], for one-atom contacts [16, 321] and for atomic chains of Al [47, 325, 326, 327], Na [322, 325, 326, 327], and C [323, 324]. In these calculations the metal electrodes are

described using the uniform-background (jellium) model and the atomic cores, whose positions are pre-assigned, using a pseudopotential. Since the electrostatic potential is also self-consistently calculated, it is possible to study systems under finite voltages [324]. This type of calculations are very demanding computationally and the number of atoms that can be included is very limited. Simplified (non-selfconsistent) approaches to the calculation of the conductance have been followed by several authors to study Al wires [272, 328] and Na wires [329].

First-principle molecular dynamics simulations have been used to simulate the breaking of an atomic-sized sodium wire at high (190 K) [275] and low temperature [211]. In these calculations the electronic structure, total energy and forces on the ions are calculated self-consistently, while the current is obtained from the KS orbitals using the linear-response Kubo formula [275] or by calculating the transmission probability through the self-consistent potential [211]. Barnett and Landman [275] find that, at high temperature, as the nanowires are stretched to just a few atoms, the structure of the neck can be described in terms of the configurations observed in sodium clusters. However, at this temperature the structure is undergoing perpetual thermally excited configuration changes and it is not clear whether the cluster-derived structures have a significant weight in the time-averaged structure of the contact. Nakamura *et al.* [211] study the interplay between conductance modes and structural deformation.

In *ab initio* studies of structural properties the atomic configuration are allowed to relax under a given constraint until the total forces on the atoms is negligible. The atomic and electronic structure and stability of atomic chains of Au have been studied extensively [55, 330, 331, 332, 333, 334], triggered by the experimental evidence on the formation of atomic gold chains. Atomic chains of Al [335, 336], C [323], Ca, Cu, and K [337] have also been investigated. The bond strength and breaking forces in Au [93], and Ni, Pd, Pt, Cu, Ag, and Au [338] have been studied, in conjunction with EMT MD to gain insight on the formation mechanisms of atomic chains. Okamoto *et al.* [330] also calculated the conductance of Au chains of different lengths using a non-selfconsistent recursion-transfer-matrix method. Taraschi *et al.* [335] investigated the structural properties of Al nanowires with cross sections from one to a few atoms, studying the crossover from the atomic wire behavior.

Recently, Mehrez *et al.* [247] and Brandbyge *et al.* [132] presented fully self-consistent DFT calculations of the conductance of atomic contacts in which the atomic structure of the whole system (the contact and the electrodes) is considered on the same footing. The effect of the finite potential is also taken into account using non-equilibrium Green's functions. The effect of the detailed atomistic description of the electrodes in the conductance within *ab initio* calculations has been discussed by Palacios *et al.* [339]. They find that, in contrast to the case of

Au, the conductance in Al atomic contacts is very sensitive to the precise geometry of the whole system.

Most of the results of first-principles calculations are related to atomic chains, since in this case the size of system is sufficiently small to be handled. These results will be reviewed in Sect. XI.

VIII. THE CHARACTER OF THE CONDUCTANCE MODES IN A SINGLE ATOM

Conductance measurements, discussed in Sect. V, reveal that the last plateau before the contact breaks is of the order of G_0 for most metallic elements. A closer inspection shows that there are important differences between different materials. Thus, while noble metals like Au exhibit typically a rather constant last plateau very close to G_0 , in other metals like Al and Pb the last plateau usually exhibits a clear slope when elongating the contact, which is positive for Al and negative for Pb.

These typical behaviors are certainly reflecting important differences in the electronic structure of all these metals, which give rise to differences in the structure of its conductance modes in an atomic-sized contact. However, conductance measurements by themselves do not yield much information on these modes. They only give us the sum of the corresponding transmission coefficients and its variation upon elongation or compression of the contact. Although we can be sure that more than a single channel contributes to the conductance when G is larger than G_0 we cannot claim that only one mode is contributing when $G \leq G_0$. It is possible that several poorly transmitted channels add to give a total transmission smaller than one.

To obtain further information on the conductance modes requires the measurement of additional independent transport properties. What we need is a quantity which should be a non-linear function of the transmission coefficients, so that it provides information independent of the conductance. The aim of this section is to present different experimental techniques that have been proposed in the last few years to extract information on the conduction channels. We shall also analyze the results for several metallic elements like Al, Pb, Nb and Au. It will be shown that these results are consistent with the simple picture of conduction channels arising from the atomic orbital structure of each element, which was presented in Sect. VII C.

A. Experiments on the superconducting subgap structure

Metallic elements like Al, Pb, Nb, etc. become superconducting at temperatures routinely attainable in the laboratory. The combination of STM or MCBJ techniques and cooling to low temperatures have permitted to explore the superconducting properties of atomic-

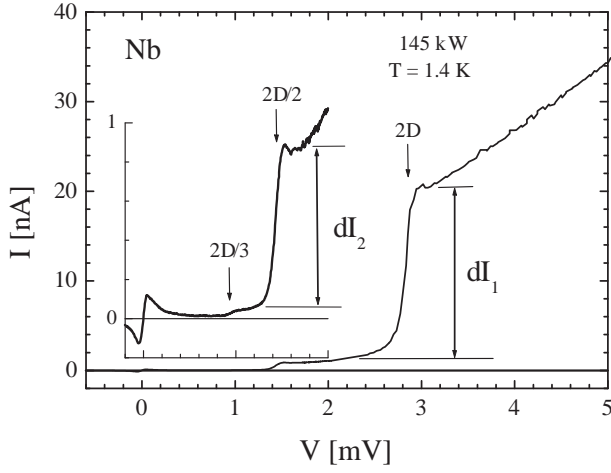


FIG. 55: Current-voltage characteristics for a Nb vacuum tunnel junction, using a MCBJ device at 1.4 K. The superconducting transition temperature is $T_c = 9.1$ K and the gap is $\Delta = 1.4$ meV. In addition to the usual steep rise of the current at $eV = 2\Delta$ there are smaller current onsets at $2\Delta/n$, as is clear on the expanded scale for $n = 2$ and 3. Reprinted with permission from [44]. Copyright 1994 American Physical Society.

sized contacts of different metallic elements [45, 48]. The highly non-linear IV characteristic of a superconducting contact, discussed theoretically in Sect. IV, has revealed to be a powerful tool to extract information on the conductance modes. This technique will be discussed below.

1. First experiments: the tunneling regime

The first quantitative analysis of the subgap structure in superconducting atomic contacts was presented by van der Post *et al.* [44]. For these experiments and the ones described below it is essential that all electrical wires to the sample space are carefully filtered to block radio-frequency radiation onto the atomic junction. Appropriate techniques for filtering are described in Refs. [340, 341]. Van der Post *et al.* studied the IV characteristic of Nb and Pb contacts in the tunneling regime produced by the MCBJ technique (Fig. 55). They showed that the sizes of the current steps in the subgap structure are proportional the n -th power of the transmission, where n is the order of the step, for $n = 1, 2$, and 3. This decrease in step height is expected, based on their explanation in terms of multiple Andreev reflections, as discussed in Sect. IV. The precise expression for the n -th current step at low transmission τ , first derived by Bratus *et al.* [42], is given by

$$\delta I_n = \frac{e\Delta}{\hbar} \tau^n \left(\frac{2n}{4^{2n-1}} \right) (n^n/n!)^2. \quad (126)$$

In fitting the experimental results of Ref. [44] a single channel was assumed. This is a natural assumption for

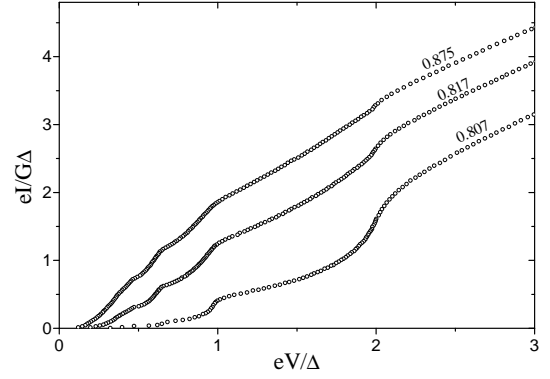


FIG. 56: Typical superconducting IV curves recorded on the last conductance plateau for Al atomic contacts at 30 mK, well below the superconducting transition temperature $T_c = 1.17$ K. The voltage has been scaled to the superconducting gap value, Δ , and the current to the product of the conductance and the gap, $G\Delta$. Three cases with similar normal conductance (0.875, 0.817 and 0.807 G_0) show very different subgap structure. Data taken from [45].

the tunneling regime in an atomic-sized contact because the various orbitals of the front-most atoms have different exponential decay lengths into the vacuum and the slowest decaying mode will soon dominate the conductance. Indeed, at closer separation (higher tunnel conductance), contributions of more than one channel have been detected [220]. The study of the IV curves in the tunneling regime was an important first step towards the analysis of the subgap structure in the contact regime.

2. *sp*-metals: Al and Pb

The first fits of the IV curves of atomic contacts in the superconducting state using the numerical results of the microscopic theory were presented by Scheer *et al.* [45]. They studied Al atomic contacts produced by the MCBJ technique in combination with lithographically defined samples, described in Sect. II C 2.

Typical IV curves recorded on the last conductance plateau are shown in Fig. 56. The normal conductance is given by the differential conductance at bias voltages much larger than 2Δ . One of the more surprising results found by these authors is that contacts having a very similar value of the normal conductance exhibit very different IV curves in the superconducting state, as can be observed in Fig. 56. This result is already suggesting that the channel decomposition of the conductance should differ from contact to contact.

The IV curves on the last plateau for Al cannot in general be fitted satisfactorily using the single channel theory. The best fit using a single channel for one of the curves in Fig. 56 is shown in Fig. 57. In the fitting procedure a set of 100 numerical IV curves with transmissions covering evenly the $(0, 1)$ range and calculated with the microscopic theory of Ref. [41] were used. As can be ob-

served, although the single channel theory reproduces the correct qualitative behavior it fails to reproduce the IV curves quantitatively. This is particularly evident for the excess current at large bias voltages.

Scheer *et al.* proposed that the discrepancy with theory is due to the fact that more than one conduction channel is contributing in the Al contacts even though the total conductance G can be smaller than G_0 . Assuming that the contribution of the different channels to the superconducting IV curves are independent the total current can be written as

$$I(V) = \sum_n I_0(V, \tau_n), \quad (127)$$

where τ_n is the set of transmission coefficients characterizing the contact and $I_0(V, \tau)$ are the IV curves given by the single channel theory. The theoretical conditions for the validity of the superposition hypothesis have been discussed in Sect. IV C.

When the number of conduction channels and the transmission for each of them are used as fitting parameters the agreement with the experimental results can be highly improved, as illustrated in Fig. 57. In general it is found that three channels are enough to fit the IV curves for Al contacts on the last conductance plateau [45, 48], with an accuracy better than 1% of the current above the gap. The quality of the fit can be measured by the so called χ^2 factor, given by the sum of the square of the deviation of the measured current at all points from the theoretical curve at the same bias voltage, divided by the number of recorded points. Typical values of χ^2 are smaller than 10^{-4} . When additional channels are included in the fitting their transmissions are found to be negligible (smaller than 0.01) and the value of χ^2 is not significantly reduced. In this way, the fitting procedure becomes a very precise method to determine the channel decomposition (or channel content) of a given contact.

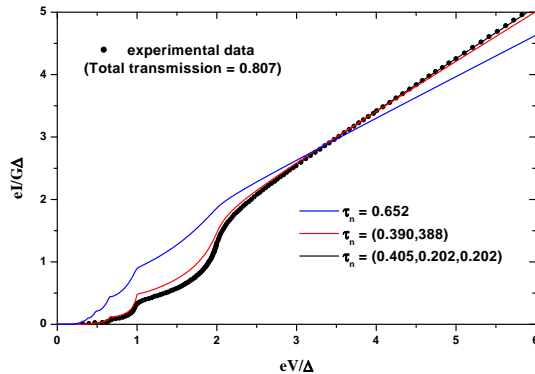


FIG. 57: Comparison of one of the experimental curves of Fig. 56 with theoretical fits using one (blue), two (red) and three channels (black). The sets of transmissions used were 0.652, (0.390, 0.388) and (0.405, 0.202, 0.202). Data taken from [45].

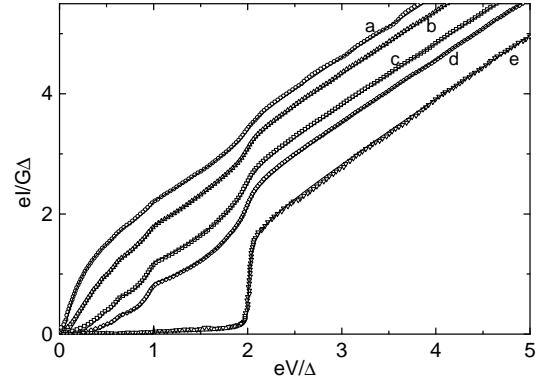


FIG. 58: Superconducting IV curves on the last plateau for Pb atomic contacts fabricated using the STM technique (taken from Ref. [48]). The channel transmissions obtained in the fitting procedure were: for curve a: $\tau_1 = 0.955$, $\tau_2 = 0.355$, $\tau_3 = 0.085$, $\tau_4 = 0.005$; curve b: $\tau_1 = 0.89$, $\tau_2 = 0.36$, $\tau_3 = 0.145$, $\tau_4 = 0.005$; curve c: $\tau_1 = 0.76$, $\tau_2 = 0.34$, $\tau_3 = 0.27$, $\tau_4 = 0.02$; curve d: $\tau_1 = 0.65$, $\tau_2 = 0.34$, $\tau_3 = 0.29$, $\tau_4 = 0.12$; curve e: $\tau_1 = 0.026$. Reprinted with permission from Nature [48]. Copyright 1998 Macmillan Publishers Ltd.

The obtained channel ensemble described by the set of transmission values $\{\tau_n\}$ was shown to be robust as a function of temperature, up to T_c , and as a function of magnetic field, up to the critical field [342]. This also confirms that the conduction channels in the normal and in the superconducting states are equivalent, and the onset of superconductivity does not modify them.

Similar results are obtained in the case of Pb [48]. The Pb atomic contacts studied in Ref. [48] were produced using a low-temperature STM with a Pb tip and Pb substrate. The superconducting IV curves for Pb contacts on the last conductance plateau at 1.5 K, well below $T_c = 7.2$ K, are shown in Fig. 58. In this figure curves a, b, c and d correspond to a very similar total conductance close to $1.4 G_0$, and curve e corresponds to the tunneling regime. In cases a to d four channels were needed to fit the experimental results, where transmission of the fourth channel was usually very small, and smaller than 0.12 in all cases. The effect of a magnetic field on the subgap structure in Pb atomic contacts was studied in Refs. [343, 344]. In [343] the IV curves were fitted using a modified MAR theory which incorporates pair-breaking effects due to the magnetic field. As in the case of Al, the set of transmission values was found to be quite robust as a function of magnetic field. In Ref. [344] it is shown that a smeared subgap structure can be observed even for magnetic fields larger than the bulk critical field.

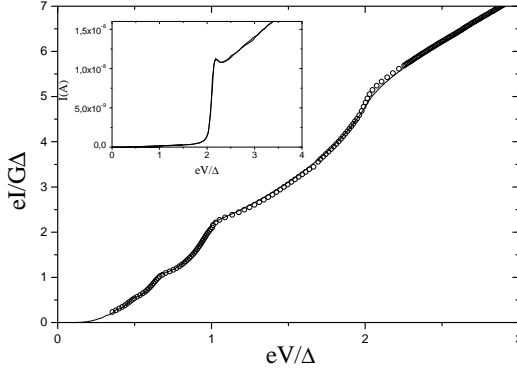


FIG. 59: Superconducting IV curve on the last plateau for a Nb atomic contact fabricated using the MCBJ technique and best fit using five conduction channels. The resulting channel transmissions were $\tau_1 = 0.731$, $\tau_2 = 0.599$, $\tau_3 = 0.351$, $\tau_4 = 0.195$ and $\tau_5 = 0.018$. The inset shows a typical IV for Nb in the tunneling regime. Data taken from [220].

3. Transition metals: Nb

In Refs. [48] and [220] the superconducting IV curves of Nb atomic contacts were analyzed both in the contact and in the tunneling regime. These contacts were produced by the MCBJ technique, and measured at a temperature of about 1.5 K, while $T_c = 9.0$ K.

The last conductance plateau in Nb is somewhat higher than in Al and Pb, with typical values ranging between 1.5 and 2.5 G_0 . These values already indicate that several channels are contributing to the conductance in a one-atom contact. An example of the superconducting IV curves recorded on the last plateau is shown in Fig. 59. These curves are best fitted using five conduction channels, with a typical χ^2 factor of the order of 10^{-3} . This agreement with the theoretical curves, although quite satisfactory, is not so remarkable as in the case of Al and Pb. The reason of this slight discrepancy becomes clear when analyzing the IV curves in the tunneling regime, illustrated as an inset in Fig. 59. As can be observed, the IV curves exhibit a “bump” around $V = 2\Delta$, a feature which is not present in the theoretical tunneling curves corresponding to a BCS superconductor. Although there is at present no clear explanation for this bump, a similar structure appears in the case of tunneling from a thin film of a normal metal on top of a superconductor, suggesting that the order parameter could be depressed in the contact region.

As a second complication, the relatively large number of fitting parameters cannot be determined to great accuracy anymore, since a shift in one value can be largely compensated by a shift in all the others. However, the number of channels, which is the most significant parameter, is very well determined at five.

4. s-metals: Au

The subgap structure analysis cannot be applied directly to non-superconducting metals like Ag or Au. However, a normal metal in contact with a bulk superconductor acquires superconducting properties due to the proximity effect [147]. This effect has been exploited to induce superconductivity in Au atomic-contacts [48, 345]. In these experiments a thin layer of Au with a thickness of 20 nm was deposited on top of a lithographically defined thick Al layer. A photograph of the device is shown in Fig. 1.

These samples exhibit less well-defined plateaus than contacts of pure Au produced by STM or the MCBJ techniques. In particular, the conductance in the smallest contacts is usually much smaller than G_0 , i.e. the typical value for pure Au one-atom contacts. These differences may be due to structural disorder induced by the fabrication process.

The superconducting IV curves in the tunneling regime exhibit a reduced energy gap and the characteristic bump around $V = 2\Delta$ denoting a non-BCS spectral density. These curves can be reasonably well described by taking into account a reduced and modified density of states in the gold layer near the contact due to the proximity effect [345]. A full microscopic theory of the proximity effect in nanoscale structures is, however, still lacking.

In spite of these limitations, the IV curves in the contact regime can be fitted satisfactorily using the theory for BCS superconductors. It is found that a single channel is sufficient to describe the IV curves for the smallest contacts with $G < G_0$, indicating that a single channel carries the current for a contact of single gold atom.

5. Summary of results and discussion

The analysis of the subgap structure has permitted to extract information on the channel content for atomic contacts of a variety of metallic elements in the periodic table. The results are consistent with the predictions of a simple model based on atomic orbitals, discussed in Sect. VII C 3. Thus, one atom contacts of monovalent metals like Au, in which the density of states at the Fermi energy is dominated by s -electrons, appear to sustain a single conduction mode. One-atom contacts of metals in groups III and IV, like Al and Pb, are characterized by a maximum of four channels, among which one is usually negligible. Atomic contacts of transition metals like Nb, where d electrons play a dominant role, are better described by five conduction channels.

Certainly, one should be critical about of these conclusions which relies on the accuracy of the fitting procedure. As discussed above, the quality of the fitting somewhat depends on the material. For both Al and Pb the more reliable results are obtained, corresponding to the fact that these metals are well described by BCS theory. On

the other hand, in the case of Nb and Au contacts the accuracy of the fitting procedure is limited by the non-BCS features in the spectral density. A detailed analysis shows that in Nb the best transmitted channels can be determined with an accuracy of nearly 10%. However, the number of channels with a significant transmission can be determined with high accuracy studying the evolution of the χ^2 factor when adding more channels to the fit [220].

For the case of Al one-atom contacts, an alternative explanation of the subgap structure assuming a single conduction channel has been proposed [346]. This explanation requires the presence of tunneling barriers close to the contact region, giving rise to an energy dependent transmission. The agreement with the experimental curves is, however, much poorer than what is obtained with the multi-channel hypothesis.

Although the subgap structure is the most powerful of the methods available to extract information on the conductance modes in atomic-sized contacts, there are several independent experiments that confirm the validity of the channel decomposition obtained from the subgap structure analysis. In particular for the monovalent metals, where the subgap analysis is complicated by the proximity effect, shot noise experiments discussed in the next section give unambiguous evidence for a single conductance channel. Further information can be obtained from measurements of thermopower and conductance fluctuations as a function of the applied bias voltage, which will be discussed in Sect. IX. The values for the transmission probabilities obtained from the superconducting subgap structure can be further tested by measuring the supercurrent, which can be quantitatively predicted from these values, as will be discussed in Sect. X.

B. Shot noise: saturation of channel transmission

For a perfect ballistic point contact, in the absence of back-scattering, i.e., all channel transmission probabilities are either 1 or 0, shot noise is expected to vanish. This can be understood from the wave nature of the electrons, since the wave function extends from the left bank to the right bank of the contact without interruption. When the state on the left is occupied for an incoming electron, it is occupied on the right as well and there are no fluctuations in this occupation number. In other words, the incoming electron is not given the choice of being transmitted or not, it is always transmitted when it enters an open mode. In order to have noise, the electron must be given the choice of being reflected at the contact. This will be the case when the transmission probability is smaller than 1 and larger than 0. In single-channel quantum point contacts, shot noise is predicted to be suppressed by a factor proportional to $\tau(1 - \tau)$, as was derived in Sect. III D 3. This quantum suppression was first observed in point contact devices in a 2-dimensional electron gas [347, 348]. Since the general expression for

shot noise in a multi-channel contact, Eq. (27), depends on the sum over the second power of the transmission coefficients, this quantity is independent of the conductance, $G = G_0 \sum \tau_n$, and simultaneous measurement of these two quantities should give information about the channel distribution.

Shot noise in atomic scale contacts was measured using the MCBJ technique [349], where its high degree of stability was further improved by careful shielding from external electromagnetic, mechanical and acoustic vibrations. By measuring at low temperatures the thermal noise is reduced. However, the noise level of the pre-amplifiers in general exceeds the shot noise to be measured. Using two sets of pre-amplifiers in parallel and measuring the cross-correlation, this undesired noise is reduced. By subtracting the zero-bias thermal noise from the current-biased noise measurements, the pre-amplifier noise, present in both, is further eliminated. For currents up to $1 \mu\text{A}$ the shot noise level was found to have the expected linear dependence on current. For further details on the measurement technique, we refer to [349].

First we discuss the results for the monovalent metal gold, for which a single atom contact is expected to transmit a single conductance mode. In Fig. 60 the experimental results for a number of conductance values are shown (filled circles), where the measured shot noise is given relative to the classical shot noise value $2eI$. All data are strongly suppressed compared to the full shot noise value, with minima close to 1 and 2 times the conductance quantum. We compare our data to a model that assumes a certain evolution of the values of τ_n as a function of the total conductance. In the simplest case, the conductance is due to only fully transmitted modes ($\tau_n = 1$) plus a single partially transmitted mode (full curve). The model illustrated in the inset gives a measure for the deviation from this ideal case in terms of the contribution x of other partially open channels; the corresponding behavior of the shot noise as a function of conductance is shown as the dashed curves in Fig. 60. This model has no physical basis but merely serves to illustrate the extent to which additional, partially open channels are required to describe the measured shot noise. For a more physical model fitting the data of Fig. 60 see [309].

We see that for $G < G_0$ the data are very close to the $x = 0\%$ curve, while for $G_0 < G < 2G_0$ the data are closer to the $x = 10\%$ curve. For $G > 2G_0$ the contribution of other partially open channels continues to grow. For all points measured on the last conductance plateau before the transition to tunneling, which is expected to consist of a single atom (or a chain of single atoms, see Sect. XI), the results are well-described by a single conductance channel, in agreement with the fact that gold has only a single valence orbital.

When the experiment is repeated for aluminum contacts, a different behavior is observed. For contacts between $0.8G_0$ and $2.5G_0$ the shot noise values vary from 0.3 to 0.6 ($2eI$), which is much higher than for gold (see Fig. 60). A systematic dependence of the shot noise

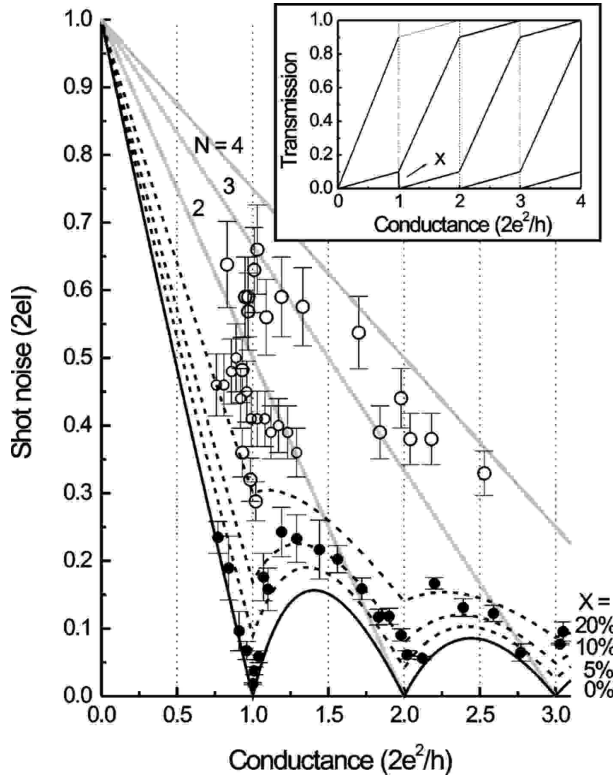


FIG. 60: Measured shot noise values for gold (filled circles) and aluminum contacts (open circles) at 4.2 K with a bias current of $0.9 \mu\text{A}$. For gold, comparison is made with calculations described in the text and in the inset (full and dashed black curves). For aluminum, comparison is made with the maximum shot noise that can be produced by N modes (gray curves), as explained in the text. The minimum shot noise is given by the full black curve. Note that in the limit of zero conductance, the theoretical curves all converge to full shot noise. *Inset:* Model for visualizing the effect of contributions of different modes to the conductance and shot noise. The model gives a measure for the deviation from the ideal case of channels opening one by one, by means of a fixed contribution $(1 - \tau_{n-1}) + \tau_{n+1} = x$ of the two neighboring modes. As an illustration the case of a $x = 10\%$ contribution from neighboring modes is shown. Reprinted with permission from [350]. Copyright 2000 Springer-Verlag.

power on the conductance seems to be absent. From the two measured parameters, the conductance, G , and the shot noise, S_I , one cannot determine the full set of transmission probabilities. However, the shot noise values found for aluminum, especially the ones at conductance values close to G_0 , agree with Eq. (27) only if we assume that more than one mode is transmitted. The maximum shot noise that can be generated by two, three or four modes as a function of conductance is plotted as the gray curves in Fig. 60; the minimum shot noise in all cases is given by the full black curve. Hence, for a contact with shot noise higher than indicated by the gray N -mode maximum shot noise curve, at least $N + 1$ modes are contributing to the conductance. From this

simple analysis we can see that for a considerable number of contacts with a conductance close to $1 G_0$, the number of contributing modes is at least three. Again, this is consistent with the number of modes expected based on the number of valence orbitals, and with results of the subgap structure analysis. Note that the points below the line labeled $N = 2$ should not be interpreted as corresponding to two channels: the noise level observed requires at least two channels, but there may be three, or more.

More recently, shot noise measurements by Cron *et al.* [351] have provided a very stringent experimental test of the multichannel character of the electrical conduction in Al. In these experiments the set of transmissions τ_n are first determined independently by the technique of fitting the subgap structure in the superconducting state, discussed in Sect. VIII A. In words of the authors of Ref. [351], these coefficients constitute the ‘mesoscopic PIN code’ of a given contact. The knowledge of this code allows a direct quantitative comparison of the experimental results on the shot noise with the theoretical predictions of Eq. (27). The experiments were done using Al nanofabricated break junctions which exhibit a large mechanical stability. The superconducting IV curves for the smallest contacts were measured below 1 K and then a magnetic field of 50 mT was applied in order to switch into the normal state. The voltage noise spectrum was measured in a frequency window from 360 to 3560 Hz. To extract the intrinsic current noise of the contact, S_I , other sources of background noise arising from the preamplifiers and from the thermal noise due to the bias resistor were subtracted (for details see [351]). The measured voltage dependence of S_I is shown in Fig. 61a for a typical contact in the normal state at three different temperatures, together with the predictions of Eq. (27), using the mesoscopic pin code τ_n measured independently. The noise measured at the lowest temperature for four contacts having different sets of transmission coefficients is shown in Fig. 61b, together with the predictions of the theory. This excellent agreement between theory and experiments provides an unambiguous demonstration of the presence of several conduction channels in the smallest Al contacts and serve as a test of the accuracy that can be obtain in the determination of the τ ’s from the subgap structure in the superconducting IV curve. The experimental results of Ref. [351] for the shot noise in the superconducting state will be discussed in X C.

C. Strain dependence of the conductance

As already commented, the behavior of the conductance on the last plateaus before breaking the contact is a characteristic of each metallic element. Krans *et al.* [30] were the first who pointed out the characteristic tendencies of several metals when elongating or contracting the contact. They used the MCBJ to study the case of Cu, Al and Pt, which exhibit different behaviors. In Cu the

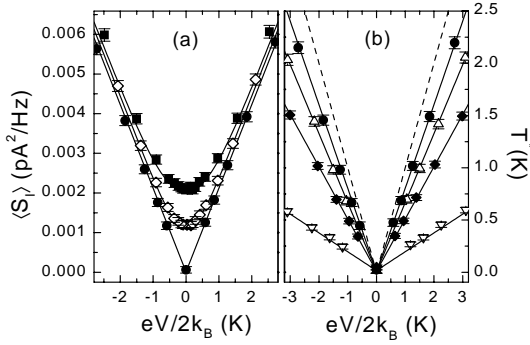


FIG. 61: (a) Symbols: measured average current noise power density $\langle S_I \rangle$ and noise temperature T^* , defined as $T^* = S_I/4k_B G$, as a function of reduced voltage, for a contact in the normal state at three different temperatures (from bottom to top: 20, 428, 765 mK). The solid lines are the predictions of Eq. (27) for the set of transmissions $\{0.21, 0.20, 0.20\}$ measured independently from the IV in the superconducting state. (b) Symbols: measured effective noise temperature T^* versus reduced voltage for four different contacts in the normal state at $T = 20$ mK. The solid lines are predictions of Eq. (27) for the corresponding set of transmissions (from top to bottom: $\{0.21, 0.20, 0.20\}$, $\{0.40, 0.27, 0.03\}$, $\{0.68, 0.25, 0.22\}$, $\{0.996, 0.26\}$). The dashed line is the Poisson limit. Reprinted with permission from [351]. Copyright 2001 American Physical Society.

plateaus show a slightly negative slope upon elongation but the last plateaus are rather flat, specially the last one which is rather constant around $1 G_0$. The reduction of the conductance with elongation coincides with the intuitively expected result. However, in the case of Al and Pt the opposite behavior is found.

Within a free-electron model Torres and Sáenz [260] have suggested that the different slopes on the last plateaus may arise as a result of variations in the effective length of the contact. They are able to reproduce different slopes for the plateaus in their calculations, but the sign of the slopes is not element specific: positive or negative slopes are found both for Au and for Al. The variation in the slopes they observe is probably related to resonances in the electron waves due to scattering from the interfaces between the cylindrical slabs used in their model calculation.

A different explanation of the characteristic tendencies has been proposed by Cuevas *et al.* [229]. They analyzed in particular the case of Au, Al and Pb which exhibit three different behaviors, as illustrated in Fig. 62. In order to describe the electronic properties of these contacts, Cuevas *et al.* used an atomic orbital basis and an idealized model geometry following the proposal of Ref. [46]. Upon elongation, the elastic deformation of a one-atom contact was assumed to produce a slight increase in the distance between the central atom and its nearest neighbors. For deformations not larger than 5 or 10% of the equilibrium distances, the variation of the hopping integrals within the parameterization of Ref. [317] can be

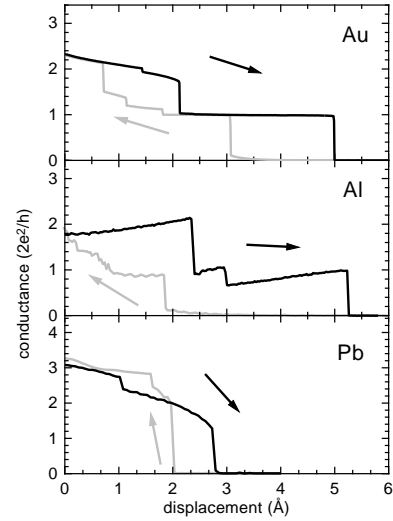


FIG. 62: Typical behavior of the experimental conductance at the last plateaus before breaking the contact for Au, Al and Pb. The contacts were produced by the STM technique at low temperatures. Reprinted with permission from [229]. Copyright 1998 American Physical Society.

described by power laws of the form

$$t_{l,l'} \sim \frac{1}{d^{l+l'+1}}, \quad (128)$$

where d is the interatomic distance and l, l' denote the corresponding angular momenta.

The theoretical results of Ref. [229] for the evolution of the conductance upon elastic deformation are shown in Fig. 63. These results correspond to the simplest model geometry of a single atom in between to semi-infinite fcc crystals exposing (111) surfaces. As can be observed, the results are in qualitative agreement with the observed experimental tendencies. Moreover, these model calculations allow understanding the microscopic origin of these tendencies, as will be discussed below.

In the case of Au, the calculations predict a fully open single conduction channel arising from the $6s$ orbital on the central atom slightly hybridized with the $6p_z$ orbital. The LDOS on the central atom exhibits a resonance located around the Fermi energy, as can be observed in Fig. 54. In this case, the condition of charge neutrality plays a major role in pinning this resonance at the Fermi energy when the contact is elongated, which yields to a rather constant conductance of $1 G_0$. These results coincide with more sophisticated calculations for Au based on LDA by Brandbyge *et al.* [198].

The case of Al is qualitatively different, as both $3s$ and $3p$ orbitals give a significant contribution to the conductance. The Fermi energy is in this case located somewhere in between the center of the s and the p bands in order to accommodate three electrons per atom. In the equilibrium situation there is a widely open channel with sp_z character and two degenerate poorly transmit-

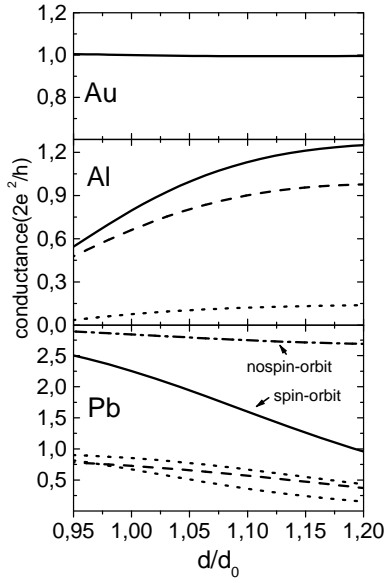


FIG. 63: Theoretical results for the total conductance (full line) and its channel decomposition for Au, Al and Pb one-atom contacts as a function of the distance d between the central atom and its nearest neighbors, in units of the equilibrium distance d_0 . Reprinted with permission from [229]. Copyright 1998 American Physical Society.

ted channels of p_x and p_y character, as was discussed in Sect VII C. The elongation of the contact induces a narrowing of the sp_z and the $p_{x,y}$ bands, which is more pronounced in this last case, as expected from the scaling laws of the hopping elements. As a result, the Fermi energy tends to be located around the sp_z resonance and the transmission on the $p_{x,y}$ modes tends to vanish, leaving a single fully open channel. Again, more sophisticated first-principles calculations have been performed by Kobayashi *et al.*, which confirm that three channels participate in the conductance for Al single-atom contacts [327]. However, they propose a different explanation for the slope of the plateau: the decreasing conductance results from straightening the linear arrangement of Al atoms.

Also in Pb both s and p orbitals play an important role. As already commented in Sect VII C, this model predicts the same number of channels for Al and Pb. However, there is an extra valence electron in Pb which forces the Fermi energy to a region where both the sp_z and $p_{x,y}$ channels are widely open, leading to a total conductance of $2.8 G_0$ in equilibrium. Using the parameterization of Ref. [317] together with the scaling laws, Eq. (128), a slight decrease of the conductance upon elongation was found [229], which is less pronounced than in the experimental results. As was pointed out, the inclusion of spin-orbit coupling within the model leads to a better agreement between the theoretical and experimental results. This coupling is of the order of 1 eV in Pb and produces a splitting of the p resonance into a $p_{1/2}$ and a $p_{3/2}$ resonance, with the Fermi level in between. This

splitting would be responsible of the pronounced decrease of conductance upon elongation.

IX. CORRECTIONS TO THE BARE CONTACT CONDUCTANCE

The electronic transport properties of atomic-sized contacts are predominantly determined by the properties of the narrowest part of the contact, as we have seen above. With a single atom forming the contact – the configuration that we are especially interested in – the chemical nature of this atom determines the number of conductance channels. The transmission probabilities for these channels depend on connection of this atom to the neighboring atoms in the metallic leads. We will define the atom plus its direct environment as the ‘bare’ contact. Only in the absence of defects and surface corrugations in the leads close to the central atom, and in the absence of excitations of other degrees of freedom, would we measure the transmission probabilities for the bare contact unaltered. In reality, any sudden variation in the cross section of the conductor as we move away from the center gives rise to partial reflection of the electron wave, as a result of the mismatch of the waves at both sides of this jump in the wire cross section. More generally, the electron wave can be reflected off surface corrugations, defects and impurities. This reflected partial wave only alters the current, and therefore the conductance, to the extent that it passes back through the contact. As we move further away from the center of the contact, the probability for returning to the contact is reduced by the solid angle at which the contact is seen from the scattering object. Therefore, only scatterers close to the contact center will have a significant effect on the conductance of the junction.

The scattering centers near the contact give rise to a number of corrections, the most obvious of which is a reduction of the total conductance.⁶ All transmissions will be reduced and the shift in the averaged sum of the transmission values is often discussed in terms of an effective ‘series resistance’ to the contact. Quantum interference between different partial waves in this scattering problem further gives rise to conductance fluctuations. We will address the latter first (Sect. IX A) because it will provide a good basis for the discussion of series resistance corrections.

Next we will discuss corrections to the conductance due to electron-phonon scattering at finite bias, and the related problem of heating in point contacts. When we include correlations between the electrons additional effects arise that produce an anomalous dip in the differ-

⁶ In view of the fluctuations to be discussed below, we take this conductance to be the ensemble-averaged conductance, i.e. averaged over all possible defect configurations for the same contact geometry.

ential conductance centered at zero bias voltage. Widely different mechanisms all lead to a similar kind of zero-bias anomaly. When magnetic impurities are introduced into the metal at sufficiently high concentrations to have a measurable effect, a zero-bias conductance minimum is observed due to Kondo scattering of the electrons (Sect. IX D). The Kondo scattering appears to be sensitive to the size of the contact. Non-magnetic scattering centers have been observed to produce similar zero-bias anomalies. This has been attributed to fast two-level systems and it has been proposed that a 2-channel Kondo model gives an accurate description of these observations (Sect. IX E). Finally, Coulomb interactions between the conduction electrons themselves give rise to a feature similar to Coulomb blockade in tunnel junctions. In order to observe this effect one needs to tailor the electromagnetic environment of the junctions (Sect. IX F).

A. Conductance fluctuations

Universal conductance fluctuations (UCF) are observed in a mesoscopic conductor for which the phase coherence length is much longer than the sample size, while, on the other hand, the elastic scattering length is much smaller than the size of the system [352, 353]. Electrons entering the system have many possible trajectories for being scattered back to the lead from which they entered and all partial waves sum up coherently. For every new configuration of scattering centers the conductance is slightly different and varies randomly. The root-mean-square amplitude of the conductance fluctuations resulting from the interference has a universal value, independent of sample size, $\delta G_{\text{rms}} \simeq e^2/h$. In practice it is not feasible to measure an ensemble average by modifying the defect distribution for one and the same sample. A practical way to obtain an equivalent result is to measure the conductance as a function of magnetic field. The field enclosed by the electron trajectories modifies the phase, and this phase shift is different for each different size of electron loop.

The universality of this fluctuation amplitude breaks down as soon as the sample size falls below the average distance between elastic scattering events. Therefore, it is not surprising that the amplitude for conductance fluctuations in a ballistic point contact is much smaller than e^2/h . Holweg *et al.* [354] studied the fluctuations for relatively large nanofabricated contacts of the type described in Sect. II E, with a typical size corresponding to a resistance of $\sim 10\Omega$. The amplitude of the fluctuations in the conductance as a function of magnetic field that they obtained was reduced by two orders of magnitude compared to the universal value. This is due to the geometrical factor that enters when we take into account that it is unlikely for the electron to return to the contact from a remote region. For the contributions from interference of two partial waves scattering back to the contact one typically obtains $\delta G_{\text{rms}} \simeq (a/\ell)^2(e^2/h)$ [355], where a is

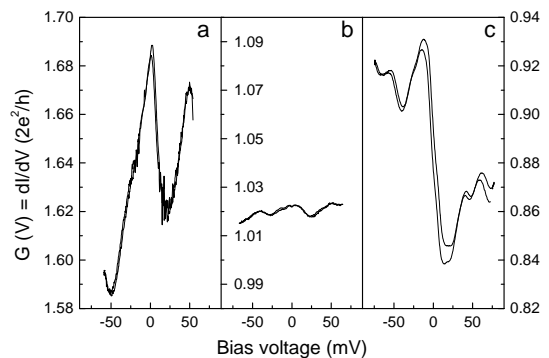


FIG. 64: Differential conductance dI/dV as a function of bias voltage, measured with a modulation amplitude of less than 0.35 mV, for three different gold contacts, with $G \simeq 1.65 G_0$ (a), $\simeq 1.02 G_0$ (b), and $\simeq 0.88 G_0$ (c). For all three curves the vertical scale spans $0.12 G_0$. The curves have been recorded twice, once for decreasing bias voltage, and back, to illustrate the reproducibility of the features. Reprinted with permission from [202]. Copyright 1999 American Physical Society.

the radius of the contact and ℓ is the elastic mean free path. However, Kozub *et al.* [355] noted that this gives an estimate that is far smaller than the observed fluctuations. They proposed to repair this discrepancy by assuming a dominant scatterer near the contact. However, as explained below, the contact itself can be regarded as a scatterer, which automatically resolves this problem, and it turns out that δG is reduced by only a single factor $\sim (a/\ell)$.

Nevertheless, when a becomes as small as a single atom this geometrical reduction factor is so severe that conductance fluctuations as a function of magnetic field are extremely weak. In this case the fluctuations are more sensitively probed by following the differential conductance as a function of bias voltage. Examples are shown in Fig. 64, which illustrates the fact that a different pattern is obtained for each new realization of the contact.

1. Theory for defect scattering near a point contact

For an evaluation of the dominant correction terms arising from defect scattering we will model the contact as illustrated in Fig. 65. It has a ballistic central part (the ‘bare’ contact), which can be described by a set of transmission values for the conductance modes. This is sandwiched between diffusive banks, where electrons are scattered by defects characterized by an elastic scattering length ℓ . An electron wave of a given mode n falling onto the contact is transmitted with probability amplitude t_n and part of this wave is reflected back to the contact by the diffusive medium, into the same mode, with probability amplitude $a_n \ll 1$. This back-scattered wave is then *reflected* again at the contact with proba-

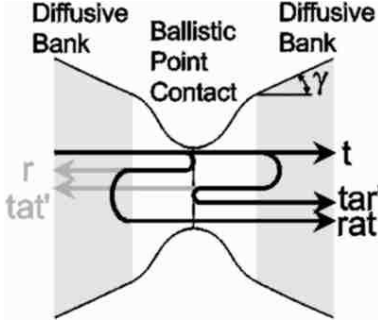


FIG. 65: Diagram showing the bare contact (light) sandwiched between diffusive regions (gray). The dark lines with arrows show the paths that interfere with each other and contribute to the conductance fluctuations in lowest order.

bility amplitude⁷ r_n . The latter wave interferes with the original transmitted wave. This interference depends on the phase accumulated by the wave during the passage through the diffusive medium. The probability amplitude a_n is a sum over all trajectories of scattering, and the phase for such a trajectory of total length L is simply kL , where k is the wave vector of the electron. The wave vector can be influenced by increasing the voltage over the contact, thus launching the electrons into the other electrode with a higher speed. The interference of the waves changes as we change the bias voltage, and therefore the total transmission probability, or the conductance, changes as a function of V . This describes the dominant contributions to the conductance fluctuations, and from this description it is clear that the fluctuations are expected to vanish either when $t_n = 0$, or when $r_n = 0$. For those events only the much smaller higher order terms involving two diffusive trajectories remain.

Elaborating this model Ludoph *et al.* [202, 207] obtained the following analytical expression for the root-mean-square value of the variation of the conductance with voltage, $\sigma_{GV} = \langle dG/dV \rangle_{\text{rms}}$, to lowest order in the return amplitudes a_n :

$$\sigma_{GV} = \frac{2.71 e G_0}{\hbar k_F v_F \sqrt{1 - \cos \gamma}} \left(\frac{\hbar v_F / \ell}{e V_m} \right)^{3/4} \sqrt{\sum_n \tau_n^2 (1 - \tau_n)}. \quad (129)$$

Here, k_F and v_F are the Fermi wave vector and Fermi velocity, respectively, and ℓ is the scattering length. The shape of the contact is taken into account in the form of the opening angle γ (see Fig. 65), and V_m is the voltage modulation amplitude used in the experiment. Here, it is assumed that $eV_m \gg \max(k_B T, \hbar v_F / L_\varphi)$, with L_φ the phase coherence length. In deriving expression (129) the diffusive banks were treated semi-classically: the probability to return to the contact after a time t_s was

assumed to be given by the classical diffusion expression. In adding over all diffusion times t_s a phase factor, $\exp(-iEt_s/\hbar)$ that an electron with energy E accumulates during its traversal of the diffusive region was taken into account.

The choice of where the boundary between the contact and the diffusive banks is taken is somewhat arbitrary. It does not explicitly appear in (129), because a new choice for the boundary is absorbed in modified values for the transmission probabilities τ_n . For any choice of boundaries we can find a set of eigenchannels, but they will only slightly differ as long as the distance D between the contact center and the boundary is large compared to the contact diameter. On the other hand, this implies that the effects of surface corrugation very close to the contact are represented by a reduction of the τ_n 's, which will then also have a distinct dependence on energy. The fluctuations in the τ_n 's will be visible on a large voltage scale only, as long as D is small enough, i.e. $D \ll \hbar v_F / eV$. For metallic contacts and on the voltage scales considered here both conditions can be fulfilled reasonably well when we take $D \sim 1$ nm.

Apart from the fluctuations in the conductance there is a shift in the total conductance of the contact. Including only the lowest order correction the average total transmission probability is given by $\sum_{n=1}^N \tau_n (1 - \sum_{m=1}^N \tau_m (\langle |a_{l_{mn}}|^2 \rangle + \langle |a_{r_{mn}}|^2 \rangle))$. The last term, $a_{r_{mn}}$, describes the partial amplitude for an electron that is transmitted through the contact in mode n , scattered back towards the contact in the right diffusive bank, and then transmitted through the contact a second time, in mode m , in the opposite direction. The term $a_{l_{mn}}$ describes a similar trajectory for diffusion in the left lead. These processes will lead to a smaller conductance than expected for the bare contact conductance alone since part of the transmitted electrons are scattered back, reducing the net forward current flow.

At higher conductance values, we expect a significant contribution of higher order terms in the return probabilities $a_{l_{mn}}$ and $a_{r_{mn}}$ to the conductance. Hence, the lowest order correction used above will not suffice. Keeping track of higher order terms, becomes very complicated for many channels. However, using random matrix theory an expression for the correction to the conductance of a quantum point contact connected to diffusive leads has been derived [356, 357],

$$\langle G \rangle = \frac{2e^2}{h} \left[\frac{N}{1 + \gamma_N} - \frac{1}{3} \left(\frac{\gamma_N}{1 + \gamma_N} \right)^3 \right]. \quad (130)$$

Here, $\gamma_N = (N + 1)G_0 R_s$ is roughly equal to the ratio of the conductance of the bare contact to that of the banks. The diffusive scattering in the banks is represented through a sheet resistance R_s . In the theory all open channels were assumed to be perfectly transmitting, $\tau_n = 0$, or 1. To lowest order Eq. (130) is consistent with the correction to the average total transmission probability derived from the backscattering above. The first term

⁷ The partial wave amplitudes are related to the transmission probability of this mode as $\tau_n = |t_n|^2 = 1 - |r_n|^2$.

in (130) is nearly equal to the expression for the classical addition of a resistor R and a conductor G , which would give a conductance $G/(1 + GR) = NG_0/(1 + NG_0R)$. The second term in (130) is a weak localization correction, and can usually be neglected because it results from interference of two partial waves scattered in the banks. Explicit calculations for model systems show that the expression describes the shifts of the peaks in a conductance histogram correctly [346, 358, 359]. Note, however, that Eq. (130) was derived for a 2D electron system, with leads of constant width. For the metallic point contacts considered here a three dimensional analysis is applicable, with leads that widen out to infinity far away from the contact, and we anticipate a significantly different result.

Indeed, for metallic point contacts of larger size one has since long made use of the expression due to Wexler [360],

$$G_W = G_S \left[1 + \frac{3\pi}{8} \Gamma\left(\frac{\ell}{a}\right) \frac{a}{\ell} \right]^{-1}, \quad (131)$$

which interpolates between the Sharvin conductance G_S , Eq. (8) and the Maxwell classical conductance (6) that applies for large contact radius a . The function $\Gamma(K)$ is a slowly varying function, with $\Gamma(0) = 1$ and $\Gamma(\infty) = 0.694$. We propose to replace G_S by the bare quantum conductance of the contact, to obtain an interpolation formula that will predict the conductance of metallic contacts in the presence of disorder scattering.

2. Experimental results

We will mainly discuss results for gold, which has been best characterized, and for which example curves are presented in Fig. 64, while the similarities and differences for other metals will be briefly mentioned. Slight modifications of a metallic constriction, induced by displacing the two banks over a small distance, can have a dramatic effect on the interference pattern seen in the voltage dependence of the conductance (see e.g. Fig. 64), while the overall value of the conductance remains almost constant [207, 361]. This agrees with the idea that the interference terms are sensitive to changes in the electron path length on the scale of λ_F .

The amplitudes of the spectral components of the conductance as a function of bias voltage for a single contact decrease with their frequency roughly as the inverse of the distance d traveled by the partial wave, where d is deduced from this frequency, as shown in Fig. 66 [361]. This is what is to be expected when the scattering from the banks is dominated by single-scattering events. Contributions of scattering paths up to 100 nm long are observable. For higher temperatures the high frequency (long path) components are gradually suppressed, reflecting the decrease in coherence length, but even at room temperature conductance fluctuations remain visible [361].

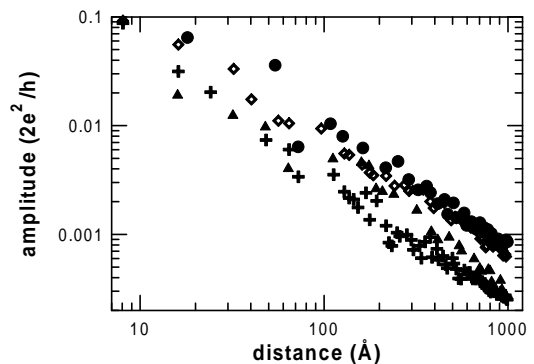


FIG. 66: Dependence of the amplitude of the components of the conductance fluctuations as a function of the distance traveled in the banks, for several contacts for gold at 4.2K. The distance d is obtained from the period of the oscillation, ΔV , via $d = \lambda_F(E_F/e\Delta V)$. The amplitude for the components is obtained by taking the Fourier transform of the differential conductance measured as a function of the bias voltage. Reprinted with permission from [361]. Copyright 2000 American Physical Society.

In contrast to UCF studied in mesoscopic samples, for point contacts one can make, to a very good approximation, a direct ensemble average. This can be done by recording the conductance and its derivative simultaneously and collecting the data for many contact-breaking cycles [202, 207]. In practice this is done by simultaneously recording the first and second harmonic of the modulation frequency with two lock-in amplifiers. The values for the derivatives of the conductance from all these contacts, having the same average conductance $\langle G \rangle$, are used to calculate the standard deviation $\sigma_{GV} = \sqrt{\langle (\partial G / \partial V)^2 \rangle}$ for each value of $\langle G \rangle$. Results obtained using the MCBJ technique for gold at 4.2 K are shown in Fig. 67. A fairly large modulation voltage was used in order to permit fast data acquisition. This enhances the sensitivity for the long-period components but in the theory for the ensemble average, Eq. (129), the finite modulation amplitude has been explicitly taken into account.

The full curves in Fig. 67a are obtained from Eq. (129), assuming a single partially-open channel at any point, i.e., assuming that in the interval $G/G_0 \in [0, 1]$ there is a single channel contributing to the conductance with $G = \tau_1 G_0$, in the interval $[1, 2]$ there are two channels, one of which is fully open, $G = (1 + \tau_2) G_0$, etc. This is the same succession of channel openings as giving rise to the full black curve for the shot noise in Fig. 60. The amplitude of the curves in Fig. 67a is adjusted to best fit the data, from which a value for the mean free path $\ell = 5 \pm 1$ nm is obtained. Similar experiments [202, 207] for the monovalent metals Cu and Ag and for Na also show the quantum suppression of conductance fluctuations observed here for Au, while for the *sp* metal Al and the *sd* metals Nb and Fe this is not observed. The absence of pronounced minima in σ_{GV} for the non-*s* metals agrees again with the results discussed in Sect. VIII,

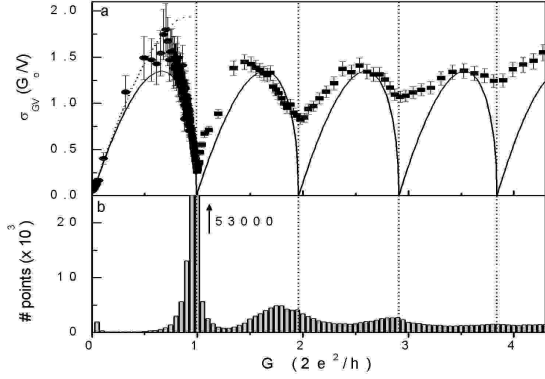


FIG. 67: (a) Standard deviation of the voltage dependence of the conductance, σ_{GV} , versus the conductance, G , obtained from 3500 contact-breaking cycles. The circles are the averages for 300 points, and the solid squares for 2500 points. The solid curves depict the calculated behavior for a single partially-open channel. The dashed curve is for a random distribution over two channels. The vertical dotted lines are the corrected integer conductance values (see text). The modulation voltage amplitude was 20 mV at a frequency of 48 kHz. (b) Conductance histogram obtained from the same data set. The peak in the conductance histogram at G_0 extends to 53000 on the y-scale. Reprinted with permission from [202]. Copyright 1999 American Physical Society.

showing that for those metals typically several partially transmitted modes are participating in a single atom for any accessible value of the conductance.

The minimum observed at $1 G_0$ in Fig. 67 is very sharp, close to the full suppression of fluctuations predicted for the case of a single channel. In order to describe the small deviation from zero, it is sufficient to assume that there is a second channel which is weakly transmitted, $\tau_2 \ll 1$, and $\tau_1 \simeq 1$ such that $\tau_1 + \tau_2 = 1$. For this case it is easy to show that the value of σ_{GV} at the minimum is proportional to $\sqrt{\langle \tau_2 \rangle}$, from which $\langle \tau_2 \rangle = 0.005$ is obtained. This implies that, on average, only 0.5 % of the current is carried by the second channel. For the minima near 2, 3 and $4 G_0$ higher values are obtained: 6, 10 and 15 %, respectively. The well-developed structure observed in σ_{GV} for gold in Fig. 67a, with a dependence which closely follows the $\sqrt{\sum \tau_n^2 (1 - \tau_n)}$ behavior of Eq. (129), agrees with the saturation of transmission channels [202] that was also seen in the shot noise experiments in Sect. VIII B.

Note that the minima in Fig. 67a are found slightly below the integer values. A similar shift was obtained in simulations of the shot noise for quantum point contacts by Bürki and Stafford [309]. The shift can be described by taking a total return probability $\langle \sum_m |a_{mn}|^2 \rangle = 0.005$, from which we derive a value for the mean free path of $\ell = 4 \pm 1$ nm. This value agrees well with the value obtained from the fluctuation amplitude. This gives strong

experimental support for the notion of a shift of the average conductance by scattering on defects that can approximately be described by a series resistance, which in this case is about 130Ω . We will return to discuss the accuracy of this statement in Sect. IX B below.

It is interesting to compare the positions of the maxima in the conductance histogram and those for the minima in σ_{GV} in Fig. 67. It appears that these positions do not all coincide, which is most evident for the peak in the histogram at about $G = 1.8 G_0$. As discussed in Sect. V D, the histograms give preferential conductance values, which may reflect a quantization effect in the conductance as a function of contact diameter, but also a preference for forming contacts of certain effective diameters. Such preferential contact diameters may be expected based on the fact that the contact is only a few atoms in cross section, which limits the freedom for choosing the diameter. It appears that at least the peak at $1.8 G_0$ in the histogram for gold arises from this atomic geometry effect. Although the shot noise (Fig. 60) and conductance fluctuation experiments (Fig. 67a) both show that the conductance for gold contacts with $G \simeq 2 G_0$ is carried by two nearly perfectly transmitted modes, this conductance is not preferred, as evidenced by the conductance histogram. This interpretation agrees with *ab-initio* calculations for a double strand of gold atoms for which Häkkinen *et al.* [333] obtain a conductance of $1.79 G_0$ corresponding to two channels, one of which is nearly fully open.

The validity of Eq. (129) has been tested by measuring the amplitude of the conductance fluctuations in gold at modulation voltages ranging from 10 to 80 mV and the expected dependence $V_m^{-3/4}$ was obtained [207]. The agreement with the fluctuations in the thermopower described below may serve as a further test on smaller energy scales.

3. Thermopower fluctuations

In a linear response approximation the thermal voltage induced by a temperature difference ΔT over a contact is given by

$$V_{tp} = S \cdot \Delta T = - \frac{\pi^2 k_B^2 T}{3e} \frac{\partial \ln G}{\partial \mu} \Delta T \quad (132)$$

This expression illustrates that the thermopower S is a quantity that is qualitatively similar to the voltage dependence of the conductance. The role of voltage is now taken by the chemical potential μ and the scale is set by the temperature difference over the contact, ΔT . It can be expressed in terms of the transmission probabilities of the conductance channels with the help of Eq. (33). Based on a free electron model of a quantum point contact Bogachek *et al.* [301] suggested that the thermopower should be positive, having maxima midway between the contact widths for which the conductance is at integer multiples of the conductance quantum.

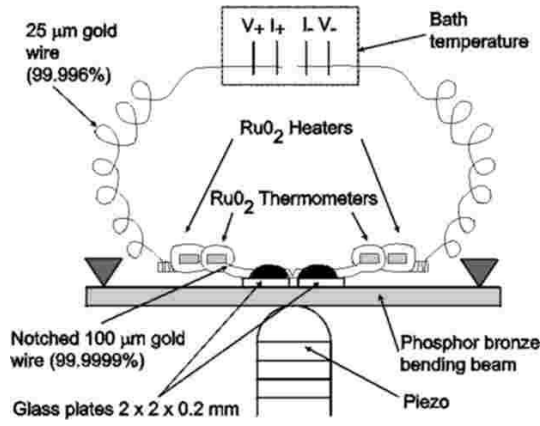


FIG. 68: Schematic diagram of the modified MCBJ configuration, used for the simultaneous measurement of conductance and thermopower. Reprinted with permission from [362]. Copyright 1999 American Physical Society.

In experiment however, the values measured for atomic-sized gold contacts have both positive and negative values, showing a random distribution centered around zero [362]. The principle of the measurement is illustrated in Fig. 68.

By applying a constant temperature difference over the contacts, the thermally induced potential could be measured simultaneously with the conductance. Large thermopower values were obtained, which jump to new values simultaneously with the jumps in the conductance. The values are randomly distributed around zero with a roughly bell-shaped distribution. The thermopower signal was demonstrated to be dominantly of the same origin as the conductance fluctuations discussed in the previous section. An expression similar to (129) can be derived to describe the results [207, 362]. The experimental results follow the law obtained from this defect-scattering model, and quantum suppression of the thermopower at $G = 1 G_0$ was observed. In fact, a scaling relation between the amplitude of the fluctuations in the thermopower and that of the conductance can be derived, free of any adjustable parameters [207]. The two experimental techniques are very different, and the typical energy scales of excitation are at least an order of magnitude apart. This scale is set by the modulation voltage amplitude, 10–80 mV, in one case and the temperature, ~ 10 K, equivalent to $\simeq 1$ mV, in the other. Therefore, these results give strong support for the description and interpretation presented above.

B. The series resistance of a quantum point contact

In the interpretation of conductance histograms a phenomenological series resistance is often taken into account in order to describe the shift of the peaks to lower values [33, 76, 107, 108, 199], as was discussed in Sect. V D. This practice was inspired on a similar proce-

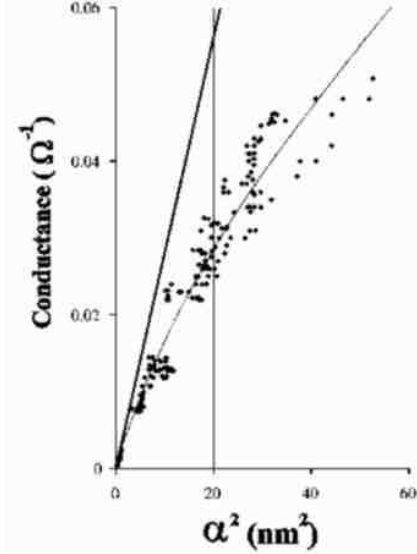


FIG. 69: Measured conductance of gold point contacts as a function of the square of the contact radius, as determined from simultaneously recorded TEM images. The measurements were taken at room temperature at a voltage bias of 10 mV. The straight line gives the Sharvin conductance, while the curve through the data points is obtained from Wexler's interpolation formula, taking $\Gamma = 0.7$. The only adjustable parameter is the mean free path, for which $\ell = 3.8$ nm was obtained. Reprinted with permission from [363]. Copyright 2000 American Physical Society.

dure commonly applied in point contact experiments for 2DEG systems [14]. However, as was pointed out at the end of Sect. IX A 1 although this can be justified for 2D systems, it is less accurate for metallic leads that widen out to macroscopic size in three dimensions.

The dependence of the conductance of a contact on its diameter was tested in a direct measurement by Erts *et al.* [363]. They measured the size of contacts encountered in transmission electron microscopy images of an STM tip contact at room temperature in vacuum. The conductance measured simultaneously, was then plotted against the contact area, see Fig. 69. From a fit to the Wexler formula, Eq. (131) they obtain a value for the mean free path of $\ell = 3.8$ nm, which agrees closely with the value obtained from the conductance fluctuation analysis for gold contacts Sect. IX A 2). The agreement is perhaps better than one should expect, in view of the difference in experimental conditions, notably the temperature. The values for the mean free path obtained are much shorter than what is normally found for bulk samples, and can probably be attributed to scattering on defects and surface roughness near the contact, introduced in the process of mechanical contact formation. Assuming surface scattering is indeed responsible, an important property of the mean free path which has been neglected here is

that ℓ will not be a constant as a function of the conductance, but rather increase as the contact diameter becomes larger. However, this size dependence of the mean free path is not expected to be very significant as long as the contact size is smaller than ℓ .

It has been proposed in several places in the literature that all deviations from integer values in a conductance trace for the noble metals can be attributed to backscattering. Although the relatively short ℓ observed is responsible for a significant shift in the ensemble averaged conductance, it is still too long to hold backscattering responsible for the frequent measurement of non-quantized values. Also, if scattering is held primarily responsible for reducing the conductance from, e.g., a perfect conductance of $2G_0$ to $1.5G_0$, then it is not unreasonable to assume that contacts with a perfect conductance of $1G_0$ are reduced to $0.5G_0$ with a probability of the same order of magnitude. This is not observed (at least in the low-temperature experiments), as contacts with a conductance of $0.5G_0$ occur more than 500 times less frequent for silver and copper than contacts with a conductance of $1.5G_0$. (The formation of atomic chains, see Sect. XI, reduces this ratio to about 20 times in the case of gold, since the conductance of the chains is quite sensitive to distortions making contacts with a conductance of $0.5G_0$ occur with an enhanced frequency). If, on the other hand, one assumes that contributions from tunneling, e.g. due to geometrical considerations, are more important, the appearance of non-quantized values above $1G_0$ finds a natural explanation. The formation of geometries with a conductance smaller than $1G_0$ is highly unlikely since the smallest contact geometry is that of a single atom with conductance $1G_0$ and when the contact breaks, the banks relax back in a jump to tunneling (Sect. VB). On the other hand, defect scattering is clearly responsible for a shift of the peak positions, as was demonstrated in a study of Cu-Ni random alloys as a function of concentration [238]. The experiment also showed that a straightforward application of a series resistance correction does not work in the high-concentration regime.

C. Inelastic scattering

1. Electron-phonon scattering

When we say that a conductor is ballistic, we usually mean that its characteristic length L is much smaller than the mean distance between scattering events. However, this does not imply that scattering is entirely absent or unimportant. From the sections above it is clear that elastic scattering plays a role in atomic-sized contacts in reducing the average conductance and in producing random conductance fluctuations as a function of the applied bias voltage. In addition, at finite bias voltage the electrons can undergo inelastic scattering events, which leads to heating of the contact. This does not contradict the notion of a ballistic contact: the contact is

ballistic as long as the electrons travel on average a distance much larger than the contact size before scattering. When speaking about the most common form of inelastic excitations, the phonons, every electron that traverses the contact has a small, but finite, probability to deposit some of its energy in the lattice vibrations inside the contact itself.

Traditionally, electron-phonon spectroscopy in (large) metallic contacts is described by considering the non-equilibrium electron distribution near the contact that results from the applied bias voltage, as illustrated in Fig. 15 [62, 64, 65]. Electrons that arrive in the left electrode, coming from the right, are represented in a Fermi surface picture by a cone with an angle corresponding to the solid angle at which the contact is viewed from that position in the metal. These electrons have eV more energy than the other Fermi surface electrons, and they can be scattered inelastically to all other angles outside the cone. Only those that scatter back into the contact will have a measurable effect on the current.

As the energy difference eV increases this backscattering increases due to the larger phonon density of states, which will be observed as a decreasing conductance. Ignoring higher order processes, the decrease of the conductance comes to an end for energies higher than the top of the phonon spectrum, which is typically 20–30 meV. By taking the derivative of the conductance with voltage one obtains a signal that directly measures the strength of the electron-phonon coupling. An example for gold is illustrated in Fig. 2. One can derive the following expression for the spectrum, [65, 364]

$$\frac{d^2I}{dV^2} = \frac{4}{3\pi} \frac{e^3 m^2 v_F}{\hbar^4} a^3 \alpha^2 F_p(eV), \quad (133)$$

where a is the contact radius, and the function $\alpha^2 F$ is given by

$$\begin{aligned} \alpha^2 F_p(\epsilon) = & \frac{m^2 v_F}{4\pi \hbar^3} \int d^2 n \int d^2 n' |g_{nn'}|^2 \\ & \times \eta(\theta(\mathbf{n}, \mathbf{n}')) \delta(\epsilon - \hbar \omega_{nn'}). \end{aligned} \quad (134)$$

Here, the integrals run over the unit vectors of incoming and outgoing electron wave vectors ($\mathbf{n} = \mathbf{k}/|k|$), $g_{nn'}$ is the matrix element for the electron-phonon interaction, and η is a function of the scattering angle that takes the geometry into account, such that only backscattering through the contact is effective, $\eta(\theta) = (1 - \theta/\tan\theta)/2$. From this expression, and by considering Fig. 15, it is clear that the contribution of scattering events far away from the contacts is suppressed by the effect of the geometric angle at which the contact is seen from that point. The probability for an electron to return to the contact decreases as $(a/d)^2$, with a the contact radius and d the distance from the contact. This implies that the spectrum is dominantly sensitive to scattering events within a volume of radius a around the contact, thus the *effective volume* for inelastic scattering in the case of a clean opening (the contact) between two electrodes is proportional

to a^3 . Clearly, this effective volume must depend on the geometry of the contact. For a long cylindrical constriction, the electrons scattered within the constriction will have larger return probability, the effective volume, in this case, increases linearly with the length [365].

There is still very little theoretical work on phonon scattering in the quantum-size limit of point contacts. In this case, we must view the inelastic scattering process as mixing between the different conductance eigenchannels. Furthermore, as the contact becomes smaller, the signal will come from scattering on just a few atoms surrounding the contact. The spectrum will no longer measure the bulk phonons, but rather local vibration modes of the contact atoms. This is also what leads to the interest in measuring it. Bonča and Trugman [366] have introduced a formalism to calculate the interaction of tunneling electrons with localized inelastic excitations. This method was extended to the interaction of conduction electrons in a single-mode quantum wire with local vibration modes [137, 138, 367]. The extension to quantum conductors with many channels, allowing for transitions between the channels, has not been made, to our knowledge.

In attempting to measure the phonon signal for small contact sizes one encounters the problem that the phonon signal intensity decreases, according to (133), while the amplitude of the conductance fluctuations remains roughly constant, or slightly increases. The result is that the phonon signal is drowned in the conductance fluctuations for the smallest contacts. A solution to this problem is obtained for the special and interesting event of a contact made up of a single channel with nearly perfect transmission probability [361]. Indeed, for this situation according to (129) the conductance fluctuations are suppressed. Under these conditions the features due to phonon scattering become clearly visible, as illustrated in Fig. 70. Surprisingly, one observes a spectrum that still closely resembles the bulk phonon spectrum, although the relative intensities of the features in the spectrum are different. More interesting spectra are obtained for a chain of metal atoms, where the one-dimensional features can be clearly identified [368], as will be discussed in Sect. XI.

2. Heating in atomic-sized contacts

From the presence of a phonon signal in the current-voltage characteristics we deduce that there is a finite amount of heating of the lattice by the current. Nevertheless it appears to be possible to apply a voltage of up to nearly 2 V over a contact made up of a single gold atom without destroying it [361]. This gives an astonishingly high current density of $2 \cdot 10^9$ A/cm², which is more than five orders of magnitude higher than for macroscopic metallic wires. The reason that this is possible is, of course, that almost all of the electrical power $P = IV$ that is taken up by the junction is converted into kinetic energy of the ballistic electrons. On average, this excess

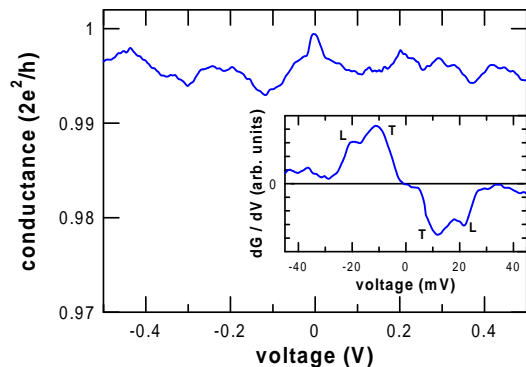


FIG. 70: Differential conductance as a function of the applied bias voltage for a one-atom Au contact at 4.2 K. The contact was tuned to have a conductance very close to $1 G_0$, which suppresses the amplitude of the conductance fluctuations. This allows the observation of a phonon signal, which is seen as a maximum at zero bias. Inset: By taking the derivative of the conductance the transverse (T) and longitudinal (L) acoustic branches can be recognized symmetrically positioned around zero. Note the expanded scale of the voltage axis in the inset. Reprinted with permission from [361]. Copyright 2000 American Physical Society.

kinetic energy is deposited into the phonon system away from the contact at a distance equal to the inelastic mean free path, l_i . Since l_i can be as large as $1 \mu\text{m}$ the thermal energy is strongly diluted in the banks on either side of the contact.

Experimental evidence for an increase in the lattice temperature of the contacts is obtained from the study of two-level fluctuations (TLF). As outlined in Sect. V A, when a contact is stretched one observes a sequence of steps in the conductance that are usually associated with hysteresis, at least when the contact has been ‘trained’ a little (Fig. 27). For other steps, such hysteresis is not observed, but instead the conductance shows spontaneous fluctuations of a two-level type, between the values before and after the step, also known as random telegraph noise. This phenomenon is observed only in a very narrow range of the piezo voltage controlling the contact elongation; at the plateaus the conductance assumes stable values. In some cases it is even possible to tune the ‘duty cycle’ of the TLF, i.e. the relative portion of the time spent in the upper compared to the lower state, by fine adjustment of the piezo voltage [58].

As illustrated in Fig. 27 the hysteresis becomes smaller, and can often be suppressed, by increasing the bath temperature. The same effect can be obtained by increasing the current through the contact. Once the hysteresis is fully suppressed, at still higher currents the system shows TLF, fluctuating between the conductance values of the plateaus left and right of the conductance step [169], as illustrated for a Cu contact in Fig. 71. The fluctuation rate increases very rapidly for larger currents.

The mechanism of these current-induced fluctuations can be understood as an energy transfer of the non-

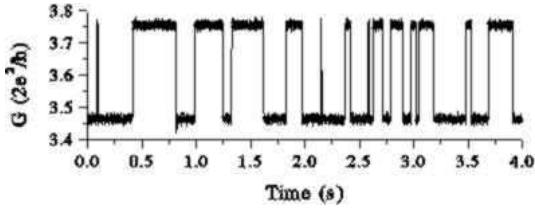


FIG. 71: Two-level fluctuation observed for a copper point contact measured with a bias current of $3\mu\text{A}$ at $T = 4.2\text{ K}$. From [369].

equilibrium electrons to the degrees of freedom of the atomic structure. The way atoms rearrange during breaking or making of the contact can be described in terms of a potential landscape in configuration space. The total potential energy $V(x_1, y_1, z_1; \dots; x_N, y_N, z_N)$ of the contact is a function of the position coordinates (x_i, y_i, z_i) of all N atoms making up the contact. The actual positions of the atoms in a given stable configuration correspond to a local minimum in this space. By pulling or pushing the contact we impose a subset of the atomic coordinates and the other coordinates rearrange to find a new minimum.

Before atoms actually rearrange, the configuration has to be lifted over an energy barrier E_B . This lifting corresponds to elastic deformation, while a jump over the barrier results in an atomic rearrangement. When we reverse the piezo-voltage sweep direction immediately after a jump, the contact can behave in two distinct ways: either the potential landscape is such that the previous configuration is the most favorable one, or a third nearby minimum presents itself. In the first case the result will be a closed loop of hysteresis. In the second case, the contact will take a different configuration, which is observed as a non-retraceable step [169]. In the latter case the contact will eventually search for the two lowest minima in the neighborhood, when the contact is cycled over a small range of the electrode displacement. After a few cycles the contact will then be ‘trained’ [90]. If E_B is low enough and the two available positions on both sides have nearly equal energy, thermally activated jumps back and forth will appear, manifesting themselves in the form of TLF, as in Fig. 71.

An estimate for the typical values of the barrier E_B can be obtained by considering the typical force jumps between two configurations, which we have seen in Sect. VI are of the order of 1 nN . Combining this number with the distance over which the contacts need to be stretched between two jumps, $\sim 0.1\text{ nm}$, we obtain $E_B \sim 1\text{ eV}$. From molecular dynamics simulations for atomic-sized contacts estimates in the range of 0.1 to 1 eV were obtained by Sørensen *et al.* [191]. They developed a method to calculate the lowest energy trajectory for an atomic structure in the transition between two stable states. Although it is not clear whether the calculated configurations are representative for a typical contact jump, it appears that $E_B \sim 0.1 - 1\text{ eV}$ is a reasonable value.

The fluctuation rate of the observed TLF as function of the current may be regarded as a local atomic-sized thermometer giving information on the heating inside the contact. A study of the temperature and current dependence of TLF was first done by Ralls, Ralph and Buhrman for larger nanofabricated contacts of fixed size, of the type described in Sect. II E [97, 370, 371]. For these larger contacts, the TLF are due to unknown defects somewhere in or near the contact. Most contacts show one or more TLF, but they have a distribution in activation energies that cannot be controlled. It was argued that a large collection of interacting TLF likely form a microscopic mechanism for the ubiquitous $1/f$ -noise in macroscopic conductors. Moreover, by studying the dependence of the fluctuations on the polarity of the voltage bias it was possible to show that the current exerts a net force on the defects. These forces are responsible for electromigration of defects known to occur in metallic systems that are subjected to long-term high current densities.

In Refs. [97, 370, 371] the fluctuation rate of individual TLF was measured, both as a function of temperature and as a function of the bias voltage. By combining values for the temperature and the bias voltage that give similar fluctuation rates they observed that the effective temperature of the two-level system could be described as $k_B T_{\text{eff}} = \gamma eV$, for $eV \gg k_B T$, with $\gamma \simeq 0.15$. Ralls *et al.* [370] proposed a model to describe these results that allows for energy exchange between the non-equilibrium electrons and the local fluctuator. They set up a rate equation that takes heating and cooling by the electrons into account, plus a parameter that allows for relaxation to the lattice.

For the nanofabricated contacts the effective temperature of the defect is higher than that of the lattice, because of the poor relaxation coupling to the bulk phonons. For atomic-sized contacts, however, the TLF presumably result from collective rearrangements of all the atoms that make up the contacts, so that this distinction does not exist. Todorov [372] has proposed to describe heating in atomic-sized contacts by regarding each atom as an independent oscillator, taking up energy from the electrons. The thermal energy that assists the atomic configurations responsible for TLF to cross the barrier is again given by γeV , with $\gamma = 5/16 = 0.3125$ in a simple free-electron approximation. However, relaxation of the vibrations by thermal conduction through the lattice cannot be neglected. The estimates Todorov makes for the local temperature including lattice thermal conduction are about an order of magnitude smaller, but the relevant parameters cannot be determined with great confidence.

In the limit of a classical point contact (Maxwell limit, Sect. III B) the Joule heating produces an effective temperature at the contact center given by [373]

$$T_{\text{eff}}^2 = T_b^2 + V^2/4L \quad (135)$$

This simple relation was derived by assuming that the

heat conductivity, κ , is dominated by the electronic part, and that this is related to the electrical conductivity, σ , by the Wiedemann-Franz law, $\kappa/\sigma = LT$, where L is the Lorentz number. For low bath temperature T_b , the effective temperature in the contact is proportional to the bias voltage V , and we obtain $k_B T = \gamma eV$ with $\gamma = 0.275$, which is not very different from the value of η for ballistic contacts quoted above.

Returning to the experiments in atomic-sized contacts, we note that the transition rate for jumps over the barrier is expected to be of Arrhenius form, $\nu = \nu_0 \exp(-E_B/k_B T_{\text{eff}})$. Here, ν_0 is the attempt frequency, which is of the order of phonon frequencies, $\sim 10^{13} \text{ s}^{-1}$; the Boltzmann factor $\exp(-E_B/k_B T_{\text{eff}})$ should be such that the TLF are observable on the laboratory time scale, i.e. have a minimal frequency of order 0.1 s^{-1} . Hence in order to observe TLF at the temperature of the helium bath, 4.2 K, we must have a barrier E_B smaller than about 0.01 eV. Since this is one or two orders of magnitude smaller than our estimate for E_B this explains why we observe mostly steps with hysteresis. For those events when spontaneous TLF at 4.2 K are observed a low-barrier fluctuating system must be present. This could perhaps be a single atom at the surface of the constriction with two equally favorable positions separated by a small distance.

The bias dependence of the switching rate has been investigated for TLF in Cu and Pt contacts in [26, 374]. For large bias voltages, the rate ν increases as a function of bias voltage and can be described by,

$$\nu = \nu_0 \exp\left(-\frac{E_B}{\alpha eV}\right), \quad (136)$$

as is illustrated in Fig. 72. This suggests that the effective temperature is indeed proportional to the bias voltage. However, for some TLS a cross over was observed at low voltages, where the rate becomes independent of the bias voltage. Assuming that this occurs when the local temperature αeV becomes of the order of the bath temperature, one obtains estimates for α of $\sim 0.1 - 0.5$ [369]. Adopting this estimate for α we conclude that for experiments performed at helium temperature, the lattice temperature at 100 mV is of order 100–500 K. Indeed, the fact that we can convert a hysteretic loop into a TLF by increasing the current implies that the thermal energy injected by the current into the two-state system must be considerable. Single-atom gold contacts have been found to survive bias voltages of nearly 2 V, for which the lattice temperature must approach the melting point. Note that we explicitly distinguish the lattice temperature from the electron temperature. At high bias the system is far from equilibrium and a true temperature can probably not be properly defined. Any effective values for the temperature of the lattice and that of the electron gas are expected to be very different and strongly position dependent.

In order to exploit TLF quantitatively as a local thermometer a single two-level system for a contact needs to

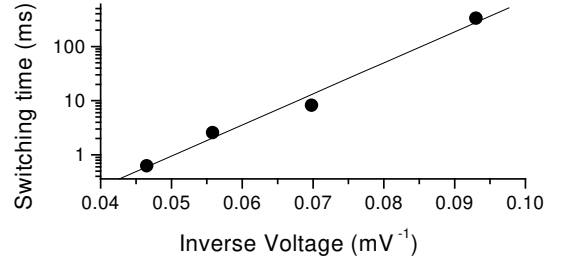


FIG. 72: Semi-logarithmic plot of the switching time as a function of the inverse bias voltage, for TLF in an atomic-sized Cu contact, with a mean conductance of $3.6 G_0$ at a bath temperature of 4.2 K. From [369].

be measured as a function of temperature *and* voltage. However, upon heating the contact appears to undergo uncontrolled changes that were attributed to thermal expansion of the substrate and the electrodes [374], and attempts at measuring the lattice temperature of the contact have not yet produced reliable results.

D. Kondo scattering on magnetic impurities

The Kondo effect is a prototypical electron correlation effect in condensed matter physics. It arises in dilute magnetic alloys due to the interaction between conduction electrons and the localized magnetic moments. This interaction gives rise to a minimum in the electrical resistivity as a function of temperature [375]. If the concentration of local moments is sufficiently small, the effect of interactions between the impurities is negligible and it is then appropriate to consider just a single impurity coupled to the conduction electrons. This problem, known as the ‘Kondo problem’, is by now well understood theoretically. The development of its solution started with the work by Kondo [376], continued with the scaling ideas of Anderson and the renormalization group analysis by Wilson, until the finding of exact solutions based on the Bethe ansatz [377]. However, a renewed interest in this problem has emerged in more recent years associated with the possibility of exploring ‘Kondo physics’ in nanofabricated devices [378, 379, 380, 381, 382].

The basic energy scale in Kondo physics is determined by the Kondo temperature T_K . This is related to the exchange coupling constant J between the conduction electrons and the local magnetic moment, and to the density of states at the Fermi energy, N_F , through $T_K = T_F \exp(-1/JN_F)$, where T_F is the Fermi temperature [383].

The use of point contact spectroscopy to study metals with magnetic impurities started almost two decades ago [384]. It revealed many features analogous to the well-known phenomena in the electrical resistivity of bulk alloys, the voltage playing the role of temperature in this analogy. With the development of the MCBJ technique it has become possible to study size effects in Kondo phe-

nomena for contact diameters decreasing from ~ 50 nm down to the atomic scale. Yanson *et al.* [385] reported a large broadening and increase of the relative amplitude in the zero bias maximum of the differential resistance for various noble metals (Cu, Au) doped with magnetic impurities (Mn) as the contact diameter was decreased. They interpreted their data as due to an enhancement of the exchange coupling parameter J , leading to a surprisingly large increase in the Kondo temperature T_K for small contact diameters. In a subsequent paper, van der Post *et al.* [386] using the same technique studied the case of Fe impurities in Cu and found a much weaker increase of T_K with decreasing contact diameter. It was also argued that the large variation in T_K observed in the first experiments [385] arises due to the application of the standard weak-scattering result, which breaks down for large T_K . This leaves still a very strong enhancement of T_K . A possible explanation was proposed by Zarand and Udvardi [387], where the increase of T_K was associated with fluctuations in the local density of states in the contact region.

The enhancement of the Kondo scattering observed in these experiments appears to contradict a suppression of the Kondo resistivity observed for thin-films and microfabricated wires of Kondo alloys [379, 388]. These results, in turn, were disputed by Ref. [380], where no size effect was detected at all. An explanation for size effects in terms of surface-induced anisotropies due to spin-orbit coupling was proposed by Ujsaghy and Zawadowski [389, 390], and they present arguments that may bring the various experiments into agreement. More recently, a very pronounced size effect in the thermopower of mesoscopic AuFe Kondo wires was discovered by Strunk *et al.* [391], that appears to agree with the proposed spin-orbit induced anisotropy near the surface of the wires.

Using a different experimental setup Ralph and Buhrman [378] were able to observe for the first time Kondo-assisted tunneling and simple resonant tunneling from a single impurity. The devices used by Ralph and Buhrman were nanofabricated Cu point contacts produced by the method described in Sect. II E. Although in most cases the electron transport in such devices is through the metal filament, on certain occasions they found in parallel a contribution due to tunneling via charge traps in the silicon nitride adjacent to the narrowest region of the Cu contact. Ralph and Buhrman identified this system as an experimental realization of the Anderson model out of equilibrium, a problem that has received considerable attention from theory [140, 392, 393, 394]. The presence of a charge trap in the silicon nitride gives rise to a very narrow peak in the differential conductance around $V = 0$, in agreement with the theoretical predictions for the Anderson model [140, 392, 393, 394]. The peak was shown to exhibit Zeeman splitting, which is unambiguous evidence that is due to a magnetic defect. The fact that the signal shows up as a peak in the conductance allowed to identify it as Kondo-assisted tunneling through the silicon nitride

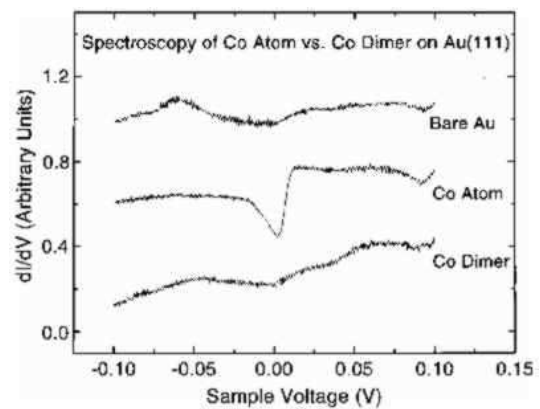


FIG. 73: dI/dV spectra obtained with an STM tip held over a single cobalt atom, an atomically fabricated dimer, and the clean gold surface. The curves are offset vertically for clarity. The Kondo resonance can be seen for the individual cobalt atom, but is absent for the dimer. Reprinted with permission from [396]. Copyright 1999 American Physical Society.

rather than scattering from a magnetic impurity within the Cu, which would produce a dip in the conductance at $V = 0$.

More recently, the use of scanning tunneling microscopes has allowed to study the Kondo effect on a single magnetic atom on a metal surface [382, 395, 396, 397]. One of the first experiments of this kind by Madhavan *et al.* [382] was performed on a Au(111) surface after deposition of 0.001 of a monolayer of Co. The dI/dV spectra taken in the vicinity of a single Co atom revealed the presence of a narrow feature (of the order of a few mV) around $V = 0$. Instead of a simple lorentzian peak Madhavan and coworkers observed a dip followed by a shoulder, a form which is characteristic of Fano resonances [398]. These type of resonances arise from the interference between two possible channels for tunneling between tip and sample. According to Madhavan *et al.* one channel would be provided by the Kondo resonance associated with d orbitals in the Co atom and the other would be due to the surrounding continuum of conduction band states. Similar findings were reported by Li *et al.* [395] for Ce atoms on Ag(111) surfaces. These authors showed that the Fano type resonances were not observed for nonmagnetic Ag adatoms. The systematic behavior of the dI/dV spectrum for 3d transition metal adatoms was studied by Jamneala *et al.* [397]. They found very pronounced features around $V = 0$ only for Ni, Co and Ti. No traces of a Kondo type resonance were found in the case of Fe, Mn, Cr or V, which can be explained by T_K being less than the experimental temperature of 6 K in these experiments. For the ‘end’ elements (Ni and Ti) the features around $V = 0$ could be due to a combination of the Kondo resonance and the bare d band resonances, which are closer to the Fermi energy for these elements.

The use of STM to study the Kondo effect on magnetic adatoms is even allowing us to analyze magnetic inter-

actions in man-made nanostructures obtained by atomic manipulation on a metal surface. Chen *et al.* [396] studied the case of artificially fabricated Co dimers on a Au (111) surface. They found an abrupt disappearance of the Kondo resonance for cobalt-cobalt separations less than 6 Å, a behavior attributed to the reduction of the exchange coupling between Au conduction electrons and the magnetic Co dimers (see Fig. 73). Kondo features in scanning tunneling spectroscopy have recently provided the basis for a striking demonstration of quantum coherence on a metal surface by Manoharan *et al.* [399]. They used atomic manipulation to create an elliptical ‘quantum corral’ of Co atoms on a Cu surface. When a Co atom was placed at one focus of the ellipse, the Kondo feature was detected not only at the atom but also at the empty focus. This focusing effect has been described as a ‘quantum mirage’.

E. Non-magnetic Kondo scattering: the 2-channel Kondo problem

In two seminal papers Ralph *et al.* [400, 401] reported the observation of a Kondo-like zero-bias anomaly in the differential conductance that could not be attributed to the presence of magnetic impurities. They studied Cu contacts, of the type described in Sect. IIE. The non-magnetic origin of the signals was illustrated by the absence of a splitting of the feature in an applied magnetic field. The shape of the dip in the conductance was not logarithmic in bias voltage V , or temperature T , as would be expected for a Kondo minimum. In stead, a $T^{1/2}$ and $V^{1/2}$ dependence was observed, with the appropriate scaling behavior that is expected for a 2-channel Kondo system [402]. It was argued that defects in the contact that act as fast (low transition barrier) two-level tunneling systems form the active scattering systems. It had been proposed earlier that such two level-systems are candidates to show 2-channel Kondo behavior [403, 404].

A strong argument in favor of an interpretation in terms of fast TLF was found in the fact that the signals disappear when the samples are kept (annealed) at room temperature for a few days. Further support comes from experiments on point contacts made by the MCBJ technique on metallic glasses, where a high concentration of TLF centers is expected [405, 406]. However, Wingreen *et al.* [407] raised a number objections against this interpretation, and proposed an alternative mechanism in terms of electron-electron interactions enhanced by defect scattering. Although strong arguments were given in the reply [408] that refute the alternative model, the discussion is still not completely settled. The amplitude of the signal implies that many (of order 10 or more) TLF should contribute to the signal. Furthermore, the two-level systems should have a very narrow distribution of separation of the energy levels in the two available states, at a very low value. It remains to be demonstrated that such systems exist in large concentrations.

The nature of the defects involved in producing the signals is also not yet established. A serious candidate was proposed by Vegge *et al.* [409], who showed by molecular dynamics calculations that dislocation kinks in a copper crystal have appropriately low energy barriers and low effective masses to allow fast quantum tunneling. For further information we refer the reader to two recent extensive review papers by von Delft *et al.* [410, 411].

F. Environmental Coulomb blockade

A common simplifying assumption in the analysis of electron transport in quantum coherent structures is that the system is connected to an ideal voltage source. In practice the voltage source is never ideal but contains a finite internal impedance $Z(\omega)$. At the same time, an atomic-sized contact will have a certain capacitance C . Although the capacitance associated strictly with the atomic-sized conductor is in theory extremely small (of the order of an aF, see Ref. [412]), the capacitance C will be dominated by the contribution of the much wider leads in which the atomic conductor is embedded. The value of C depends thus greatly on the fabrication technique that is used. In the case of microfabricated break junctions C is typically of the order of one fF.

In principle, one should take both C and $Z(\omega)$ into account in determining the transport properties of the contact. At low temperatures the voltage across the contact develops quantum fluctuations and the electrical properties of the circuit cannot be inferred from the conductance of the separate elements. This problem has been extensively studied in the case of small tunnel junctions, where the conductance of the series circuit can be completely suppressed at sufficiently low voltages and temperatures. This phenomenon is called *environmental* Coulomb blockade (for a review see Ref. [413]). Qualitatively, it arises when the impedance of the environment is high enough that the charge of a single electron tunneling across the junction leaks away only slowly. In that case the charging energy associated with the contact capacitance $E_C = e^2/2C$ starts to play a role, which results in a suppression of the tunneling current when both the applied bias, eV and the temperature $k_B T$ are smaller than E_C .

A question which has been recently addressed in the literature [414, 415] considers how this phenomenon is modified when one replaces the tunnel junction by a generic quantum coherent structure. The case of an atomic-sized contact is particularly interesting as it provides a system characterized by a few conduction channels whose transmissions can be determined using the techniques discussed in Sect. VIIIA. Moreover, the impedance of the environment embedding such contacts can be tuned within a desired range using nanolithography [162].

A simple argument can be used to demonstrate that the environmental Coulomb blockade in such systems should disappear when the perfect transmission limit

is reached. As we have seen, a quantum point contact is characterized by a current fluctuation spectrum, which at low frequency and zero temperature is given by $S = 2eVG_0 \sum \tau_i(1 - \tau_i)$. One may then speculate that when the transmissions approach unity the contact cannot be ‘felt’ by the series impedance $Z(\omega)$ and, conversely, the transport properties of the contact should not be affected by the presence of a series impedance. In fact, rigorous calculation predicts that the Coulomb blockade features in the current-voltage characteristics should vanish for perfect transmission in the same way as shot noise does [415].

In Ref. [415] environmental Coulomb blockade for a single channel contact of transmission τ in series with an arbitrary frequency-dependent impedance $Z_t(\omega)$ (including the contact capacitance, i.e. $Z_t^{-1}(\omega) = Z^{-1} + i\omega C$) was studied starting from a model Hamiltonian and using the Keldysh Green function technique. It was shown that the correction to the contact conductance, δG , to the lowest order in $Z_t(\omega)$ is given by

$$\frac{\delta G}{G} = -G_0(1 - \tau) \int_{eV}^{\infty} d\omega \frac{\text{Re}[Z_t(\omega)]}{\omega}. \quad (137)$$

It should be noted that the correction to the conductance is affected by the same reduction factor, $(1 - \tau)$, that applies for shot noise (see Sect. III D 3). In the simple but realistic case for which the impedance $Z_t(\omega)$ is composed by the resistance R of the leads embedding the contact in parallel with the capacitance C of the contact itself, the integral in (137) yields

$$\frac{\delta G}{G} = -G_0 R(1 - \tau) \ln \sqrt{1 + \left(\frac{\hbar\omega_R}{eV}\right)^2}, \quad (138)$$

where $\omega_R = 1/RC$. At finite temperature the singularity in Eq. (138) at $V = 0$ becomes progressively rounded. The finite temperature version of this equation can be found in [416].

In order to verify these predictions Cron *et al.* [416] fabricated an atomic contact embedded in an electromagnetic environment essentially equivalent to a pure ohmic resistor of the order of 1 k Ω , defined by e-beam lithography. The material chosen for both the atomic contact and the series resistor was aluminum, which allowed them to extract the channel composition, or the ‘mesoscopic PIN code’ $\{\tau_1 \dots \tau_N\}$ for the contacts, using the techniques discussed in Sect. VIII A. The environmental Coulomb blockade was then measured in the presence of a 0.2 T magnetic field which brings the sample in the normal state. The results for two contacts with very different transmissions are shown in Fig. 74. The standard theory of environmental Coulomb blockade [418] is able to account for the results obtained for the contact in the left panel, which has a single weakly transmitted channel. On the other hand, for the contact in the right panel, with one well-transmitted channel ($\tau \simeq 0.83$) the relative amplitude of the dip at zero bias is markedly reduced with respect to the tunnel limit predictions (dashed line). The

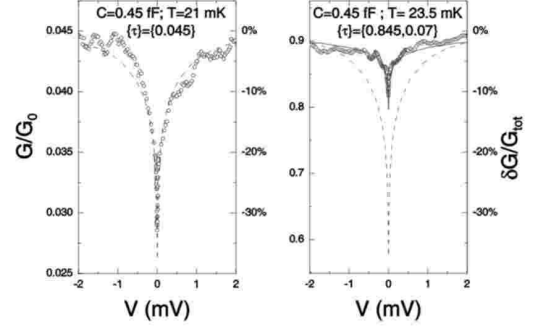


FIG. 74: Measured differential conductance curves for two atomic contacts. The scale of the left axis applies for the measured data points (circles), in units of G_0 . In the left panel the contact consists of a single weakly transmitted channel, and the conductance around zero bias is well-described by the standard theory of environmental Coulomb blockade, valid for tunnel contacts, as expected (dashed curve, right axes, relative to the total conductance) [417]. In the right panel, the contact has a well-transmitted channel with $\tau_1 = 0.835$ plus a second smaller contribution $\tau_2 = 0.07$. In this case, the relative reduction of conductance is much less than expected from the expression for tunnel junctions and is in agreement with the predictions of Eq. (137) (full curve). The wiggles and asymmetry seen in the experimental curves are reproducible conductance fluctuations due to the interference effects discussed in Sect. IX A. Reprinted with permission from [416]. Copyright 2001 EDP Sciences.

experimental results are in good agreement with the predictions of Ref. [415] summing the contributions of all channels (solid line).

In spite of this qualitative understanding, the issue of Coulomb blockade in atomic sized contacts remains to be explored in further detail.

X. SUPERCONDUCTING QUANTUM POINT CONTACTS

In Sect. VIII we discussed the experiments on the IV characteristic of superconducting atomic contacts and their use to extract information on the conductance modes. In this section we shall analyze another series of experiments in superconducting contacts. Most of these experiments have been conducted in order to test some of the theoretical predictions presented in Sect. IV, like the quantization of the supercurrent through a narrow constriction, the supercurrent-phase relation for arbitrary transmission and the increase of shot noise associated with multiple Andreev reflections.

A. Supercurrent quantization

A rather straightforward consequence of the quantization of the conductance in a smooth constriction with a cross section comparable to the Fermi wavelength is the quantization of the supercurrent when the constriction connects two superconducting leads [154]. For such ideal system the supercurrent should be quantized in units of $e\Delta/\hbar$.

Although this prediction was originally proposed for a 2DEG device it was soon realized that it should be also valid for a superconducting atomic contact provided the condition of conductance quantization was reached. The first experiments in this direction were performed by Muller *et al.* [26] who studied Nb contacts made by the MCBJ technique. They measured the critical current (defined as the current value at a set point voltage near $V = 0$) at 1.2 K while the piezo voltage was varied periodically. In the scans for rising piezo voltage they observed steps in the critical current of a size close to $e\Delta/\hbar$. In another experiment, reducing the range of the piezovoltage scans they measured simultaneously I_c and R_N . Their results are shown in Fig. 75. As can be observed, the steps in I_c are correlated with steps in R_N at the same positions. The variations of 50% in I_c and R_N separately are reduced to variations of only 7% in the product. The average value for $I_c R_N$ was 1.75 ± 0.05 mV, which is of the same order but considerably smaller than the predicted value $\pi\Delta/e$. A reduction of $I_c R_N$ below the theoretical value was also observed in a systematic study [24]. The authors suggested thermal or quantum fluctuations as a possible source for this discrepancy. In a subsequent study Muller and de Bruyn Ouboter [419] analyzed the slope in the supercurrent branch and the maximum current near zero voltage that they called threshold current. As discussed in Sect. IV D, the slope and the actual value of this maximum current is very sensitive to the electromagnetic environment in which the contact is embedded.

Finally, in Ref. [420] it was shown that the threshold current for a one-atom contact exhibits large variations even when the normal conductance is nearly constant. As already pointed out in Sect. VIII A, even when the total conductance is fixed the channel decomposition can fluctuate. This points towards the need of more controlled experiments in which the channel content of the contact be determined while measuring the supercurrent.

B. Current-phase relation

An even more ambitious goal than the measurement of the critical current is the measurement of the whole current-phase relation (CPR) in a superconducting point contact. In Sect. IV we have already discussed the different theoretical predictions for the CPR ranging from tunnel junctions to ballistic contacts. In this last case one expects a non-sinusoidal behavior with a maximum

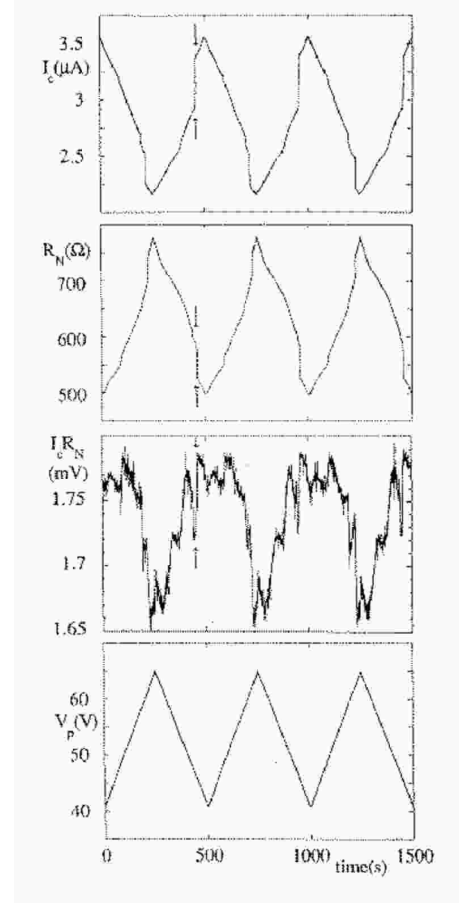


FIG. 75: Critical current and normal-state resistance measurement for a periodic variation of the piezo voltage. The fine structure in I_c lines up with that in R_N . The relatively large changes in I_c and R_N at the steps almost compensate the other in the product $I_c R_N$. Reprinted with permission from [26]. Copyright 1992 American Physical Society.

at $\phi = \pi$ [421]. Again, atomic contacts have been viewed as ideal tools to test these predictions in the quantum regime. The measurement of the CPR requires, however, a rather sophisticated setup in which the phase can be fixed by an external magnetic flux.

To this end, Koops *et al.* [422] fabricated superconducting loops of micrometric size in which a MCBJ was placed. They used Nb and Ta foils and laser cutting techniques. On top of the loop they placed a flux-detection coil which allowed for measuring the CPR inductively. The enclosed area of the loop was chosen such as to have a small self-inductance (smaller than 1 nH). This condition is necessary to prevent a multivalued relation between the external flux, Φ_e , and the total flux through the loop $\langle\Phi_t\rangle$ (observed mean value). Φ_e and $\langle\Phi_t\rangle$ differ due to the presence of the self-induced flux $\langle\Phi_s\rangle = L\langle I_s\rangle$, where L is the self-inductance of the loop, i.e. $\langle\Phi_t\rangle = \Phi_e + \langle\Phi_s\rangle$. The mean phase difference $\langle\varphi\rangle$ over the contact is equal to $-2\pi\langle\Phi_t\rangle/\Phi_0$ where $\Phi_0 = h/2e$ is the flux quantum. By measuring $\langle\Phi_t\rangle$ for a given value of Φ_e the self-induced

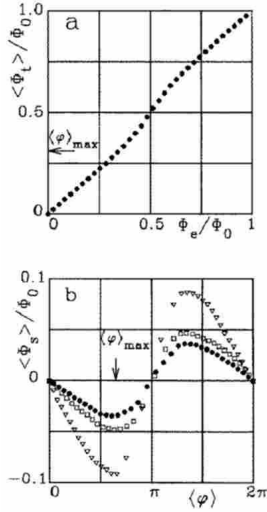


FIG. 76: Determination of the current-phase relation in the experiment by Koops *et al.* The relation between the total flux $\langle \Phi_t \rangle$ and the applied flux Φ_e (shown in (a)) allows to determine the self-induced flux $\langle \Phi_s \rangle$ which is proportional to the current. Reprinted with permission from [422]. Copyright 1996 American Physical Society.

flux, which is proportional to the current, can be detected. An example of the measured $\langle \Phi_t \rangle$ vs. Φ_e relation is shown in Fig. 76a for Nb at 1.3K. Fig. 76b shows the corresponding $\langle \Phi_s \rangle$ vs. $\langle \varphi \rangle$ relation.

Although the measurements were performed on the last contact before jump to the tunnel regime, none of the measured CPRs was found to correspond to the theoretical predictions for perfect transmission. In particular, the position of the maximum current in the CPR (ϕ_{max}) was found to be displaced towards lower values with respect to the theoretical predictions. The authors attributed this fact to thermal fluctuations and to the impossibility to reach perfect transmission for such contacts. A theory of the displacement of the maximum in the CPR of a ballistic contact due to thermal fluctuations was presented in [423]. In this theory the amplitude of the phase fluctuations is controlled by the self-inductance of the loop and decreases for decreasing inductance. Koops *et al.* observed that ϕ_{max} tended to the expected theoretical value at perfect transmission for decreasing inductance. Their analysis suggested that the contact transmissions should be somewhere between 0.9 and 1.0.

The impossibility to determine the contact transmissions independently was clearly one of the main limitations of the experiments by Koops *et al.* [422]. The more recently developed techniques to extract the information on the conductance modes, discussed in Sect. 8, could ideally be combined with loop measurements to test the predictions of the theory for the CPR in atomic contacts. Although this is still an open challenge for the experimentalists, recent work by Goffman *et al.* [162] constitutes an

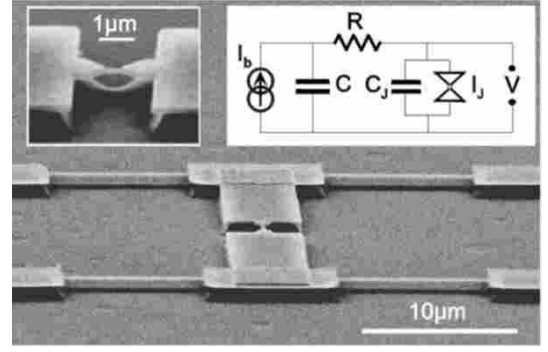


FIG. 77: Micrograph of the experimental setup used in Ref. [162] to study the supercurrent in an atomic contact. Each probe contains a AuCu resistor (thin lines of $10 \mu\text{m}$ length) and a large capacitor with the metallic substrate. The left inset shows a close-up of the microfabricated MCBJ and the right inset illustrates the equivalent circuit.

important step in this direction. This work will be discussed below.

Goffman *et al.* studied the supercurrent in aluminum microfabricated MCBJs. In order to have good control of the thermal and quantum fluctuations they designed an on-chip dissipative environment with small resistors of known value placed close to the atomic contact in a four probe geometry. A micrograph of the device is shown in Fig. 77. With the correct choice of the environment parameters the current-voltage curve becomes hysteretic, which allows detecting the supercurrent and the dissipative branch simultaneously. This in turn permits the determination of the set of transmission values $\{\tau_i\}$ for the modes in each atomic contact by the analysis of the subgap structure as discussed in Sect. VIII A. This ‘mesoscopic PIN code’ [351] fully characterizes the junction. A typical IV recorded in this work is shown in Fig. 22.

Goffman *et al.* concentrated in the analysis on the threshold or switching current I_S at which the jump from the supercurrent branch to the dissipative branch takes place. The switching takes place close to the maximum in the supercurrent branch just before the region of negative differential resistance. This value is very sensitive to thermal fluctuations and decreases with increasing temperature. The experimental results for the switching current can be analyzed in terms of a generalized RSJ model discussed in Sect. IV D. The corresponding Langevin equations were numerically integrated and using the set $\{\tau_i\}$ that characterizes the contact this was shown to fit the experimental results without any adjustable parameter, as is illustrated in Fig. 78. An excellent agreement is found except for contacts having a well transmitted channel (with transmissions between 0.95 and 1.0). In this last case it is found that the switching current is less sensitive to thermal fluctuations than predicted by the theoretical model. Landau-Zener transitions between the lower and the upper Andreev states were pointed out as

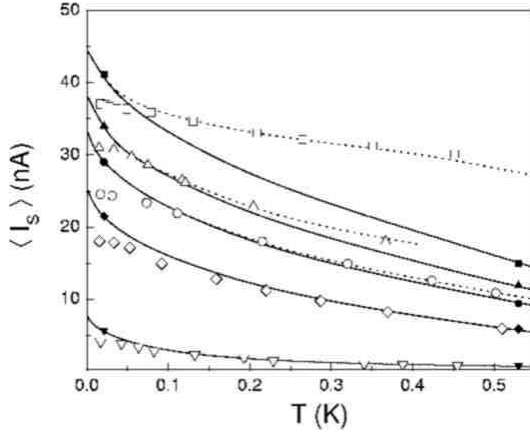


FIG. 78: Experimental (open symbols) and theoretical (lines) results for the switching current obtained in Ref. [162]. The results correspond to one atom contacts with different channel content. (∇) $\{\tau_i\} = \{0.21, 0.07, 0.07\}$. From the fit a zero-temperature supercurrent of $I_0 = 8.0 \pm 0.1$ nA is obtained. (\diamond) $\{\tau_i\} = \{0.52, 0.26, 0.26\}$, $I_0 = 25.3 \pm 0.4$ nA. (\circ) $\{\tau_i\} = \{0.925, 0.02, 0.02\}$, $I_0 = 33.4 \pm 0.4$ nA. (\triangle) $\{\tau_i\} = \{0.95, 0.09, 0.09, 0.09\}$, $I_0 = 38.8 \pm 0.2$ nA. (\square) $\{\tau_i\} = \{0.998, 0.09, 0.09, 0.09\}$, $I_0 = 44.2 \pm 0.9$ nA. The full lines are the predictions of the adiabatic theory and the dotted lines correspond to the non-adiabatic theory, which allows for Landau-Zener transitions between Andreev states. Reprinted with permission from [162]. Copyright 2000 American Physical Society.

a possible source for this effect.

Although quite indirectly, the experiments by Goffman *et al.* provide a test of the theoretically predicted CPR in atomic contacts. An interesting aspect of these experiments is that all the relevant parameters in the problem could be determined independently, which opens very promising perspectives for future studies.

C. Shot noise in the subgap regime

As discussed in Sect. IV C, the subgap structure in the IV curve of a SNS junction can be understood in terms of multiple Andreev reflection processes. A fundamental question, which is attracting growing attention in recent years, is that regarding the statistics of the transferred charge associated with these quantum mechanical processes. Shot noise measurements can provide a first insight into this problem by the determination of the effective transferred charge q as the ratio $q = S/2I$ between the shot noise value S and twice the average current I . Taking into account that at a given subgap voltage V the current is mainly due to MAR processes of order $n \sim 2\Delta/eV$ in which a net charge ne is transferred, one can expect that q increases at low bias roughly as $1/V$.

These ideas were first explored in an experiment by Dieleman *et al.* in 1997 [424]. They measured the shot noise in NbN/MgO/NbN tunnel junctions with small de-

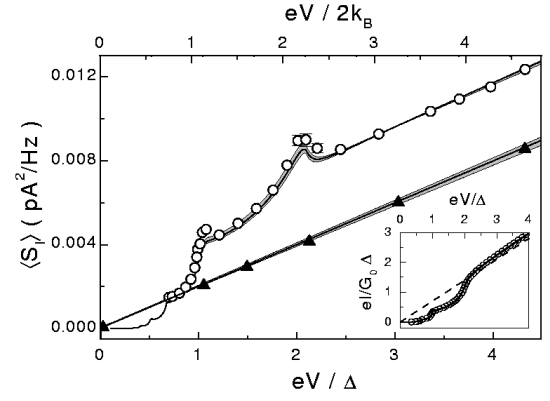


FIG. 79: Measured current noise power density versus voltage for a typical contact both in the normal (triangles) and in the superconducting state (circles) for a single-atom Al contact at $T = 20$ mK. The solid lines are predictions using Eq. (27) for the normal state and using the theory of Ref. [124] for the superconducting state. Inset: IV in the superconducting state. The solid line is a fit which provides the values $\{\tau_i\} = \{0.40, 0.27, 0.003\}$ for the transmissions. Reprinted with permission from [351]. Copyright 2001 American Physical Society.

fects in the oxide barrier acting as ‘pinholes’. Due to these defects the system consisted basically of a set of SNS point contacts in parallel. This interpretation was confirmed by the observation of a finite subgap current exhibiting the typical structure at $eV = 2\Delta/n$. In spite of the rather large error bars in the noise determination, it was possible to observe a clear increase of the effective charge $q = S/2I$ at low bias voltage. Dieleman *et al.* developed a qualitative explanation of their experimental data within the framework of the semiclassical theory of MAR given in Ref. [38].

The increase of the effective charge at low voltages was also observed by Hoss *et al.* [425] in diffusive SNS junctions. They used high transparency Nb/Au/Nb, Al/Au/Al and Al/Cu/Al junctions prepared by lithographic techniques. Although being diffusive, the normal region in these junctions was smaller than the coherence length L_ϕ , which allows to observe the *coherent* MAR regime. On the other hand, the junctions presented a very small critical current, which permitted to reach the low voltage regime. The excess noise in these experiments exhibited a pronounced peak at very low voltages (of the order of a few μV) which leads to an effective charge increasing much faster than $1/V$. It should be pointed out that there is at present no clear theory for the shot noise in diffusive SNS junctions in the coherent MAR regime.

As we have emphasized throughout this review, atomic-sized contacts provide an almost ideal situation where theory and experiments can meet. Fully quantum mechanical calculations are available for the low frequency noise in a single channel superconducting point contact with arbitrary transmission [124, 125]. On the

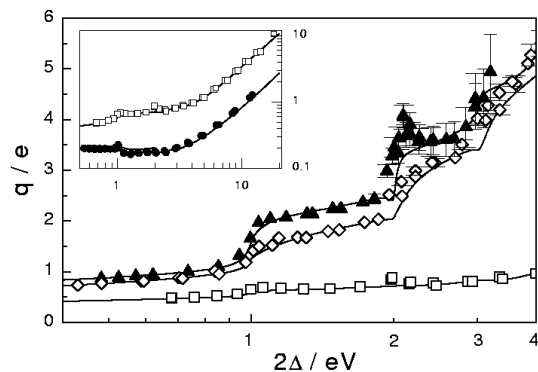


FIG. 80: Effective charge $q = S/2I$ versus reduced inverse voltage for three different single-atom Al contacts in the superconducting state. The symbols are experimental results and the solid lines are the predictions of the theory of MAR for noise. From top to bottom the corresponding set of transmissions are $\{0.40, 0.27, 0.03\}$, $\{0.68, 0.25, 0.22\}$ and $\{0.98, 0.55, 0.24, 0.22\}$. Inset: data for two contacts containing a channel close to perfect transmission (top $\{0.98, 0.55, 0.24, 0.22\}$, bottom $\{0.996, 0.26\}$) shown over a wider range. Reprinted with permission from [351]. Copyright 2001 American Physical Society.

other hand the channel content of an actual contact can be extracted using the technique discussed in Sect. VIII A allowing for a direct comparison between theory and experiments without any fitting parameter. This was the strategy followed in the work by Cron *et al.* [351], already discussed in connection with shot noise in the normal state in Sect. VIII B.

In a second step, Cron *et al.* measured the noise in the superconducting state. Fig. 79 shows the comparison between the experimental results and the theoretical predictions of Refs. [124, 125], using the measured PIN code $\{\tau_i\}$ as the input parameters. As can be observed, the agreement between theory and experiment is quantitative. The structure in the noise as a function of voltage has the same physical origin as the subgap structure in the IV , i.e. it is due to multiple Andreev reflection processes having a threshold at $eV = 2\Delta/n$. This is better visualized by analyzing the effective transmitted charge $q = S/2I$ as a function of the inverse voltage, as shown in Fig. 80. As can be seen, q/e does not necessarily correspond to integer values and for a given voltage it strongly depends on the set of transmissions. Only in the tunnel limit, $\tau_i \rightarrow 0$, the theory [124] predicts $q/e \rightarrow \text{Int}[1 + 2e\Delta/V]$. Although this limit cannot be reached experimentally, the emergence of a staircase pattern in q for decreasing values of the transmissions can be clearly recognized in Fig. 80. This work thus provides strong support for the quantum theory of electronic transport in superconducting point contacts developed in recent years.

XI. FORMATION OF A CONDUCTING WIRE OF SINGLE ATOMS

In the October 22 issue of Nature 1998 two independent groups demonstrated that chains of atoms self-assemble when thinning the contact diameter for gold nanocontacts [53, 54]. The atomic wires have a conductance very close to the quantum unit G_0 , sustain very large currents, and can be held stable for very long times at low temperatures. The formation of these atomic structures was unexpected, and many new properties are predicted.

One-dimensional conductors of different kinds have been investigated intensively in recent years. Foremost are the carbon nanotubes [6], which have a structure that can be viewed as a rolled-up graphite sheet. Other types of molecular conducting wires have been investigated, including Mo_6Se_6 [426]. Even electrical conduction across more complicated molecular wires, notably strands of DNA molecules, has been reported [7, 8]. The molecular structure of all these systems provides stability at room temperature and above, and a rich spectrum of physical properties has been investigated, in particular for the carbon nanotubes.

Ultimately-thin wires of individual carbon atoms have been prepared by chemical methods. The fabricated substances contain carbon chains up to 20 atoms in length (see [427] and references therein). Similarly, inorganic chemistry has allowed the preparation of a compound containing regular arrays of silver metallic wires [428]. As yet another example, chains of metal atoms have been found to self-assemble when adsorbed at the surface of other metals or semiconductors, in many cases at step edges [429, 430, 431]. For these metallic wire systems it has not yet been possible to contact individual wires, to our knowledge.

Although each of these one-dimensional conductors is of great interest, the metallic wires discussed here have a number of aspects that make them particularly attractive. First, they are freely suspended so that there is no complicating interaction with a substrate, which facilitates comparison with theory and enhances the one-dimensional character. Second, by their nature they are already connected to metallic leads, allowing straightforward measurement of the electrical transport properties of an individual atomic chain.

Among the experiments preceding the two 1998 papers the experiment by Yazdani *et al.* [56] comes closest to this ideal. These authors used STM-manipulation techniques to fabricate a two-atom chain of Xe atoms between the tip of an STM and a metallic substrate. Although the results showed a favorable agreement with calculated conductance characteristics, the electronic structure of Xe leads to a rather poor transmission, i.e. a conductance several orders of magnitude below the conductance quantum, and the method is not easily extended to longer wires or other materials.

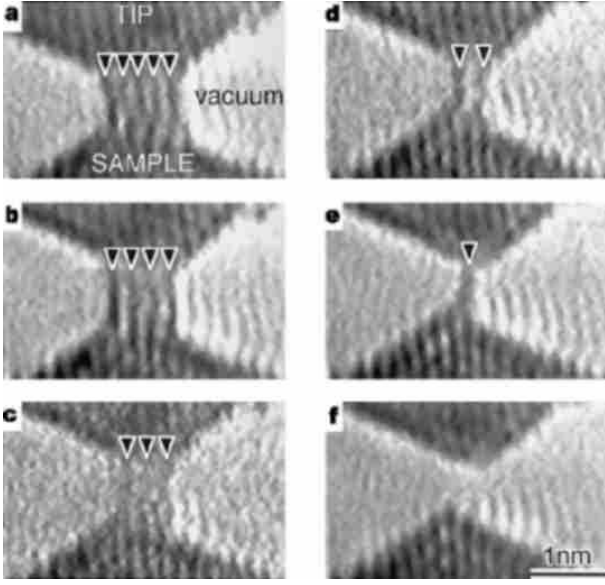


FIG. 81: TEM images of a gold contact recorded while withdrawing the tip from the sample. A gold bridge formed between the gold tip (top) and the sample (bottom) thins down when going from (a) to (e), where the conductance drops to $2G_0$. The contact finally ruptures at (f), for which the conductance drops to zero. The recording takes 33 ms per frame and the images are taken at times 0, 0.47, 1.23, 1.33, 1.80 and 2.17 s, respectively. Reprinted with permission from Nature [54]. Copyright 1998 Macmillan Publishers Ltd.

A. Atomic chains in Transmission Electron Microscopy

By High Resolution Transmission Electron Microscopy (HR-TEM) imaging it is possible to resolve individual atoms for the heavier elements. Ohnishi, Kondo and Takayanagi [54] exploited this capability by combining their ultra-high vacuum HR-TEM setup with two different manipulation techniques to produce atomic wires. First, they constructed a miniature STM that fits into the specimen space of the TEM. It is fascinating to see the atomically-resolved video images they show of a tip scanning a sample surface, and subsequently indenting it. When retracting a gold tip from a gold sample the team observed that the connecting bridge gradually thins down, see Fig. 81. All experiments are performed at room temperature, giving the atoms enough mobility to optimize the configuration, and as a result it is seen that the bridge connecting the two electrodes, oriented along the [110] direction, often consists of a straight wire section. As the number of atomic rows in the connecting nanowire decreases the conductance is also seen to decrease in a step-wise fashion, as expected. The conductance of a one atom strand in the images is close to $2e^2/h$. However, twice this value is also found, and it is argued that this is due to a double strand overlapping in the viewing direction. Evidence for this interpretation is obtained by analyzing the contrast profile in the images.

In order to resolve the individual atoms in the chain a second technique was employed. Here, the STM was replaced by a very thin gold film specimen, where an intense electron beam current was used to melt two adjacent holes in this film. For (110) oriented films a gold bridge along the [001] direction between these two holes was seen to evolve into an atomic chain that survived for about two minutes, see Fig. 82. Note that in this configuration the conductance of the chain cannot be measured. Remarkably, the spacing between the atoms in the chain was found to be 0.35–0.40 nm, much larger than the nearest neighbor distance in bulk gold (0.288 nm). This is much larger than any model calculation predicts, since the overlap between the electron clouds of the gold atoms is too small to provide sufficient stability for the atomic chain. Several explanations have been put forward. One proposal is based on the observation that the calculated equilibrium structure for a Au monatomic chain appears to have a zigzag geometry, as will be discussed in Sect. XID below. Sánchez-Portal *et al.* [55] proposed that every second atom in the zigzag chain could be thermally excited into a spinning motion around the chain axis, which would blur their image. Koizumi *et al.* [432] show by comparison of the experimental images to simulations that a spinning zigzag geometry can be excluded based on the expected smeared image of the spinning atoms. Other explanations involve the inclusion of ‘glue atoms’, such as C, O, or S [332, 433, 434, 435]. The simulations [432] suggest that adatoms of Si and S would be resolved, but the contrast for C (and presumably O) would not exceed the noise level. Only minute amounts of contaminants are required, since the regular gold surface is not very reactive, while the low-coordination gold atoms in the chain bind strongly to different species, as shown by first-principles calculations [332, 433, 434]. Despite the high vacuum conditions of the experiment, there will be small amounts of adsorbed molecules running over the surface, and these will stick preferentially at the strong binding sites in the gold chain. Oxygen would be a good candidate, since it would not be resolved in the images and the calculations suggest that a Au-O-Au-O chain would have Au-Au distance close to the observed values and the chain would be conducting, with a single open channel [433, 434]. It would be interesting to test this suggestion experimentally.

The experimental observation of the atomic chain formation and the long inter-atomic distances have been confirmed in an independent experiment by Rodrigues and Ugarte [106], using the thin-film double-hole technique at 10^3 times higher residual gas pressure. Similarly, these authors claim that the spinning zigzag structure can be excluded based on the absence of ghost features. Short chains have also been seen for silver [214], although much less frequent than for gold, and the large and irregular bond lengths observed suggest the presence of light interstitial atoms that may stabilize the chains [435]. In high resolution images taken with a new generation defocus-imaging modulation processing electron

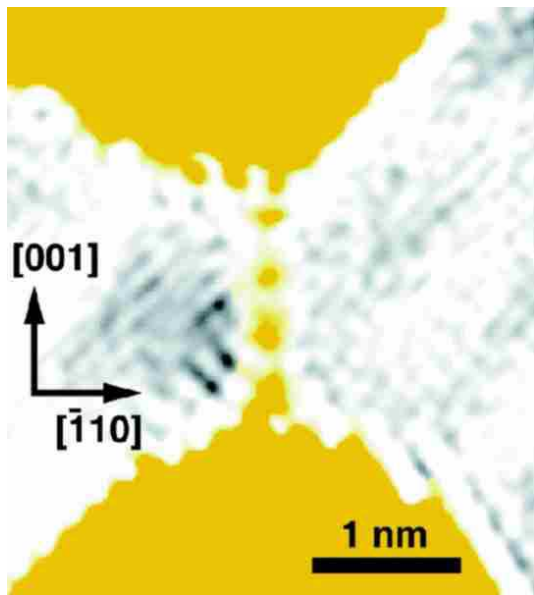


FIG. 82: TEM image of a gold atomic chain (four colored dots) forming a bridge between two gold banks (colored areas; the colors have been edited for clarity). Reprinted with permission from Nature [54]. Copyright 1998 Macmillan Publishers Ltd.

microscope by Takai *et al.* [267] much smaller Au-Au distances of 0.25-0.29 nm were found. The vacuum pressure was comparable to that of [106].

A further study by Kizuka *et al.* [268] appears to be at variance with most of the earlier results. Here, a miniature STM is operated inside a HR-TEM at regular-vacuum conditions. Again, for gold it is frequently observed that upon separation of the contact between tip and sample it ends with the formation of a chain of atoms. Similar to the results of Takai *et al.*, a distance of only 0.27 ± 0.02 nm was obtained between the atoms in the chain, which can be stretched at the break point to 0.30 ± 0.02 nm. Surprisingly, the atomic wires were found to be insulating. At the moment when the structure is seen to jump from a multi-atom cross section to a single-atom chain the conductance drops to zero. Moreover, the chains were found to be bent even under stretched conditions. Very long atomic chains, up to 10 atoms in a row, were observed, that were stable for longer times than reported before. Although the authors make a few suggestions to explain these observations, the discrepancy with the other experiments was not addressed.

We propose that these observations can be understood if we assume the presence of specific adsorbates. As shown by Bahn *et al.* [433, 434], CO binds strongly to the gold chain, turns it into an insulator, introduces kinks in the wire, and the CO bonded gold chain has the lowest energy among all the structures investigated. This would suggest that CO, or another contaminant of similar nature, is present in the vacuum space. At a typical pressure of 10^{-5} Pa the probability of this mechanism is

high.

B. Atomic chains in low-temperature experiments

The second paper in the 1998 issue of Nature used different techniques in several important aspects [53]. The atomic structure was not imaged directly, but the formation of chains was deduced from the experimental observations of the conductance as a function of stretching. The advantages, on the other hand, are the low temperature (4.2 K) at which the experiment is performed. This allows for a long-term stability of the gold atomic chains so that detailed spectroscopy can be done. In addition, the cryogenic vacuum conditions avoid any contamination on the nanowires.

By standard low-temperature STM and MCBJ techniques atomic-sized contacts of gold were produced. In contrast to many other metals, for Au it was found that the last conductance plateau, at a value of $\sim 1 G_0$, can often be stretched far beyond a length corresponding to an atomic diameter. An example is presented in Fig. 83, where a plateau of about 2 nm length is found. Since it has been established that the conductance is predominantly determined by the narrowest cross section, and that a single-atom contact for Au has a conductance near $1 G_0$ (Sect. VIII), this observation led Yanson *et al.* to speculate that a chain of atoms was being formed. This is indeed very surprising, even more so than in the case of the room temperature TEM experiments. For the latter, the atoms have enough mobility to produce at an earlier stage a stable, straight nanowire several atoms in cross section, and the atomic rows in the wire are removed one after the other by thermal diffusion of the atoms on the surface. This leaves a single atomic row standing before contact is finally lost. However, at low temperatures the atomic structure is frozen into the configuration in which it lands after an atomic rearrangement, forced by the stretching of the contact. When arriving at a single-atom contact one would expect the contact to break at this weakest spot. Instead, atoms are apparently being pulled out of the banks to join in the formation of a linear atomic arrangement. Clearly, it is important to critically evaluate the interpretation of atomic chain formation. By now, a large set of experiments has been performed which confirm the picture, and we will now summarize this evidence.

1. Return distance

A simple test involves recording the distance required to bring the electrodes back into contact after the conductance has suddenly dropped to zero, as at the end of the plateau in Fig. 83. We imagine that a chain has formed, which finally ruptures at this moment. The atoms in the chain are then expected to fall back onto the banks, which implies that the separation between the electrodes

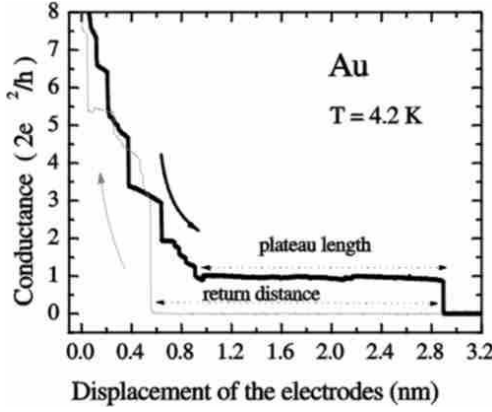


FIG. 83: The conductance as a function of the displacement of the two gold electrodes with respect to each other in an MCBJ experiment at 4.2 K. The trace starts at the upper left, coming from higher conductance values (thick curve). A long plateau with a conductance near $1 G_0$ is observed and after a jump to tunneling one needs to return by a little more than the length of the long plateau to come back into contact (thin curve). Data taken from [53].

should be approximately equal to the length of the chain, being approximately the length of the plateau. Fig. 83 illustrates that this is indeed the case for this particular example, although one may anticipate variations in the return length according to the actual arrangement of the atoms after the collapse. By recording many curves similar to the one in Fig. 83, Yanson *et al.* obtained an average return distance as a function of the length of the last plateau. They observed a linear dependence of the return distance on the plateau length, with a slope between 1.0 and 1.3 and an offset of about 0.5 nm. The latter can be understood in terms of the elastic deformation of the banks: Even when no chain is formed and the contact breaks at a single-atom, the atomic structure relaxes after rupture of the contact, giving rise to a finite return length.

2. Length histograms

Further evidence for the chain structure comes from an analysis of the distribution of lengths of the last conductance plateaus for many cycles of contact breaking. Fig. 84 shows a histogram of plateau lengths. We see that the probability for early breaking is very low, it then rises to a first peak at 0.25 nm length, after which it drops before rising to a second peak, which is usually higher than the first. After the second peak the distribution of lengths drops steeply, but shows three additional peaks in the tail. The peak distance of 0.25–0.26 nm agrees with the expected bond distance in a chain of gold atoms (see Sect. XID) and the natural interpretation of the peaks in the length histogram is in terms of a preferential breaking of the chain at lengths corresponding to an integer

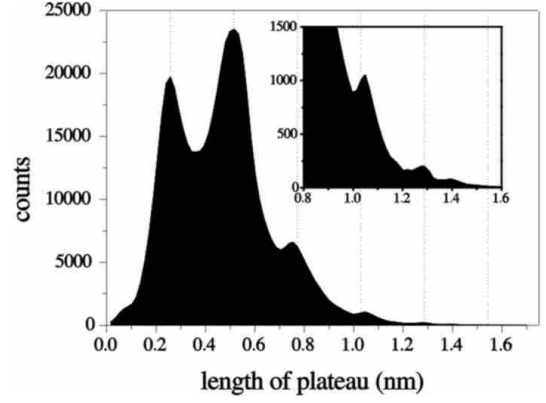


FIG. 84: The distribution of lengths for the last conductance plateau for Au, obtained from 10 000 experiments similar to those described in Fig. 83. It shows a number of equidistant maxima, at multiples of 0.257 nm. The data were recorded with an MCBJ at 4.2 K, in cryogenic vacuum. The length of the last plateau was defined as the distance between the points at which the conductance drops below $1.2 G_0$ and $0.8 G_0$, respectively. The inset shows the tail of the distribution on a $\sim 10\times$ expanded scale. A smoothing function that averages over three bins has been applied to the data. The accuracy for the calibration of the length (horizontal scale) is 10%. Data taken from [436].

number of atoms in the chain. The peaks in the distribution are broadened by the variation in starting and end configurations of the banks connecting the chain. In fact, a strict periodicity of the peaks would not be expected to continue much further than the first few, because the atoms making up the chain are removed from the banks, which then become shorter. Occasionally plateaus of up to 2 nm in length have been found, which suggests that the system can self-assemble chains of up to 7–8 atoms long. It is often possible to obtain similar peak structure in a histogram of return distances [206].

In the original paper [53] the distance between the peaks was reported to be larger, $0.36 \text{ nm} (\pm 30\%)$. The larger value, and the rather large uncertainty, later turned out to result from the presence of He thermal exchange gas in the vacuum space. As was recently shown by Kolesnychenko *et al.* [84], adsorbed He gas has an unexpectedly large influence on the work function of metal surfaces. This introduces an error in the calibration of the displacement of the MCBJ and STM, when using the exponential tunneling dependence, as pointed out in Sect. IIC3. More recently, Untiedt *et al.* [436] have combined several calibration techniques to obtain a more reliable value for the inter-peak distance in the length histograms, and the value obtained for Au, $0.26 \pm 0.02 \text{ nm}$, is in excellent agreement with the calculated Au-Au distance in the chains [55, 274, 277, 330, 331, 333, 334, 338, 437].

3. Evolution of the force in atomic chains

Rubio-Bollinger *et al.* measured the force evolution simultaneously with the conductance while drawing out a chain of atoms at 4.2 K [93]. They employed an auxiliary STM at the back of a cantilever beam, on which the sample was mounted, in order to detect the deflection, and therewith the force on the sample (Sect. IID). An example of such a measurement is shown in Fig. 85, where the contact is stretched at a constant speed of 0.5 nm/s. The force shows a saw-tooth-like pattern corresponding to elastic deformation stages interrupted by sudden force relaxations. The conductance on the last plateau remains nearly constant and just below $1 G_0$, but note that the force jumps are accompanied with simultaneous jumps in the conductance with a magnitude of only a small fraction of G_0 .

In each measurement, the largest force on the last conductance plateau is reached at the end, as expected. For a series of 200 experiments this final breaking force shows a narrowly peaked distribution, centered at 1.5 nN, with a standard deviation of only 0.2 nN. The force calibration has an accuracy of 20%. The break force was found to be independent of the chain length. The force is considerably larger than the force required to break individual bonds in bulk gold, which is estimated at only 0.8–0.9 nN, and this large force agrees very well with theory, as will be discussed below.

It was at first sight surprising to find that the slopes of the force as a function of displacement are nearly constant in experiment. One would expect a smaller force constant for longer chains. This observation is explained by the fact that the chain is unusually stiff. The bonds are much stronger than bulk bonds, and the largest elastic deformation takes place in the banks next to the chain. The calculated deformation of the banks amounts to 0.5–1.0 nm, which agrees well with the offset observed in the return distance.

4. Phonon modes in atomic chains

The phonon modes in Au atomic chains have been investigated experimentally [368, 438] by means of point contact spectroscopy (see Sects. II A and IX C). The differential conductance dI/dV was measured using lock-in detection with a 1 mV modulation voltage, from which dG/dV was calculated numerically. The energy resolution was limited by the temperature of 4.2 K to 2 meV. The results are shown in Fig. 86. At ± 15 mV bias the differential conductance of a chain of atoms shows a rather sharp drop by about 1% (top panel in Fig. 86). In the second derivative d^2I/dV^2 this produces a pronounced single peak, point-symmetric about zero bias. The chains of Au atoms have the fortuitous property of having a single nearly perfectly transmitted conductance mode, which suppresses conductance fluctuations that would otherwise drown the phonon signal, see Sect. IX C. Some

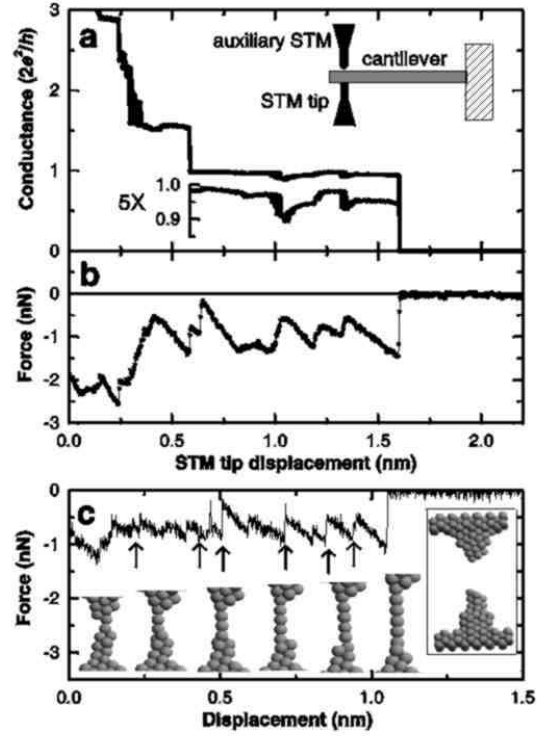


FIG. 85: Simultaneous conductance (a) and force (b) measurements during chain fabrication and breaking. The conductance on the last plateau is shown on an expanded scale to illustrate small variations in the conductance. The inset shows a schematic drawing of the experimental setup. (c) Calculated force evolution obtained from molecular dynamics simulations. The arrows indicate the points at which a new atom pops into the chain and snapshots of the structure at these positions are shown. Reprinted with permission from [93]. Copyright 2001 American Physical Society.

asymmetry that can still be seen in the conductance curves is attributed to the residual elastic scattering and interference contributions.

Bulk gold point contact spectra have peaks at 10 and 18 mV (Fig. 2), due to transversal and longitudinal acoustic phonon branches, respectively. The first of these has a higher intensity. At point S in Fig. 86 the contact consists of a single atom and the spectrum still resembles the spectrum for bulk contacts, although the energy of the first peak is significantly shifted downward due to the reduced coordination of the atom.

For the linear chain configuration the electron-phonon interaction simplifies considerably. By energy and momentum conservation the signal only arises from electrons that are back scattered, changing their momentum by $2k_F$. With $\hbar\omega_{2k_F}$ the energy for the corresponding phonon, the derivative of the conductance is expected to show a single peak at $eV = \pm\hbar\omega_{2k_F}$. The transverse

phonon mode cannot be excited in this one-dimensional configuration and only the longitudinal mode is visible.

The position of the peak shifts as a function of the strain in the wire. It is somewhat like the pitch of a guitar string that changes as a function of the tension. Except that for atomic wires the frequency decreases as a function of tension because of the decreasing bond strength between the atoms. The frequency decreases, and the amplitude increases, until an atomic rearrangement takes place, signaled by a small jump in the conductance. At such points the amplitude and energy of the peak in dG/dV jump back to smaller and larger values, respectively. This is consistent with the phonon behavior of Au atomic chains found in *ab initio* calculations [55]. The growing amplitude is due, in part, to the softening of the phonon modes with tension. The 1% drop in conductance for a wire of 2 nm length implies a mean free path for the electrons of about 200 nm, much longer than the nanowire itself.

C. Other properties of atomic chains at low temperatures

The most striking properties are the long-time stability of the chains and the large current densities that the chains can survive. Even the longest ones can be held stable for times of at least an hour (no real record-breaking attempts have been made so far). Bias voltages as high as 2 V have been applied without damage, although the maximum decreases with the length of the chain [248, 361]. With a conductance equal to $2e^2/h$ this corresponds to $150 \mu\text{A}$, and with the cross section equal to one atom we obtain a current density of $2.1 \cdot 10^{15} \text{ A/m}^2$. This current density is more than seven orders of magnitude larger than the current density that turns the tungsten wire inside a light bulb white-hot. This is an amazing fact. Although we understand that it is related to the ballistic nature of the transport, a significant amount of inelastic scattering inside and near the wires should be expected at such high biases. More quantitative studies of this phenomenon are needed. Preliminary studies suggest that the limiting current values decrease roughly proportional to the inverse of the length of the chains, $\sim 1/L$ [439]. Todorov *et al.* [440] have calculated the current-induced forces in atomic chains, and find that the forces on the atoms weaken the atomic structure, in particular at the junction with the banks. This was confirmed by *ab initio* calculations by Brandbyge *et al.* [132]. Nevertheless, it is most likely it is the heat generated by the current that causes the wire to break [440]. A phenomenon related to the high current carrying capacity is the fact that the current-voltage characteristics for the chains is highly linear. This is confirmed by tight-binding calculations under application of a large voltage bias [246]. More recently, non-equilibrium DFT calculations [132] predict a significantly reduced conductance above 0.5 V for a 3-atom Au chain, but this is probably

a specific feature for the (111)-oriented substrate.

When pulling a contact in forming a chain the conductance on a plateau, once it drops below $1 G_0$ never rises above it. The conductance stays almost invariably very close to $1 G_0$. This implies that the conductance of any additional channels is negligible and that a nearly perfect adiabatic coupling with the banks is attained. This is surprising, since the atomic structure at the coupling with the banks is not controlled and should vary quite a bit, but it agrees with results of calculations [327, 329, 330, 333, 441]. Sim *et al.* [329] argue that a conductance of exactly $1 G_0$ is a robust property for a contact having a single conductance channel, when imposing charge neutrality and inversion symmetry.

Still, deviations of the conductance below $1 G_0$ are observed. In particular jumps are seen due to atomic rearrangements when the chain is being built up, see e.g. Fig. 85. This implies that there is a finite amount of scattering at the interface between chain and banks, or inside the banks close to the interface. Such small jumps are also seen when the chain is swung sideways in an STM experiment [53], in which case these can be due to jumps in the anchoring point of the chain on the banks. The latter experiment also illustrates the robustness of the chains, and the fact that the freedom for lateral displacement is over a distance comparable to the length of the chains forms an additional element in verifying the chain-interpretation of the experiments.

D. Numerical calculations of the stability and conductance of Au chains

Several molecular dynamics simulations have preceded these experiments in suggesting the formation of chains [198, 274, 442, 443]. However, the effective potentials employed in these simulations were not regarded to be sufficiently reliable for such exceptional atomic configurations to be predictive. Nevertheless, in many cases the simulations agree with the observations, and they are very helpful in visualizing the mechanism by which the chains unfold from the banks. Full DFT molecular dynamics modeling of this process is still too demanding. More recently da Silva *et al.* [277] have used a method that forms a compromise between accuracy and computational efficiency, involving tight-binding molecular dynamics. The results for gold are generally consistent with the previously employed methods. First-principles DFT molecular dynamics was used by Häkkinen *et al.* [333] by limiting the number of possible configurations. Taking a starting configuration of two atomic gold tips connected by two parallel two-atom long strands, the stretching of this double-chain was seen to evolve into a four-atom long single-atom chain via a bent chain structure.

In order to investigate the equilibrium structure, bond length and breaking force many model systems of moderate size have been considered, using first principles calculations based on the local density approximation. The

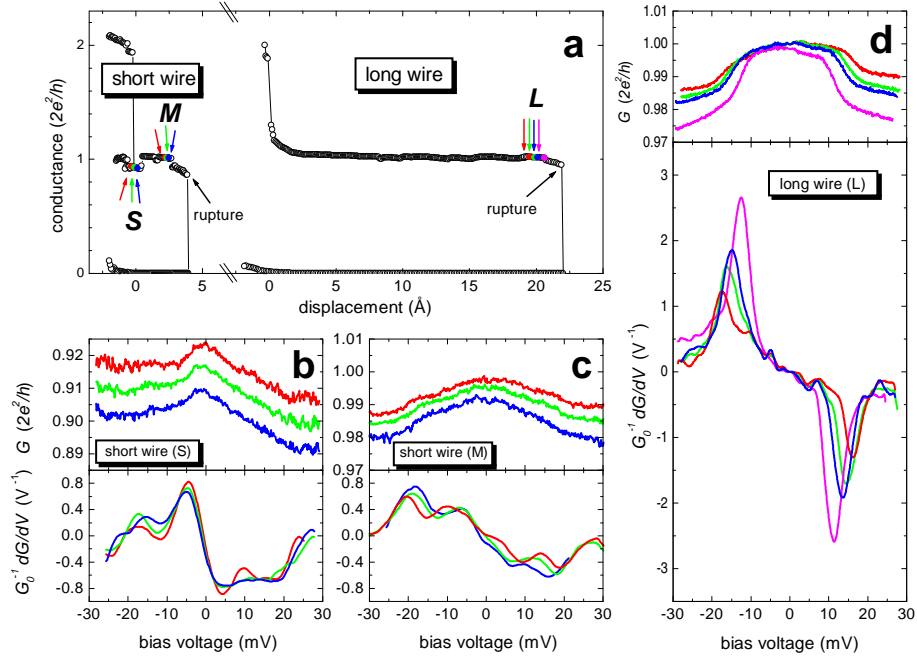


FIG. 86: (a) Short and long atomic wire, ~ 0.4 and ~ 2.2 nm, respectively, as given by the length of the conductance plateau. Panels (b–d) show the differential conductance and its derivative at points S, M, and L, respectively. The various curves in (b–d) were acquired at intervals of 0.03, 0.03 and 0.05 nm, respectively. Note that the vertical scales for the last three panels are chosen to be identical, which brings out the relative strength of the electron-phonon interaction for the longer chains. The wire in (d) has a length of about 7 atoms. Reprinted with permission from [368]. Copyright 2002 American Physical Society.

structures considered are infinite chains, using periodic boundary conditions [55, 331, 334, 338], finite isolated chain sections [55, 334], or finite wires connected to an atomic base on either side [55, 93, 330]. Sanchez-Portal *et al.* [55] have investigated all structures by various computational approximations and find only minor quantitative and no qualitative differences. All calculations agree on the equilibrium bond length, ranging only between 0.250 and 0.262 nm, and agree on the maximum bond distance at which the chain breaks, 0.28 – 0.30 nm. The break force is more sensitive to the type of approximations involved, ranging from 0.91 nN in Ref. [330] to 2.2 nN in Ref. [55]. Rubio-Bollinger *et al.* [93] made the most extensive analysis of the breaking force and obtain a force between 1.55 and 1.68 nN, in good agreement with the experimental value of 1.5 ± 0.3 nN.

Sanchez-Portal *et al.* [55] found for the optimized geometry a planar zigzag structure with two atoms per unit cell. The zigzag deformation was even found for free standing wire sections and the origin was argued to be related to a reduction in the transverse kinetic energy for the electrons due to the increased effective wire width. This mechanism is of the same nature as the shell structure observed for alkali metal wires, as discussed in Sect. XII. The chain is stretched to a linear configuration only for bond lengths above about 0.275 nm, shortly before breaking. The zigzag structure is confirmed in the work of Refs. [334, 433]. On the other hand, Häkkinen *et al.* [333] find for a four atom chain between two tips that,

before the chain is fully stretched, it assumes a bent configuration, that appears to be lower in energy than the zigzag conformation.

For a linear chain with a single half-filled conduction band a Peierls distortion towards a string of dimers is generally expected to occur. The majority of the calculations suggest that this dimerization only sets in just before stretching to the point of breaking. The variation in bond lengths observed for a four-atom chain by Häkkinen *et al.* [332] that was argued to be related to a Peierls distortion may also be due to end-effects [330]. De Maria and Springborg [334] provide fairly general arguments that the half-filled band for this chain system should lead to dimerization when the bond length becomes larger than 0.29 nm. Below 0.27 nm a second band was found to cross the Fermi level and the σ orbital becomes partially depleted. Since the σ orbital is no longer half filled the driving mechanism to dimerization is suppressed. A second band crossing the Fermi level for short distances was also found for linear chains by Sanchez-Portal. However, in their calculations it is removed by the zigzag deformation. The presence of a second conduction band should be visible in the conductance. Calculations of the conductance by other groups [246, 330, 333] consistently find a conductance equal to $1 G_0$ or slightly below, in agreement with the experiments.

The atomic chain configuration is clearly a meta-stable structure. Bahn [434] calculated the time to break a chain for various temperatures by the EMT molecular

dynamics method. He found that the chains would be unstable on a time scale of nanoseconds at room temperature. The barrier to breaking is only about 0.03 eV, with an attempt frequency of $5 \cdot 10^{11} \text{ s}^{-1}$. Only higher temperature break times could be obtained in the time span accessible by these calculations. The mean time to breaking at 200 K is found to be $\sim 0.1 \text{ ns}$, while extrapolation of the numbers obtained gives a lifetime of hours or even days at 4.2 K. The lack of predicted long-time stability poses a second challenge to understanding of the room-temperature TEM results.

Again, the presence of other chemical species, such as CO and O, may resolve the problem, since they would provide stronger bonding [433, 434]. A chain with oxygen atoms inserted between the Au atoms would, surprisingly, still be conducting, with a single conductance channel. A similar result was obtained by Häkkinen *et al.* [332] for the insertion of methylthiol, SCH_3 , into a gold chain.

E. The mechanism behind atomic chain formation: Ir, Pt and Au

All the discussion above has been limited to gold chains. Surprisingly, Au appears to be favorable for chain formation while Ag and Cu do not (or to a very limited extent) have this property. This led Smit *et al.* [216] and Bahn and Jacobsen [338] to investigate the mechanism behind this phenomenon. It turns out that gold is distinct from the other noble metals in another surface property: Clean gold surfaces reconstruct in remarkable ways (see [444] and references therein). The (110) surface shows a ‘missing row’ reconstruction, where every second row along the [001] direction is removed. The (001) surface has a hexagonally packed top layer, that is more densely packed than the bulk. Even the (111) surface has a herringbone reconstruction that is slightly more densely packed than the bulk. It turns out that the three end-of-series $5d$ elements Ir, Pt, and Au have similar surface reconstructions, which are absent in the related $4d$ elements Rh, Pd and Ag, suggesting that the explanation for the reconstructions cannot lie in any particular detail of d band electronic structure. There appears to be a growing consensus that an explanation can be found in a stronger bonding of low-coordination atoms of the $5d$ metals with respect to the $4d$ metals as a result of relativistic effects in the electronic structure [445, 446, 447, 448]. From numerical work that uses relativistic local-density-functional calculations to evaluate the various contributions to the atomic binding energies qualitatively the following picture emerges. The effective Bohr radius for $1s$ electrons of the heavier (5^{th} row) elements contracts due to the relativistic mass increase. Higher s shells also undergo a contraction, both because they have to be orthogonal against the lower ones and because they feel the same mass-velocity terms directly. As Takeuchi *et al.* explain [446] the contraction of the s shell

allows those electrons to profit more from the Coulomb interaction with the positively charged core and reduces the energy of the s shell, increasing the s occupation at the expense of the d electrons. Since the top of the d band consists of states with anti-bonding character that are now partially depleted, the d bond becomes stronger. While the d electrons thus tend to compress the lattice the s electrons exert an opposing Fermi pressure. At the surface, the spill-out of the s electron cloud into the vacuum relieves some of the s electron pressure, and allows a contraction of the inter-atomic distance and a strengthening of the bonds at the surfaces, giving rise to the observed reconstructions. Since the relativistic corrections grow roughly as the square of the nuclear charge [449], Z^2 , they are more important for the $5d$ elements than for the equivalent $4d$ and $3d$ transition metals.

As for the reconstructions, the bonding in atomic chains will be influenced by a tilting of the balance between s and d electrons by relativistic effects. This difference in bonding becomes revealed when the Fermi pressure of the s electrons can be released by spill-out of the wave functions into the vacuum. As a result, there is a gain in energy from the stronger d bonds and a reduction of the inter-atomic distance. Clearly, the 1D chain geometry allows for an even larger s pressure release than at a flat surface. This provides an explanation for the difference observed between the tendency to chain formation for Au, Ag and Cu.

De Maria and Springborg [334] argue that including relativistic effects in numerical calculations for the chains is important. DFT calculations commonly include the scalar relativistic effects in the choice of the pseudo-potentials and in the molecular dynamics simulations they are effectively included by adjustment of the parameters to known properties of the materials. Bahn and Jacobsen [338] investigated by these numerical methods the mechanism and energy balances for chain formation in a series of transition metals: Ni, Pd, Pt, Cu, Ag and Au. By performing a large number of molecular dynamics simulations of contact breaking, using the EMT method (see Sect. VII), they found that among this selection of elements only Au and Pt spontaneously form atomic chains. The break of other metals occurred at best with two atomic tips touching, which can then be viewed as a chain of two atoms.

Smit *et al.* [216] used the MCBJ technique for a similar set of transition metals, namely the $4d$ metals Rh, Pd, and Ag, and the $5d$ series Ir, Pt, and Au, to demonstrate experimentally that all of the latter form chains of atoms, in contrast to the corresponding $4d$ elements. In order to show this the length of the last conductance plateau was measured in a length histogram similar to the one shown for Au in Fig. 84. Since only Au and Ag have a sharply defined conductance for a single-atom contact or wire of nearly $1 G_0$, there is an additional difficulty for the other metals. They are expected to have a partially filled d shell giving rise to five conduction channels with transmission values that are smaller than unity

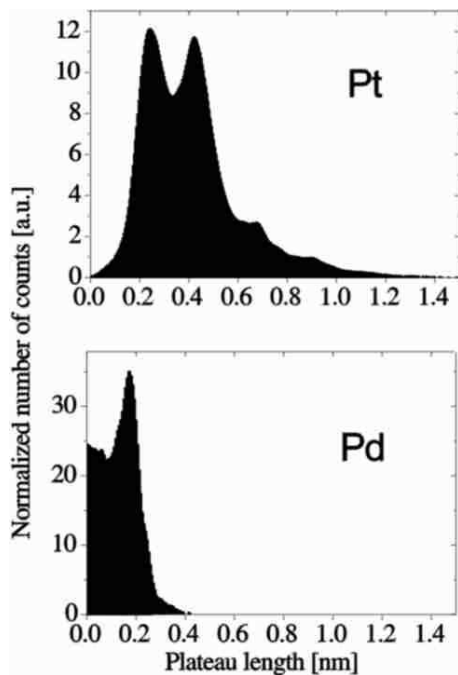


FIG. 87: Histogram of the distribution of lengths for the last conductance plateau for platinum contacts (top panel) and for its iso-electronic neighbor palladium (bottom panel). Pd breaks essentially at the level of a single atom, while Pt spontaneously forms chains of atoms, which is apparent from the tail of the distribution towards long plateau lengths, and from the peaks at multiples of the inter-atomic distance. Data taken from [216].

and depend sensitively on the coupling to the banks, see Sect. VIII. The procedure followed was as follows: first a conductance histogram was recorded for each of the metals. As for the niobium histogram shown in Fig. 35 they all show a single rather broad peak, with little other structure in most cases. The peak is taken to represent the typical conductance of a single-atom contact. Taking the high-conductance tail of the peak as the starting-point for a chain, and the low-conductance tail as the end value, a large series of conductance traces was analyzed. The length of the ‘plateaus’ between the start and stop values for the given metal were accumulated into a length-histogram. In addition to Au, also Pt and Ir showed a plateau-length distribution with a tail toward long lengths, up to 1.5 to 2 nm, with well-defined peaks at regular spacing. Neither Ag, nor Pd or Rh showed these properties. Fig. 87 shows a comparison of the length histograms measured for Pt and Pd. Although the criteria taken as the start and end of a chain seem to be a bit arbitrary, the results were not very sensitive to variations in the definition of these values. The experiment demonstrates a perfect correspondence between the metals that have surface reconstructions and those that form chains, in agreement with a common mechanism of relativistic shifts in the *sp* and *d* bonding, described above.

It still needs to be explained why a single bond in a

linear chain wins out against many bulk bonds when a chain is being formed by low-temperature pulling. It is typical for metallic bonding that the bond strength increases as the coordination number is decreased. Bahn and Jacobsen [338] calculated for the series of six transition metals the force required to break a bond in a linear chain relative to the force to break a bulk bond, using density functional theory. They discovered that this ratio is larger for Au and Pt than for any of the other metals in the study, and attains a value of about 3 for Au and 3.2 for Pt. Thus a single linear bond is able to compete with three bulk bonds in these metals. When the structure of the banks is such that the atoms can roll-over to break only one or two bonds at a time, then the chain atoms are bound to prevail and pull new atoms into the linear arrangement.

1. Odd-even behavior in the conductance of atomic chains

Lang reported calculations that suggest that the conductance of an atomic chain of simple monovalent metals, where he used sodium as a model system, depends in a non-monotonous and even oscillatory way on the length of the chain [322]. His model consists of two semi-infinite jellium electrodes connected by a chain of N sodium atoms. For $N = 1$, a single atom contact he reported a surprisingly small conductance of only $0.39 G_0$. The conductance was then seen to increase to $0.79 G_0$ for $N = 2$ and then oscillating from 0.66 at $N = 3$ to $0.75 G_0$ at $N = 4$. Such odd-even oscillations in the conductance of an atomic chain had already been reported from tight binding calculations by Pernas *et al.* [130] and more recently several other workers reported odd-even oscillations in model calculations [323, 324, 329, 441, 450]. Based on earlier work by Datta and Tian [451], Sim *et al.* [329] show, using the Friedel sum rule, that a perfect conductance of $1 G_0$ is expected for an odd number of monovalent atoms in the chain, when the system obeys inversion symmetry and charge neutrality. For an even number of atoms the conductance is lower, depending on the structure of the banks on either side of the chain. The effect is corroborated by a DFT calculation of a chain of Na atoms between two Na-atom tips.

There appears to be a contradiction with the results obtained earlier by Lang [322], since the more recent works find the minima in the conductance for the even-atom chains. However, Gutiérrez *et al.* [450] repeated calculations by the same method as Lang, for Na chain in between jellium banks, and showed that the proper odd-even behavior is obtained when changing the coupling-distance between the chain and the banks. For a slightly larger distance than used by Lang the odd chains, including the single-atom junction, obtain a conductance of $1 G_0$ and the even-atom chains have a lower conductance.

The reason for the anomalous dependence observed by Lang has been attributed to the fact that he effectively

considers a heterogeneous system. Kobayashi *et al.* [327] showed that the conductance for a chain of 3 Na atoms coincides with G_0 , provided that the jellium electrodes are chosen to have an electron density that matches that for sodium, and a small atomic pyramid structure is inserted to connect the chain with the jellium electrodes. Both features bring the model closer to the experimental conditions, and are important to avoid reflection of the electron wave function at the interfaces. Moreover, a mismatch between the charge density of the Na atoms and the jellium electrodes results in charge transfer, which moves the Fermi energy away from the central position in the DOS resonance of the wire.

In addition, Emberly and Kirczenow [441] showed that the effective wire length may be greater than suggested by the atomic structure, because a heterogeneous system, having a chain composed of a different atomic element than the banks, effectively gives a longer wire. They show that the oscillations can be interpreted in terms of a standing wave pattern that develops between the two ends of the chain, due to the finite reflection amplitude of the waves at the connections. When the chain has strictly one conduction channel it reduces the problem effectively to a one-dimensional system. In this way, the transmission of conduction electrons through an atomic chain is a problem equivalent to that of the Fabry-Perot interferometer in optics.

The odd-even oscillations are not restricted to monovalent metals. As can be judged from the calculations on carbon atom chains [323, 324, 339, 441, 452] the amplitude can be a lot stronger, going from nearly 1 G_0 to about twice this value between even and odd chains, respectively. The actual periodicity and amplitude, however, is expected to depend sensitively on the type of atoms of the chain.

Atomic chains can be regarded as unusual atomic configurations belonging to a larger class of recently discussed “weird wire” structures [453, 454] that will be discussed in Sect. XII D below.

XII. SHELL-FILLING EFFECTS IN METALLIC NANOWIRES

Apart from their role in determining the electronic transport properties of the contacts, the quantization of the conductance modes also affects the cohesion energy of the contact. In Sect. VII B we discussed the fluctuations in the tensile force on a nanowire as a result of the successive occupation of individual quantum modes. While the relevance of this free-electron model approach to the actual cohesion of metallic atomic-scale wires is still being debated, there is a related quantum effect on the cohesion for which already clear experimental evidence has been obtained. This can be seen for alkali metal contacts at contact diameters well above those for which the quantization peaks in the histograms are observed (see e.g. Fig. 33), and for temperatures well above the tempera-

ture of liquid helium. During the stretching of the contact under these conditions a nanowire is formed, which shows a periodic structure of stable diameters. The periodic structure is closely related to the well-known magic number series for metal clusters, and in the next section we will briefly summarize these earlier results from the field of cluster physics. The initial series of magic numbers arise as a result of fermionic shell-closing effects similar to those leading to the periodic table of the elements and the stable atomic nuclei, and the theory for electronic shell effects in clusters will be briefly summarized. In Sect. XII B the theory will be extended for application to nanowires. The subsequent sections then present the experimental evidence for electronic shell effects and supershell effects in metallic nanowires. At still larger diameters of the clusters a new set of magic numbers is observed, which derives from geometric shell closing of atomic layers at the surface. This will also be included in the next section, and the analogous atomic shell structure in nanowires is presented in Sect. XII D. For a more complete discussion of shell closing effects in metallic clusters we refer to excellent recent review papers on this subject [455, 456, 457, 458].

A. Introduction: shell effects in metallic clusters

When a hot metal vapor is allowed to expand through a nozzle into vacuum in the presence of an inert carrier gas the metal atoms fuse together to form clusters of various sizes. The size distribution for these clusters can be measured using a mass spectrometer. In a seminal experiment Knight *et al.* [459] discovered that this distribution for sodium is not a smooth bell-type shape, as one might naively expect, but rather shows a series of so-called magic numbers. Those clusters that are composed of a number of atoms corresponding to one of these magic numbers are found to be exceptionally abundant. Fig. 88 shows the experimental abundance spectrum for sodium. One recognizes peaks or discontinuities in the abundance spectrum at 8, 20, 40, 58, 70 and 92 atoms. The explanation for these numbers is based on a shockingly simple model. The clusters are regarded as spherically symmetric potential wells containing a number of free and independent electrons equal to the number of atoms forming the cluster (since we consider monovalent metals). For hard-wall boundary conditions the wave functions for the electrons are given by the product of the spherical harmonics $Y_{lm}(\theta, \phi)$, and the spherical Bessel functions, $j_l(\gamma_{nl}r/r_0)$, with r_0 the radius of the cluster. The ground state of the system is determined by the filling of the energy levels starting at the bottom. The levels are given by $E_{nlm} = \hbar^2 \gamma_{nl}^2 / 2m_e r_0^2$, where m_e is the electron mass and γ_{nl} is the n^{th} zero of the l^{th} order Bessel function: $j_l(\gamma_{nl}) = 0$. The lowest energy level corresponds to the first zero of the $l = 0$ Bessel function, the only possible value for the quantum number m is 0, and including spin degeneracy two electrons can be accom-

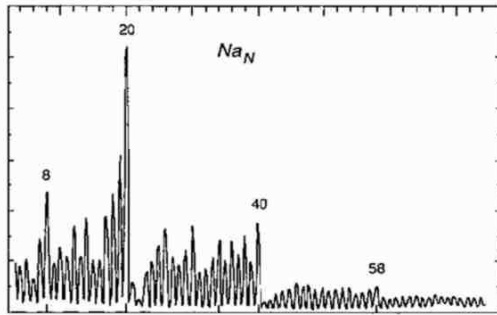


FIG. 88: Cluster abundance spectrum for Na. Reprinted with permission from [459]. Copyright 1984 American Physical Society.

modated in the lowest level. The next level is three-fold degenerate ($m = 0, \pm 1$) so that it is completed with a total number of 8 electrons in the cluster. For the monovalent metal considered in the experiment, this implies that also 8 atoms are required to allow filling the electronic shell. The next shell of electrons is characterized by the quantum number $l = 2$, which is five-fold degenerate and would be complete with a total of 18 electrons in the cluster. However, there is only a small distance to the next electron level that corresponds to the second zero of the zeroth order Bessel function, $(n, l) = (2, 0)$. Since the latter is not m -degenerate it takes only two electrons to fill it, and the completion of the shell is observed at 20 electrons (Fig. 88), and so forth. The difference in the total energy of the cluster makes a large jump each time a degenerate level is completed, and the energy gap to the next level needs to be bridged. This explains the stability of the filled-shell clusters, just as the stability of the noble gases is explained by the filling of the electronic shells for the elements in the periodic table.

Thus the dominant structure in the experimental abundance spectrum can be understood by considering the clusters as smooth spheres filled with free and independent electrons. This interpretation in its simplest form works best for the alkali metals, for which the quasi-particle spectrum in the bulk metals is known to be well-approximated by a free and independent electron gas. Moreover, the outer s -electron of the alkali metal atoms is weakly bound to the atom core and orbits at a rather large distance around the nucleus. This leads to a smoothening of atomic surface corrugation, to such an extent that the electron distribution around a di-atomic molecule is not a dumbbell, as one would naively expect, but is rather more closely approximated by a spherical electron cloud.

Evidently, an explanation of cluster properties such as ionization energies, static polarizability, optical properties, etc. requires refinements of the model. To begin with, the walls confining the electrons are not infinitely hard potentials, but smooth potentials that result from self-consistent evaluation of the interaction with the ion

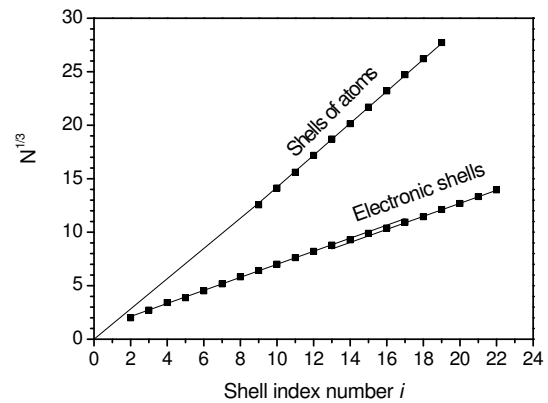


FIG. 89: Cube root of the cluster magic numbers obtained from abundance spectra for Na, plotted against the index of the magic number. The data set labeled as 'Electronic shells' is taken from [460]. The break in the linear dependence signifies a phase shift in the points at a beat minimum due to the supershell structure. The data set labeled 'Shells of atoms' is taken from [461] and is obtained for the largest clusters in a relatively cold cluster beam.

cores and with all other electrons in the cluster. Various groups have performed such calculations, and although the electronic levels are shifted, the principle described above largely survives [455, 456]. Furthermore, ellipsoidal deformations of the clusters have to be taken into account in order to explain structure observed in surface plasma resonances for non-magic cluster sizes. We will not discuss these complications here, but refer the interested reader to the review papers on this subject.

When the magic numbers are indicated as N_i , with i an index giving the sequential number of the magic number, e.g. $N_1 = 2$, $N_2 = 8$, $N_3 = 20$ etc., then a plot of the cube root of the magic numbers against the index number shows a linear dependence, see Fig. 89. In other words, the magic numbers form a periodic series as a function of the cube root of the number of atoms in the cluster, which is proportional to the cluster radius. The explanation for this periodic appearance of the magic numbers is given in terms of the bunching of energy levels, which is conveniently described in a semi-classical approximation. We will briefly summarize the ideas behind this.

The individual-level picture described above only works for the lowest quantum numbers, and even there we observe already that due to the closeness of the levels $(n, l) = (1, 2)$ and $(2, 0)$, they are not separately visible in the experiment. The experiment shows shell structure up to very large diameters, much further than is visible in the experiment of Fig. 88, but for larger quantum numbers we cannot even approximately identify the shells with individual quantum numbers. For these large quantum numbers, i.e. in the limit of large cluster sizes, it is instructive to approximate the true quantum properties of the clusters by a semi-classical approximation. This makes use of the work on the distribution of the resonant modes in a cavity that has been discussed in terms

of classical trajectories by Guzwiller [462] and by Balian and Bloch [463]. In this approximation the allowed orbits for the electrons inside a steep-walled potential well can be identified with the closed classical trajectories of the electron as it bounces back and forth between the walls. For a circular system the lowest order trajectories are given in Fig. 90. The allowed wave vectors are then obtained by applying the Bohr-Sommerfeld quantization condition for each closed trajectory. It is then immediately obvious that for each solution at a given radius R of the system, a new solution will be found when the length of the trajectory is increased by a full electron wavelength. Therefore, the distribution of modes (as a function of R or as a function of wave vector k_F , or more generally as a function of $k_F R$) has a periodic structure. However, we do not have a single period, since each of the classical trajectories (Fig. 90) gives rise to its own periodicity. Taking the amplitude factors into account it can be shown that the dominant contributions to the level distribution for a spherical system come from the triangular and square orbits. The difference in the periods for the level distribution belonging to these two orbits gives rise to a beating pattern: in some range of $k_F R$ the two orbits will give rise to levels that nearly coincide, thus amplifying the shell structure in this range. On the other hand at other ranges of $k_F R$ the levels of the square orbits will fall in between the levels of the triangular orbit, thus smoothening out the shell effects. This beating pattern in the shell structure is known as supershell structure, and it has been observed for Na, Li and Ga metallic clusters [460, 464, 465]. The length of the triangular orbit is $3\sqrt{3}R$ while that of the square orbit is $4\sqrt{2}R$. The ratio of these two lengths is 1.09 from which we see that it requires about 11 periods of the individual oscillations to complete a beat of the combined pattern. For metallic clusters one or two beat-minima have been observed. Nature does not provide enough chemical elements to observe supershell structure in the periodic table or in the stability pattern of the nuclei.

For the simple, spherical, independent-electron quantum well system under consideration one can, of course, obtain all the quantum levels directly from the exact solutions of the Schrödinger equation. However, one cannot identify the periodic structure with any particular quantum numbers. The periodic structure of the levels, in other words the modulation in the density of levels, is a result of a bunching of individual levels. A bunch of levels together forms a wave packet that approximates the motion along the classical trajectories.

At still larger cluster sizes one observes a crossover to a new series of magic numbers, having a different periodicity, which is seen in the plot of Fig. 89 as a crossover to a new slope in the data points. The new series is a result of the filling of *geometric* shells of atoms, rather than electronic shells [457]. The clusters form regular faceted crystalline structures, which attain an energy minimum each time a new layer of atoms filling all facets is completed. For some metals (e.g. Al and Ca) one

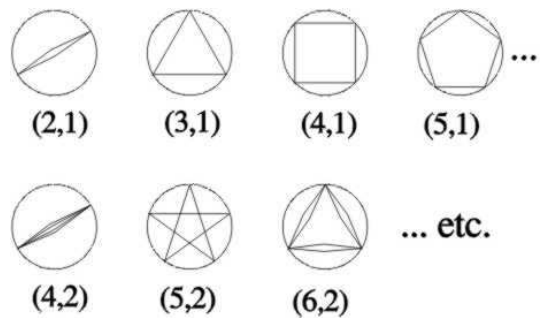


FIG. 90: The lowest-order semi-classical trajectories for a particle inside a steep-walled spherical or cylindrical cavity. The orbits are labeled by two integers (p, t) , where p is the number of vertices of the orbit and t is the winding number, i.e. the number of times the particle encircles the center before the orbit is closed.

observes additional structure due to the filling of partial atomic shells, corresponding to the completion of individual facets. The facet-completing sub-shell structure can in some cases be as strong as the full atomic shell structure.

B. Theory for electronic shell effects in nanowires

The shell effects discussed previously concerning atomic nuclei, the elements or metallic clusters, are all based on models of fermions that are completely confined inside symmetric potential wells. We now want to apply these concepts to nanowires, for which one of the three dimensions is open and connected to infinitely long metallic leads. In this case there are no true gaps in the density of states, since the conductance modes have a continuous degree of freedom along the current direction. However, a modulation of the density of levels is still present. At the points where a new mode (the bottom of a 1-dimensional sub-band) crosses the Fermi energy, the density of states shows a $1/\sqrt{E - E_n}$ singularity. These singularities are smeared out by the finite length of the wire and would not have a very pronounced effect if they were homogeneously distributed. However, by the same mechanism that leads to the shell structure for closed fermion systems the symmetry of the wire gives rise to a bunching of the singularities, and these bunches of singularities can be associated with the electronic shells in metal clusters. The resulting density of states oscillations have been analyzed using independent-electron models [49, 50, 172, 310, 466] and by local-density functional methods [305, 467]. In Sect. VII B these models have already been discussed in view of quantum contributions to the cohesion of nanowires. All models reproduce the basic features, namely the fluctuations in the density of states resulting in local minima in the free energy for the nanowire. The minima give rise to the preferential appearance self-selecting magic wire configurations. As for metallic clusters, one can make a semi-classical expansion

of the density of states and this was done by Yannouleas *et al.* [305] and in spirit of Balian and Bloch by Höppler and Zwerger and by Kassubek *et al.* [172, 466]. The stable wire diameters predicted from this model are in fairly good agreement with the observed periodic peak structure in the histograms [52], as we will discuss below. The periodic pattern has again a supershell modulation due to the contribution of several types of orbits. The types of orbits are the same as for spherical clusters, Fig. 90, but the relative weight for each is different. The diametric orbit (2,1) has only a minor contribution to the structure in the density of states for clusters, while it is of comparable weight as the triangular and square orbits for a cylindrical system. The reason for this can be seen when one considers the degeneracy of the orbits: after fixing the position of a vertex of the orbit at a particular point on the surface of the sphere (for clusters) the triangular and square orbits have a further degree of freedom in choosing the rotation of the orbit around the vertex point. This extra degree of freedom is absent for the diametric orbit, explaining its smaller weight for spherical systems. However, for a cylindrical model the advantage of the higher-order orbits over the diametric orbit disappears. The result is a dominant supershell structure due to the beating of the period corresponding to the diametric orbit, with the combined period of the triangular and square orbits. The length of the diametric orbit is $4R$ and the ratio to the mean of the other two is 1.36. This implies that the beating pattern is only about 3 periods of the principal oscillation wide, and as a result the supershell structure is more readily observable. This can be verified by a straightforward calculation of the density of states for a free electron gas inside a hard-wall cylindrical wire [206], which is shown in Fig. 91. After subtraction of a smooth background density of states the Fourier transform shows three prominent peaks. A more complete DFT calculation for a jellium-model cylindrical nanowire confirms the global features of the Fourier transform [467]. The first peak at 0.63 can be identified with the diametric orbit in the semi-classical analysis, while the triangular and square orbits give rise to the peaks at 0.83 and 0.90, which are just resolved in Fig. 91. Indeed, when L is the length of a particular orbit we can express it in units of the Fermi wavelength as L/λ_F . For the diametric orbit we then have $L/\lambda_F = 4R/\lambda_F = (2/\pi)(k_F R) \simeq 0.637(k_F R)$. This is just the frequency of the first peak in the Fourier spectrum. Similarly, we obtain for the triangular orbit $L/\lambda_F = 3\sqrt{3}R/\lambda_F \simeq 0.827(k_F R)$ and for the square orbit $L/\lambda_F = 4\sqrt{2}R/\lambda_F \simeq 0.900(k_F R)$. The peak just above 1.5 may be attributed to the (5,2)-orbit, but the other structure in the Fourier spectrum is mostly due to harmonics that are suppressed after rounding of the sharp peaks in the density of states [467].

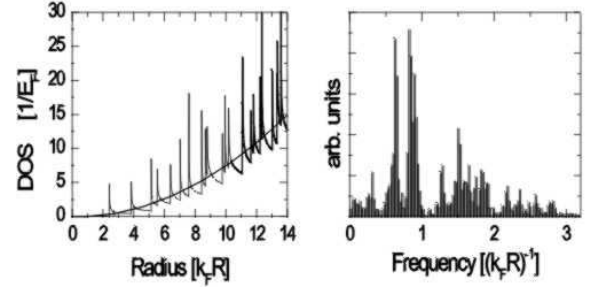


FIG. 91: The density of states (left) in a cylindrical nanowire. A singularity is found for each opening of a new conductance mode, and the singularities are arranged in groups. After subtracting a smooth bulk-metal background density of states the Fourier transform of the density of states (right) shows three main peaks, one at 0.63 and a double peak at 0.83 and 0.90, in units of $(k_F R)^{-1}$.

C. Observation of electronic shell effects in nanowires

The shell effects nanowires have been observed most clearly for the alkali metals Li, Na, K, and Cs [52, 206]. The experiments were performed using the MCBJ technique described in Sect. II C 4. For atomic-sized contacts at low temperatures the conductance histograms for the alkali metals show the characteristic series of peaks at 1, 3, 5, and 6 times G_0 . As was discussed in Sect. V D 2, this observation strongly suggests that one forms nanowires of nearly-perfect circularly-symmetric shape while stretching the contact, and the conduction electrons behave nearly free-electron like. When the experiment is extended to higher conductance one observes a number of rather broad but reproducible peaks. The peaks are not as sharp as the ones associated with conductance quantization at low conductance (Fig. 33) and cannot be identified with multiples of the conductance quantum. However, these peaks become more pronounced as the temperature is raised to about 80 K (Fig. 92) and more of them become visible at still higher conductance. At 80 K up 17 peaks can be seen for sodium in Fig. 93. The separation between the peaks grows for increasing conductance, but a regular periodic peak structure is obtained when plotting the spectrum as a function of the square root of the conductance. The square root of the conductance is to a good approximation proportional to the radius of the nanowire, see Eq. (8). A semi-classical relation between the conductance and the radius taking higher-order terms into account is given by [210, 295],

$$G = gG_0 \simeq G_0 \left[\left(\frac{k_F R}{2} \right)^2 - \frac{k_F R}{2} + \frac{1}{6} + \dots \right], \quad (139)$$

as we have seen in Sect. VII B 2. Using the radius of the nanowire obtained from the conductance through Eq. (139) we plot the values of $k_F R$ at the positions of the peaks in the histogram versus the index of the peaks, as shown in Fig. 94. The linear dependence illustrates the

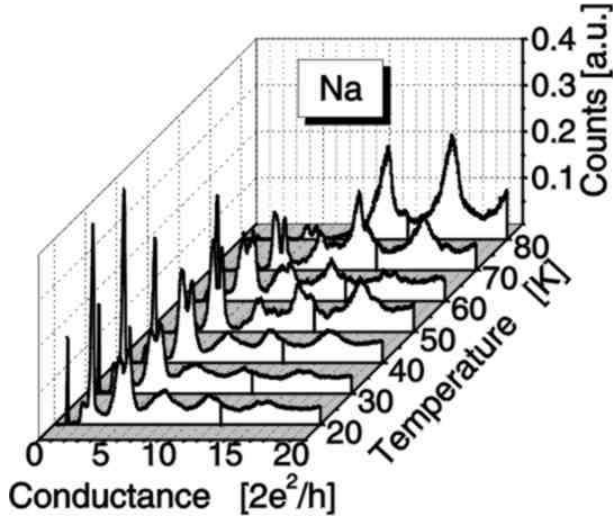


FIG. 92: Temperature evolution of sodium histograms in the range from 0 to $20 G_0$. The voltage bias was 10 mV and each histogram is constructed from 1000-2000 individual scans. The amplitude has been normalized by the total area under each histogram. Reprinted with permission from Nature [52]. Copyright 1999 Macmillan Publishers Ltd.

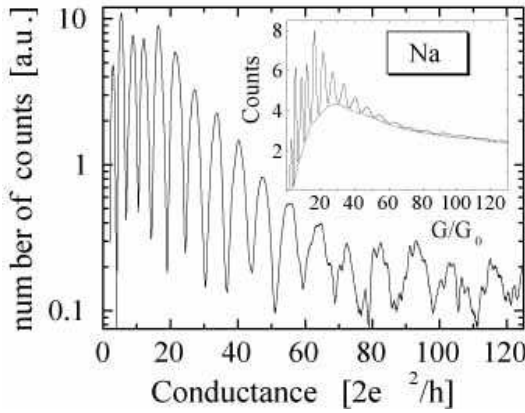


FIG. 93: Histogram of the number of times each conductance is observed versus the conductance in units of G_0 for sodium at $T=80$ K and at a bias voltage of $V=100$ mV, constructed from over 10 000 individual scans. The logarithmic scale for ordinate axis helps to display the smaller amplitude features at high conductance values. The inset shows the raw data and the smooth background (dashed curve), which is subtracted in the main graph. Reprinted with permission from Nature [52]. Copyright 1999 Macmillan Publishers Ltd.

fact that the peaks in the histogram are found at regular intervals in the radius of the nanowire and this periodicity suggests an analogy with the shell structure observed for clusters. But it is more than an analogy: when we take the cluster magic numbers for the electronic shell structure from Fig. 89 and convert the number of atoms N_i into the cluster radius through $k_F R_i = 1.92 N_i^{1/3}$, appropriate for sodium, we obtain the black dots in Fig. 94.

The close agreement between the two sets of data suggests an intimate relation between the cluster magic numbers and the peaks in the conductance histogram. Applying the semi-classical theory outlined in Sect. XII B for shell structure in nanowires produces the open triangles in the figure. The agreement with the experimental points is quite good, especially in the beginning. The deviation for larger cluster sizes requires further study, but it may be due to approximations in the calculation, where hard wall boundaries have been assumed, and to ignoring contributions from electron trajectories beyond the lowest three.

The shell structure only clearly appears when the temperature is raised well above liquid helium temperature, see Fig. 92. This finds a natural interpretation within the framework of the shell effect. The shell structure makes the free energy for specific wire configurations favored above the average. When a contact is stretched at very low temperatures, the shape and size of the contact evolves along a local energy minimum trajectory. Only when the system is exposed to large enough thermal fluctuations it can explore the various contact configurations in order to find the deeper minimum at the magic wire configurations. Also for metallic clusters temperature has a significant influence on the degree to which shell structure is expressed in the experiments [455].

The interpretation of the periodic peak structure in the conductance histograms is based on the relation $G \propto R^2$, Eq. (139), in order to extract the radius of the wire. Modifications of this relation are expected to arise from back scattering on defects (Sect. IX). However, the data suggest that this shift of the conductance values is small otherwise the peaks would be smeared over a much wider range. An important series resistance correction would also lead to a deviation from the linear dependence in Fig. 94. The scattering on defects is probably

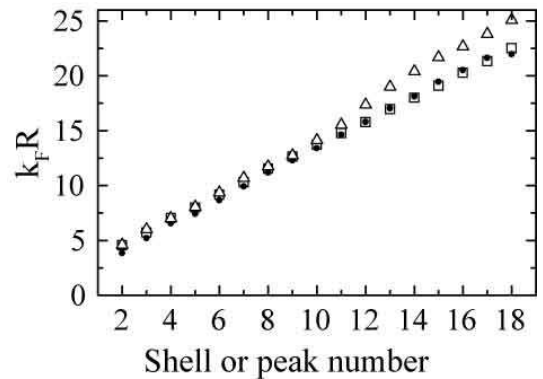


FIG. 94: Radius of the nanowire at the positions of the maxima in Fig. 93 versus peak number (\square), where R is given in units k_F^{-1} . The radii at the peak positions are compared to the radii corresponding to the magic numbers for sodium metal clusters (\bullet) [468] and to those expected from a semi-classical description for the fluctuations in the free energy for the nanowire (\triangle) [305, 466].

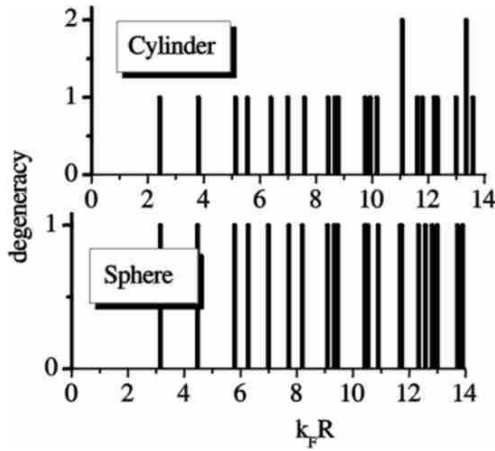


FIG. 95: Distribution of zeros for the Bessel functions (giving the solutions for a cylindrical nanowire) and the spherical Bessel functions (giving the solutions for spherical clusters). After application of a small shift it can be seen the the two spectra have a very similar structure.

suppressed also by the higher temperatures. As pointed out in Sect. IX, surface roughness is expected to be one of the major sources for electron scattering in the contacts. A higher temperature in the experiment promotes a smoother surface and a gradual variation of the contact cross-section along the wire length.

The use of Eq. (139) further ignores all quantum modulation, which is clearly not entirely justified. Indeed, for low conductance this is just what is believed to be responsible for the peaks at 1, 3, 5, and 6 multiples of the conductance quantum. However, this modulation rapidly smears out due to tunneling contributions of additional conductance channels as the cross section of the contact grows. Any residual modulation would lead to a peak structure of the same nature as the shell structure observed here, and it would have the same origin. Indeed, this effect has been seen in simulations of conductance histograms that take quantum effects in the electronic states into account for a free-electron gas model [469]. However, the temperature dependence observed in the experiment clearly demonstrates that the shell structure is mainly a result of the enhanced stability at the magic wire configurations. The stability was included in the calculations in an approximate way by Ksuubek *et al.* [172] and the simulated conductance histogram reproduces the experimental data surprisingly well.

The similarity between the magic wire radii for clusters and nanowires observed in Fig. 94 is striking, but it is also surprising in the sense that one would at first sight expect a very different series of magic numbers for a spherical system compared to a cylindrical one. The reason for the correspondence is in the similarity of the distribution of zeros for Bessel function and spherical Bessel function. As illustrated in Fig. 95 the bunching of the zeros and the gaps in the distributions of zeros are very similar, apart from a small shift.

The electronic shell structure has so far only been observed for the alkali metals Li, Na, K and Cs. From shell effects observed for metal clusters one may infer that shell effects in nanowires may be observable in other metals as well. In view of the much higher melting point for some of the favorable candidates (Au, Al, ...) observation of such effects will probably require experiments under UHV conditions at elevated temperatures.

1. Supershell effects

On top of the shell structure a pronounced modulation due to supershell structure can be observed for metallic nanowires. Fig. 96 shows a conductance histogram for Na, similar to the one in Fig. 93, for which the periods in the structure are made visible by taking a Fourier transform. Similar results have been obtained for Li and K [206]. The modulation in the histogram peak amplitudes already suggests a beating pattern of two dominant frequencies, which is confirmed by the Fourier spectrum. The two peaks in the spectrum correspond very well to the ones in Fig. 91 for the density of states in a cylindrical wire. By implication, the free energy for the nanowire has similar periods in its structure [470]. We conclude that the first peak is due to the diametric orbit, which is prominent in the spectrum in contrast to that for metallic clusters. The second peak is due to a combination of the triangular and the square orbits, which are not resolved here. The larger separation of the period of the diametric orbit from that of the triangular/square orbits results in a shorter beat-period compared to the situation for clusters, for which the beat is due to interference of the square with the triangular orbits. As a result, for the nanowires the two main periods can be directly resolved in the Fourier transform. The small peak at 1.5 possibly results from the (5, 2) orbit, as was suggested by Puska *et al.* [467]. The simulations of the latter work reproduce the supershell features, not only as regards the periods involved, but also the phase, i.e. the sizes of the nanowires that produce a minimum in the beating pattern.

D. Geometric shell effects

There is evidence for geometric atomic shell structure for the alkali metals and, of a very different nature, for gold. The results for the alkali metals extend the results discussed above and it is convenient to present this work first.

Beyond a certain diameter a new periodic structure was encountered in the conductance histograms for Na, K and Cs, which points at a transition from electronic shell effect to atomic shell structure [206, 471], in close analogy to what has been observed for the clusters (Fig 89). The position of the transition region between the two periodic features depends strongly on experimental parameters such as the sample temperature, the voltage bias

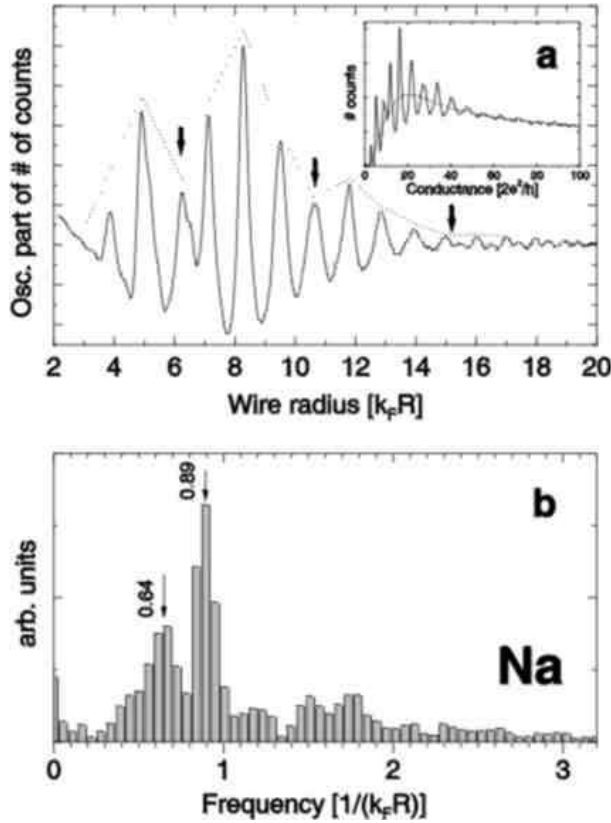


FIG. 96: (a) Conductance histogram for sodium after subtraction of a smooth background. $T = 90$ K, bias voltage $V = 100$ mV, and the number of curves included in the histogram is 13 800. The original curve and the background are shown in the inset. The arrows indicate the positions of minimal amplitude, which are the nodes of the supershell structure. When taking the Fourier transform of the curve in (a) the spectrum in panel (b) is obtained, which shows two dominant frequency components. Data taken from [206, 470].

and the depth of indentation. The transition shifts to smaller diameters when the metal is found further down the first column of the periodic table of the elements. The new oscillating phenomenon has approximately a three times smaller period than that for the electronic shell structure. The points for the electronic shell effect in sodium nanowires plotted in Fig. 94 have a slope of 0.56 ± 0.01 . Beyond the cross-over (not shown in the figure) the points obey a linear relation with a much smaller slope of 0.223 ± 0.001 . By varying the experimental conditions one can greatly extend the conductance range over which the electronic shell structure is observed, while the slope always agrees with the periodicity expected for this effect. As an interpretation for the new periodic structure it was proposed that geometric shell closing takes over, where the dominant effect comes from a wire atomic arrangement with only close-packed surfaces. For a bcc stacking a hexagonal wire with exclusively low-energy [110] facets can be formed having its axis along [111]. Similar geometrical shell configurations

were obtained in a simplified model calculation by Jagla and Tosatti [472], where even the facet-related structure can be recognized.

By the MCBJ technique shell effects have only been uncovered for alkali metals. However, they are expected to be more general and by a completely different approach geometric shell effects have been recently discovered for gold. Using the same technique as used in the discovery of chains of atoms (Sect. XI) Kondo and Takayanagi [473] found helical atomic shells in their images of gold nanowires by HRTEM at room temperature. By electron-beam thinning two adjacent holes are formed *in situ* in a thin gold film. As the gold bridge separating the two holes is narrowed further 3–15 nm long nanowires are formed having unusual structure for diameters in the range of 0.6 to 1.5 nm. The unusual structures are described as coaxial tubes of atoms, each tube consisting of linear arrangements of atoms, that are coiled around the wire axis. It bears some resemblance to the structure of multiwalled carbon nanotubes. The various diameters observed in many images were collected in a histogram, which showed a number of distinct preferred diameters. These peaks in the histogram are interpreted in terms of a special geometric shell structure, which is illustrated in Fig. 97. The structures are characterized by the number of atomic rows in each coaxial tube, e.g. as $n - n' - n''$ for a nanowire having an outer tube with n rows, inside of which we find a second tube with n' rows and in the center a tube of n'' rows of atoms. The difference in the number of atomic rows per layer is 7, with the provision that when this ends in a central tube with 0 rows (next tube has 7) then the central tube will be a linear chain of atoms, $n'' = 1$. The magic wire structures observed then correspond to 7–1, 11–4, 13–6, 14–7–1 and 15–8–1 (Fig. 97) and there are two less-well resolved structures that may fit to 12–5 and 16–9–2. For larger diameters there is a cross-over to bulk fcc stacking. Similar nanowire structures have been found for Pt [474].

Novel types of atomic packing, including helical arrangements had already been observed in molecular dynamics simulations for unsupported wires of Pb and Al by Gülsiren *et al.* in 1998 [453]. Structures they refer to as ‘weird wires’ are found below a characteristic radius R_c , which is of the order of three times the inter-atomic spacing. These structures are formed in order to minimize the surface energy, and the shape of the wires depends sensitively on the anisotropy of the surface energy for the metallic elements considered. Hasmy *et al.* [228] have made simulations of histograms of nanowire diameters by repeated molecular dynamics simulations for aluminum⁸. For higher temperatures, 450 K, broader peaks

⁸ The use of the word supershell structure in Ref. [228] is not appropriate in this context. In the molecular dynamics type calculation employed the electronic density of states is not evaluated, so that effects of electronic (super)shell structure cannot be observed.

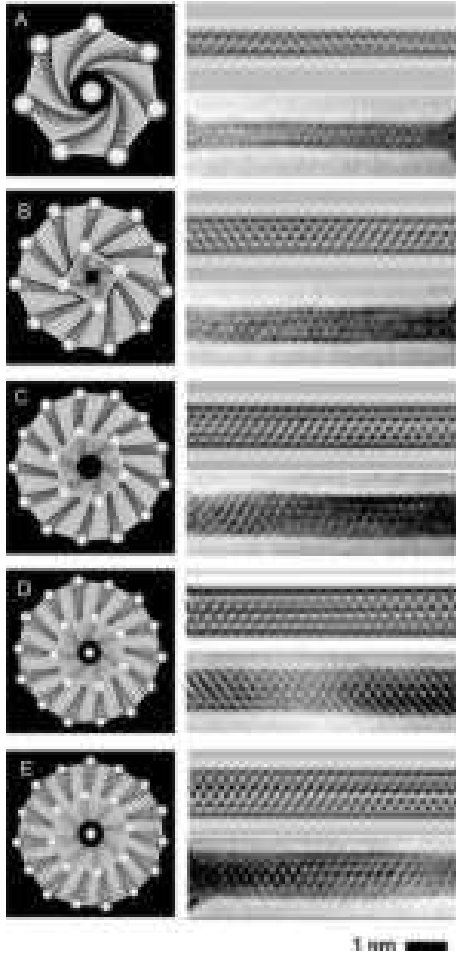


FIG. 97: Panels A–E give an axial view of the most prominent helical shell arrangements proposed as an interpretation of the gold nanowire images obtained in HRTEM. The observed images are shown for each structure in the lower right panel, while the upper right panel shows the corresponding simulated images for comparison. The atomic row numbers for the structures are 7-1 (A), 11-4 (B), 13-6 (C), 14-7-1 (D), and 15-8-1 (E). Reprinted with permission from Science [473]. Copyright 2000 American Association for the Advancement of Science.

are observed in the simulation at 5, 8–9, 12–13 and 15 atoms. These are attributed to shell structure. The nature of the atomic packing at these magic numbers was not reported.

The seminal work of Gülseren *et al.* was extended to gold by several groups [454, 475, 476], partly stimulated by the experimental observations. The simulations confirm that the structure of the thinnest gold nanowires can be viewed as consisting of concentric cylindrical sheets of atoms. Tosatti *et al.* [454] have made a series of successive refinements of the calculations finishing with a full density functional calculation of the electronic structure and the wire tension. They point out that the appropriate thermodynamic function to consider is the wire tension $f = (F - \mu N)/L$, rather than the free energy

F . Here, μ is the chemical potential, N the total number of atoms in the wire and L its length. The chemical potential takes into account the fact that the wire diameter changes by diffusion of atoms to and fro between the nanowire and the banks between which it is suspended. They find for the thinnest structure an optimal arrangement in perfect agreement with the experimental observation by Kondo and Takayanagi [473]. They explicitly verify that there is no contribution of *electronic* shell closing for these structures. The particular type of magic wire structure involves a mechanism of *s-d* competition that is also believed to be responsible for the formation of atomic chains (Sect. XI), and may therefore apply to Au, Pt and Ir. For diameters larger than about 2.5 nm the core of the nanowires is fcc crystalline, with a few layers of non-crystalline arrangement covering the surface, referred to as curved surface epitaxy by Wang *et al.* [476].

It is to be expected that shell effects will be observable for many other metals, as suggested by the observations for metal clusters, and new surprising structures may yet be found. The implications of the chiral atomic ordering in gold nanowires on observable effects in electron transport properties deserve further investigation.

XIII. CONCLUSION AND OUTLOOK

Let us summarize what we view as the central achievement of the research described above, and what we feel deserves to be known: Metallic atomic-sized contacts can be characterized by a finite set of conductance eigenchannels with transmission probabilities $\{\tau_i\}$; this set $\{\tau_i\}$ has been nicknamed ‘the mesoscopic PIN code’ by Urbina’s group in Saclay [477]. For a point contact of just a single atom in cross section the number of valence orbitals of the atom fixes the number of eigenchannels. A single atom can thus carry many channels, up to 5 or 6 for *sd* metals, and they are generally only partially open. By measuring the current-voltage characteristics in the superconducting state we can obtain the PIN code experimentally. When the metal is not a superconductor this is somewhat less straight forward, but making use of the proximity effect it can still be done. The knowledge of the PIN code allows predicting other transport properties such as shot noise, the Josephson supercurrent or the dynamical Coulomb blockade effect, that can all be expressed in terms of the set $\{\tau_i\}$. Atomic-sized contacts have thus become an ideal test bench for mesoscopic and nanophysics, where a high degree of accuracy can be reached. This accuracy is remarkable for a system whose geometrical characteristics cannot be completely controlled.

There are still many open questions to be answered. Other properties, such as the mean amplitude of conductance fluctuations, are also expected to be described by an average over sets $\{\tau_i\}$, but this has not yet been verified. Similarly, the experiment by Koops *et al.* (Sect. XB)

on the current phase relation of an atomic contact in a superconducting loop deserves to be taken one step further by first establishing the PIN code of the atomic contact. This problem has attracted interest from a different perspective since the two Andreev bound states for a single-channel contact inside a superconducting loop have been proposed as the basic qubit element for applications in quantum computing [478, 479]. The question as to the limits in accuracy of the PIN code determination has not been addressed very generally. How many channels can be determined unambiguously? An experiment is under way (G. Rubio-Bollinger, private communication) to attempt to determine the distribution of channel transmissions for large contacts, having thirty or more channels. Is this procedure reliable and does the distribution obtained correctly predict other properties, such as shot noise, for the same contact?

At the start of this field the question of whether or not the concept of conductance quantization applies for atomic-sized contacts has played a central role. Although there are many ways of interpreting this concept, it has become clear that it makes no sense to speak about conductance quantization for metals other than the monovalent metals. And even for those it requires some specification of the concept when discussing the data in such terms. What we have learned is that for a one-atom contact the monovalent metals have a single conductance channel that is nearly perfectly transmitted, and for larger contacts (up to three to six atoms) the next channels show a tendency to open one after the other. This phenomenon has been referred to as the saturation of channel transmission. For still larger contacts several partially open channels are active simultaneously.

We can see many directions in which this field of research may be further developed in the near future. A prominent problem to be attacked is the investigation, both from theory and experiment, of many-body interactions in atomic-sized contacts. These are not included in the conventional scattering approach and new descriptions are required. One type of interaction is the electron-phonon scattering. Some level of perturbative description of the interaction has been given (Sect. IX C 1), but a more detailed understanding of electron-phonon interactions in atomic-sized conductors is still lacking. The phonons in this description should be replaced by the local vibration modes of the atomic structure, coupled to the continuum modes of the banks. Experimentally, only very few results are available, mostly for Au. Many-body effects may also arise as a result of electron-electron interactions through the charge or spin degrees of freedom. Charge effects are believed to be small as a result of the effective screening provided by the metallic electrodes on either side of the atomic contact. Still, the screening is less effective than in bulk metals. The spin degrees of freedom may give rise to Kondo-like physics. Experimentalists should keep an open eye to characteristics that may be indications of these effects, which are most likely seen as anomalies around zero bias in the differential con-

ductance. We may need to explore different metals and we are likely to find new surprises in the uncharted parts of the periodic table. In particular the lanthanides and actinides have not received much attention, to date.

New directions in experiment will be found by adding parameters to be measured or controlled. Force measurements in atomic contacts have been very successful, but only very few results are available, exclusively for Au. New experiments are under way, which combine a tuning-fork piezo resonator, as a sensor of the force constant, with the advantages of the MCBJ technique. This will open the way to explore quantum properties in the force, and its relation to the conduction, in a wide range of materials. A challenge that has been recognized by many is introducing a gate electrode to a one-atom contact. It would allow controlling the transmission of the eigenchannels, and possibly even the number of eigenchannels, by adjusting an external electrical potential. Implementing this will require new experimental approaches, possibly similar to the techniques used in two recent papers to demonstrate Kondo behavior in a single atom embedded between electrodes inside a molecular structure [480, 481].

Chains of atoms constitute the ultimate one-dimensional metallic nanowires. For gold, the current is carried by a single mode, with nearly unit transmission probability. They may form a source for many discoveries in the near future. New properties may be discovered when considering, for example, the thermal conductance [482] or magnetic order, that is predicted for Pt chains under strain [338]. One may expect that mixed chains, e.g. Au chains containing Pt impurity atoms, will give access to interesting Kondo-type physics in a purely one-dimensional system. More work is needed to elucidate the mechanism of chain formation, and in particular to understand what limits the length of the chains. It is most likely that the length is currently limited by having sufficient weakly bonded atoms available. Once the structure in the tips, between which the chain is suspended, acquires a regular and stable configuration new atoms cannot be coaxed to join in the formation of a longer chain, as was illustrated by the simulations by da Silva *et al.* [277].

If we can develop methods to produce much longer chains electron-electron interactions may start to dominate, converting the electron spectrum in the chain into that of a Luttinger liquid [483]. Evidence for Luttinger-liquid behavior has already been obtained for carbon nanotubes [484] and for chains of gold atoms self-assembled on Si surfaces [429]. A Peierls transition is predicted for gold atomic chains when stressed close to the breaking point. No evidence for this phenomenon has been reported yet, but it is worthwhile investigating this further.

One of the least understood aspects of atomic-sized contacts is the role of heating by the electron current and possible forces on the atoms resulting from the large current density. Joule heating and electromigration are

important problems in integrated circuit technology and atomic contacts are probably ideal model systems to study these effects, since the maximum current density is larger than in any other system. A large current may drive the contacts over time towards the more stable configurations. This brings us immediately to the related question whether shell effects exist for other metals than the alkali. In a limited sense, atomic shell configurations have already been observed for Au in HRTEM studies, but the electronic and atomic shell effects are expected to be found for a wide range of elements. The challenge is to find the proper experimental conditions that will bring them out.

We want to end this review by pointing at one of the most promising directions of future research: The study of conductance through individual organic molecules is part of a world-wide effort towards building electronic circuits that exploit the intrinsic functionality of specially designed molecules. The possibility of having molecules that function as diodes [485], electronic mixers [486] or switching elements [487, 488, 489] has inspired hope

of developing entirely new, molecular based electronics. The first steps have been made [217, 480, 481, 490, 491, 492] and the developments in this field are so rapid that they deserve a separate review paper, and some reviews have already appeared [493, 494]. The subject is intimately connected with that of the present review: the STM and MCBJ are the most widely employed tools for contacting the molecules. Some of the fundamental concepts described above for atomic contacts will apply directly to molecular systems, while on the other hand new and unexpected physical phenomena will surface.

Acknowledgements

We have profited from many discussions with Gabino Rubio-Bollinger, Helko van den Brom, Juan Carlos Cuevas, Michel Devoret, Daniel Esteve, Fernando Flores, Bas Ludoph, Alvaro Martín Rodero, Yves Noat, Elke Scheer, Roel Smit, Carlos Untiedt, Cristian Urbina, Alex Yanson and Igor Yanson. This work has been supported by Spanish CICYT under contract PB97-0044 and by the Dutch ‘Stichting FOM’, that is financially supported by NWO.

-
- [1] R. Wiesendanger. *Scanning Probe Microscopy and Spectroscopy*. Cambridge University Press, Cambridge, (1994).
 - [2] M. Rief, M. Gautel, F. Oesterhelt, J.M. Fernandez, and H.E. Gaub. Reversible unfolding of individual Titin Immunoglobulin domains by AFM. *Science*, **276**, 1109–1112, (1997).
 - [3] M.F. Crommie, C.P. Lutz, and D.M. Eigler. Confinement of electrons to quantum corrals on a metallic surface. *Science*, **262**, 218–220, (1993).
 - [4] Y. Imry. *Introduction to mesoscopic physics*. Oxford University Press, Oxford, (1997).
 - [5] R. Landauer. Spatial variation of currents and fields due to localized scatterers in metallic conduction. *IBM J. Res. Dev.*, **1**, 223–231, (1957).
 - [6] C. Dekker. Carbon nanotubes as molecular quantum wires. *Physics Today*, **May**, 22–28, (1999).
 - [7] H.-W. Fink and C. Schönenberger. Electrical conduction through DNA molecules. *Nature*, **398**, 407–410, (1999).
 - [8] D. Porath, A. Bezryadin, S. de Vries, and C. Dekker. Direct measurement of electrical transport through dna molecules. *Nature*, **403**, 635–638, (2000).
 - [9] A.Yu. Kasumov, M. Kociak, S. Guéron, B. Reulet, V.T. Volkov, D.V. Klinov, and H. Bouchiat. Proximity-induced superconductivity in DNA. *Science*, **291**, 280–282, (2001).
 - [10] B.N.J. Persson and E. Tosatti, editors. *Physics of sliding friction*, volume 311, Dordrecht, (1996). Kluwer Academic Publishers.
 - [11] B. Bhushan, J.N. Israelachvili, and U. Landman. Nanotribology: friction, wear and lubrication at the atomic scale. *Nature*, **374**, 607–616, (1998).
 - [12] J.K. Gimzewski and R. Möller. Transition from the tunneling regime to point contact studied using scanning tunneling microscopy. *Physica B*, **36**, 1284–1287, (1987).
 - [13] U. Dürig, O. Züger, and D. W. Pohl. Observation of metallic adhesion using the scanning tunneling microscope. *Phys. Rev. Lett.*, **65**, 349–352, (1990).
 - [14] B.J. van Wees, H. van Houten H., C.W.J. Beenakker, J.G. Williamson, L.P. Kouwenhoven, D. van der Marel, and C.T. Foxon. Quantised conductance of point contacts in a two-dimensional electron gas. *Phys. Rev. Lett.*, **60**, 848–850, (1988).
 - [15] D.A. Wharam, T.J. Thornton, R. Newbury, M. Pepper, H. Ahmed, J.E.F. Frost, D.G. Hasko, D.C. Peacock, D.A. Ritchie, and G.A.C. Jones. One-dimensional transport and the quantisation of the ballistic resistance. *J. Phys. C*, **21**, L209–L214, (1988).
 - [16] N.D. Lang. Resistance of a one-atom contact in the scanning tunneling microscope. *Phys. Rev. B*, **36**, 8173–8176, (1987).
 - [17] J. Ferrer, A. Martín-Rodero, and F. Flores. Contact resistance in the scanning tunneling microscope at very small distances. *Phys. Rev. B*, **38**, 10113–10115, (1988).
 - [18] S. Ciraci and E. Tekman. Theory of transition from the tunneling regime to point contact in scanning tunneling microscopy. *Phys. Rev. B*, **40**, 11969–11972, (1989).
 - [19] N. Garcia and L. Escapa. Elastic oscillatory resistances of small contacts. *Appl. Phys. Lett.*, **54**, 1418–1420, (1989).
 - [20] A.M. Zagorin and I.O. Kulik. Quantum oscillations of electrical conductivity of two-dimensional ballistic contacts. *Sov. J. Low Temp. Phys.*, **16**, 533–542, (1990).
 - [21] E. Tekman and S. Ciraci. Theoretical study of transport through a quantum point contact. *Phys. Rev. B*, **43**, 7145–7169, (1991).
 - [22] U. Landman, W.D. Luedtke, N.A. Burnham, and R.J. Colton. Atomistic mechanisms and dynamics of adhesion, nanoindentation, and fracture. *Science*, **248**, 454–461, (1990).

- [23] A.P. Sutton and J.B. Pethica. Inelastic flow processes in nanometre volumes of solids. *J. Phys.: Condens. Matter*, **2**, 5317–5326, (1990).
- [24] C.J. Muller, J.M. van Ruitenbeek, and L.J. de Jongh. Experimental observation of the transition from weak link to tunnel junction. *Physica C*, **191**, 485–504, (1992).
- [25] J. Moreland and J.W. Ekin. Electron tunneling experiments using Nb-Sn ‘break’ junctions. *J. Appl. Phys.*, **58**, 3888–3895, (1985).
- [26] C.J. Muller, J.M. van Ruitenbeek, and L.J. de Jongh. Conductance and supercurrent discontinuities in atomic-scale metallic constrictions of variable width. *Phys. Rev. Lett.*, **69**, 140–143, (1992).
- [27] T.N. Todorov and A.P. Sutton. Jumps in electronic conductance due to mechanical instabilities. *Phys. Rev. Lett.*, **70**, 2138–2141, (1993).
- [28] N. Agraït, J.G. Rodrigo, and S. Vieira. Conductance steps and quantization in atomic-size contacts. *Phys. Rev. B*, **47**, 12345–12348, (1993).
- [29] J.I. Pascual, J. Méndez, J. Gómez-Herrero, A.M. Baró, N. García, and V. Thien Binh. Quantum contact in gold nanostructures by scanning tunneling microscopy. *Phys. Rev. Lett.*, **71**, 1852–1855, (1993).
- [30] J.M. Krams, C.J. Muller, I.K. Yanson, Th.C.M. Govaert, R. Hesper, and J.M. van Ruitenbeek. One-atom point contacts. *Phys. Rev. B*, **48**, 14721–14724, (1993).
- [31] L. Olesen, E. Lægsgaard, I. Stensgaard, F. Besenbacher, J. Schiøtz, P. Stoltze, K.W. Jacobsen, and J.K. Nørskov. Quantised conductance in an atom-sized point contact. *Phys. Rev. Lett.*, **72**, 2251–2254, (1994).
- [32] L. Olesen, E. Lægsgaard, I. Stensgaard, F. Besenbacher, J. Schiøtz, P. Stoltze, K.W. Jacobsen, and J.K. Nørskov. Reply on comment on quantized conductance in an atom-sized point contact. *Phys. Rev. Lett.*, **74**, 2147, (1995).
- [33] J.M. Krams, J.M. van Ruitenbeek, V.V. Fisun, I.K. Yanson, and L.J. de Jongh. The signature of conductance quantization in metallic point contacts. *Nature*, **375**, 767–769, (1995).
- [34] Zheng Gai, Yi He, Hongbin Yu, and W.S. Yang. Observation of conductance quantization of ballistic metallic point contacts at room temperature. *Phys. Rev. B*, **53**, 1042–1045, (1996).
- [35] J.L. Costa-Krämer, N. García, P. García-Mochales, and P.A. Serena. Nanowire formation in macroscopic metallic contacts: quantum mechanical conductance tapping a table top. *Surface Science*, **342**, L1144–L1149, (1995).
- [36] J.M. Krams, J.M. van Ruitenbeek, and L.J. de Jongh. Atomic structure and quantized conductance in metal point contacts. *Physica B*, **218**, 228–233, (1996).
- [37] G. Rubio, N. Agraït, and S. Vieira. Atomic-sized metallic contacts: Mechanical properties and electronic transport. *Phys. Rev. Lett.*, **76**, 2302–2305, (1996).
- [38] T.M. Klapwijk, G.E. Blonder, and M. Tinkham. Explanation of subharmonic energy gap structure in superconducting contacts. *Physica B*, **109 & 110**, 1657–1664, (1982).
- [39] G.B. Arnold. Superconducting tunneling without the tunneling hamiltonian. II. subgap harmonic structure. *J. Low Temp. Phys.*, **68**, 1–27, (1987).
- [40] D. Averin and A. Bardas. ac Josephson effect in a single quantum channel. *Phys. Rev. Lett.*, **75**, 1831–1834, (1995).
- [41] J.C. Cuevas, A. Martín-Rodero, and A. Levy Yeyati. Hamiltonian approach to the transport properties of superconducting quantum point contacts. *Phys. Rev. B*, **54**, 7366–7379, (1996).
- [42] E.N. Bratus’, V.S. Shumeiko, and G. Wendin. Theory of subharmonic gap structure in superconducting mesoscopic tunnel contacts. *Phys. Rev. Lett.*, **74**, 2110–2113, (1995).
- [43] E.N. Bratus’, V.S. Shumeiko, E.V. Bezuglyi, and G. Wendin. dc-current transport and ac Josephson effect in quantum junctions at low voltage. *Phys. Rev. B*, **55**, 12666–12677, (1997).
- [44] N. van der Post, E.T. Peters, I.K. Yanson, and J.M. van Ruitenbeek. Subgap structure as function of the barrier in atom-size superconducting tunnel junctions. *Phys. Rev. Lett.*, **73**, 2611–2613, (1994).
- [45] E. Scheer, P. Joyez, D. Esteve, C. Urbina, and M.H. Devoret. Conduction channel transmissions of atomic-size aluminum contacts. *Phys. Rev. Lett.*, **78**, 3535–3538, (1997).
- [46] J.C. Cuevas, A. Levy Yeyati, and A. Martín-Rodero. Microscopic origin of conducting channels in metallic atomic-size contacts. *Phys. Rev. Lett.*, **80**, 1066–1069, (1998).
- [47] N.D. Lang. Resistance of atomic wires. *Phys. Rev. B*, **52**, 5335–5342, (1995).
- [48] E. Scheer, N. Agraït, J.C. Cuevas, A. Levy Yeyati, B. Ludoph, A. Martín-Rodero, G. Rubio Bollinger, J.M. van Ruitenbeek, and C. Urbina. The signature of chemical valence in the electrical conduction through a single-atom contact. *Nature*, **394**, 154–157, (1998).
- [49] C.A. Stafford, D. Baeriswyl, and J. Bürki. Jellium model of metallic nanocoherence. *Phys. Rev. Lett.*, **79**, 2863–2866, (1997).
- [50] J.M. van Ruitenbeek, M.H. Devoret, D. Esteve, and C. Urbina. Conductance quantization in metals: The influence of subband formation on the relative stability of specific contact diameters. *Phys. Rev. B*, **56**, 12566–12572, (1997).
- [51] C. Yannouleas and U. Landman. On mesoscopic forces and quantized conductance in model metallic nanowires. *J. Phys. Chem. B*, **101**, 5780–5783, (1997).
- [52] A.I. Yanson, I.K. Yanson, and J.M. van Ruitenbeek. Observation of shell structure in sodium nanowires. *Nature*, **400**, 144–146, (1999).
- [53] A.I. Yanson, G. Rubio Bollinger, H.E. van den Brom, N. Agraït, and J.M. van Ruitenbeek. Formation and manipulation of a metallic wire of single gold atoms. *Nature*, **395**, 783–785, (1998).
- [54] H. Ohnishi, Y. Kondo, and K. Takayanagi. Quantized conductance through individual rows of suspended gold atoms. *Nature*, **395**, 780–785, (1998).
- [55] D. Sánchez-Portal, E. Artacho, J. Junquera, P. Ordejón, A. García, and J.M. Soler. Stiff monatomic gold wires with a spinning zigzag geometry. *Phys. Rev. Lett.*, **83**, 3884–3887, (1999).
- [56] A. Yazdani, D.M. Eigler, and N.D. Lang. Off-resonance conduction through atomic wires. *Science*, **272**, 1921–1924, (1996).
- [57] H. van Houten and C.W.J. Beenakker. Quantum point contacts. *Physics Today*, **49**, 22–27, (1996).
- [58] J.M. van Ruitenbeek. Quantum point contacts between metals. In L.L. Sohn, L.P. Kouwenhoven, and G. Schön, editors, *Mesoscopic Electron Transport*, volume 345 of

- NATO-ASI Series E: Appl. Sci.*, pages 549–579, Dordrecht, (1997). Kluwer Academic Publishers.
- [59] J.M. van Ruitenbeek. Conductance quantisation in metallic point contacts. In K.H. Meiwes-Broer, editor, *Metal Clusters on Surfaces: Structure, Quantum Properties, Physical Chemistry*, pages 175–210, Heidelberg, (2000). Springer-Verlag.
 - [60] P.A. Serena and N. García, editors. *Nanowires*, volume 340, Dordrecht, (1997). Kluwer Academic Publishers.
 - [61] E.L. Foley, D. Candela, K.M. Martini, and M.T. Tuominen. An undergraduate laboratory experiment on quantized conductance in nanocontacts. *Am. J. Phys.*, **67**, 389–393, (1999).
 - [62] A.V. Khotkevich and I.K. Yanson. *Atlas of point contact spectra of electron-phonon interactions in metals*. Kluwer Academic Publishers, Dordrecht, (1995).
 - [63] J.M. van Ruitenbeek and A.G.M. Jansen, editors. *Proceedings of the second international conference on point contact spectroscopy*, volume 218 of *Physica B*. North Holland, Amsterdam, (1996).
 - [64] I.K. Yanson. Nonlinear effects in the electric conductivity of point junctions and electron-phonon interaction in metals. *Zh. Eksp. Teor. Fiz.*, **66**, 1035–1050, (1974). [*Sov. Phys.-JETP* **39** (1974) 506–513].
 - [65] A.G.M. Jansen, A.P. van Gelder, and P. Wyder. Point contact spectroscopy in metals. *J. Phys. C: Solid St. Phys.*, **13**, 6073–6118, (1980).
 - [66] V.S. Tsoi. Focussing of electrons in a metal by a transverse magnetic field. *ZhETF Pis. Red.*, **19**, 114–116, (1974). [*JETP Lett.* **19** (1974) 70–71].
 - [67] P.A.M. Benistant, H. van Kempen, and P. Wyder. Direct observation of Andreev reflection. *Phys. Rev. Lett.*, **51**, 817–820, (1983).
 - [68] D. Abraham, H.J. Mamin, E. Ganz, and J. Clarke. Surface modification with the scanning tunneling microscope. *IBM J. Res. Dev.*, **30**, 492–499, (1986).
 - [69] H. van Kempen and G.F.A. van de Walle. Applications of a high-stability scanning tunneling microscope. *IBM J. Res. Dev.*, **30**, 509–514, (1986).
 - [70] N. Agraït, J.G. Rodrigo, C. Sirvent, and S. Vieira. Atomic-scale connective neck formation and characterization. *Phys. Rev. B*, **48**, 8499–8501, (1993).
 - [71] C. Sirvent, J.G. Rodrigo, N. Agraït, and S. Vieira. STM study of the atomic contact between metallic electrodes. *Physica B*, **218**, 238–241, (1996).
 - [72] C. Sirvent, J.G. Rodrigo, S. Vieira, L. Jureczyszyn, N. Mingo, and F. Flores. Conductance step for a single-atom contact in the scanning tunneling microscope: Noble and transition metals. *Phys. Rev. B*, **53**, 16086–16090, (1996).
 - [73] J.I. Pascual, J. Méndez, J. Gómez-Herrero, A.M. Baró, N. García, U. Landman, W.D. Luedtke, E.N. Bogachek, and H.-P. Cheng. Properties of metallic nanowires: From conductance quantization to localization. *Science*, **267**, 1793–1795, (1995).
 - [74] V.V. Dremov and S.Yu. Shapoval. Quantization of the conductance of metal nanocontacts at room temperature. *JETP Lett.*, **61**, 336–339, (1995).
 - [75] U. Landman, W.D. Luedtke, B.E. Salisbury, and R.L. Whetten. Reversible manipulations of room temperature mechanical and quantum transport properties in nanowire junctions. *Phys. Rev. Lett.*, **77**, 1362–1365, (1996).
 - [76] M. Brandbyge, J. Schiøtz, M.R. Sørensen, P. Stoltze, K.W. Jacobsen, J.K. Nørskov, L. Olesen, E. Lægsgaard, I. Stensgaard, and F. Besenbacher. Quantized conductance in atom-sized wires between two metals. *Phys. Rev. B*, **52**, 8499–8514, (1995).
 - [77] T. Kizuka, K. Yamada, S. Deguchi, M. Naruse, and N. Tanaka. Cross-sectional time-resolved high-resolution transmission electron microscopy of atomic-scale contact and noncontact-type scanings on gold surfaces. *Phys. Rev. B*, **55**, R7398–R7401, (1997).
 - [78] T. Kizuka. Atomic process of point contact in gold studied by time-resolved high-resolution transmission electron microscopy. *Phys. Rev. Lett.*, **81**, 4448–4451, (1998).
 - [79] T. Kizuka. Atomistic visualization of deformation in gold. *Phys. Rev. B*, **57**, 11158–11163, (1998).
 - [80] Y. Kondo and K. Takayanagi. Gold nanobridge stabilized by surface structure. *Phys. Rev. Lett.*, **79**, 3455–3458, (1997).
 - [81] C. Zhou, C.J. Muller, M.R. Deshpande, J.W. Sleight, and M.A. Reed. Microfabrication of a mechanically controllable break junction in silicon. *Appl. Phys. Lett.*, **67**, 1160–1162, (1995).
 - [82] J.M. van Ruitenbeek, A. Alvarez, I. Piñeyro, C. Grahmann, P. Joyez, M.H. Devoret, D. Esteve, and C. Urbina. Adjustable nanofabricated atomic size contacts. *Rev. Sci. Instrum.*, **67**, 108–111, (1996).
 - [83] O.Yu. Kolesnychenko, O.I. Shklyarevskii, and H. van Kempen. Calibration of the distance between electrodes of mechanically controlled break junctions using field-emission resonance. *Rev. Sci. Instrum.*, **70**, 1442–1446, (1999).
 - [84] O.Yu. Kolesnychenko, O.I. Shklyarevskii, and H. van Kempen. Giant influence of adsorbed helium on field emission resonance measurements. *Phys. Rev. Lett.*, **83**, 2242–2245, (1999).
 - [85] H. van Kempen and O.I. Shklyarevskii. Mechanically controlled fractured junctions and their possible applications in point-contact spectroscopy. *Low Temp. Phys.*, **19**, 583–589, (1993).
 - [86] J.M. Krams and J.M. van Ruitenbeek. Subquantum conductance steps in atom-sized contacts of the semimetal Sb. *Phys. Rev. B*, **50**, 17659–17661, (1994).
 - [87] N. van der Post and J.M. van Ruitenbeek. High stability STM made of a break junction. *Czech. J. Phys.*, **46**, Suppl.S5, 2853–2854, (1996).
 - [88] R.J.P. Keijsers, J. Voets, O.I. Shklyarevskii, and H. van Kempen. Electrode geometry influencing the tunnel resistance in a mechanically controllable break junction. *Physica B*, **218**, 283–286, (1996).
 - [89] C. Untiedt, A.M.C. Houkes Valkering, A. Hulea, T.H. Oosterkamp, K. Babaiedyawan, J.M. van Ruitenbeek, G. Rubio-Bollinger, P. Joyez, and N. Agraït. Measurement of the force constant of atomic contacts using a quartz tuning-fork resonator in a break junction device. unpublished.
 - [90] N. Agraït, J.G. Rodrigo, G. Rubio, C. Sirvent, and S. Vieira. Plastic deformation in atomic size contacts. *Thin Solid Films*, **253**, 199–203, (1994).
 - [91] N. Agraït, G. Rubio, and S. Vieira. Plastic deformation of nanometer-scale gold connective necks. *Phys. Rev. Lett.*, **74**, 3995–3998, (1995).
 - [92] N. Agraït, G. Rubio, and S. Vieira. Plastic deformation in nanometer scale contacts. *Langmuir*, **12**, 4504–4509, (1996).

- [93] G. Rubio-Bollinger, S.R. Bahn, N. Agraït, K.W. Jacobsen, and S. Vieira. Mechanical properties and formation mechanisms of a wire of single gold atoms. *Phys. Rev. Lett.*, **87**, 026101, (2001).
- [94] P.E. Marszalek, W.J. Greenleaf, H. Li, A.F. Oberhauser, and J.M. Fernandez. Atomic force microscopy captures quantized plastic deformation in gold nanowires. *Proc. Nat. Acad. Sci.*, **97**, 6282–6286, (2000).
- [95] S.P. Jarvis, M.A. Lantz, H. Ogiso, H. Tokumo, and U. Dürig. Conduction and mechanical properties of atomic scale gold contacts. *Appl. Phys. Lett.*, **75**, 3132–3134, (1999).
- [96] A. Stalder and U. Dürig. Study of yielding mechanics in nanometer-sized Au contacts. *Appl. Phys. Lett.*, **68**, 637–639, (1996).
- [97] K.S. Ralls and R.A. Buhrman. Defect interactions and noise in metallic nanoconstrictions. *Phys. Rev. Lett.*, **60**, 2434–2437, (1988).
- [98] E.S. Snow, P.M. Campbell, and D. Park. Metal point contacts and metal-oxide tunnel barriers fabricated with an AFM. *Superlattices and Microstructures*, **20**, 545–553, (1996).
- [99] E.S. Snow, D. Park, and P.M. Campbell. Single-atom point contact devices fabricated with an atomic force microscope. *Appl. Phys. Lett.*, **69**, 269–271, (1996).
- [100] T. Schmidt, R. Martel, R.L. Sandstrom, and Ph. Avouris. Current-induced local oxidation of metal films: mechanism and quantum-size effects. *Appl. Phys. Lett.*, **73**, 2173–2175, (1998).
- [101] C.Z. Li and N.J. Tao. Quantum transport in metallic nanowires fabricated by electrochemical deposition/dissolution. *Appl. Phys. Lett.*, **72**, 894–896, (1998).
- [102] C.Z. Li, A. Bogoz, W. Huang, and N.J. Tao. Fabrication of stable metallic nanowires with quantized conductance. *Nanotechnology*, **10**, 221–223, (1999).
- [103] A.F. Morpurgo, C.M. Marcus, and D.B. Robinson. Controlled fabrication of metallic electrodes with atomic separation. *Appl. Phys. Lett.*, **74**, 2084–2086, (1999).
- [104] T. Junno, S.-B. Carlsson, H. Xu, L. Montelius, and L. Samuelson. Fabrication of quantum devices by Ångström-level manipulation of nanoparticles with an atomic force microscope. *Appl. Phys. Lett.*, **72**, 548–550, (1998).
- [105] A. Anaya, A.L. Korotkov, M. Bowman, and D. Davidovic. Zero-bias anomalies and g-factors in atomic-scale gold contacts. *preprint*, (2002). <http://arXiv.org/abs/cond-mat/0202372>.
- [106] V. Rodrigues and D. Ugarte. Real-time imaging of atomistic process in one-atom-thick metal junctions. *Phys. Rev. B*, **63**, 073405, (2001).
- [107] K. Hansen, E. Laegsgaard, I. Stensgaard, and F. Besenbacher. Quantized conductance in relays. *Phys. Rev. B*, **56**, 2208–2220, (1997).
- [108] J.L. Costa-Krämer, N. García, P. García-Mochales, P.A. Serena, M.I. Marqués, and A. Correia. Conductance quantization in nanowires formed between micro and macroscopic metallic electrodes. *Phys. Rev. B*, **55**, 5416–5424, (1997).
- [109] H. Yasuda and A. Sakai. Conductance of atomic-scale gold contacts under high-bias voltages. *Phys. Rev. B*, **56**, 1069–1072, (1997).
- [110] S. Gregory. Inelastic tunneling spectroscopy and single-electron tunneling in an adjustable microscopic tunnel junction. *Phys. Rev. Lett.*, **64**, 689–692, (1990).
- [111] S. Datta. *Electronic Transport in Mesoscopic Systems*. Cambridge University Press, Cambridge, UK, (1997).
- [112] S. Washburn. Resistance fluctuations in small samples: Be careful when playing with ohm’s law. In B. Kramer, editor, *Quantum Coherence in Mesoscopic Systems*, pages 341–367. Plenum Press, New York, (1991).
- [113] J.C. Maxwell. *A treatise on electricity and magnetism*, volume 1. Dover Publ., inc., New York, (1954).
- [114] Yu.V. Sharvin. A possible method for studying Fermi surfaces. *Sov. Phys.-JETP*, **21**, 655–656, (1965). [*Zh. Eksp. Teor. Fiz.* 48, 984–985 (1965)].
- [115] M. Knudsen. *Kinetic theory of gases*. Methuen, London, (1934).
- [116] M. Büttiker. Transmission, reflection and the resistance of small conductors. In J. M. Chamberlain, L. Eaves, and J. C. Portal, editors, *Electronic Properties of Multilayers and low Dimensional Semiconductors*, pages 51–73. Plenum Press, New York, (1990).
- [117] Y. Imry. Physics of mesoscopic systems. In G. Grinstein and G. Mazenko, editors, *Directions in Condensed Matter Physics*, pages 101–163. World Scientific, Singapore, (1986).
- [118] M. Büttiker. Scattering theory of current and intensity noise correlations in conductors and wave guides. *Phys. Rev. B*, **46**, 12485–12507, (1992).
- [119] R. Landauer. Electrical resistance of disordered one-dimensional lattices. *Phil. Mag.*, **21**, 863–867, (1970).
- [120] M.J.M. de Jong and C.W.J. Beenakker. Shot noise in mesoscopic systems. In L.L. Sohn, L.P. Kouwenhoven, and G. Schön, editors, *Mesoscopic Electron Transport*, volume 345 of *NATO-ASI Series E: Appl. Sci.*, pages 225–258, Dordrecht, (1997). Kluwer Academic Publishers.
- [121] Ya. M. Blanter and M. Büttiker. Shot noise in mesoscopic conductors. *Phys. Rep.*, **336**, 2–166, (2000).
- [122] L. Saminadayar, D.C. Glatli, Y. Jin, and B. Etienne. Observation of the $e/3$ fractionally charged Laughlin quasiparticle. *Phys. Rev. Lett.*, **79**, 2526–2529, (1997).
- [123] R. de Picciotto, M. Reznikov, M. Heiblum, V. Umansky, G. Bunin, and D. Mahalu. Direct observation of a fractional charge. *Nature*, **389**, 162–164, (1997).
- [124] J.C. Cuevas, A. Martín-Rodero, and A. Levy Yeyati. Shot noise and coherent multiple charge transfer in superconducting quantum point contacts. *Phys. Rev. Lett.*, **82**, 4086–4089, (1999).
- [125] Y. Naveh and D.V. Averin. Nonequilibrium current noise in mesoscopic disordered superconductor-normal-metal-superconductor junctions. *Phys. Rev. Lett.*, **82**, 4090–4093, (1999).
- [126] V.A. Khlus. Excess quantum noise in 2D ballistic point contacts. *Sov. Phys. JETP*, **66**, 592, (1989). [*Zh. Eksp. Teor. Fiz.* **93** (1987) 2179].
- [127] U. Sivan and Y. Imry. Multichannel landauer formula for thermoelectric transport with application to thermopower near the mobility edge. *Phys. Rev. B*, **33**, 551–558, (1986).
- [128] P. Streda. Quantised thermopower of a channel in the ballistic regime. *J. Phys.: Condens. Matter*, **1**, 1025–1027, (1989).
- [129] H. van Houten, L.W. Molenkamp, C.W.J. Beenakker, and C.T. Foxon. Thermo-electric properties of quantum point contacts. *Semicond. Sci. Technol.*, **7**, B215–B221, (1992).

- [130] P.L. Pernas, A. Martín-Rodero, and F. Flores. Electrochemical-potential variations across a constriction. *Phys. Rev. B*, **41**, 8553–8556, (1990).
- [131] T.N. Todorov. Non-linear conductance of disordered quantum wires. *J. Phys.: Condens. Matter*, **12**, 8995–9006, (2000).
- [132] M. Brandbyge, J. Taylor, K. Stokbro, J.-L. Mozos, and P. Ordejon. Density functional method for nonequilibrium electron transport. *preprint*, (2002). <http://arXiv.org/abs/cond-mat/0110650>.
- [133] M. Büttiker. Role of quantum coherence in series resistors. *Phys. Rev. B*, **33**, 3020–3026, (1986).
- [134] J.L. D’Amato and H. Pastawski. Conductance of a disordered linear chain including inelastic scattering events. *Phys. Rev. B*, **41**, 7411–7420, (1990).
- [135] S. Datta. A simple kinetic equation for steady-state quantum transport. *J. Phys.: Condens. Matter*, **2**, 8023–8052, (1990).
- [136] S. Hershfield. Equivalence of the multilead approach to dephasing and the self-consistent born approximation. *Phys. Rev. B*, **43**, 11586–11594, (1991).
- [137] J. Bonča and S.A. Trugman. Inelastic quantum transport. *Phys. Rev. Lett.*, **75**, 4874–4877, (1997).
- [138] H. Ness and A.J. Fisher. Quantum inelastic conductance through molecular wires. *Phys. Rev. Lett.*, **83**, 452–455, (1999).
- [139] H. van Houten, C.W.J. Beenakker, and A.A.M. Staring. Coulomb-blockade oscillations in semiconductor nanostructures. In H. Grabert and M.H. Devoret, editors, *Single Electron Tunneling*, pages 167–216. Plenum Press, New York, (1991).
- [140] Y. Meir and N.S. Wingreen. Landauer formula for the current through an interacting electron region. *Phys. Rev. Lett.*, **68**, 2512–2515, (1992).
- [141] J. Mahan. *Many-Particle Physics*. Plenum Press, New York, (1990).
- [142] E.N. Economou. *Green’s functions in Quantum Physics*. Springer, Berlin, (1983).
- [143] P.A. Lee and D.S. Fisher. Relation between conductivity and transmission matrix. *Phys. Rev. B*, **23**, 6851–6854, (1981).
- [144] H.U. Baranger and A.D. Stone. Electrical linear-response theory in an arbitrary magnetic field: a new fermi-surface formation. *Phys. Rev. B*, **40**, 8169, (1989).
- [145] J. Bardeen. Tunnelling from a many-particle point of view. *Phys. Rev. Lett.*, **6**, 57–59, (1961).
- [146] A. Barone and G. Paterno. *Physics and Applications of the Josephson Effect*. Wiley, New York, (1982).
- [147] P.G. de Gennes. *Superconductivity of Metals and Alloys*. W.A. Benjamin, New York, (1966).
- [148] A.F. Andreev. The thermal conductivity of the intermediate state in superconductors. *Sov. Phys. JETP*, **19**, 1228–1231, (1964).
- [149] G.E. Blonder, M. Tinkham, and T.M. Klapwijk. Transition from metallic to tunneling regimes in superconducting microconstrictions: Excess current, charge imbalance, and supercurrent conversion. *Phys. Rev. B*, **25**, 4515–4532, (1982).
- [150] C.W.J. Beenakker. Three ‘universal’ mesoscopic Josephson effects. In H. Fukuyama and T. Ando, editors, *Proceedings of the 14th Taniguchi International Symposium on Transport Phenomena in Mesoscopic Systems*, pages 235–253, Berlin, (1992). Springer-Verlag.
- [151] I.O. Kulik. Macroscopic quantization and the proximity effect in S-N-S junctions. *Sov. Phys. JETP*, **30**, 944–950, (1970). [*Zh. Eksp. Teor. Fiz.* **57** (1969) 1745–1759].
- [152] A. Furusaki and M. Tsukada. A unified theory of clean Josephson junctions. *Physica B*, **165** & **166**, 967–968, (1990).
- [153] I.O. Kulik and A.N. Omelyanchuk. Properties of superconducting microbridges in the pure limit. *Sov. J. Low Temp. Phys.*, **3**, 459–461, (1977). [*Fiz. Nizk. Temp.* **3** (1977) 945].
- [154] C.W.J. Beenakker and H. van Houten. Josephson current through a superconducting quantum point contact shorter than the coherence length. *Phys. Rev. Lett.*, **66**, 3056–3059, (1991).
- [155] W. Haberkorn, H. Knauer, and J. Richter. A theoretical study of the current-phase relation in Josephson contacts. *Phys. Stat. Sol.*, **47**, K161–K164, (1978).
- [156] G.B. Arnold. Superconducting tunneling without the tunneling hamiltonian. *J. Low Temp. Phys.*, **59**, 143–183, (1985).
- [157] A. Martín-Rodero, F.J. García-Vidal, and A. Levy Yeyati. Microscopic theory of Josephson mesoscopic constrictions. *Phys. Rev. Lett.*, **72**, 554–557, (1994).
- [158] B.D. Josephson. Possible new effects in superconductive tunnelling. *Phys. Lett.*, **1**, 251–253, (1962).
- [159] A. Levy Yeyati, A. Martín-Rodero, and F.J. García-Vidal. Self-consistent theory of superconducting mesoscopic weak links. *Phys. Rev. B*, **51**, 3743–3753, (1995).
- [160] D. Averin and H.T. Imam. Supercurrent noise in quantum point contacts. *Phys. Rev. Lett.*, **76**, 3814–3817, (1996).
- [161] A. Martín-Rodero, A. Levy Yeyati, and F.J. García-Vidal. Thermal noise in superconducting quantum point contacts. *Phys. Rev. B*, **53**, R8891–R8894, (1996).
- [162] M. Goffman, R. Cron, A. Levy Yeyati, P. Joyez, M.H. Devoret, D. Esteve, and C. Urbina. Supercurrent in atomic point contacts and Andreev states. *Phys. Rev. Lett.*, **85**, 170–173, (2000).
- [163] B.N. Taylor and E. Burstein. Excess currents in electron tunneling between superconductors. *Phys. Rev. Lett.*, **10**, 14–17, (1963).
- [164] C.J. Adkins. Two-particle tunnelling between superconductors. *Phil. Mag.*, **8**, 1051–1061, (1963).
- [165] J.R. Schrieffer and J.W. Wilkins. Two-particle tunneling processes between superconductors. *Phys. Rev. Lett.*, **10**, 17–20, (1963).
- [166] N.R. Werthamer. Non-linear self-coupling of Josephson radiation in superconducting tunnel junctions. *Phys. Rev.*, **147**, 255–263, (1966).
- [167] M. Octavio, G.E. Blonder, M. Tinkham, and T.M. Klapwijk. Subharmonic energy-gap structure in superconducting constrictions. *Phys. Rev. B*, **27**, 6739–6746, (1983).
- [168] V. Ambegaokar and B.I. Halperin. Voltage due to thermal noise in the dc Josephson effect. *Phys. Rev. Lett.*, **22**, 1364–1366, (1969).
- [169] H. van den Brom, A.I. Yanson, and J.M. van Ruitenbeek. Characterization of individual conductance steps in metallic quantum point contacts. *Physica B*, **252**, 69–75, (1998).
- [170] J. M. Krams. *Size effects in atomic-scale point contacts*. PhD thesis, Universiteit Leiden, The Netherlands, (1996).
- [171] W.A. de Heer, S. Frank, and D. Ugarte. Fractional

- quantum conductance in gold nanowires. *Z. Phys. B*, **104**, 469–473, (1997).
- [172] F. Kassubek, C.A. Stafford, H. Grabert, and R.E. Goldstein. Quantum suppression of the rayleigh instability in nanowires. *Nonlinearity*, **14**, 167–177, (2001).
- [173] G. Binnig, N. García, H. Rohrer, J.M. Soler, and F. Flores. Electron-metal surface interaction potential with vacuum tunneling: Observation of the image force. *Phys. Rev. B*, **30**, 4816–4818, (1984).
- [174] N.D. Lang. Apparent barrier height in scanning tunneling microscopy. *Phys. Rev. B*, **37**, 10395–10398, (1988).
- [175] J.H. Coombs, M.E. Welland, and J.B. Pethica. Experimental barrier heights and the image potential in scanning tunneling microscopy. *Surface Science*, **198**, L353–L358, (1988).
- [176] L. Olesen, B. Brandbyge, M.R. Sørensen, K.W. Jacobsen, E. Lægsgaard, I. Stensgaard, and F. Besenbacher. Apparent barrier height in scanning tunneling microscopy revisited. *Phys. Rev. Lett.*, **76**, 1485–1488, (1996).
- [177] J. Voets, R.J.P. Keijsers, O.I. Shklyarevskii, and H. van Kempen. Effects of electrode interactions observed in a mechanically controllable break junction. *Phys. Rev. B*, **53**, 1072–1075, (1996).
- [178] J. Wintterlin, J. Wiechers, H. Brune, T. Gritsch, H. Höfer, and R.J. Behm. Atomic-resolution imaging of close-packed metal surfaces by scanning tunneling microscopy. *Phys. Rev. Lett.*, **62**, 59–62, (1989).
- [179] S. Ciraci, A. Baratoff, and I.P. Batra. Tip-sample interaction effects in scanning-tunneling and atomic-force microscopy. *Phys. Rev. B*, **41**, 2763–2775, (1990).
- [180] S. Ciraci, A. Baratoff, and I.P. Batra. Site-dependent electronic effects, forces, and deformations in scanning tunneling microscopy of flat metal surfaces. *Phys. Rev. B*, **42**, 7618–7621, (1990).
- [181] A.R.H. Clarke, J.B. Pethica, J.A. Nieminen, F. Besenbacher, E. Laegsgaard, and I. Stensgaard. Quantitative scanning tunneling microscopy at atomic resolution: Influence of forces and tip configuration. *Phys. Rev. Lett.*, **76**, 1276–1279, (1996).
- [182] J.B. Pethica and A.P. Sutton. On the stability of a tip and flat at very small separations. *J. Vac. Sci. Technol. A*, **6**, 2490–2494, (1988).
- [183] J.R. Smith, G. Bozzolo, A. Banerjee, and J. Ferrante. Avalanche in adhesion. *Phys. Rev. Lett.*, **63**, 1269–1272, (1989).
- [184] S. Ciraci and E. Tekman. Theoretical study of short- and long-range forces and atom transfer in scanning force microscopy. *Phys. Rev. B*, **46**, 10411–10422, (1992).
- [185] D.P.E. Smith. Quantum point contact switches. *Science*, **269**, 371–373, (1995).
- [186] B.S. Good and A. Banerjee. Simulation of tip-sample interaction in the atomic force microscope. *J. Phys.: Condens. Matter*, **8**, 1325–1333, (1996).
- [187] G. Cross, A. Schirmeisen, A. Stalder, P. Grütter, M. Tschudy, and U. Dürig. Adhesion interaction between atomically defined tip and sample. *Phys. Rev. Lett.*, **80**, 4685–4688, (1998).
- [188] L. Kuipers and J.W.M. Frenken. Jump to contact, neck formation and surface melting in the scanning tunneling microscope. *Phys. Rev. Lett.*, **70**, 3907–3910, (1993).
- [189] Z. Gai, X. Li, B. Gao, R.G. Zhao, W.S. Yang, and J.W.M. Frenken. Spontaneous breaking of nanowires between a STM tip and the Pb(110) surface. *Phys. Rev. B*, **58**, 2185–2190, (1998).
- [190] C.J. Muller, J.M. Krans, T.N. Todorov, and M.A. Reed. Quantization effects in the conductance of metallic contacts at room temperature. *Phys. Rev. B*, **53**, 1022–1025, (1996).
- [191] M.R. Sørensen, K.W. Jacobsen, and H. Jónsson. Thermal diffusion processes in metal-tip-surface interactions: contact formation and adatom mobility. *Phys. Rev. Lett.*, **77**, 5067–5070, (1996).
- [192] R. Hasunuma, T. Komeda, H. Mukaida, and H. Tokumoto. Formation of Si nanowire by atomic manipulation with a high temperature scanning tunneling microscope. *J. Vac. Sci. Technol. B*, **15**, 1437–1441, (1997).
- [193] J. Abellán, A. Arenas, R. Chicón, and F. Reyes. Stable nanowire in macroscopic metallic contacts in air. *Surface Science*, **372**, L315–L318, (1997).
- [194] J. Abellán, R. Chicón, and A. Arenas. Properties of nanowires in air. Controlled values of the conductance. *Surf. Sci.*, **418**, 493–501, (1998).
- [195] A. Correia, J.-L. Costa-Krämer, Y.W. Zhao, and N. García. Non-linear contribution to intensity-voltage characteristics of gold nanowires. *Nanostruct. Mater.*, **12**, 1015–1020, (1999).
- [196] K. Hansen, S. K. Nielsen, M. Brandbyge, E. Lægsgaard, I. Stensgaard, and F. Besenbacher. Current-voltage curves of gold quantum point contacts revisited. *Appl. Phys. Lett.*, **77**, 708–710, (2000).
- [197] J.L. Costa-Krämer. Conductance quantization at room temperature in magnetic and nonmagnetic metallic nanowires. *Phys. Rev. B*, **55**, R4875–R4878, (1997).
- [198] M. Brandbyge, M.R. Sørensen, and K.W. Jacobsen. Conductance eigenchannels in nanocontacts. *Phys. Rev. B*, **56**, 14956–14959, (1997).
- [199] J.L. Costa-Krämer, N. García, and H. Olin. Conductance quantization histograms of gold nanowires at 4 K. *Phys. Rev. B*, **55**, 12910–12913, (1997).
- [200] C.Z. Li, H. Sha, and N.J. Tao. Adsorbate effect on conductance quantization in metallic nanowires. *Phys. Rev. B*, **58**, 6775–6778, (1998).
- [201] W.B. Jian, C.S. Chang, W.Y. Li, and T.T. Tsong. Geometrical dependence of conductance quantization in metal point contacts. *Phys. Rev. B*, **59**, 3168–3172, (1999).
- [202] B. Ludoph, M.H. Devoret, D. Esteve, C. Urbina, and J.M. van Ruitenbeek. Evidence for saturation of channel transmission from conductance fluctuations in atomic-size point contacts. *Phys. Rev. Lett.*, **82**, 1530–1533, (1999).
- [203] K. Itakura, K. Yuki, S. Kurokawa, H. Yasuda, and A. Sakai. Bias dependence of the conductance of Au nanocontacts. *Phys. Rev. B*, **60**, 11163–11169, (1999).
- [204] C. Shu, C.Z. Li, H.X. He, A. Bogozzi, J.S. Bunch, and N.J. Tao. Fractional conductance quantization in metallic nanoconstrictions under electrochemical potential control. *Phys. Rev. Lett.*, **84**, 5196–5199, (2000).
- [205] K. Yuki, A. Enomoto, and A. Sakai. Bias-dependence of the conductance of Au nanocontacts at 4 K. *Appl. Surf. Sci.*, **169–170**, 489–492, (2001).
- [206] A.I. Yanson. *Atomic chains and electronic shells: Quantum mechanisms for the formation of nanowires*. PhD thesis, Universiteit Leiden, The Netherlands, (2001).
- [207] B. Ludoph and J.M. van Ruitenbeek. Conductance fluctuations as a tool for investigating the quantum modes

- in atomic-size metallic contacts. *Phys. Rev. B*, **61**, 2273–2285, (2000).
- [208] A.I. Yanson, I.K. Yanson, and J.M. van Ruitenbeek. Shell effects in the alkali metals li, na, k and cs. unpublished.
- [209] E.N. Bogachek, A.N. Zagorskin, and I.O. Kulik. Conductance jumps and magnetic flux quantization in ballistic point contacts. *Sov. J. Low Temp. Phys.*, **16**, 796–800, (1990).
- [210] J.A. Torres, J.I. Pascual, and J.J. Sáenz. Theory of conduction through narrow constrictions in a three-dimensional electron gas. *Phys. Rev. B*, **49**, 16581–16584, (1994).
- [211] A. Nakamura, M. Brandbyge, L.B. Hansen, and K.W. Jacobsen. Density functional simulation of a breaking nanowire. *Phys. Rev. Lett.*, **82**, 1538–1541, (1999).
- [212] J.L. Costa-Krämer, N. García, P. García-Mochales, M.I. Marqués, and P.A. Serena. Metallic nanowires: conductance statistics, stability, IV curves, and magnetism. In P.A. Serena and N. García, editors, *Nanowires, NATO-ASI series E: Appl. Sci., Vol. 340*, pages 171–190, Dordrecht, (1997). Kluwer Academic Publishers.
- [213] T. Ono, Y. Ooka, H. Miyajima, and Y. Otani. $2e^2/h$ to e^2/h switching of quantum conductance associated with a change in nanoscale ferromagnetic domain structure. *Appl. Phys. Lett.*, **75**, 1622–1624, (1999).
- [214] V. Rodrigues, J. Bettini, A.R. Rocha, L.G.C. Rego, and D. Ugarte. Quantum conductance in silver nanowires: correlation between atomic structure and transport properties. *Preprint*, (2002). <http://arXiv.org/abs/cond-mat/0201156>.
- [215] C.Z. Li, H.X. He, A. Bogozi, J.S. Bunch, and N.J. Tao. Molecular detection based on conductance quantization of nanowires. *Appl. Phys. Lett.*, **76**, 1333–1335, (2000).
- [216] R.H.M. Smit, C. Untiedt, A.I. Yanson, and J.M. van Ruitenbeek. Common origin for surface reconstruction and the formation of chains of metal atoms. *Phys. Rev. Lett.*, **87**, 266102, (2001).
- [217] Y. Noat, R.H.M. Smit, C. Untiedt, N.D. Lang, M. van Hemert, and J.M. van Ruitenbeek. Measurement of the conductance of a hydrogen molecule. *Nature*, (2002). submitted.
- [218] K. Itakura, H. Yasuda, S. Kurokawa, and A. Sakai. Conductance of Rh and Ru nanocontacts. *J. Phys. Soc. Jap.*, **69**, 625–626, (2000).
- [219] K. Yuki, S. Kurokawa, and A. Sakai. Conductance in breaking nanocontacts of some transition metals. *Jpn. J. Appl. Phys.*, **40**, 803–808, (2001).
- [220] B. Ludoph, N. van der Post, E.N. Bratus', E.V. Bezuglyi, V.S. Shumeiko, G. Wendin, and J.M. van Ruitenbeek. Multiple Andreev reflection in single atom niobium junctions. *Phys. Rev. B*, **61**, 8561–8569, (2000).
- [221] E. Scheer, P. Brenner, R. Cron, and H. von Löhneisen. Fabrication of zn-whisker break-junctions. unpublished.
- [222] F. Ott, S. Barberan, J.G. Lunney, J.M.D. Coey, P. Berthlet, A.M. de Leon-Guevara, and A. Revcolevschi. Quantized conductance in a contact between metallic oxide crystals. *Phys. Rev. B*, **58**, 4656–4659, (1998).
- [223] H. Oshima and K. Miyano. Spin-dependent conductance quantization in nickel point contacts. *Appl. Phys. Lett.*, **73**, 2203–2205, (1998).
- [224] F. Komori and K. Nakatsuji. Quantized conductance through atomic-sized iron contacts at 4.2 K. *J. Phys. Soc. Jap.*, **68**, 3786–3789, (1999).
- [225] N. García, M. Muñoz, and Y.-W. Zhao. Magnetoresistance in excess of 200% in ballistic Ni nanocontacts at room temperature and 100 Oe. *Phys. Rev. Lett.*, **82**, 2923–2926, (1999).
- [226] G. Tatara, Y.-W. Zhao, M. Muñoz, and N. García. Domain wall scattering explains 300% ballistic magnetoresistance of nanocontacts. *Phys. Rev. Lett.*, **83**, 2030–2033, (1999).
- [227] A.I. Yanson and J.M. van Ruitenbeek. Do histograms constitute a proof for conductance quantization? *Phys. Rev. Lett.*, **79**, 2157–2157, (1997).
- [228] A. Hasmy, E. Medina, and P.A. Serena. From favorable atomic configurations to supershell structures: a new interpretation of conductance histograms. *Phys. Rev. Lett.*, **86**, 5574–5577, (2001).
- [229] J.C. Cuevas, A. Levy Yeyati, A. Martín-Rodero, G. Rubio Bollinger, C. Untiedt, and N. Agrait. Evolution of conducting channels in metallic atomic contacts under elastic deformation. *Phys. Rev. Lett.*, **81**, 2990–2993, (1998).
- [230] B.B. Lewis, K.G. Vandervoort, and R.D. Foster. Measurements of quantized conductance in gallium as a function of temperature. *Solid State Commun.*, **109**, 525–530, (1999).
- [231] R. Hasunuma, T. Komeda, and H. Tokumoto. Electric properties of nanoscale contacts on Si(111) surfaces. *Appl. Surf. Sci.*, **130–132**, 84–89, (1998).
- [232] J.L. Costa-Krämer, N. García, and H. Olin. Conductance quantization in bismuth nanowires at 4 K. *Phys. Rev. Lett.*, **78**, 4990–4993, (1997).
- [233] L.I. Glazman and A.V. Khaetskii. Nonlinear quantum conductance of a lateral microconstraint in a heterostructure. *Europhys. Lett.*, **9**, 263–267, (1989).
- [234] J.I. Pascual, J.A. Torres, and J.J. Sáenz. Non-linear ballistic conductance in atomic-scale metallic contacts. *Phys. Rev. B*, **55**, 16029–16032, (1997).
- [235] E.N. Bogachek, A.G. Scherbakov, and U. Landman. Nonlinear magnetoresistance of nanowires. *Phys. Rev. B*, **56**, 14917–14920, (1997).
- [236] J.G. Rodrigo, A. García-Martín, J.J. Sáenz, and S. Vieira. Quantum conductance in semimetallic bismuth nanocontacts. *Phys. Rev. Lett.*, **88**, 246801, (2002).
- [237] A. Enomoto, S. Kurokawa, and A. Sakai. Quantized conductance in AuPd and AuAg alloy nanocontacts. *Phys. Rev. B*, **65**, 125410, (2002).
- [238] D. J. Bakker, Y. Noat, A. I. Yanson, and J. M. van Ruitenbeek. Effect of disorder on the conductance of a Cu atomic point contact. *Phys. Rev. B*, **65**, 235416, (2002).
- [239] J.W.T. Heemskerk, Y. Noat, D.J. Bakker, B.J. Thijsse, P. Klaver, and J.M. van Ruitenbeek. A current induced transition in atomic-size contacts of metallic alloys. *preprint*, (2002).
- [240] B.A. Volkov, D.N. Davydov, A.E. Svistov, and E.G. Chizhevskii. Quantum conductance of metal-narrow-gap semiconductor $Pb_{1-x}Sn_xSe$. *Phys. Solid State*, **37**, 1576–1577, (1995).
- [241] B. Ludoph. *Quantum conductance properties of atomic-size contacts*. PhD thesis, Universiteit leiden, The Netherlands, (1999).
- [242] S. Frank, P. Poncharal, Z.L. Wang, and W.A. de Heer. Carbon nanotube quantum resistors. *Science*, **280**,

- 1744–1746, (1998).
- [243] J. Kong, E. Yenilmez, T.W. Tombler, W. Kim, H. Dai, R.B. Laughlin, L. Liu, C.S. Jayanthi, and S.Y. Wu. Quantum interference and ballistic transmission in nanotube electron waveguides. *Phys. Rev. Lett.*, **87**, 106801, (2001).
 - [244] H. Srikanth and A.K. Raychaudhuri. Transition from metallic to tunneling-type conductance in metal-metal and normal-metal-superconductor point contacts. *Phys. Rev. B*, **46**, 14713–14719, (1992).
 - [245] K. Hansen, S. K. Nielsen, E. Lægsgaard, I. Stensgaard, and F. Besenbacher. Fast and accurate current-voltage curves of metallic quantum point contacts. *Rev. Sci. Instrum.*, **71**, 1793–1803, (2000).
 - [246] M. Brandbyge, N. Kobayashi, and M. Tsukada. Conduction channels at finite bias in single-atom gold contacts. *Phys. Rev. B*, **60**, 17064–17070, (1999).
 - [247] H. Mehrez, A. Wlasenko, B. Larade, J. Taylor, P. Grütter, and H. Guo. I-V characteristics and differential conductance fluctuations of Au nanowires. *Phys. Rev. B*, **65**, 195419, (2002).
 - [248] S.K. Nielsen, M. Brandbyge, K. Hansen, K. Stokbro, J.M. van Ruitenbeek, and F. Besenbacher. Current-voltage curves of atomic-sized transition metal contacts: An explanation of why Au is ohmic and Pt is not. *Phys. Rev. Lett.*, **89**, 066804, (2002).
 - [249] B. Bhushan, J.N. Israelachvili, and U. Landman. Nanotribology: friction, wear and lubrication at the atomic scale. *Nature*, **374**, 607–616, (1995).
 - [250] U. Landman, W.D. Luedtke, and J. Gao. Atomic-scale issues in tribology: interfacial junctions and nano-elastohydrodynamics. *Langmuir*, **12**, 4514–4528, (1996).
 - [251] L.D. Landau and E.M. Lifshitz. *Theory of Elasticity*, volume 7 of *Landau and Lifshitz Course of Theoretical Physics*. Pergamon Press, Oxford, 3rd edition, (1986).
 - [252] T.H. Courtney. *Mechanical Behavior of Materials*. Materials science and engineering series. McGraw-Hill, Singapore, 2nd edition, (2000).
 - [253] K.L. Johnson. *Contact Mechanics*. Cambridge University Press, Cambridge, (1985).
 - [254] J. Frenkel. Zur theorie der elastizitätsgrenze und der festigkeit kristallinischer körper. *Z. Phys.*, **37**, 572–609, (1926).
 - [255] A. Kelly and N.H. MacMillan. *Strong Solids*. Oxford University Press, Oxford, 3rd edition, (1986).
 - [256] S.P. Timoshenko and J.N. Goodier. *Theory of Elasticity*. Engineering Mechanics Series. McGraw-Hill, Singapore, 3rd edition, (1970).
 - [257] P. Tangyuyong, R.C. Thomas, J.E. Houston, T.A. Michalske, R.M. Crooks, and A.J. Howard. Nanometer-scale mechanics of gold films. *Phys. Rev. Lett.*, **71**, 3319–3322, (1993).
 - [258] R.W. Carpick, N. Agrait, D.F. Ogletree, and M. Salmeron. Variation of the interfacial shear strength and adhesion of a nanometer-sized contact. *Langmuir*, **12**, 3334–3340, (1996).
 - [259] R.W. Carpick, N. Agrait, D.F. Ogletree, and M. Salmeron. Measurement of interfacial shear (friction) with an ultrahigh vacuum atomic force microscope. *J. Vac. Sci. Techn. B*, **14**, 1289–1295, (1996).
 - [260] J.A. Torres and J.J. Sáenz. Conductance and mechanical properties of atomic-size metallic contacts: A simple model. *Phys. Rev. Lett.*, **77**, 2245–2248, (1996).
 - [261] C. Untiedt, G. Rubio, S. Vieira, and N. Agrait. Fabrication and characterization of metallic nanowires. *Phys. Rev. B*, **56**, 2154–2160, (1997).
 - [262] A. Stalder and U. Dürig. Study of plastic flow in ultra-small Au contacts. *J. Vac. Sci. Technol. B*, **14**, 1259–1263, (1996).
 - [263] N. Gane and F. P. Bowden. Microdeformation of solids. *J. Appl. Phys.*, **39**, 1432–1435, (1968).
 - [264] R.C. Thomas, J.E. Houston, T.A. Michalske, and R.M. Crooks. The mechanical response of gold substrates passivated by self-assembling monolayer films. *Science*, **259**, 1883–1885, (1993).
 - [265] J.K. Gimzewski, R. Möller, D.W. Pohl, and R.R. Schlittler. Transition from the tunneling regime to point contact investigated by scanning tunneling microscopy and spectroscopy. *Surface Science*, **189/190**, 15–23, (1987).
 - [266] V. Rodrigues, T. Fuhrer, and D. Ugarte. Signature of atomic structure in the quantum conductance of gold nanowires. *Phys. Rev. Lett.*, **85**, 4124–4127, (2000).
 - [267] Y. Takai, T. Kawasaki, Y. Kimura, T. Ikuta, and R. Shimizu. Dynamic observation of an atom-sized gold wire by phase electron microscopy. *Phys. Rev. Lett.*, **87**, 106105, (2001).
 - [268] T. Kizuka, S. Umehara, and S. Fujisawa. Metal-insulator transition in stable one-dimensional arrangements of single gold atoms. *Jpn. J. Appl. Phys.*, **40**, L71–L74, (2001).
 - [269] T.N. Todorov, G.A.D. Briggs, and A.P. Sutton. Elastic quantum transport through small structures. *J. Phys.: Condens. Matter*, **5**, 2389–2406, (1993).
 - [270] A.M. Bratkovsky, A.P. Sutton, and T.N. Todorov. Conditions for conductance quantization in realistic models of atomic-scale metallic contacts. *Phys. Rev. B*, **52**, 5036–5051, (1995).
 - [271] T.N. Todorov and A.P. Sutton. Force and conductance jumps in atomic-scale metallic contacts. *Phys. Rev. B*, **54**, R14234–R14237, (1996).
 - [272] H. Mehrez and S. Ciraci. Yielding and fracture mechanisms of nanowires. *Phys. Rev. B*, **56**, 12632–12642, (1997).
 - [273] H. Mehrez, C. Ciraci, C.Y. Fong, and S. Erkoç. An atomistic study on the stretching of nanowires. *J. Phys.: Condens. Matter*, **9**, 10843–10854, (1997).
 - [274] M.R. Sørensen, M. Brandbyge, and K.W. Jacobsen. Mechanical deformation of atomic-scale metallic contacts: structure and mechanisms. *Phys. Rev. B*, **57**, 3283–3294, (1998).
 - [275] R.N. Barnett and U. Landman. Cluster-derived structures and conductance fluctuations in nanowires. *Nature*, **387**, 788–791, (1997).
 - [276] M. Heinemann and R.A. de Groot. Aluminium break-point contacts. *Phys. Rev. B*, **55**, 9375–9378, (1997).
 - [277] E.Z. da Silva, A.J.R. da Silva, and A. Fazzio. How do gold wires break? *Phys. Rev. Lett.*, **87**, 256102, (2001).
 - [278] M.J. Mehl and D.A. Papaconstantopoulos. Applications of a tight-binding total-energy method for transition and noble metals: Elastic constants, vacancies, and surfaces of monatomic metals. *Phys. Rev. B*, **54**, 4519–4530, (1996).
 - [279] S.M. Foiles, M.I. Baskes, and M.S. Daw. Embedded-atom-method functions for the fcc metals Cu, Ag, Au, Ni, Pd, Pt and their alloys. *Phys. Rev. B*, **33**, 7983–7991, (1986).
 - [280] K.W. Jacobsen, J.K. Nørskov, and M.J. Puska. In-

- teratomic interactions in the effective medium theory. *Phys. Rev. B*, **35**, 6423–7442, (1987).
- [281] M.J. Stott and E. Zaremba. Quasiatoms: An approach to atoms in uniform electronic systems. *Phys. Rev. B*, **22**, 1564–1583, (1980).
- [282] J. K. Nørskov and N. D. Lang. Effective-medium theory of chemical binding: Application to chemisorption. *Phys. Rev. B*, **21**, 2131–2136, (1980).
- [283] H. Rafii-Tabar. Modelling the nano-scale phenomena in condensed matter physics via computer-based numerical simulations. *Phys. Rep.*, **325**, 239–310, (2000).
- [284] Y. Mishin, D. Farkas, M.J. Mehl, and D.A. Papaconstantopoulos. Interatomic potentials for monoatomic metals from experimental data and *ab initio* calculations. *Phys. Rev. B*, **59**, 3393–3407, (1999).
- [285] U. Landman and W.D. Luedtke. Nanomechanics of tip-substrate interactions. *J. Vac. Sci. Technol. B*, **9**, 414–423, (1991).
- [286] A.P. Sutton, J.B. Pethica, H. Rafii-Tabar, and J.A. Nieminen. Mechanical properties of metals at the nanometre scale. In D.G. Pettifor and A.H. Cottrell, editors, *Electron theory in alloy design*, pages 191–233. The Institute of Materials, London, (1992).
- [287] A.P. Sutton and T.N. Todorov. Mechanical and electrical properties of metallic contacts at the nanometre-scale. *J. Phys. Chem. Solids*, **55**, 1169–1174, (1994).
- [288] J.I. Pascual, J. Méndez, J. Gómez-Herrero, A.M. Baró, N. Garcia, U. Landman, W.D. Luedtke, E.N. Bogachek, and H.-P. Cheng. Electrical and mechanical properties of metallic nanowires: Conductance quantization and localization. *J. Vac. Sci. Technol. B*, **13**, 1280–1284, (1995).
- [289] A.P. Sutton. Deformation mechanisms, electronic conductance and friction of metallic nanocontacts. *Solid State & Materials Science*, **1**, 827–833, (1996).
- [290] M. Brandbyge, K.W. Jacobsen, and J.K. Nørskov. Scattering and conductance quantization in three-dimensional metal nanocontacts. *Phys. Rev. B*, **55**, 2637–2650, (1997).
- [291] A.M. Bratkovsky and S.N. Rashkeev. Electronic transport in nanoscale contacts with rough boundaries. *Phys. Rev. B*, **53**, 1–11, (1996).
- [292] T. López-Ciudad, A. García-Martín, A.J. Caamaño, and J.J. Sáenz. Conductance histograms and conducting channels in atomic-scale metallic contacts. *Surf. Science*, **440**, L887–L890, (1999).
- [293] A.G. Scherbakov, E.N. Bogachek, and U. Landman. Quantum electronic transport through three-dimensional microconstrictions with variable shapes. *Phys. Rev. B*, **53**, 4054–4064, (1996).
- [294] K. Hirose and M. Tsukada. First-principles calculation of the electronic structure for a bielectrode junction system under strong field and current. *Phys. Rev. B*, **51**, 5278–5290, (1995).
- [295] C. Höppler and W. Zwerger. Comment on jellium model of metallic nanocoheion. *Phys. Rev. Lett.*, **80**, 1792, (1998).
- [296] H. Weyl. Über die asymptotische Verteilung der Eigenwerte. *Kgl. Ges. d. Wiss. Nachrichten. Math. Phys. Klasse Heft*, **2**, 110–117, (1911).
- [297] P.M. Morse and H. Feshbach. *Methods of Theoretical Physics*. McGraw-Hill, New York, (1953). See p. 760.
- [298] M. Kac. Can we hear the shape of a drum? *Am. Math. Monthly*, **73**, 1–23, (1966).
- [299] A. García-Martín, J.A. Torres, and J.J. Sáenz. Finite size corrections to the conductance of ballistic wires. *Phys. Rev. B*, **54**, 13448–13451, (1996).
- [300] E.N. Bogachek, A.G. Scherbakov, and U. Landman. Shape effects on conductance quantization in three-dimensional nanowires: Hard versus soft potentials. *Phys. Rev. B*, **56**, 1065–1068, (1997).
- [301] E.N. Bogachek, A.G. Scherbakov, and U. Landman. Thermopower of quantum nanowires in a magnetic field. *Phys. Rev. B*, **54**, R11094–R11097, (1996).
- [302] A.G. Scherbakov, E.N. Bogachek, and U. Landman. Noise in three-dimensional nanowires. *Phys. Rev. B*, **57**, 6654–6661, (1998).
- [303] A. García-Martín, M. del Valle, J. J. Sáenz, J. L. Costa-Krämer, and P. A. Serena. Nonlinear effects in conductance histograms of atomic-scale metallic contacts. *Phys. Rev. B*, **62**, 11139–11145, (2000).
- [304] V.V. Pogosov, D.P. Koltlyarov, A. Kiejna, and K.F. Wojciechowski. Energetics of finite metallic nanowires. *Surface Science*, **472**, 172–178, (2001).
- [305] C. Yannouleas, E.N. Bogachek, and U. Landman. Energetics, forces, and quantized conductance in jellium-modeled metallic nanowires. *Phys. Rev. B*, **57**, 4872–4882, (1998).
- [306] N. Zabala, M.J. Puska, and R.M. Nieminen. Electronic structure of cylindrical simple-metal nanowires in the stabilized jellium model. *Phys. Rev. B*, **59**, 12652–12660, (1999).
- [307] S. Blom, H. Olin, J. L. Costa-Krämer, N. García, M. Jonson, P. A. Serena, and R. I. Shekhter. Free-electron model for mesoscopic force fluctuations in nanowires. *Phys. Rev. B*, **57**, 8830–8833, (1998).
- [308] C.A. Stafford. Quantum theory of metallic nanocoheion. *Physica E*, **1**, 310–312, (1998).
- [309] J. Bürki and C.A. Stafford. Comment on “quantum suppression of shot noise in atom-size metallic contacts”. *Phys. Rev. Lett.*, **83**, 3342, (1999).
- [310] F. Kassubek, C.A. Stafford, and H. Grabert. Force, charge, and conductance of an ideal metallic nanowire. *Phys. Rev. B*, **59**, 7560–7574, (1999).
- [311] C.A. Stafford, F. Kassubek, J. Bürki, and H. Grabert. Universality in metallic nanocoheion: a quantum chaos approach. *Phys. Rev. Lett.*, **83**, 4836–4839, (1999).
- [312] C. Caroli, R. Combescot, P. Nozieres, and D. Saint-James. Direct calculation of the tunneling current. *J. Phys. C: Solid St.*, **4**, 916–929, (1971).
- [313] A. Levy Yeyati. Non linear conductance fluctuations in quantum wires: appearance of two different energy scales. *Phys. Rev. B*, **45**, 15189–14195, (1992).
- [314] A. Martín-Rodero, J. Ferrer, and F. Flores. Contact resistance and saturation effects in the scanning tunneling microscope: the resistance quantum unit. *J. Microscopy*, **152**, 317–323, (1988).
- [315] A. Levy Yeyati, A. Martín-Rodero, and F. Flores. Conductance quantization and electron resonances in sharp tips and atomic-size contacts. *Phys. Rev. B*, **56**, 10369–10372, (1997).
- [316] S. Kirchner, J. Kroha, and E. Scheer. Generalized conductance sum rule in atomic break junctions. In V. Chandrasekhar, C. van Haesendonck, and A. Zawadowski, editors, *Kondo Effect and Dephasing in Low-Dimensional Metallic Systems*, pages 215–218, Dordrecht, (2001). Kluwer Academic Publishers.

- [317] D.A. Papaconstantopoulos. *Handbook of the band structure of elemental solids*. Plenum Press, New York, (1986).
- [318] R.N. Barnett and U. Landman. Born-oppenheimer molecular-dynamics simulations of finite systems: Structure and dynamics of $(\text{H}_2\text{O})_2$. *Phys. Rev. B*, **48**, 2081–2097, (1993).
- [319] W. Kohn and L.J. Sham. Self-consistent equations including exchange and correlation effects. *Phys. Rev.*, **140**, A1113–A1138, (1965).
- [320] P. Hohenberg and W. Kohn. Inhomogeneous electron gas. *Phys. Rev.*, **136**, B864–B871, (1964).
- [321] N.D. Lang. Negative differential resistance at atomic contacts. *Phys. Rev. B*, **55**, 9364–9366, (1997).
- [322] N.D. Lang. Anomalous dependence of resistance on length in atomic wires. *Phys. Rev. Lett.*, **79**, 1357–1360, (1997).
- [323] N.D. Lang and Ph. Avouris. Oscillatory conductance of carbon-atom wires. *Phys. Rev. Lett.*, **81**, 3515–3518, (1998).
- [324] N.D. Lang and Ph. Avouris. Carbon-atom wires: charge-transfer doping, voltage drop, and the effect of distortions. *Phys. Rev. Lett.*, **84**, 358–361, (2000).
- [325] N. Kobayashi, M. Brandbyge, and M. Tsukada. Conductance through atoms: Dot or channel? *Jpn. J. Appl. Phys.*, **38**, 336–338, (1999).
- [326] N. Kobayashi, M. Brandbyge, and M. Tsukada. Transmission channels through Na and Al atom wire. *Surf. Sci.*, **433–435**, 854–857, (1999).
- [327] N. Kobayashi, M. Brandbyge, and M. Tsukada. First-principles study of electron transport through monatomic Al and Na wires. *Phys. Rev. B*, **15**, 8430–8437, (2000).
- [328] C.C. Wan, J.-L. Mozos, G. Taraschi, J. Wang, and H. Guo. Quantum transport through atomic wires. *Appl. Phys. Lett.*, **71**, 419–421, (1997).
- [329] H.-S. Sim, H.-W. Lee, and K.J. Chang. Even-odd behavior of conductance in monatomic sodium wires. *Phys. Rev. Lett.*, **87**, 096803, (2001).
- [330] M. Okamoto and K. Takayanagi. Structure and conductance of a gold atomic chain. *Phys. Rev. B*, **60**, 7808–7811, (1999).
- [331] J.A. Torres, E. Tosatti, A. Dal Corso, F. Ercolessi, J.J. Kohanoff, F.D. Di Tolla, and J.M. Soler. The puzzling stability of monatomic gold wires. *Surface Science*, **426**, L441–L446, (1999).
- [332] H. Häkkinen, R.N. Barnett, and U. Landman. Gold nanowires and their chemical modifications. *J. Phys. Chem. B*, **103**, 8814–8816, (1999).
- [333] H. Häkkinen, R.N. Barnett, A.G. Scherbakov, and U. Landman. Nanowire gold chains: formation mechanisms and conductance. *J. Phys. Chem. B*, **104**, 9063–9066, (2000).
- [334] L. De Maria and M. Springborg. Electronic structure and dimerization of a single monatomic gold wire. *Chem. Phys. Lett.*, **323**, 293–299, (2000).
- [335] G. Taraschi, J.L. Mozos, C. C. Wan, H. Guo, and J. Wang. Structural and transport properties of aluminum atomic wires. *Phys. Rev. B*, **58**, 13138–13145, (1998).
- [336] P. Sen, S. Ciraci, A. Buldum, and I. Batra. Structure of aluminum atomic chains. *Phys. Rev. B*, **64**, 195420, (2001).
- [337] D. Sanchez-Portal, E. Artacho, J. Junquera, A. Garcia, and J.M. Soler. Zigzag equilibrium structure in monatomic wires. *Surf. Sci.*, **482**, 1261–1265, (2001).
- [338] S.R. Bahn and K.W. Jacobsen. Chain formation of metal atoms. *Phys. Rev. Lett.*, **87**, 266101, (2001).
- [339] J.J. Palacios, A.J. Pérez-Jiménez, E. Louis, E. San-Fabian, and J.A. Vergés. First-principles approach to electrical transport in atomic-scale nanostructures. *Phys. Rev. B*, **66**, 035322, (2002).
- [340] D. Vion, P.F. Orfila, P. Joyez, D. Esteve, and M.H. Devoret. Miniature electrical filters for single electron devices. *J. Appl. Phys.*, **77**, 2519–2524, (1995).
- [341] D.C. Glatli, P. Jacques, A. Kumar, P. Pari, and L. Saminadayar. A noise detection scheme with 10 mK noise temperature resolution for semiconductor single electron tunneling devices. *J. Appl. Phys.*, **81**, 7350–7356, (1997).
- [342] E. Scheer, J.C. Cuevas, A. Levy Yeyati, A. Martín-Rodero, P. Joyez, M.H. Devoret, D. Esteve, and C. Urbina. Conduction channels of superconducting quantum point contacts. *Physica B*, **280**, 425–431, (2000).
- [343] H. Suderow, E. Bascones, W. Belzig, F. Guinea, and S. Vieira. Andreev scattering in nanoscopic junctions at high magnetic fields. *Europhys. Lett.*, **50**, 749–755, (2000).
- [344] H. Suderow, A. Izquierdo, and S. Vieira. Superconducting lead nanobridges under magnetic fields. *Physica C*, **332**, 327–332, (2000).
- [345] E. Scheer, W. Belzig, Y. Naveh, M.H. Devoret, D. Esteve, and C. Urbina. Proximity effect and multiple Andreev reflections in gold atomic contacts. *Phys. Rev. Lett.*, **86**, 284–287, (2001).
- [346] E. Bascones and F. Guinea. Subgap resonances and conduction channels in mesoscopic superconducting devices. *Preprint*, (1998). <http://arXiv.org/abs/cond-mat/9809352>.
- [347] M. Reznikov, M. Heiblum, H. Shtrikman, and D. Mahalu. Temporal correlation of electrons: suppression of shot noise in a ballistic quantum point contact. *Phys. Rev. Lett.*, **75**, 3340–3343, (1995).
- [348] A. Kumar, L. Saminadayar, D.C. Glatli, Y. Jin, and B. Etienne. Experimental test of the quantum shot noise reduction theory. *Phys. Rev. Lett.*, **76**, 2778–2781, (1996).
- [349] H.E. van den Brom and J.M. van Ruitenbeek. Quantum suppression of shot noise in atom-size metallic contacts. *Phys. Rev. Lett.*, **82**, 1526–1529, (1999).
- [350] H.E. van den Brom and J.M. van Ruitenbeek. Shot noise suppression in metallic quantum point contacts. In D. Reguera, G. Platero, L.L. Bonilla, and J.M. Rubí, editors, *Statistical and Dynamical Aspects of Mesoscopic Systems*, pages 114–122, Berlin Heidelberg, (2000). Springer-Verlag.
- [351] R. Cron, M.F. Goffman, D. Esteve, and C. Urbina. Multiple-charge-quanta shot noise in superconducting atomic contacts. *Phys. Rev. Lett.*, **86**, 4104–4107, (2001).
- [352] P.A. Lee and A.D. Stone. Universal conductance fluctuations in metals. *Phys. Rev. Lett.*, **55**, 1622–1625, (1985).
- [353] B.L. Al'tshuler and D.E. Khmel'nitskii. Fluctuation properties of small conductors. *JETP Lett.*, **42**, 359–363, (1985).
- [354] P.A.M. Holweg, J.A. Kokkedee, J. Caro, A.H. Ver-

- bruggen, S. Radelaar, A.G.M. Jansen, and P. Wyder. Conductance fluctuations in a ballistic metallic point contact. *Phys. Rev. Lett.*, **67**, 2549–2552, (1991).
- [355] V.I. Kozub, J. Caro, and P.A.M. Holweg. Local-interference theory of conductance fluctuations in ballistic metallic point contacts: combination of near and remote backscattered trajectories. *Phys. Rev. B*, **50**, 15126–15137, (1994).
- [356] P.A. Mello and A.D. Stone. Maximum-entropy model for quantum-mechanical interference effects in metallic conductors. *Phys. Rev. B*, **44**, 3559–3576, (1991).
- [357] C.W.J. Beenakker and J.A. Melsen. Conductance fluctuations, weak localization, and shot noise for a ballistic constriction in a disordered wire. *Phys. Rev. B*, **50**, 2450–2457, (1994).
- [358] J. Bürki, C.A. Stafford, X. Zotos, and D. Baeriswyl. Cohesion and conductance of disordered metallic point contacts. *Phys. Rev. B*, **60**, 5000–5008, (1999).
- [359] P. García-Mochales, P.A. Serena, N. García, and J.L. Costa-Krämer. Conductance in disordered nanowires: Forward and backscattering. *Phys. Rev. B*, **53**, 10268–10280, (1996).
- [360] G. Wexler. The size effect and the non-local Boltzmann transport equation in orifice and disk geometry. *Proc. Phys. Soc.*, **89**, 927–941, (1966).
- [361] C. Untiedt, G. Rubio Bollinger, S. Vieira, and N. Agraït. Quantum interference in atomic-sized point-contacts. *Phys. Rev. B*, **62**, 9962–9965, (2000).
- [362] B. Ludoph and J.M. van Ruitenbeek. Thermopower of atomic-size metallic contacts. *Phys. Rev. B*, **59**, 12290–12293, (1999).
- [363] D. Erts, H. Olin, L. Ryen, E. Olssen, and A. Thölén. Maxwell and Sharvin conductance in gold point contacts investigated using TEM-STM. *Phys. Rev. B*, **61**, 12725–12727, (2000).
- [364] N.V. Zavaritskiĭ. Electron-phonon interaction and characteristics of metal electrons. *Sov. Phys. USP.*, **15**, 608–625, (1973). [*Usp. Fiz. Nauk* **108** (1972) 241–272].
- [365] I. K. Yanson and O. I. Shklyarevskii. Point-contact spectroscopy of metallic alloys and compounds (review). *Sov. J. Low Temp. Phys.*, **12**, 509–528, (1986).
- [366] J. Bonča and S.A. Trugman. Effect of inelastic processes on tunneling. *Phys. Rev. Lett.*, **75**, 2566–2569, (1995).
- [367] E.G. Emberly and G. Kirczenow. Landauer theory, inelastic scattering, and electron transport in molecular wires. *Phys. Rev. B*, **61**, 5740–5750, (2000).
- [368] N. Agraït, C. Untiedt, G. Rubio-Bollinger, and S. Vieira. Onset of dissipation in ballistic atomic wires. *Phys. Rev. Lett.*, **88**, 216803, (2002).
- [369] H.E. van den Brom. *Fluctuation phenomena in atomic-size contacts*. PhD thesis, Universiteit Leiden, The Netherlands, (2000).
- [370] K.S. Ralls, D.C. Ralph, and R.A. Buhrman. Individual-defect electromigration in metal nanobridges. *Phys. Rev. B*, **40**, 11561–11570, (1989).
- [371] P.A.M. Holweg, J. Caro, A.H. Verbruggen, and S. Radelaar. Ballistic electron transport and two-level resistance fluctuations in noble-metal nanobridges. *Phys. Rev. B*, **45**, 9311–9319, (1992).
- [372] T.N. Todorov. Local heating in ballistic atomic-scale contacts. *Philosophical Magazine B*, **77**, 965–973, (1998).
- [373] R. Holm. *Electric contacts*. Springer Verlag, Berlin, (1967).
- [374] H.E. van den Brom, Y. Noat, and J.M. van Ruitenbeek. Two-level systems in atomic-size point contacts. In V. Chandrasekhar, C. van Haesendonck, and A. Zawadowski, editors, *Kondo Effect and Dephasing in Low-Dimensional Metallic Systems*, pages 249–252, Dordrecht, (2001). Kluwer Academic Publishers.
- [375] K.G. Wilson. *The Theory of Metals*. Cambridge University Press, Cambridge, 3rd edition, (1953).
- [376] J. Kondo. Resistance minimum in dilute magnetic alloys. *Prog. Theor. Phys.*, **32**, 37–49, (1964).
- [377] A.C. Hewson. *The Kondo Problem to Heavy Fermions*. Cambridge University Press, Cambridge, 3rd edition, (1993).
- [378] D.C. Ralph and R.A. Buhrman. Kondo-assisted and resonant tunneling via a single charge trap: a realisation of the Anderson model out of equilibrium. *Phys. Rev. Lett.*, **72**, 3401–3404, (1994).
- [379] G. Chen and N. Giordano. Thickness dependence of the Kondo effect in AuFe films. *Phys. Rev. Lett.*, **66**, 209–211, (1991).
- [380] V. Chandrasekhar, P. Santhanam, N.A. Penebre, R.A. Webb, H. Vloeberghs, C. Van Haesendonck, and Y. Bruynseraede. Absence of size dependence of the Kondo resistivity. *Phys. Rev. Lett.*, **72**, 2053–2056, (1994).
- [381] D. Goldhaber-Gordon, H. Shtrikman, D. Mahalu, D. Abusch-Magder, U. Meirav, and M.A. Kastner. Kondo effect in a single-electron transistor. *Nature*, **391**, 156–159, (1998).
- [382] V. Madhavan, W. Chen, T. Jamneala, M.F. Crommie, and N.S. Wingreen. Tunneling into a single magnetic atom: Spectroscopic evidence of the Kondo resonance. *Science*, **280**, 567–569, (1998).
- [383] M. Daybell. The *s-d* model and the Kondo effect: thermal and transport properties. In G.T. Rado and H. Suhl, editors, *Magnetism*, volume 5, pages 121–147. Academic Press, New York, (1973).
- [384] A.A. Lysykh, I.K. Yanson, O.I. Shklyarevskii, and Yu.G. Naydyuk. Point-contact spectroscopy of electron-phonon interaction in alloys. *Solid State Commun.*, **35**, 987–989, (1980).
- [385] I.K. Yanson, V.V. Fisun, R. Hesper, A.V. Khotkevich, J.M. Krams, J.A. Mydosh, and J.M. van Ruitenbeek. Size dependence of Kondo scattering in point contacts. *Phys. Rev. Lett.*, **74**, 302–305, (1995).
- [386] N. van der Post, F.L. Mettes, J.A. Mydosh, J.M. van Ruitenbeek, and I.K. Yanson. Size dependence of Kondo scattering in point contacts: Fe impurities in Cu. *Phys. Rev. B*, **53**, R476–R479, (1996).
- [387] G. Zarand and L. Udvardi. Enhancement of the Kondo temperature of magnetic impurities in metallic point contacts due to the fluctuations of the local density of states. *Phys. Rev. B*, **54**, 7606–7609, (1996).
- [388] M.A. Blachly and N. Giordano. Kondo effect in systems of reduced dimensionality. *Phys. Rev. B*, **51**, 12537–12550, (1995).
- [389] O. Ujsaghy and A. Zawadowski. Spin-orbit-induced magnetic anisotropy for impurities in metallic samples. I. Surface anisotropy. *Phys. Rev. B*, **57**, 11598–11608, (1998).
- [390] O. Ujsaghy and A. Zawadowski. Spin-orbit-induced magnetic anisotropy for impurities in metallic samples. II. Finite-size dependence in the Kondo resistivity. *Phys. Rev. B*, **57**, 11609–11622, (1998).

- [391] C. Strunk, M. Henny, C. Schönenberger, G. Neuttiens, and C. Van Haesendonck. Size dependent thermopower in mesoscopic AuFe wires. *Phys. Rev. Lett.*, **81**, 2982–2985, (1998).
- [392] S. Hershfield, J.H. Davies, and J.W. Wilkins. Probing the Kondo resonance by resonant tunneling through an Anderson impurity. *Phys. Rev. Lett.*, **67**, 3720–3723, (1991).
- [393] T.K. Ng. Nonlinear resonant tunneling through an Anderson impurity at low temperature. *Phys. Rev. Lett.*, **70**, 3635–3638, (1993).
- [394] A. Levy Yeyati, A. Martín-Rodero, and F. Flores. Electron correlation resonances in the transport through a single quantum level. *Phys. Rev. Lett.*, **71**, 2991–2994, (1993).
- [395] J. Li, W.-D. Schneider, R. Berndt, and B. Delley. Kondo scattering observed at a single magnetic impurity. *Phys. Rev. Lett.*, **80**, 2893–2896, (1998).
- [396] W. Chen, T. Jamneala, V. Madhavan, and M.F. Crommie. Disappearance of the Kondo resonance for atomically fabricated cobalt dimers. *Phys. Rev. B*, **60**, R8529–R8532, (1999).
- [397] T. Jamneala, V. Madhavan, W. Chen, and M.F. Crommie. Scanning tunneling spectroscopy of transition-metal impurities at the surface of gold. *Phys. Rev. B*, **61**, 9990–9993, (2000).
- [398] U. Fano. Effects of configuration interaction on intensities and phase shifts. *Phys. Rev.*, **124**, 1866–1878, (1961).
- [399] H. C. Manoharan, C.P. Lutz, and D.W. Eigler. Quantum mirages formed by coherent projection of electronic structure. *Nature*, **403**, 512–515, (2000).
- [400] D.C. Ralph and R.A. Buhrman. Observation of Kondo scattering without magnetic impurities: a point contact study of two-level tunneling systems in metals. *Phys. Rev. Lett.*, **69**, 2118–2121, (1992).
- [401] D.C. Ralph, A.W.W. Ludwig, J. von Delft, and R.A. Buhrman. 2-channel Kondo scaling in conductance signals from 2-level tunneling systems. *Phys. Rev. Lett.*, **72**, 1064–1067, (1994).
- [402] P. Nozières and A. Blandin. Kondo effect in real metals. *J. Phys. (Paris)*, **41**, 193–211, (1980).
- [403] A. Zawadowski. Kondo-like state in a simple model for metallic glasses. *Phys. Rev. Lett.*, **45**, 211–214, (1980).
- [404] K. Vladar and A. Zawadowski. Theory of the interaction between electrons and the two-level system in amorphous metals. I. Noncommutative model hamiltonian and scaling of first order. *Phys. Rev. B*, **28**, 1564–1581, (1983).
- [405] R.J.P. Keijzers, O.I. Shklyarevskii, and H. van Kempen. Point-contact study of fast and slow two-level fluctuators in metallic glasses. *Phys. Rev. Lett.*, **77**, 3411–3414, (1996).
- [406] O.P. Balkashin, R.J.P. Keijzers, H. van Kempen, Yu.A. Kolesnichenko, and O.I. Shklyarevskii. Relaxation of two-level fluctuators in point contacts. *Phys. Rev. B*, **58**, 1294–1299, (1998).
- [407] N.S. Wingreen, B.L. Altshuler, and Y. Meir. Comment on “2-channel Kondo scaling in conductance signals from 2-level tunneling systems”. *Phys. Rev. Lett.*, **75**, 769, (1995).
- [408] D.C. Ralph, A.W.W. Ludwig, J. von Delft, and R.A. Buhrman. Ralph *et al.* reply. *Phys. Rev. Lett.*, **75**, 770, (1995).
- [409] T. Vegge, J.P. Sethna, S.-A. Cheong, K.W. Jacobsen, C.R. Myers, and D.C. Ralph. Calculation of quantum tunneling for a spatially extended defect: The dislocation kink in copper has a low effective mass. *Phys. Rev. Lett.*, **86**, 1546–1549, (2001).
- [410] J. von Delft, D.C. Ralph, R.A. Buhrman, S.K. Upadhyay, R.N. Louie, A.W.W. Ludwig, and V. Ambegaokar V. The 2-channel Kondo model I. Review of experimental evidence for its realization in metal nanoconstrictions. *Ann. Phys. - New York*, **263**, 1–55, (1998).
- [411] J. von Delft, A.W.W. Ludwig, and V. Ambegaokar V. The 2-channel Kondo model II. CFT calculation of non-equilibrium conductance through a nanoconstriction containing 2-channel Kondo impurities. *Ann. Phys. - New York*, **273**, 175–241, (1999).
- [412] J. Wang, J.-L. Mozos H. Guo and, C.C. Wan, G. Taraschi, and Q. Zheng. Capacitance of atomic junctions. *Phys. Rev. Lett.*, **80**, 4277–4280, (1998).
- [413] H. Grabert and M.H. Devoret, editors. *Single Charge Tunneling*. Plenum Press, New York, (1992).
- [414] D.S. Golubev and A.D. Zaikin. Coulomb interaction and quantum transport through a coherent scatterer. *Phys. Rev. Lett.*, **86**, 4887–4890, (2001).
- [415] A. Levy Yeyati, A. Martín-Rodero, D. Esteve, and C. Urbina. Direct link between Coulomb blockade and shot noise in a quantum coherent structure. *Phys. Rev. Lett.*, **87**, 46802, (2001).
- [416] R. Cron, E. Vecino, M.H. Devoret, D. Esteve, P. Joyez, A. Levy Yeyati, A. Martín-Rodero, and C. Urbina. Dynamical Coulomb blockade in quantum point contacts. In T. Martin, G. Montambaux, and J. Trần Thanh Vân, editors, *Electronic Correlations: from Meso- to Nano-Physics*, pages 17–22, Les Ulis, France, (2001). EDP Sciences.
- [417] G.-L. Ingold and Yu.V. Nazarov. Charge tunneling rates in ultrasmall junctions. In H. Grabert and M.H. Devoret, editors, *Single Charge Tunneling*, chapter 2, pages 21–107. Plenum Press, New York, (1992).
- [418] M.H. Devoret, D. Esteve, H. Grabert, G.-L. Ingold, H. Pothier, and C. Urbina. Effect of the electromagnetic environment on the coulomb blockade in ultrasmall tunnel junctions. *Phys. Rev. Lett.*, **64**, 1824–1827, (1990).
- [419] C.J. Muller and R. de Bruyn Ouboter. Observation of the ‘skew supercurrent’ in josephson vacuum barrier tunnel junctions as a function of the junction normal resistance. *Physica B*, **194-196**, 1043–1044, (1994).
- [420] B.J. Vleeming, C.J. Muller, M.C. Koops, and R. de Bruyn Ouboter. Single-atom point contacts in the superconducting state. *Phys. Rev. B*, **50**, 16741–16744, (1994).
- [421] I.O. Kulik and A.N. Omelyanchuk. Contribution to the microscopic theory of the Josephson effect in superconducting bridges. *JETP Lett.*, **21**, 96–97, (1975).
- [422] M.C. Koops, G.V. van Duynveldt, and R. de Bruyn Ouboter. Direct observation of the current-phase relation of an adjustable superconducting point contact. *Phys. Rev. Lett.*, **77**, 2542–2545, (1996).
- [423] R. de Bruyn Ouboter and A.N. Omelyanchouk. On the influence of thermal fluctuations on the current-phase relation in superconducting point contacts. *Physica B*, **216**, 37–42, (1996).
- [424] P. Dieleman, H.G. Bukkems, T.M. Klapwijk, M. Schicke, and K.H. Gundlach. Observation of

- Andreev reflection enhanced shot noise. *Phys. Rev. Lett.*, **79**, 3486–3489, (1997).
- [425] T. Hoss, C. Strunk, T. Nussbaumer, R. Huber, U. Staufer, and C. Schönenberger. Multiple Andreev reflection and giant excess noise in diffusive superconductor/normal-metal/superconductor junctions. *Phys. Rev. B*, **62**, 4079–4085, (2000).
- [426] L. Venkataraman and C.M. Lieber. Molybdenum selenide molecular wires as one-dimensional conductors. *Phys. Rev. Lett.*, **83**, 5334–5337, (1999).
- [427] G. Roth and H. Fischer. On the way to heptahexaenylidene complexes: Trapping of an intermediate with the novel $M=C=C=C=C=C=CR_2$ moiety. *Organometallics*, **15**, 5766–5768, (1996).
- [428] B.H. Hong, S.C. Bae, C.-W. Lee, S. Jeong, and K.S. Kim. Ultrathin single-crystalline silver nanowire arrays formed in an ambient solution phase. *Science*, **294**, 348–351, (2001).
- [429] P. Segovia, D. Purdie, M. Hengsberger, and Y. Baer. Observation of spin and charge collective modes in one-dimensional metallic chains. *Nature*, **402**, 504–507, (1999).
- [430] C. Pampuch, O. Rader, T. Kachel, W. Gudat, C. Carbone, R. Kläsges, G. Bihlmayer, S. Blügel, and W. Eberhardt. One-dimensional spin-polarized quantum-wire states in Au on Ni(110). *Phys. Rev. Lett.*, **85**, 2561–2564, (2000).
- [431] S.J. Koh and G. Ehrlich. Self-assembly of one-dimensional surface structures: long-range interactions in the growth of Ir and Pd on W(110). *Phys. Rev. Lett.*, **87**, 106103, (2001).
- [432] H. Koizumi, Y. Oshima, Y. Kondo, and K. Takayanagi. Quantitative high-resolution microscopy on a suspended chain of gold atoms. *Ultramicroscopy*, **88**, 17–24, (2001).
- [433] S.R. Bahn, N. Lopez, J.K. Nørskov, and K.W. Jacobsen. Adsorption-induced restructuring of gold nano-chains. *preprint*, (2001).
- [434] S.R. Bahn. *Computer simulations of nanochains*. PhD thesis, Technical University of Denmark, Lyngby, (2001).
- [435] S.B. Legoas, D.S. Galvão, V. Rodrigues, and D. Ugarte. Origin of anomalously long interatomic distances in suspended gold chains. *Phys. Rev. Lett.*, **88**, 076105, (2002).
- [436] C. Untiedt, A.I. Yanson, R. Grande, G. Rubio-Bollinger, N. Agraït, S. Vieira, and J.M. van Ruitenbeek. Calibration of the length of a chain of single gold atoms. *Phys. Rev. B*, (2002). in print.
- [437] J. Nakamura, N. Kobayashi, S. Watanabe, and M. Aono. Structural stability and electronic states of gold nanowires. *Surf. Sci.*, **482–485**, 1266–1271, (2001).
- [438] N. Agraït, C. Untiedt, G. Rubio-Bollinger, and S. Vieira. Electron transport and phonons in atomic wires. *Chem. Phys.*, **281**, 231–234, (2002).
- [439] C. Untiedt, R.H.M. Smit, and J.M. van Ruitenbeek. Length dependence of the maximum current in atomic gold chains. *Preprint*, (2002).
- [440] T.N. Todorov, J. Hoekstra, and A.P. Sutton. Current-induced embrittlement of atomic wires. *Phys. Rev. Lett.*, **86**, 3606–3609, (2001).
- [441] E.G. Emberly and G. Kircznov. Electron standing wave formation in atomic wires. *Phys. Rev. B*, **60**, 6028–6033, (1999).
- [442] G.M. Finbow, R.M. Lynden-Bell, and I.R. McDonald. Atomistic simulation of the stretching of nanoscale metal wires. *Molecular Physics*, **92**, 705–714, (1997).
- [443] A.P. Sutton and T.N. Todorov. Atomic chains in molecular dynamics simulation for Al contacts. unpublished.
- [444] A. Bartolini, F. Ercolessi, and E. Tosatti. The (111) surface reconstruction of gold in the glue model. In J.F. van der Veen and M.A. Van Hove, editors, *The structure of surfaces II*, pages 132–136, Berlin, (1988). Springer-Verlag.
- [445] K.-M. Ho and K.P. Bohnen. Stability of the missing-row reconstruction on fcc (110) transition metal surfaces. *Phys. Rev. Lett.*, **59**, 1833–1836, (1987).
- [446] N. Takeuchi, C.T. Chan, and K.M. Ho. Theoretical study of noble-metal (100) surface reconstructions using first-principles techniques. *Phys. Rev. Lett.*, **63**, 1273–1276, (1989).
- [447] N. Takeuchi, C.T. Chan, and K.M. Ho. Reconstructions of the (100) surfaces of Au and Ag. *Phys. Rev. B*, **43**, 14363–14370, (1991).
- [448] A. Filippetti and V. Fiorentini. Reconstructions of Ir(110) and (100): an ab initio study. *Surf. Sci.*, **377–379**, 112–116, (1997).
- [449] P. Pykkö. Relativistic effects in structural chemistry. *Chem. Rev.*, **88**, 563–594, (1988).
- [450] R. Gutiérrez, F. Grossmann, and R. Schmidt. Resistance of atomic sodium wires. *Acta Phys. Pol. B*, **32**, 443–449, (2001).
- [451] S. Datta, W. Tian, S. Hong, R. Reifenberger, J.I. Henderson, and C.P. Kubiak. Current-voltage characteristics of self-assembled monolayers by scanning tunneling microscopy. *Phys. Rev. Lett.*, **79**, 2530–2533, (1997).
- [452] B. Larade, J. Taylor, H. Mehrez, and H. Guo. Conductance, i - v curves, and negative differential resistance of carbon atomic wires. *Phys. Rev. B*, **64**, 075420, (2001).
- [453] O. Gülseren, F. Ercolessi, and E. Tosatti. Noncrystalline structures of ultrathin unsupported nanowires. *Phys. Rev. Lett.*, **80**, 3775–3778, (1998).
- [454] E. Tosatti, S. Prestipino, S. Kostlmeier, A. Dal Corso, and F.D. Di Tolla. String tension and stability of magic tip-suspended nanowires. *Science*, **291**, 288–290, (2001).
- [455] W.A. de Heer. The physics of simple metal clusters: experimental aspects and simple models. *Rev. Mod. Phys.*, **65**, 611–676, (1993).
- [456] M. Brack. The physics of simple metal clusters: self-consistent jellium model and semiclassical approaches. *Rev. Mod. Phys.*, **65**, 677–732, (1993).
- [457] T.P. Martin. Shells of atoms. *Phys. Rep.*, **273**, 199–241, (1996).
- [458] W.A. de Heer. Confinement and size effects in free metal clusters. In K.-H. Meiwes-Broer, editor, *Metal clusters at surfaces: structure, quantum properties, physical chemistry*, pages 1–35. Springer, Berlin, (2000).
- [459] W.D. Knight, K. Clemenger, W.A. de Heer, W.A. Saunders, M.Y. Chou, and M.L. Cohen. Electronic shell structure and abundance of sodium clusters. *Phys. Rev. Lett.*, **52**, 2141–2143, (1984).
- [460] J. Pedersen, S. Bjørnholm, J. Borggreen, K. Hansen, T.P. Martin, and H.D. Rasmussen. Observation of quantum supershells in clusters of sodium atoms. *Nature*, **353**, 733–735, (1991).
- [461] T.P. Martin, T. Bergmann, H. Göhlich, and T. Lange. Electronic shells and shells of atoms in metallic clusters. *Z. Phys. D*, **19**, 25–29, (1991).

- [462] M.C. Guzwiller. Periodic orbits and classical quantization conditions. *J. Math. Phys.*, **12**, 343–358, (1971).
- [463] R. Balian and C. Bloch. Distribution of eigenfrequencies for the wave equation in a finite domain: III. Eigenfrequency density oscillations. *Ann. Phys. (N.Y.)*, **69**, 76–160, (1972).
- [464] C. Bréchnignac, Ph. Cahuzac, M. de Frutos, J.Ph. Roux, and K. Bowen. Observation of electronic shells in large lithium clusters. In P. Jena, S.N. Khanna, and B.K. Rao, editors, *Physics and chemistry of finite systems: from clusters to crystals*, pages 369–374, Netherlands, (1992). Kluwer Academic.
- [465] M. Pellarin, E. Cottancin, B. Baguenard, J. Lermé, J.L. Vialle, and M. Broyer. Observation of two successive quantum supershells in a 15 000-electron fermionic system. *Phys. Rev. B*, **52**, 16807–16811, (1995).
- [466] C. Höppler and W. Zwerger. Quantum fluctuations in the cohesive force of metallic nanowires. *Phys. Rev. B*, **59**, R7849–R7851, (1999).
- [467] M.J. Puska, E. Ogando, and N. Zabala. Shell and super-shell structures of nanowires: A quantum-mechanical analysis. *Phys. Rev. B*, **64**, 033401, (2001).
- [468] T.P. Martin, S. Bjørnholm, J. Borggreen, C. Bréchnignac, Ph. Cahuzac, K. Hansen, and J. Pedersen. Electronic shell structure of laser-warmed Na clusters. *Chem. Phys. Lett.*, **186**, 53–57, (1991).
- [469] J. Bürki and C.A. Stafford. Statistics of quantum transport in metal nanowires with surface disorder. In T. Martin, G. Montambaux, and J. Trần Thanh Vân, editors, *Electronic Correlations: from Meso- to Nano-Physics*, pages 27–30, Les Ulis, France, (2001). EDP Sciences.
- [470] A.I. Yanson, I.K. Yanson, and J.M. van Ruitenbeek. Supershell structure in alkali metal nanowires. *Phys. Rev. Lett.*, **84**, 5832–5835, (2000).
- [471] A.I. Yanson, I.K. Yanson, and J.M. van Ruitenbeek. Crossover from electronic to atomic shell structure in alkali metal nanowires. *Phys. Rev. Lett.*, **87**, 216805, (2001).
- [472] E.A. Jagla and E. Tosatti. Structure and evolution of a metallic nanowire-tip junction. *Phys. Rev. B*, **64**, 205412, (2001).
- [473] Y. Kondo and K. Takayanagi. Synthesis and characterization of helical multi-shell gold nanowires. *Science*, **289**, 606–608, (2000).
- [474] Y. Oshima, H. Koizumi, K. Mouri, H. Hirayama, K. Takayanagi, and Y. Kondo. Evidence of a single-wall platinum nanotube. *Phys. Rev. B*, **65**, 121401, (2002).
- [475] G. Bilalbegović. Structure and stability of finite gold nanowires. *Phys. Rev. B*, **58**, 15412–15415, (1998).
- [476] B. Wang, S. Yin, G. Wang, A. Buldum, and J. Zhao. Novel structures and properties of gold nanowires. *Phys. Rev. Lett.*, **86**, 2046–2049, (2001).
- [477] R. Cron. *Atomic contacts: a test-bed for mesoscopic physics*. PhD thesis, Université P. et M. Curie, Paris, France, (2001).
- [478] M.A. Despósito and A. Levy Yeyati. Controlled dephasing of andreev states in superconducting quantum point contacts. *Phys. Rev. B*, **64**, 140511, (2001).
- [479] J. Lantz, V.S. Shumeiko, E. Bratus, and G. Wendin. Flux qubit with a quantum point contact. *Physica C*, **368**, 315–319, (2002).
- [480] J. Park, A.N. Pasupathy, J.I. Goldsmith, C. Chang, Y. Yaish, J.R. Petta, M. Rinkoski, J.P. Sethna, H.D. Abruña, P.L. McEuen, and D. Ralph. Coulomb blockade and the Kondo effect in single atom transistors. *Nature*, **417**, 722–725, (2002).
- [481] W. Liang, M.P. Shores, M. Bockrath, J.R. Long, and H. Park. Kondo resonance in a single-molecule transistor. *Nature*, **417**, 725–729, (2002).
- [482] A. Ozpineci and S. Ciraci. Quantum effects of thermal conductance through atomic chains. *Phys. Rev. B*, **63**, 125415, (2001).
- [483] M.P.A. Fisher and L.I. Glazman. Transport in a one-dimensional Luttinger liquid. In L.L. Sohn, L.P. Kouwenhoven, and G. Schön, editors, *Mesoscopic Electron Transport*, volume 345 of *NATO-ASI Series E: Appl. Sci.*, pages 331–373, Dordrecht, (1997). Kluwer Academic Publishers.
- [484] M. Bockrath, D.H. Cobden, J. Lu, A.G. Rinzler, R.E. Smalley, L. Balents, and P.L. McEuen. Luttinger-liquid behaviour in carbon nanotubes. *Nature*, **397**, 598–601, (1999).
- [485] R.M. Metzger and M.P. Cava. Rectification by a single molecule of hexadecylquinolinium tricyanoquinodimethanide. *Ann. New York Acad. Sci.*, **852**, 93–115, (2000).
- [486] J. Chen, M.A. Reed, A.M. Rawlett, and J.M. Tour. Large on-off ratios and negative differential resistance in a molecular electronic device. *Science*, **286**, 1550–1552, (1999).
- [487] C.P. Collier, E.W. Wong, M. Belohradský, F.M. Raymo, J.F. Stoddart, P.J. Kuekes, R.S. Williams, and J.R. Heath. Electronically configurable molecular-based logic gates. *Science*, **285**, 391–394, (1999).
- [488] H.J. Gao, K. Sohlberg, Z.Q. Xue, H.Y. Chen, S.M. Hou, L.P. Ma, X.W. Fang, S.J. Pang, and S.J. Pennycook. Reversible, nanometer-scale conductance transitions in an organic complex. *Phys. Rev. Lett.*, **84**, 1780–1783, (2000).
- [489] M.A. Reed, J. Chen, A.M. Rawlett, D.W. Price, and J.M. Tour. Molecular random access memory cell. *Appl. Phys. Lett.*, **78**, 3735–3737, (2001).
- [490] M.A. Reed, C. Zhou, C.J. Muller, T.P. Burgin, and J.M. Tour. Conductance of a molecular junction. *Science*, **278**, 252–254, (1997).
- [491] C. Kergueris, J.-P. Bourgoin, S. Palacin, D. Esteve, C. Urbina, M. Magoga, and C. Joachim. Electron transport through a metal-molecule-metal junction. *Phys. Rev. B*, **59**, 12505–12513, (1999).
- [492] J. Reichert, R. Ochs, D. Beckmann, H.B. Weber, M. Mayor, and H. von Löhneisen. Driving current through single organic molecules. *Phys. Rev. Lett.*, **88**, 176804, (2002).
- [493] C. Joachim, J.K. Gimzewski, and A. Aviram. Electronics using hybrid-molecular and mono-molecular devices. *Nature*, **408**, 541–548, (2000).
- [494] A. Nitzan. Electron transmission through molecules and molecular interfaces. *Annu. Rev. Phys. Chem.*, **52**, 681–750, (2001).